

Search for Supersymmetry in opposite-sign same-flavour dilepton events with the CMS detector

Von der Fakultät für Mathematik, Informatik und Naturwissenschaften der RWTH Aachen University zur Erlangung des akademischen Grades eines Doktors der Naturwissenschaften genehmigte Dissertation

vorgelegt von
Jan-Frederik Schulte, M.Sc.
aus Münster

Berichter:
Prof. Dr. Lutz Feld
Prof. Dr. Michael Krämer

Termin der mündlichen Prüfung: xx.xx.2015

Diese Dissertation ist auf den Internetseiten der Hochschulbibliothek online verfügbar.

Contents

1	Introduction	1
1.1	Definition of variables	2
2	The Standard Model and Supersymmetry	5
2.1	The Standard Model of particle physics	5
2.2	Supersymmetry	7
2.2.1	Theoretical foundation	7
2.2.2	Dilepton mass edges in Supersymmetry	9
2.3	Standard Model processes	12
3	Experimental setup	15
3.1	CERN Large Hadron Collider	15
3.2	CMS detector	17
3.2.1	Tracking system	17
3.2.2	Electromagnetic calorimeter	19
3.2.3	Hadron calorimeter	20
3.2.4	Muon system	22
3.3	Trigger and data acquisition	24
4	Data analysis and event selection	29
4.1	Object reconstruction	29
4.1.1	Vertex reconstruction	29
4.1.2	Muon reconstruction and identification	29
4.1.3	Electron reconstruction and identification	30
4.1.4	Observables reconstructed with particle flow	32
4.2	Event processing and datasets	37
4.2.1	Primary datasets	38
4.2.2	Simulated datasets	38
4.3	Event selection	44
4.3.1	Event cleaning	44
4.3.2	Inclusive dilepton selection	45
4.3.3	Selections in E_T^{miss} and jet multiplicity	47
4.3.4	Selections in $m_{\ell\ell}$	48
5	Estimation of Standard Model backgrounds	53
5.1	Flavour-symmetric backgrounds	53
5.1.1	Direct measurement of $R_{\text{SF}/\text{OF}}$	54
5.1.2	Determination of $R_{\text{SF}/\text{OF}}$ with the factorisation method	55
5.1.3	Combined correction factors and resulting background estimates	63
5.1.4	Validation of background estimates	65
5.2	Drell–Yan backgrounds	72
5.2.1	JZB method	72
5.2.2	E_T^{miss} templates method	73

5.2.3	Extrapolation to off-Z regions	73
5.2.4	Resulting background prediction	74
6	Counting experiment	79
6.1	Results and further studies	79
6.2	Interpretation in simplified models	83
6.2.1	Statistical interpretation	87
7	Search for a kinematic edge	89
7.1	Background and signal models	89
7.1.1	Model for Drell–Yan backgrounds	89
7.1.2	Model for flavour-symmetric backgrounds	91
7.1.3	Signal model	94
7.2	Combined model	96
7.3	Fit validation	98
7.3.1	Fit performance on simulation	98
7.3.2	Fit performance studies using toy datasets	100
7.4	Fit results on data	115
8	Conclusion	121
A	Trigger paths	123
B	Simulated Samples	125
C	Dependencies of $r_{\mu e}$	127
D	Dependencies of R_T	131
E	Dependencies of $R_{\text{out/in}}$	135

1 Introduction

The desire to understand the fundamental building blocks and underlying structures of our world has driven humanity's exploration of physics at the smallest scales. What started out as a pursuit of ideas purely within the mind in ancient Greece has developed into a fruitful interplay of both experiment and theory in modern particle physics. Today the Standard Model of particle physics describes the known particles and their interactions and has withstood countless experimental challenges. However, theoretical concerns and the desire to incorporate experimental observations not yet described within the Standard Model have lead to the conviction that yet unknown physical effects will manifest themselves if particle interactions are probed at energy scales of $\mathcal{O}(\text{TeV})$.

This is the purpose of the Large Hadron Collider (LHC), which collides protons at centre-of-mass energies of several TeV. In addition to many precision measurements of established phenomena at this previously inaccessible energy scale, discovering the Higgs boson and thereby completing the Standard Model has been a large success of this undertaking. Now the focus lies even more on going beyond the Standard Model into the realm of new physics. Many ideas exists on how to extend the existing theory and an extensive search program is conducted in search of the new particles and interactions predicted by those models.

One of the most attractive concepts is that of Supersymmetry, which introduces a symmetry between fermions and bosons. In this framework, a partner particle to each of the known Standard Model particles exists, differing in spin by $\frac{1}{2}\hbar$. In principle these partners have the same mass as their Standard Model counterparts. However, none of them have been discovered yet, which implies that Supersymmetry is broken, allowing for higher masses of the supersymmetric particles.

In this analysis, evidence for the existence of heavy supersymmetric particles is sought, exploiting a characteristic signature of their decay. In the decay of a neutralino particle, two charged leptons of the same flavour and opposite sign can be produced together with a lighter neutralino, which escapes detection. This correlated production of the leptons results in a characteristic edge in the distribution of their invariant mass.

The full data sample of proton-proton collisions at a centre-of-mass energy of 8 TeV recorded by the Compact Muon Solenoid (CMS) experiment in 2012, corresponding to an integrated luminosity of 19.5 fb^{-1} , is used. The presence of a supersymmetric signal in the data is assessed in two ways. First, event counts in different selections are compared to the expectation from Standard Model backgrounds. In a second approach, the characteristic edge signature is used in a shape analysis to separate a possible signal from the backgrounds. In the both cases, the background contributions are estimated entirely from data.

This work builds upon the previous achievements by Nikals Mohr and Daniel Sprenger in their doctoral theses [1, 2] and has been performed in part in collaboration with Marco-Andrea Buchmann [3]. The results have been published by the CMS collaboration [4]. This analysis presents an update of the published result, taking into account a later reprocessing of the data sample with improved calibrations. However, the analysis techniques have not been altered

and the outcome of the analysis remains largely unchanged.

This thesis is structured as follows: The remainder of this section is dedicated to the definition of commonly used variables. Section 2 discusses the theoretical foundations relevant to the analysis. In Section 3 the LHC and the CMS detector are described. The methods used to analyse the recorded data are outlined in Section 4 and the estimation of Standard Model backgrounds from data is presented in Section 5. The results of the analysis in the two approaches discussed above are presented in Sections 6 and 7.

1.1 Definition of variables

Throughout this thesis, quantities are expressed in natural units. In this system, the speed of light and the reduced Planck constant are set to unity:

$$c = \hbar = 1. \quad (1.1)$$

Energies and momenta are measured in GeV and lengths in GeV^{-1} . However, sometimes lengths are also given in meters or centimeters, if convenient.

The cross section of a physical process is given in barn, 1 b corresponding to 10^{-24} cm^2 .

The CMS experiment uses a right-handed coordinate system where the x- and y-axis point perpendicular to the beam direction towards the center of the LHC and upwards, respectively. The z-axis points in the direction of the counter-clockwise beam. These coordinates are usually transformed into a spherical coordinate system where ϕ is the azimuthal and θ is the polar angle. Instead of θ the pseudorapidity

$$\eta = -\ln \left(\tan \left(\frac{\theta}{2} \right) \right) \quad (1.2)$$

is commonly used, which coincides with the rapidity $y = \frac{1}{2} \ln \left(\frac{E+p_z}{E-p_z} \right)$ for $E \approx |p|$. The geometric distance of two objects in the detector is given by

$$\Delta R = \sqrt{(\phi_1 - \phi_2)^2 + (\eta_1 - \eta_2)^2}. \quad (1.3)$$

As the collisions at hadron colliders involve interactions of partons carrying unknown fractions of the protons' momenta, the momentum of the initial state along the beam axis is unknown. As the momenta of the partons transverse to the beam are negligible compared to those in z direction, the transverse plane provides a well defined initial state. Therefore, the transverse momentum and energy

$$p_T = \sqrt{p_x^2 + p_y^2} = p \cdot \sin(\theta), \quad E_T = \sqrt{E_x^2 + E_y^2} = E \cdot \sin(\theta) \quad (1.4)$$

are often used. The vectorial sum of the particles' p_T must be zero because of conservation of linear momentum. This is why the missing transverse energy

$$\vec{E}_T^{\text{miss}} = - \sum_{\text{particles}} \vec{p}_T \quad (1.5)$$

is defined as a quantity sensitive to particles leaving the experiment undetected, but also to mismeasurements and resolution effects. Usually, the absolute value $E_T^{\text{miss}} = |\vec{E}_T^{\text{miss}}|$ is used.

The amount of energy deposited in an event is characterised by the scalar sum of the p_T of all selected hadronic jets (see Section 4.1.4)

$$H_T = \sum_{\text{jets}} |p_T|. \quad (1.6)$$

For the sake of simplicity, particles and anti-particles are not distinguished in expressions if the meaning remains unambiguous from the context. For example, the decay $Z^0 \rightarrow \ell^+ \ell^-$ is simplified to $Z \rightarrow \ell\ell$.

2 The Standard Model and Supersymmetry

The Standard Model (SM) of particle physics is a highly successful, commonly accepted description of the fundamental particles and their interactions and at the same time subject to several shortcomings, motivating the search for signs of new phenomena beyond its scope. In this chapter a short overview of the SM and its shortcoming is given. Supersymmetry is presented as an attractive candidate for the extension of the SM and the phenomenological consequences of its existence relevant to this analysis are discussed.

2.1 The Standard Model of particle physics

The SM describes the fundamental particles in the framework of a renormalisable quantum field theory, in which each particle is represented by one quantum field [5, 6, 7, 8]. Two fundamental classes of particles are distinguished, bosons with integer spin and fermions with half-integer spin.

The fermions are in turn classified as quarks or leptons. The different types of quarks and leptons are known as “flavours”. There are six quark flavours, called up, down, strange, charm, bottom and top, and three electrically charged lepton flavours, electron (e), muon (μ) and tau (τ). The electrically neutral leptons, called neutrinos (ν), are assigned the names of the charged lepton of their generation. Of these there are three, each consisting of a charged lepton and the corresponding neutral neutrino and two quarks. Of the latter, one is up-type with an electric charge of $+\frac{2}{3}e$ and the other is down-type with charge $-\frac{1}{3}e$. The particle content of the fermionic sector of the SM is summarised in Table 2.1.

Of the four fundamental forces, the electromagnetic, weak, strong and gravitational forces, the first three are described by the SM. Each of these forces is mediated by spin-1 gauge bosons. In the case of the electromagnetic force this is the massless photon, which couples to

Table 2.1: Fermions in the SM. All masses and their uncertainties are taken from [9]. The uncertainties on the masses of the charged leptons are at most 0.01%.

	Leptons			Quarks		
	flavour	charge [e]	mass [GeV]	flavour	charge [e]	mass [GeV]
1 st generation	e	-1	$5.1 \cdot 10^{-4}$	down	$-\frac{1}{3}$	$2.3_{-0.5}^{+0.7} \cdot 10^{-3}$
	ν_e	0	$< 2 \cdot 10^{-9}$	up	$+\frac{2}{3}$	$4.8_{-0.3}^{+0.5} \cdot 10^{-3}$
2 nd generation	μ	-1	0.1	strange	$-\frac{1}{3}$	$9.5 \pm 0.5 \cdot 10^{-2}$
	ν_μ	0	$< 2 \cdot 10^{-9}$	charm	$+\frac{2}{3}$	1.28 ± 0.03
3 rd generation	τ	-1	1.8	bottom	$-\frac{1}{3}$	4.18 ± 0.03
	ν_τ	0	$< 2 \cdot 10^{-9}$	top	$+\frac{2}{3}$	$173.18 \pm 0.51 \pm 0.71$

the electric charge of particles. The weak force is mediated by three massive bosons, the W^\pm ($m_W = 80.4 \text{ GeV}$) and the Z^0 ($m_Z = 91.2 \text{ GeV}$), coupling to the weak charge. The charge of the strong force is called colour, to which 8 massless gluons couple. Of all fermions, only the quarks carry colour and participate in the strong interaction.

The group structure of the SM is $SU(3)_C \times SU(2)_L \times U(1)_Y$. The $SU(3)_C$, with C representing the colour charge, is the gauge group associated with the strong interaction. From the non-abelian structure of this group follows the presence of three- and four-gluon interactions in the SM [10]. Therefore, the strong interaction increases with distance, leading coloured particles to only exist in bound states. So far the existence of two- and three-quark states (mesons and baryons) has been established.

The subgroup $SU(2)_L \times U(1)_Y$ describes the unification of weak and electromagnetic interaction in the electroweak theory. The index L indicates that the weak isospin T couples only to left-handed particles and Y is the weak hypercharge. The $SU(3)_L$ introduces three vector fields, of which two mix to the observed $W^\pm = \frac{1}{\sqrt{2}}(W^1 \mp iW^2)$. The remaining neutral W^3 mixes with the B^0 arising from the $U(1)_Y$ group to form the photon and Z boson [11].

To give masses to the particles, the Higgs mechanism is introduced [12, 13, 14]. It postulates a complex scalar doublet that spontaneously breaks the $SU(2)_L$ gauge symmetry, allowing to give masses to the electro-weak gauge bosons while the $U(1)_Y$ remains unbroken and the photon massless. Fermions acquire mass through a Yukawa coupling to the Higgs field. The Higgs mechanism results in the presence of a massive neutral scalar boson. The discovery of such a particle with a mass of $125.09 \pm 0.24 \text{ GeV}$ [15] by the CMS and ATLAS collaborations at the LHC in 2012 [16, 17] and the good agreement of its properties with the prediction of the SM [18] provides evidence for the validity of this theory.

Shortcomings of the Standard Model

The discovery of the Higgs boson is a large success for the SM, and only the last in a long series of experimental results supporting the decades old theory. However, for a long time also the shortcomings of the SM have been known. Here only those most relevant to the motivation of Supersymmetry are discussed.

Higgs mass and naturalness

One of the most pressing issues is directly related to the Higgs boson and its mass. Quantum loop corrections to the bare Higgs boson mass-squared change the observable mass of the particle. For example the coupling to a fermion with coupling strength λ_f results in a correction of

$$\Delta m_H^2 = -\frac{|\lambda_f^2|}{8\pi^2} \Lambda_{UV}^2 + \dots, \quad (2.1)$$

where Λ_{UV} represents the energy scale up to which the SM is valid as an effective theory, i.e. the scale at which new physics will appear. This can be as large as the reduced Planck scale $M_P = (8\pi G_{\text{Newton}})^{-\frac{1}{2}} = 2.4 \cdot 10^{18} \text{ GeV}$, where effects of gravity become important at the quantum level. Therefore, the loop corrections are of enormous magnitude and have to

precisely cancel the bare Higgs boson mass to achieve an observable Higgs boson mass at the electroweak breaking scale. This required fine-tuning is known as the *Hierarchy problem* and is considered to be unnatural and motivates the presence of new physics at the TeV scale.

Astrophysical Observations

Astrophysical observation have been suggesting the presence of non-visible forms of matter, for example from the motion of galaxy clusters or galaxy rotation curves. The most precise measurements of the energy content of the universe come from observations of the cosmic microwave background [19]. The contribution of ordinary matter is only about 4.9%, while an unidentified dark matter, interacting only gravitational and possibly weakly, accounts for about 25.9% (the remaining 69.2% are attributed to dark energy). The SM does not provide any candidate for a dark matter particle, because neutrinos are disfavoured by structure formation in the early universe [9]. Possible candidates are so far undiscovered weakly interacting massive particles with masses of the order $\mathcal{O}(100 \text{ GeV})$, which require an extension of the SM.

Unification of forces

In the past, the increasingly deeper insights into the workings of nature have often allowed to find unified theoretical frameworks to describe different physical phenomena, for example the unification of the electric and magnetic forces into electromagnetism or its further unification with the weak force into the electroweak theory discussed above. Therefore, a further unification with the strong force into a grand unified theory (GUT) at higher energy scales is hoped for. However, as shown by the dashed lines in Figure 2.1, the running couplings of the three forces do not meet at any energy scale in the SM, excluding a unification inside the existing theoretical framework. As already indicated in the Figure, this could be accomplished by extension of the SM such as Supersymmetry, where the introduction of new particles at the TeV scale changes the running of the couplings.

2.2 Supersymmetry

Of the many proposed extensions of the SM, Supersymmetry (SUSY) [21] has been considered to be the most attractive in the last decades. It postulates the existence of a fermion partner to every SM boson and vice versa. This promises a solution to the naturalness problem of the Higgs boson mass and might also lead to a unification of forces and in certain models offer candidates for the dark matter particle. In the following a short description of the theoretical framework, based on [20], is given before the phenomenological consequences and the experimental signatures relevant to this analysis are discussed.

2.2.1 Theoretical foundation

Supersymmetry introduces a symmetry between bosons and fermions. In the minimal supersymmetric extension of the SM (MSSM), one *superpartner* is assigned to each SM particle

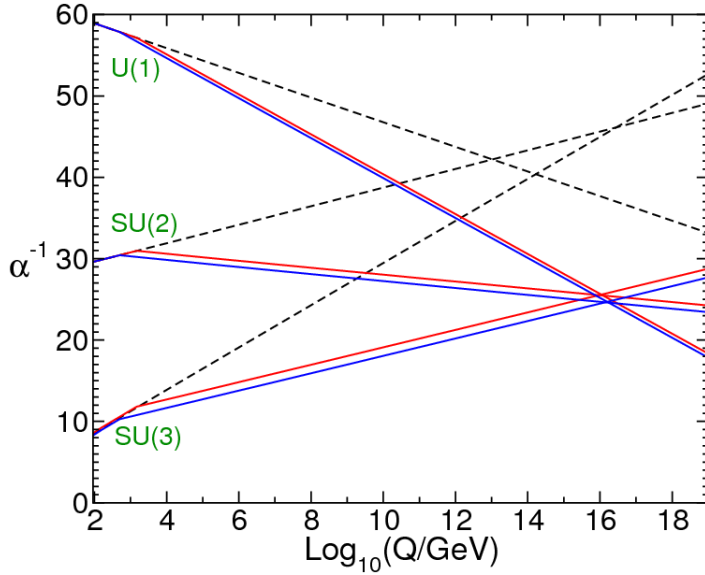


Figure 2.1: Running of the coupling α of the electromagnetic, weak and strong force in the SM (dashed lines) and Supersymmetry (red and blue lines)[20] with the energy scale Q .

which has the same quantum numbers except for the spin, which differs by $\frac{1}{2}$. The designated names of the new supersymmetric particles (*sparticles*) are derived by adding the prefix *s-* to all fermion partners and the postfix *-ino* to all boson partners. The same scheme holds also for categories of particles, so that *sleptons* and *squarks* are the partners of leptons and quarks and make up the *sfermions* while the *gauginos* are the partners of the gauge bosons.

The SM Higgs sector has to be extended to two complex scalar doublets to give masses to the particles

$$H_1 = \begin{pmatrix} H_1^0 \\ H_1^- \end{pmatrix}, \quad H_2 = \begin{pmatrix} H_2^0 \\ H_2^+ \end{pmatrix}. \quad (2.2)$$

Here, H_1 gives mass to down-type quarks and leptons while H_2 gives mass to up-type quarks. To these four Higgs states *higgsinos* are introduced as superpartners. In the spontaneous symmetry breaking eight degrees of freedom appear instead of four because of the second doublet. Three are used to give mass to the W and Z bosons, leaving five massive bosons. Therefore, SUSY results in an extended Higgs sector with two neutral scalars, h^0 and H^0 , one neutral pseudoscalar A^0 , and two charged scalars H^\pm . The observed Higgs boson can be identified with one of the two scalars, of which, by convention, h^0 is the lighter one.

The higgsinos and gauginos mix to eight mass eigenstates, the charginos $\tilde{\chi}_1^\pm$ and $\tilde{\chi}_2^\pm$ and the neutralinos $\tilde{\chi}_1^0$, $\tilde{\chi}_2^0$, $\tilde{\chi}_3^0$, and $\tilde{\chi}_4^0$. They are numbered in increasing mass. The additional particle content introduced in the MSSM is summarised in Table 2.2.

If such a model would be realised it would solve the hierarchy problem because the contributions of the superpartners to the quantum loop corrections to the Higgs boson mass have opposite sign than those of the SM particles, cancelling the quadratic dependency on the cut-off parameter Λ_{UV} . However, as no superpartners have been discovered so far, SUSY must be a broken symmetry and the sparticles can not have the same mass as the corresponding SM particles but must be heavier. Therefore, the cancellation of contributions to the Higgs boson

Table 2.2: Additional particle content of the MSSM.

particle	gauge eigenstates	mass eigenstates	spin
Standard Model			
Higgs bosons	$H_1^0, H_1^-, H_2^0, H_2^+$	h^0, H^0, A^0, H^\pm	0
Supersymmetry			
squarks	\tilde{q}	\tilde{q}	0
sleptons	\tilde{l}	\tilde{l}	0
gluino	\tilde{g}	\tilde{g}	$\frac{1}{2}$
neutralinos	$\tilde{W}^0, \tilde{B}^0, \tilde{H}_1^0, \tilde{H}_2^0$	$\tilde{\chi}_1^0, \tilde{\chi}_2^0, \tilde{\chi}_3^0, \tilde{\chi}_4^0$	$\frac{1}{2}$
charginos	$\tilde{W}^\pm, \tilde{B}^\pm, \tilde{H}_1^\pm, \tilde{H}_2^\pm$	$\tilde{\chi}_1^\pm, \tilde{\chi}_2^\pm$	$\frac{1}{2}$

mass becomes imperfect, leaving a logarithmic dependency to the cut-off scale. To prevent the need for fine-tuning, sparticle masses are expected to be at the TeV scale. Especially the top squark mass has to be small, as the top quark is the SM particle with the largest Yukawa coupling and contributes dominantly to the loop corrections.

SUSY introduces lepton- and baryon number violating couplings, which can allow for rapid proton decay, in contradiction to its extremely long lifetime. One way to keep the proton stable, is to assume that the quantum number R-parity

$$R_P = (-1)^{3(B-L)+2s}, \quad (2.3)$$

with B, L and s being the baryon number, lepton number and spin of the particle, is conserved. It is +1 for all SM particles and -1 for all SUSY particles. If R-parity is conserved, SUSY particles can only produced in even number and the lightest supersymmetric particle (LSP) must be stable. In many SUSY models the LSP is the lightest neutralino $\tilde{\chi}_1^0$, providing a possible dark matter candidate.

2.2.2 Dilepton mass edges in Supersymmetry

The multitude of superpartners offer a rich variety of experimental signatures to be observed at hadron colliders such as the LHC. The discussion here focusses on R-parity conserving models. In Figure 2.2, the pair production cross section for different combinations of SUSY particles in proton-proton collision at a centre-of-mass energy of $\sqrt{s} = 8\text{ TeV}$ is shown. It can be seen that the production of squarks and/or gluinos via the strong force is the dominant production mode. It therefore seems natural to focus on these events in the search for SUSY.

The experimental signature of SUSY are cascades of decays of the initially produced sparticles into the LSP under emission of several SM particles. In the case of the production of squarks and gluinos via the strong interaction, at least two quarks or gluons are produced in the first decays of the two decay chains in the events. These will hadronise into jets. Often even more jets are produced in the decay chains, making high jet multiplicities and large amounts of hadronic energy typical signatures of SUSY. In the models considered here, the LSP is stable and will leave the detector undetected, resulting in E_T^{miss} (see Section 1.1).

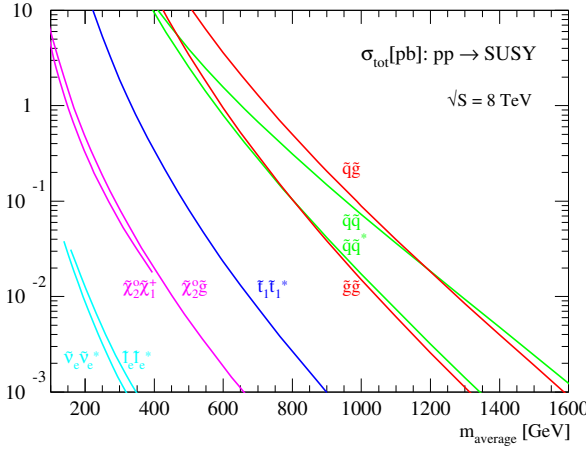


Figure 2.2: Cross sections for pair production of SUSY particles in proton-proton collision at $\sqrt{s} = 8 \text{ TeV}$ as a function of the average mass of the produced pair [22, 23, 24, 25].

As leptons are easy to identify and can be measured precisely, requiring the presence of leptons in the events helps to suppress backgrounds from SM processes such as QCD multijet production. Of particular interest to this analysis are SUSY cascades which contain the correlated production of lepton pairs of the same flavour but opposite electric charge. Due to their more challenging experimental signature, τ leptons are not considered. The relevant decay is that of a next-to-lightest neutralino into the lightest neutralino and two leptons $\tilde{\chi}_2^0 \rightarrow \tilde{\chi}_1^0 \ell^+ \ell^-$, which can occur either via an intermediate slepton or an off- or on-shell Z boson:

$$\tilde{\chi}_2^0 \rightarrow \tilde{\ell}^\pm \ell^\mp \rightarrow \ell^\pm \ell^\mp \tilde{\chi}_1^0, \quad (2.4)$$

$$\tilde{\chi}_2^0 \rightarrow Z^{(*)} \tilde{\chi}_1^0 \rightarrow \ell^+ \ell^- \tilde{\chi}_1^0. \quad (2.5)$$

The decays are illustrated in Figure 2.3, where the left graph corresponds to Equation 2.4 and the right to Equation 2.5.

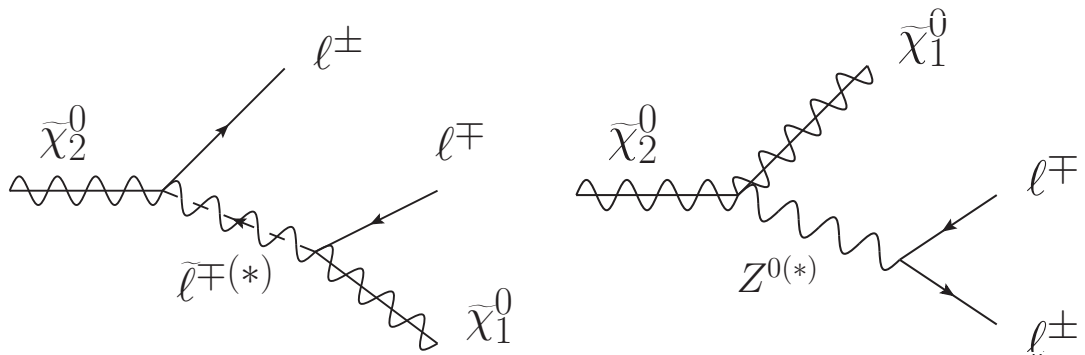


Figure 2.3: Graphs for the decays of $\tilde{\chi}_2^0$ into $\tilde{\chi}_1^0 \ell^+ \ell^-$ via an intermediate slepton (left) and off- or on-shell Z boson. The “(*)” indicates that the decay can be mediated by an off-shell particle. Graphs by Christian Schomakers.

The mass difference between the two neutralinos sets an upper bound on the invariant mass of the dilepton system $m_{\ell\ell}$ and its distribution exhibits an characteristic edge structure. The endpoint of this edge is defined by the signal kinematics. If the $\tilde{\chi}_2^0$ decays via an off-shell Z

boson, it is simply given by the mass difference itself:

$$m_{\ell\ell}^{\text{edge}} = m_{\tilde{\chi}_2^0} - m_{\tilde{\chi}_1^0}. \quad (2.6)$$

If the decay is mediated by a slepton, the edge position is modified by the slepton mass $m_{\tilde{\ell}}$:

$$m_{\ell\ell}^{\text{edge}} = \sqrt{\frac{(m_{\tilde{\chi}_2^0}^2 - m_{\tilde{\ell}}^2)(m_{\tilde{\ell}}^2 - m_{\tilde{\chi}_1^0}^2)}{m_{\tilde{\ell}}^2}}. \quad (2.7)$$

For decays via an on-shell Z boson, $m_{\ell\ell}$ will be consistent with the Z boson mass and no edge structure is present. The exact shape of the distribution is also determined by the decays. If the decays are mediated by Z bosons, it will be peaked towards m_Z if $m_{\ell\ell}^{\text{edge}}$ is below the Z boson mass. For $m_{\ell\ell}^{\text{edge}}$ on and above m_Z , the decays via an on-shell Z boson dominate and there is no edge. Decays via an intermediate slepton lead to triangular edge shapes, but the actual shape depends on model parameters, as for example negative interference between the decay channels via slepton and Z boson can occur. Examples are given in the next section.

Simplified models

As benchmark scenarios for these signatures, two “simplified models” are used that have been developed for this purpose by Christian Schomakers in the context of his master thesis [26]. In this kind of models, only the subset of sparticles relevant to the studied signature is assumed to be accessible at LHC energies. Also, the branching fractions of the sparticle decays are chosen to produce the desired signature and are often set to 100%.

Both models consider the pair production of bottom squarks. They decay into a bottom quark and a $\tilde{\chi}_2^0$ with a branching fraction of 100%. The decays of the $\tilde{\chi}_2^0$ differ between the two models. The Feynman graphs of both models are shown in Figure 2.4.

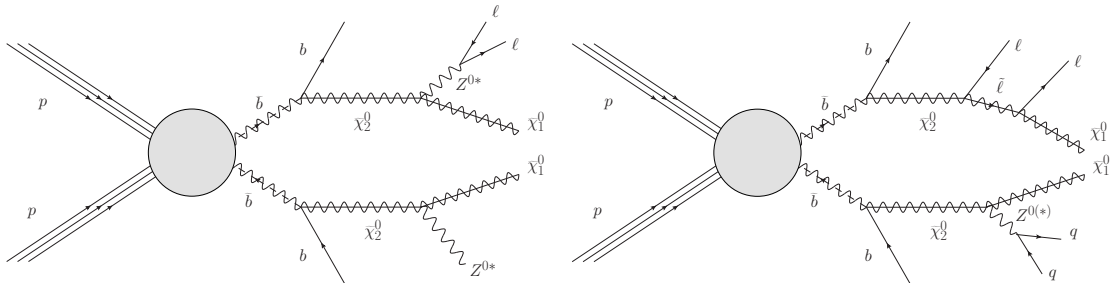


Figure 2.4: Feynman graphs for the fixed-edge (left) and slepton-edge (right) model. The “*” and “(*)” indicate that the particle is or can be off-shell. The right plot shows one of the three possible combination of decays of the $\tilde{\chi}_2^0$ in this model. Graphs by Christian Schomakers.

In the “fixed-edge” model, it decays into an off-shell Z boson and a $\tilde{\chi}_1^0$ in 100% of the cases. The Z boson decays with its SM branching ratios, producing light leptons in about 7% of the cases. The m_b - $m_{\tilde{\chi}_2^0}$ -plane is scanned, varying the masses of the two particles in steps of 25 GeV. The mass of the $\tilde{\chi}_1^0$ is fixed to 70 GeV below the mass of the $\tilde{\chi}_2^0$ to produce an edge in the $m_{\ell\ell}$ spectrum at this value.

As a mass difference between the two neutralinos larger than the Z boson mass will only result in the production of on-shell Z bosons in this model, the “slepton-edge” model introduces

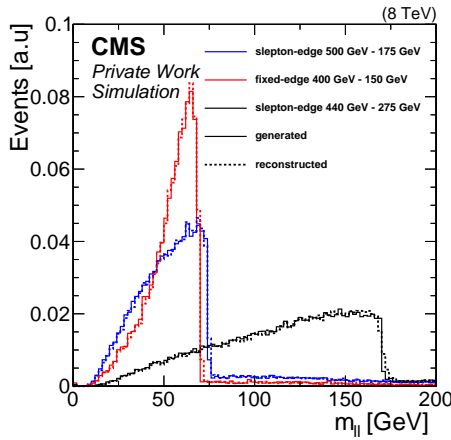


Figure 2.5: Distribution of $m_{\ell\ell}$ for one signal point of the fixed-edge model and two of the slepton-edge model, illustrating different edge positions and shapes. The masses given are those of the \tilde{b} and $\tilde{\chi}_2^0$, respectively. Shown are the generated distributions as solid lines and the reconstructed ones as dashed lines.

selectrons and smuons as additional new particles. The masses of these sleptons are assumed to be degenerate and set to lie halfway between the two neutralinos: $m_{\tilde{b}} = m_{\tilde{\chi}_1^0} + 0.5(m_{\tilde{\chi}_2^0} - m_{\tilde{\chi}_1^0})$. The branching fractions of the $\tilde{\chi}_2^0$ are chosen such that the decay in an off- or on-shell Z boson or a slepton and a lepton occur with 50% probability each. The Z boson again decays according to its SM branching fraction, while the slepton always decays into a lepton and the $\tilde{\chi}_1^0$. The $m_{\tilde{b}}\text{-}m_{\tilde{\chi}_2^0}$ -plane is scanned in steps of 25 GeV, while the $m_{\tilde{\chi}_1^0}$ is set to be 100 GeV, allowing for edges in the $m_{\ell\ell}$ spectrum also above the Z boson mass. The signal simulation is normalised to theory cross sections calculated at next-to-leading order (NLO) in α_s , including the leading logarithmic contributions of the next-to-next-to-leading order (NNLO) [25, 27, 28, 29, 30, 31].

Figure 2.5 illustrates the $m_{\ell\ell}$ distributions for three example points. The two examples from the slepton-edge model are roughly triangular in shape, while the one from the fixed-edge model is peaked towards m_Z as in this model the decay is mediated by an off-shell Z boson. Contributions outside of the edges are caused by events with more than two leptons where the wrong combination has been chosen. In addition to the generated distributions the ones reconstructed after a simulation of the CMS detector are shown, illustrating the good detector resolution for lepton pairs.

2.3 Standard Model processes

The signature of jets, E_T^{miss} and a pair of same-flavour opposite-sign leptons is not unique to the signal. Several SM processes can behave similarly and constitute backgrounds in this analysis. They can be categorised by the nature of their dilepton production.

A process exhibiting the correlated production of leptons similar to the signal is for example the Drell–Yan process $pp \rightarrow Z/\gamma^* \rightarrow \ell\ell$. In this process, jets are commonly produced as initial state radiation off the incoming partons. Even though no invisible particles are produced in this process, requiring the E_T^{miss} to be caused by mismeasurements, the large production cross section of this process leads to significant number of events with large E_T^{miss} . Other

processes with correlated production relevant to this analysis are the production of Z bosons in association with other gauge bosons (WZ, ZZ) or top quark pair production ($t\bar{t}Z$). All these processes will be summarised as “Drell–Yan” in the following for simplicity.

The other class of backgrounds exhibits uncorrelated production of leptons. The dominant contribution to this analysis comes from the dileptonic decay of top quark pair production $pp \rightarrow t\bar{t} \rightarrow WbWb \rightarrow \ell b\nu l b\nu$. This includes decays via intermediate τ leptons $W \rightarrow \tau\nu \rightarrow \ell\nu\nu\nu$. The leptons have opposite sign, but can be of same or opposite flavour with the same probability. This is also the case for the production of single top quarks in association with a W boson or in the case of τ leptons in the decay $Z \rightarrow \tau\tau \rightarrow \ell\nu\nu\ell\nu\nu$. These backgrounds are called “flavour-symmetric” throughout this analysis. They also include contributions from leptons not originating from the hard interaction. These “non-prompt” leptons include leptons from the decay of charm or bottom (summarised as “heavy flavour”) quarks inside hadronic jets or jets misidentified as leptons.

The production cross sections for different processes as a function of the centre-of-mass energy of the collisions are shown in Figure 2.6 in nb. The total interaction cross section is in the order of 10^8 nb. It is dominated by soft QCD processes which are of minor importance to this analysis. However, given the high instantaneous luminosity achieved at the LHC (see Section 3.1), many interactions occur in each collision. This leads to additional particles in the detector on top of the signature of the relevant physics process, an effect called “pileup”.

As mentioned before, the cross section for Z/γ^* boson production is very large, exceeding that for the production of top quarks by two orders of magnitude. This underlines the importance of E_T^{miss} in the signature to reduce this background. The cross section for Higgs boson production is close to that of some of the processes discussed above. However the branching fraction of the Higgs boson in decay channels relevant to this signature is too small for it to contribute significantly.

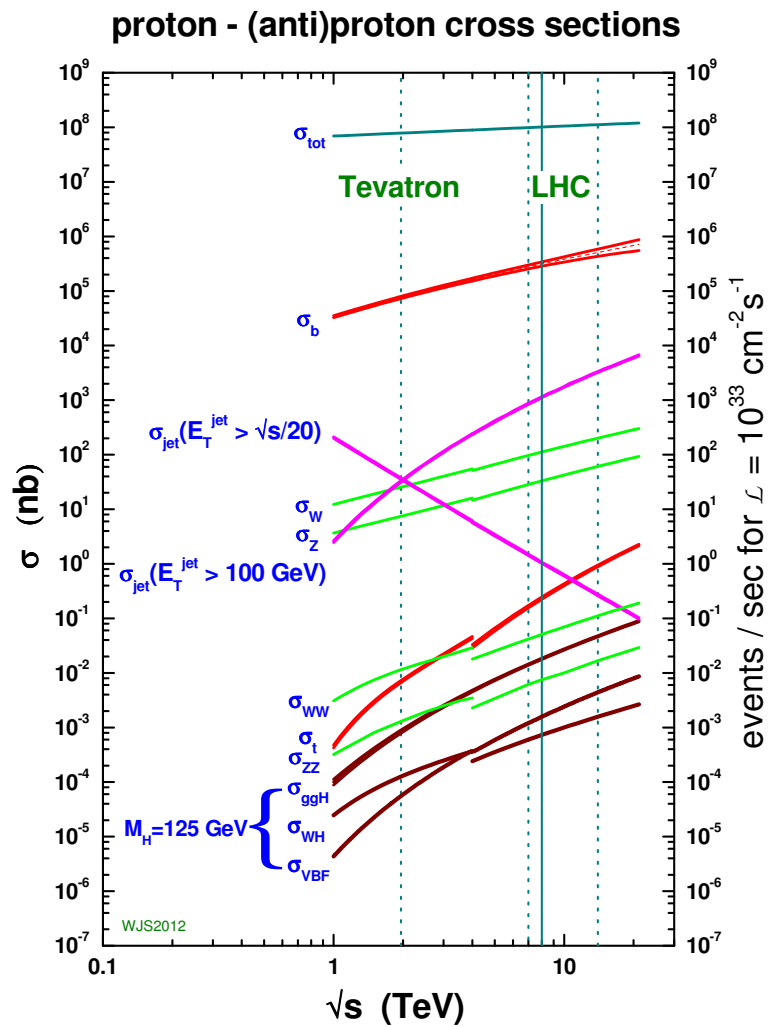


Figure 2.6: Cross sections for different Standard Model processes in proton-antiproton or proton-proton collisions as a function of the centre-of-mass energy [32].

3 Experimental setup

This analysis relies on data recorded by the CMS experiment at the CERN LHC. Both are highly complex machines and the product of decades of development and construction. Only a short summary can be given here, simplifying many intricate aspects of their designs.

3.1 CERN Large Hadron Collider

The LHC [33], located at CERN near Geneva, is capable of colliding protons and lead ions at higher energies than any of its predecessors. The instantaneous luminosity delivered to the experiments exceeds that of any previous machine at the energy frontier. It was constructed in the tunnel formerly inhabited by the LEP electron-positron collider in 100 m depths below the surface with a circumference of 27 km. The design goal was to achieve proton collisions at a centre-of-mass energy of $\sqrt{s} = 14 \text{ TeV}$ with instantaneous luminosities of $10^{34} \text{ s}^{-1} \text{ m}^{-2}$.

The LHC consists of eight arcs, as shown in Figure 3.1, where superconducting dipole magnets provide a magnetic field of up to 8.3 T to bend the charged particles along the curvature of the tunnel, while quadrupole and other specialised magnets are used to focus the beams. In straight segments between these arcs, LHC infrastructure and the experiments are located. The infrastructure components include the cooling facilities necessary to reach a temperature of 1.9 K around the ring, the superconducting cavities in which the protons are accelerated by standing electromagnetic waves, collimators for beam cleaning, and the beam dump, where the beams are ejected from the LHC at the end of fills. In the other four straight segments the beams are brought into collisions, which are studied by the four large experiments at the LHC. Of these, CMS [34] and ATLAS (A large LHC apparatus) [35] are multi-purpose detectors with a diverse physics program, while ALICE (A large ion collider experiment) [36] and LHCb (LHC beauty experiment) [37] are specialised on heavy ion collisions and flavour physics, respectively.

The protons circulating in the LHC are injected at an energy of 450 GeV after running through a chain of pre-accelerators, the Linac2, the Proton Synchrotron Booster (PSB), the Proton Synchrotron (PS), and the Super Proton Synchrotron (SPS). The proton beams are separated into bunches of about 10^{11} particles. The smallest temporal spacing between two bunches achieved during the data taking in 2012 was 50 ns, twice the design value. In these conditions, after three years of running in the years 2010 to 2012, the so called Run I of the LHC, a centre-of-mass energy of $\sqrt{s} = 8 \text{ TeV}$ has been reached. The instantaneous luminosities delivered to the experiments reached a maximum of $7.7 \cdot 10^{33} \text{ s}^{-1} \text{ m}^{-2}$ in late 2012, as can be seen on the left side of Figure 3.2. The integrated luminosity delivered to the CMS experiment in 2012 was 23.3 fb^{-1} , exceeding that of 2011 by almost a factor of four [39], as shown on the right side of Figure 3.2.

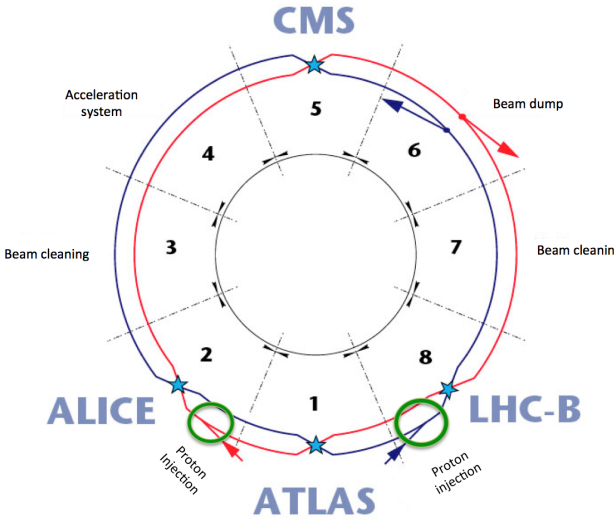


Figure 3.1: Schematic view of the LHC with its eight arcs. The four interaction points, where the experiments are located, are marked with blue stars. Other important parts of the LHC infrastructure are also indicated [38].

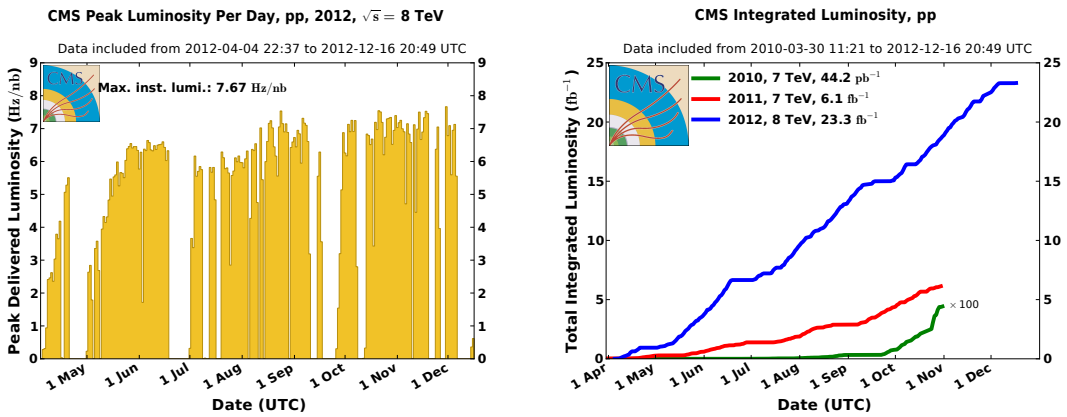


Figure 3.2: Development of instantaneous (left) and integrated (right) luminosity delivered to the CMS experiment. The right plots shows the results for all three years of data taking, while the left one only shows the 2012 data taking [39].

3.2 CMS detector

Located at one of the four intersections of the LHC beams, the CMS detector is designed to measure the resulting collisions to high precision [34]. Its key features are high precision measurements of the properties of single particles as well as a good coverage of the 4π solid angle. The central element of the CMS detector is a superconducting solenoid. Cooled to 4.45 K, it is able to produce a homogeneous magnetic field of 3.8 T, which allows to measure the momentum of charged particle by bending their trajectories. As shown in Figure 3.3, the different components of the detector are layered in cylindrical shapes around the interaction point. The magnet encompasses most of the main subdetectors, namely the tracking system which measures the trajectories of charged particles and the electromagnetic and hadron calorimeters, designed to measure the energy of particles. Located outside of the volume of the solenoid are the iron return yoke and muon detectors. This cylindrical structure is complemented on both sides by endcaps, which close the solid angle in the direction of the beams and are partly located outside the volume of the solenoid. The different components are described in more detail in the following.

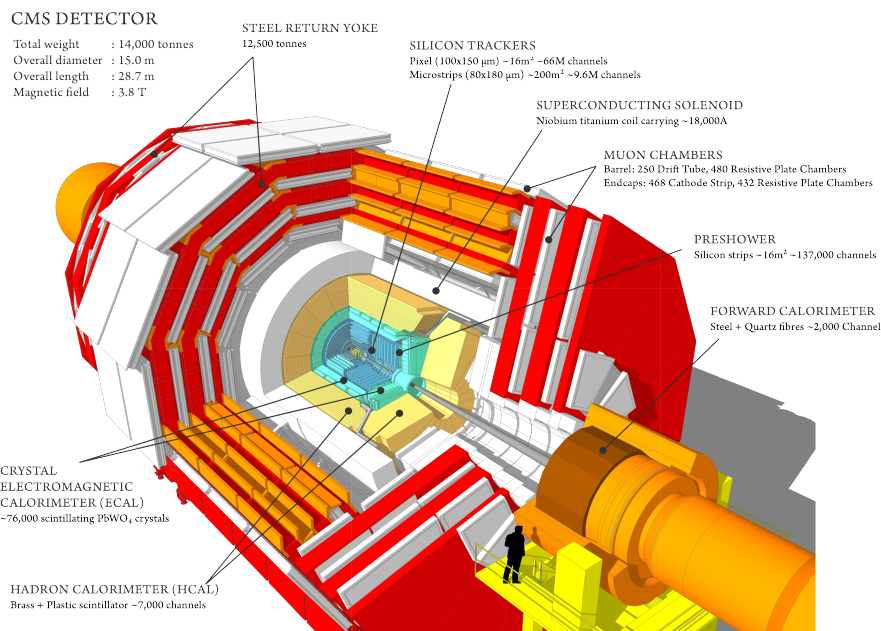


Figure 3.3: Schematic view of the CMS detector [40]. From the inside out, the tracking system is shown in blue, the electromagnetic calorimeter in green, the hadron calorimeter in light yellow, the superconducting solenoid in white, the return yoke in red, and the muon system again in white.

3.2.1 Tracking system

The tracking system of the CMS detector consists of many layers of silicon pixels and strips. The trajectories of charged particles are reconstructed from the ionisation signal they cause in the silicon. In the magnetic field these trajectories bend, allowing to determine the momentum of particles. The tracking system has a diameter of 2.5 m and a length of 5.8 m, corresponding

to a geometric coverage of $|\eta| < 2.5$. The tracking detector consists, as shown in Figure 3.4, of the pixel detector (PIXEL) surrounded by various components of the silicon strip tracker.

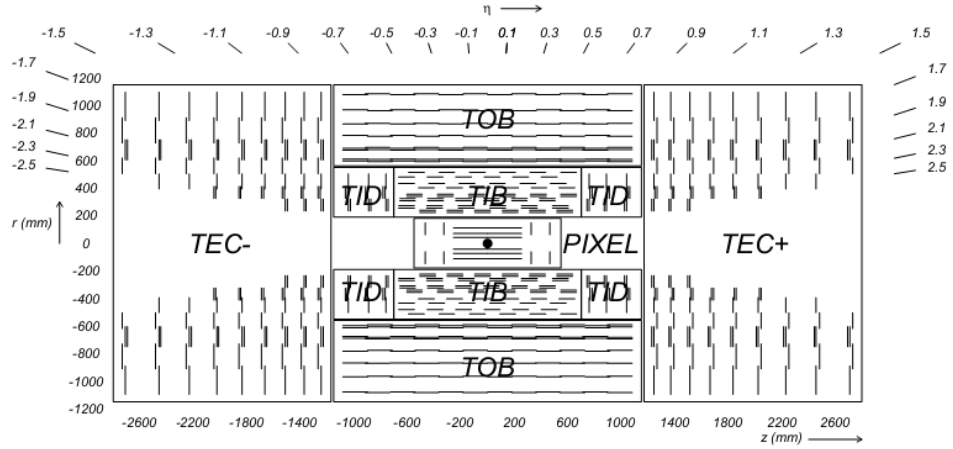


Figure 3.4: Schematic view of the CMS tracking detector. The innermost part shows the pixel detector (PIXEL), surrounded by the tracker inner barrel (TIB) and tracker inner discs (TID). The outermost parts of the tracking detector are the tracker outer barrel (TOB) and the two tracker endcaps (TEC- and TEC+) [34].

Silicon pixel detector

The innermost part of the tracking system is the pixel detector, which consists of three layers in the barrel region at radii between 4.4 cm and 10.2 cm, complemented by two discs perpendicular to the beam axis, located at $|z| = 34.5$ cm and $|z| = 46.5$ cm. As the particle density is highest close to the interaction point, a high granularity is needed to maintain a low occupancy of the pixel detector. Therefore, the pixel detector consists of roughly 66 million pixels with a combined active area of about 1 m^2 . Each pixel has a size of $150 \times 100\text{ }\mu\text{m}^2$. The analogue readout of the pixels allows to combine the measurements of neighbouring pixels, bringing the spatial resolution down to 15 to $20\text{ }\mu\text{m}$. This is especially important for the reconstruction of the interaction vertices and the tagging of the secondary vertices from the decay of b-hadrons.

Silicon strip detector

Further away from the interaction point, between 20 cm and 116 cm, the granularity of the tracking system is reduced. Silicon strip detectors are used, structured in four layers of the tracker inner barrel (TIB), complemented on each side by the three discs of the tracker inner discs (TID). All this is surrounded by the six layers of the tracker outer barrel (TOB). The tracker endcaps (TECs) consist of nine discs each. The individual strips have a length of about 10 cm and a pitch between $80\text{ }\mu\text{m}$ in the two inner layers of the TIB and $183\text{ }\mu\text{m}$ in the four inner layers of the TOB. The single point resolution in TIB and TOB depends on the layout of the specific layer and varies between $23\text{ }\mu\text{m}$ and $53\text{ }\mu\text{m}$.

Stereo modules, constructed by placing two modules back to back, rotated by 100 mrad, are placed in the first two layers of both TIB and TOB, the first two discs of TID, and the first

two and the fifth discs of the TECs. These allow for 2-D measurements, with a precision of the z position measurement of $230\text{ }\mu\text{m}$ in TIB and $530\text{ }\mu\text{m}$ in TOB.

For high momentum tracks of about 100 GeV in the region of $|\eta| < 1.6$ a p_{T} resolution of 1-2% is achieved, while the impact parameter of these tracks can be measured with a resolution of about $10\text{ }\mu\text{m}$.

Compared to gas-based tracking technologies, an all silicon tracking system, as used in CMS, consists of significantly more material. The material budget lies between 0.4 and 1.8 radiation length X_0 , as shown in Figure 3.5. For light charged particles, such as electrons, this leads to a significant probability to emit bremsstrahlung while traversing the tracking detector, which has to be taken into account in the reconstruction of particles.

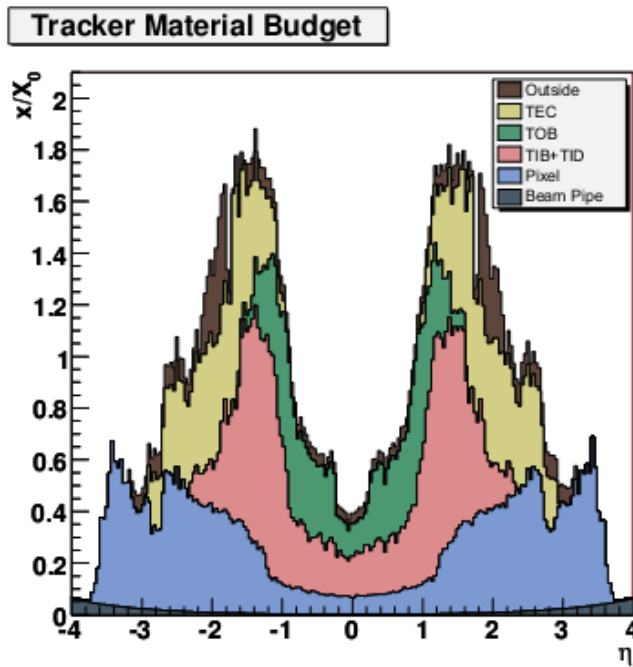


Figure 3.5: Material budget of the CMS tracking detector in units of radiation length X_0 as a function of η [34].

3.2.2 Electromagnetic calorimeter

The electromagnetic calorimeter (ECAL) measures the energy of electrons and photons. It uses lead tungstate (PbWO_4) crystals as both absorber and active material. The electromagnetic shower induced by the electron or photon leads to the emission of scintillation light in the crystal, which is measured at the backside of the crystals by avalanche photo diodes (APDs) in the barrel segment of the ECAL and more radiation hard vacuum photo triodes (VTPs) in the endcap region. The choice of lead tungstate was driven by the need for a material that is at the same time dense (8.28 g/cm^3), has a small Molière radius (2.2 cm), and has a fast response. About 80% of the scintillation light is emitted within 25 ns, which is the time between two LHC bunch crossings under design conditions. The structure of the ECAL is

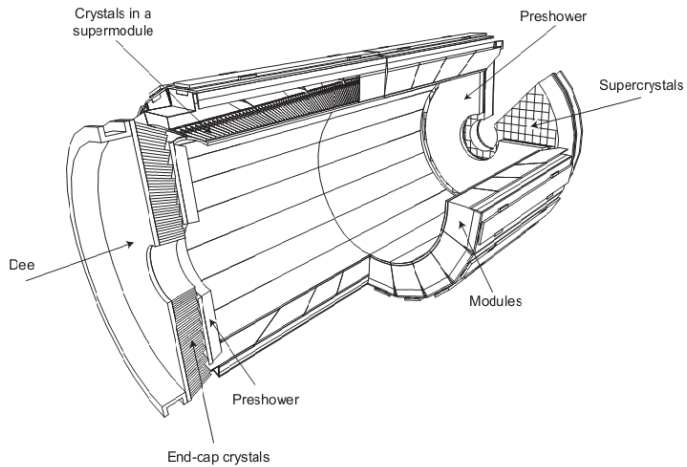


Figure 3.6: Schematic view of the CMS ECAL.

shown in Figure 3.6. The ECAL barrel (EB) covers the region of $|\eta| < 1.479$ and consists of 61200 crystals. They have a size of $2.2 \times 2.2 \text{ cm}^2$ at the front and $2.6 \times 2.6 \text{ cm}^2$ at the back, with a length of 23 cm, corresponding to $25.8 X_0$. In the ECAL endcaps (EE), consisting of 7324 crystals each, the crystals are slightly larger ($2.862 \times 2.862 \text{ cm}^2$ to $3.0 \times 3.0 \text{ cm}^2$) and shorter (22 cm, corresponding to $24.7 X_0$). The EEs extend the geometric coverage of the ECAL to $|\eta| = 3.0$.

In the region of $1.653 < |\eta| < 2.6$ a preshower detector, consisting of two layers of silicon strips and two layers of lead absorber, is installed to distinguish between prompt photons and those from the decay $\pi^0 \rightarrow \gamma\gamma$. The strips, oriented perpendicular to each other, have a pitch of 2 mm, allowing to resolve the two showers of the photons from the π^0 .

The production of scintillation photons per deposited energy is temperature dependent. Therefore, the ECAL is kept at a temperature of $18 \pm 0.05^\circ\text{C}$, which results in a yield of about 4.5 photons per MeV.

The typical energy resolution of the ECAL is parametrised as

$$\left(\frac{\sigma}{E}\right)^2 = \left(\frac{2.8\%}{\sqrt{E}}\right)^2 + \left(\frac{0.12}{E}\right)^2 + (0.30\%)^2, \quad (3.1)$$

with three terms describing different sources of uncertainty. The first term includes statistical fluctuations in the production of scintillation light as well as the energy distribution over several crystals. The second term covers such sources of noise as electronic noise or pileup. The constant term accounts for other sources of uncertainties such as calibration errors. The size of the different contributions has been confirmed in test beam measurements [41].

3.2.3 Hadron calorimeter

The hadron calorimeter (HCAL) measures the energy of charged and neutral hadrons. In the barrel region of the detector it is situated between the ECAL and the coil of the solenoid, at radii between 1.7 m and 2.95 m, limiting the amount of material that can be used in its

construction and therefore its ability to contain the hadronic showers. Therefore, additional detectors are placed outside of the volume of the magnet, forming the hadron outer calorimeter (HO). The HCAL barrel (HB) is complemented on each side by a HCAL endcap (HE) and the geometric coverage is extended to high values of $|\eta|$ by dedicated forward calorimeters (HF). The placement of these subdetectors relative to the other components of CMS is shown in Figure 3.7.



Figure 3.7: Schematic view of the CMS HCAL [34].

HCAL barrel and outer detectors (HB and HO)

The HB covers the geometric region $|\eta| \leq 1.3$. It is constructed as a sandwich calorimeter, consisting of plastic scintillator as the active material. For the absorber material, the fourteen inner layers of the HB are made from brass, while steel is used for the front and back plates of the HB to increase the stability of the construction. The scintillator is divided into 144 segments in ϕ and 32 segments in η , resulting in a spatial granularity of 0.087 in both η and ϕ . The scintillation light produced in the active material is transported to hybrid photo diodes using scintillating fibres. As all layers of one tower in η and ϕ are read out by the same photo diode, there is no segmentation in the readout in r , except for the two towers closest to the HE on each side. The material of the ECAL in front of the HB corresponds to about 1.1 interaction length λ_i . The absorber material of the HB itself amounts to only $5.82 \lambda_i$ at $\eta = 0$, which increases to $10.6 \lambda_i$ at $|\eta| = 1.3$. To measure the energy of jets not contained in the HB, the HO is placed outside the vacuum containment of the solenoid. It consists of one additional layer of scintillator, with the magnet acting as absorber, except for the most central part of the detector, where one additional layer of steel absorber and scintillator are installed. Hereby the material budget of the HCAL is increased to at least $10 \lambda_i$ over the whole barrel region.

HCAL endcaps (HE)

The HE extends the geometric coverage of the HCAL up to $|\eta| = 3.0$, coinciding with the coverage of the EEs. It is constructed from the same combination of brass absorber and

plastic scintillator as the HB and for the region $1.3 \leq |\eta| \leq 1.6$ also retains the $\Delta\eta \times \Delta\phi = 0.087 \times 0.087$ granularity in η and ϕ . For $|\eta| \geq 1.6$ the segmentation is coarser, resulting a granularity of $\Delta\eta \times \Delta\phi \approx 0.17 \times 0.17$. This structure again corresponds to about $10 \lambda_i$. The longitudinal segmentation of the readout of the towers differs based on the location of the tower. The two towers closest to the beam line are read out in three segments, while most others are divided into two segments. The two towers overlapping with HB are read out without longitudinal segmentation. Multipixel hybrid photo diodes have been chosen for the readout due to their low sensitivity to magnetic fields.

Hadron forward calorimeter (HF)

Of all subdetectors of CMS, the HF covers the highest values of $|\eta|$, extending up to $|\eta| = 5.2$. This close to the beam pipe radiation hardness is the key feature of the design, as nearly 90% of the energy deposited in the detector as the result of a proton-proton interaction is allotted to the HF. It is constructed as two 3.5 m long cylinders with a radius of 1.3 m, located at $|z| = 11.2$ m. The first 1.65 m consist of plates of steel with a thickness of 5 mm, again corresponding to about $10 \lambda_i$. The active components are quartz fibres, which are inserted into grooves in the steel plates. The particles created in showers in the absorber emit Cherenkov radiation in the fibres, which is detected by photomultiplier tubes at their end. As the Cherenkov threshold is lowest for electrons, at 190 keV, the HF is more sensitive towards electromagnetic than hadronic showers. To separate these two kinds of showers, half of the fibres start only at a depth of 22 cm inside the absorber. As electromagnetic showers develop faster, they deposit most of their energy before this point, which distinguishes them from hadronic showers.

3.2.4 Muon system

Muons are in general not stopped by any of the subdetectors of the CMS detector inside the solenoid. Therefore, they can be measured with high precision in a clean environment outside of it. Hence, the muon detectors are placed inside the return yoke of the magnet, both for the muon barrel (MB), covering up to $|\eta| = 1.2$ and the muon endcap (ME) detectors, placed between $|\eta| = 0.9$ and $|\eta| = 2.4$. Being placed so far away from the interaction point, the muon detectors have to cover a large area, which requires them to be rather inexpensive compared to other technologies used in the construction of CMS. Three different types of gaseous detectors are used to provide at the same time identification, p_T measurement, and triggering for muons. In the barrel region, drift tubes (DT) are used as the main muon detectors, whereas in the endcaps cathode strip chambers (CSC) are used which are faster and better equipped to deal with the larger and inhomogeneous magnetic field in this region of the detector. To provide a very fast muon tagging for the trigger, resistive plate chambers (RPC) complement the other two technologies in both the barrel and the endcaps.

Drift tubes (DT)

In the barrel, there are four layers of muon detectors, called muon stations, of which two are located inside the return yoke of the magnet and the other two are located between the solenoid and the yoke and outside the yoke, respectively. The muon stations consist of eight

to twelve muon chambers, which are made of two or three superlayers of DTs. The superlayers in turn consist of four layers of DTs. The first three muon stations contain chambers with superlayers measuring either in the $r - \phi$ plane or measuring the z coordinate. In the last muon station only the superlayers measuring in $r - \phi$ are present. The DTs in each layer are offset by half of the width of a tube with respect to the next one to avoid dead spots in the geometric coverage. The DT system consists of about 172000 sensitive wires. The drift tubes are filled with a mixture of 85% Ar and 15% CO_2 , and their structure is shown in Figure 3.8. The $r\phi$ resolution of a single layer of DT is about 250 μm , so that one chamber reaches a precision of 100 μm .

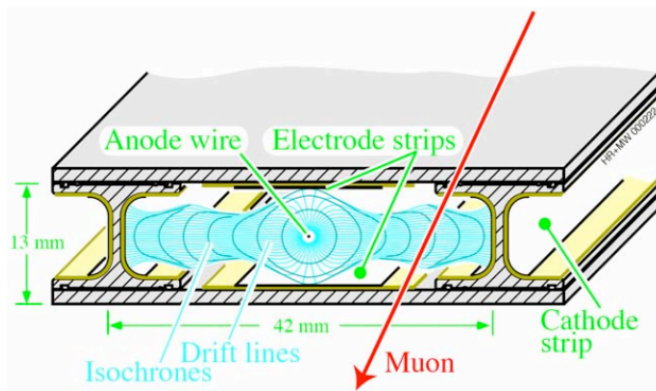


Figure 3.8: Schematic view of one drift tube [34].

Cathode strip chambers (CSC)

The CSC are multiwire proportional chambers, consisting of six planes of anode wires interleaved with seven panels of cathode strips. The chambers have trapezoidal shapes and are arranged in four discs around the beam axis, each further segmented into two or three rings. The cathode strips measure the ϕ coordinate while the anode wires measure the radial coordinate. Figure 3.9 shows the structure of one chamber on the left side and the creation of a signal due to a amplification of the initial ionisation in an avalanche close to the anode wire on the right side.

Resistive plate chambers (RPC)

The RPCs consist of three layers of bakelite, which form two small gas filled gaps and between which high voltage is applied. The amplification of the initial signal is very fast in this configuration, with drift times of about 5 ns. Therefore, this technology is well suited to associate muon candidates to the LHC bunch crossings. In the barrel region six layers of RPCs are installed, while three layers are used in the endcaps for $|\eta| \leq 1.6$.

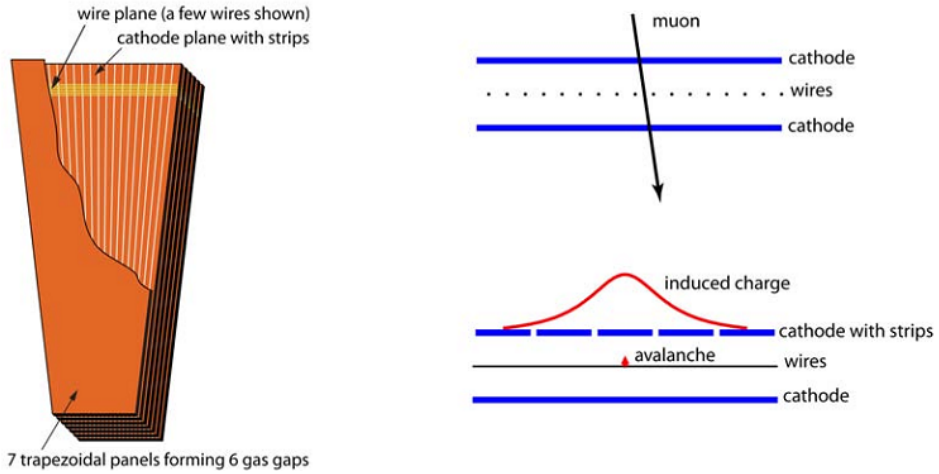


Figure 3.9: Schematic view of one CSC (left) and the creation of a signal (right) [34].

Momentum resolution

The p_T resolution of the muon system alone was expected to be about 10% for muons with p_T up to 200 GeV. Combined with the information from the inner tracking system, a resolution of about 1% was expected to be achieved in the central region of $|\eta| \leq 0.8$ for a p_T of 10 GeV, increasing to about 2% for a p_T of 200 GeV.

The p_T resolution for muons has been measured using data collected in 2010 [42]. Using the muon system alone, resolutions better than 10% have been found for the barrel region for muons with $p_T > 15$ GeV. The muon resolution improves when combining the information from the muon system with those from the inner tracking system. The precision of the tracking system dominates for a wide p_T range and averaging over η and ϕ resolutions of $1.8 \pm 0.3(\text{stat.})\%$ at $p_T = 30$ GeV to $2.3 \pm 0.3(\text{stat.})\%$ at $p_T = 50$ GeV have been achieved.

3.3 Trigger and data acquisition

If the LHC is operated at the design bunch spacing of 25 ns, bunch crossings occur with a rate of about 40 MHz. This rate has been reduced by at least factor of two during Run I of the LHC because of the increased bunch spacing. Still, event rates of this magnitude can not be handled by the available means of data processing. The total event rate is therefore reduced by a factor of about 10^6 by two subsequent trigger systems. The Level-1 (L1) trigger consists of programmable electronics, allowing for a fast primitive reconstruction of physics objects in the calorimeters and the muon system. This system reduces the event rate to a maximum of 100 kHz. Following an L1 accept (L1A), the CMS data acquisition system (DAQ) collects the event information from the readout of the different subdetectors and passes it on to the High-Level trigger (HLT). The HLT is a software trigger and has access to the full detector readout [43]. It can perform a full reconstruction of the events using similar algorithms used in offline data analysis. Events are accepted by the HLT at a rate of a few 10^2 Hz.

Level-1 trigger (L1)

The outputs of the different subdetectors are stored in pipelined buffers inside the readout electronics. This limits the time between the bunch crossing and the distribution of the L1A to the subsystems to $3.2\,\mu\text{s}$. The L1 is therefore constructed from mostly custom-built programmable electronics either directly inside the detector or located close by in the underground facilities. As the readout of the tracker and track reconstruction are not feasible on this time scale, only calorimeter and muon system information are used. The L1 system is divided into local, regional and global components, as shown in Figure 3.10.

In the calorimeter trigger the local components are the trigger primitive generators (TPGs). For $|\eta| \leq 1.74$ they have an (η, ϕ) -coverage of 0.087×0.087 , corresponding to one HCAL tower and a 5×5 matrix of ECAL crystals in front of it. The TPGs communicate the energy deposits in the trigger tower and the number of the bunch crossing to the regional calorimeter trigger. One calorimeter region consists of 4×4 trigger towers. Candidates for electrons or photons (e/γ) are formed by selecting the towers with the highest E_T in the ECAL. Based on information about the energy distribution inside the ECAL tower, the ratio of energy in ECAL and HCAL in the trigger tower and the overall distribution of energy in the neighbouring trigger towers the candidates are classified as isolated or non-isolated. Per region, four isolated and four non-isolated e/γ candidates and the transverse energy sums of the trigger towers are passed to the global calorimeter trigger (GCT). Additionally, information for τ and muon identification is provided. The GCT performs a simple jet clustering algorithm and is able to calculate per event observables such as the number of jets, the total and missing transverse energy, and sum of the transverse energy of all jets above a certain threshold (H_T^{L1}). These information are delivered to the global trigger

In the muon trigger all three detector components (DT,CSC, and RPC) are used. In the local trigger, the DT chambers deliver track segments in the ϕ -projection and hit patterns in the η -projection, while the CSCs produce three-dimensional track segments. Both use timing information to associate this information with the bunch crossing. In the regional trigger, DT and CSC information are processed in separate track finders, which produce muon candidates. These are ordered as a function of p_T and track quality and up to four candidates are delivered to the global muon trigger from each track finder. The RPCs also deliver muon candidates. With their excellent timing resolution of about $1\,\text{ns}$ they deliver an unambiguous association of the muon candidates to the correct bunch crossing. The global muon trigger receives up to four muon candidates each from the DTs, the CSCs, and the barrel and endcap RPCs. The information consists of p_T , η , ϕ , and information on the quality of the muon reconstruction. Candidates from the RPCs are matched with the ones from DT and CSC and, if matches are found, merged into single candidates. Unmatched candidates with low quality are suppressed. The track of the candidates is extrapolated back into the calorimeters to add the minimum ionising particle signature and isolation information from the regional calorimeter trigger. The four best muon candidates are forwarded to the global trigger.

The global trigger collects the information from the global muon and calorimeter triggers. Up to 128 trigger algorithms can be performed on the trigger objects at the same time, the most basic being simple p_T thresholds. If the criteria of one of the algorithms is met by the event, it is accepted by the L1 trigger and the L1A is sent to the DAQ to read out the event.

Data acquisition system (DAQ)

Following an L1A the DAQ receives the information from the different subdetectors split in about 650 data sources, each delivering about 2 kB of data. These event fragments are assembled into whole events by the event builder. The event is then sent to one filter unit in the event filter, where the HLT software is running. The DAQ has to deal with input rates of up to 100 kHz and consists of 8 nearly independent slices, each able to take input at a rate of 12.5 kHz. The DAQ includes a back-pressure system, which automatically throttles the L1 trigger in case the input rate exceeds the capability of the DAQ. This introduces dead times in the detector readout but prevents data corruption and buffer overflows. To fully utilise the capacities of the trigger system and the DAQ, trigger thresholds can be adapted during data taking. The shortest time scale on which the thresholds are kept constant is called lumi section and is defined as 2^{20} LHC orbits, corresponding to about 93 s. The structure of the DAQ is shown in Figure 3.10.

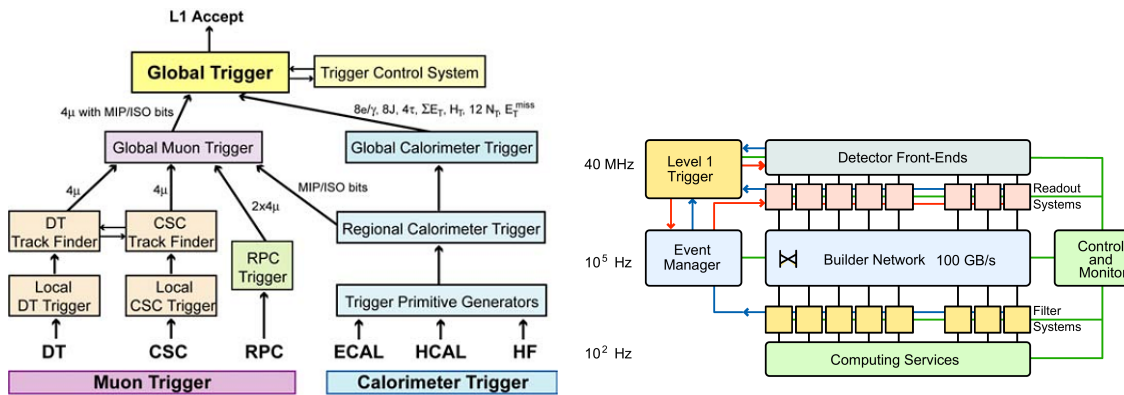


Figure 3.10: Structure of the CMS Level-1 trigger (left) and data acquisition system (DAQ) (right)

High level trigger (HLT)

The HLT software is run on a dedicated computing element, the event filter farm, located in the CMS service caverns. During the data taking in 2012 it consisted of about 13200 processor cores [44], allowing for a processing time of about 150 ms at a input rate of 100 kHz. The HLT system reduces input data rates of up to 100 GB/s to several hundred MB/s, which are sent to the CERN computer centre for storage. As a full event reconstruction can be performed at HLT level, even if it is often restricted to small regions of the detector for timing reasons, much more complex quantities can be used to separate potentially interesting signatures from the large backgrounds. However, approximate methods have to be used sometimes to maintain an acceptable processing time per event. Also, some calibration and alignment methods can only be performed after the data taking, making the HLT less precise compared to the offline reconstruction. While a large variety of triggers is used by CMS to select different kinds of events, this description will focus on the ones most relevant to this analysis.

The most important signal and control samples for this analysis are collected with dilepton triggers. In general, they select events that contain two leptons (electrons or muons), of

which one is required to have a reconstructed transverse momentum p_T of at least 17 GeV, while for the second this threshold is relaxed to 8 GeV. In general, the lepton with the higher (lower) p_T is referred to as the leading (trailing) lepton. For muons, simply the presence of a reconstructed muon with a given p_T threshold is required. For electrons additional identification and isolation requirements are applied to keep the trigger rates at an acceptable level. For the most part, the algorithms employed to reconstruct muons and electrons are the same among all possible combinations of leptons. However, for $\mu\mu$ events an additional trigger, which uses tracker information for the trailing muon, is available, increasing the efficiency in this channel. The triggers used for preselection at L1 level also differ in their thresholds [45] between the different lepton combinations. As the algorithms to reconstruct physics objects at HLT level are so similar to those used offline, no dedicated description is given here. An overview over the exact trigger definitions is given in appendix A.

Other HLT paths used in this analysis select events based on the scalar sum of the p_T of hadronic jets (H_T), the α_T variable [46], which takes into account the balance of jets in an event, and single electrons and muons, which are selected with tighter identification and isolation criteria compared to the dilepton triggers. Also, in order to study non-prompt leptons, events with low p_T single leptons are selected using trigger paths that apply the same selection as the different legs of the dilepton triggers.

As the trigger rates for the H_T , α_T , and low p_T single lepton triggers are very high, these triggers are prescaled, meaning that only a predefined fraction of the selected events are actually recorded and reconstructed.

4 Data analysis and event selection

The data recorded by the CMS experiment is processed using dedicated software that uses the detector signals to reconstruct the particles produced in the proton-proton collisions and other properties describing the events. The resulting datasets, accompanied by simulation for both SM and new physics processes, are then analysed. Events are selected using their reconstructed properties based on the characteristics of the physics processes of interest. Here, an overview on the reconstruction algorithms and software are discussed. Also, the datasets and event selections used in this analysis are motivated.

4.1 Object reconstruction

The observables most relevant to this analysis are electrons, muons, jets, and the missing transverse energy (E_T^{miss}). Here, the reconstruction of these objects from the information provided by the CMS detector as performed on the data recorded in 2012 is described. While the electron and muon candidates used in this study are reconstructed independent of each other with dedicated algorithms, jets and E_T^{miss} are provided by the particle flow (PF) algorithm [47]. It combines information from all subdetectors to achieve a consistent description of the full event.

4.1.1 Vertex reconstruction

Interaction vertices are reconstructed from the tracks of the charged particles that originate from them. Tracks fulfilling certain quality requirements are clustered into vertices with a deterministic annealing algorithm [48, 49]. The vertex position is fitted using an adaptive vertex fitter [50], where a weight w_i between 0 and 1 is assigned to every track, based on the likelihood of that track being correctly associated with the vertex. The vertex with the largest p_T^2 sum of associated tracks is considered to be the primary vertex in the event.

4.1.2 Muon reconstruction and identification

The track of a muon is reconstructed separately in the inner tracker and in the muon system, resulting in a *tracker track* and a *standalone muon*.

Tracks in the inner tracker are reconstructed using a method called combinatorial track finder [49], which performs pattern recognition and track fitting by employing a Kalman filter technique [51]. The track is described by a five-dimensional state vector, whose initial parameters are taken from track seeds, determined from three hits or two hits and a vertex constraint in the pixel detector or the innermost layers of the strip detector. The state vector is extrapolated to the next tracker layer taking into account uncertainties and energy losses

due to interactions with the tracker material. If tracker hits are found in the modules where they are expected from the extrapolation, they are added to the track candidate. If no hits are found, a ghost hit is added to the track to account for inefficiencies in the hit reconstruction. Too many ghost hits will terminate the reconstruction of the given track. A track fit is then performed to all hits associated with the track candidate, using again Kalman filtering and smoothing. This procedure is performed iteratively, each time removing the hits already associated to a track candidate and relaxing the requirements on the track seeds to allow for reconstruction of tracks with low p_T or not originating from the primary interaction [52].

For the reconstruction of *standalone muons* in the muon system, the hits inside the individual muon chambers are fitted to generate track segments, providing first estimates of the track parameters under the hypothesis that the muon was created in the interaction region and was travelling through the muon system from the inside out. These segments are used as starting points for a track reconstruction using all hits from the DTs, CSCs, and RPCs, again using the Kalman filtering technique [53].

Tracker tracks are promoted to *tracker muons* when they can be matched to a track segment in the muon detector. *Standalone muons* are matched to tracks from the inner tracker. If a compatible track is found, a combined fit to all hits of the track and the *standalone muon* is performed, resulting in a *global muon*. The PF algorithm applies further selection requirements to the reconstructed *global* and *track muons*, introducing a fourth category, the *particle flow muon* [54].

Muons selected in this analysis are required to be reconstructed as *tracker*, *global*, and *particle flow* muons. The χ^2 per degrees of freedom of the track fit must not exceed 10. Several requirements on the information available for the different track fits are made: At least one muon chamber hit must be included in the track fit of the *global muon*. For the fit of the *tracker muon* at least one hit in the pixel detector and six layers with hits in the strip detector have to be available. Also, the track from the inner tracker has to be matched to at least two track segments in the muon chambers. To ensure that the muon originates from the primary interaction and to suppress backgrounds from cosmic muons the impact parameter of the track with respect to the primary vertex must not exceed 0.02 cm in the x - y plane and 0.1 cm in z direction. Selected are muons with a p_T larger than 10 GeV and $|\eta|$ less than 2.4. The muon selection is summarised in Table 4.1.

4.1.3 Electron reconstruction and identification

The signature of an electron in the CMS detector is a track reconstructed by the tracking detectors that leads to a matching cluster of energy reconstructed in the ECAL. In practice the reconstruction is complicated by the large material budget of the tracking detectors, resulting in a high probability of an electron to loose energy in form of bremsstrahlung. About 35% of all electrons loose more than 70% of their energy and for 10% the energy loss exceeds 95% [55]. The reconstruction has to take into account the large solenoidal magnetic field, which bends the electron's trajectory away from the radiated photons, leading to a spread of the energy in ϕ direction. This has to be considered both in the tracking algorithms and in the clustering of the energy deposits in the ECAL.

In the ECAL barrel and endcaps, two different algorithms are used to group the energy deposits

Criterion	Selection
Acceptance	
p_T	$> 10 \text{ GeV}$
$ \eta $	< 2.4
Muon ID	
Required to be a	<i>tracker muon</i> <i>global muon</i> <i>particle flow muon</i>
Track quality	
χ^2/N_{dof}	< 10
valid muon hits	> 0
matched stations	> 1
valid pixel hits	> 0
tracker layers with hits	> 6
Impact parameter	
$d_0 = \sqrt{dx^2 + dy^2}$	$< 0.02 \text{ cm}$
dz	$< 0.1 \text{ cm}$

Table 4.1: Summary of the muon selection requirements.

into clusters and clusters of clusters, called super clusters (SCs). Both are designed to group together the energy deposits of the electron itself and those of the bremsstrahlung photons. In the pseudorapidity range of $1.6 < |\eta| < 2.6$ the preshower is located in front of the ECAL and electrons will deposit a fraction of their energy there. The energy deposited in the strips of the preshower between an SC in the ECAL and the primary vertex is summed and added to the energy of this SC [56].

Electron candidate tracks are refitted with a Gaussian sum filter (GSF) algorithm [57], which takes into account the energy losses caused by bremsstrahlung. GSF tracking is initiated in two ways. *ECAL driven seeding* requires the presence of a track seed that matches the position of an SC when extrapolating backwards from the ECAL to the tracker [55]. Alternatively, *tracker driven seeding* is started by tracks fitted with the Kalman filter technique discussed above, that either match the position of ECAL clusters when extrapolated to the ECAL surface, covering the case of no bremsstrahlung, or are of poor quality with only few associated tracker hits [49]. The GSF track and the energy measurement in the ECAL are combined into the final electron candidate.

The energy losses in the tracker material also impede the determination of the electron charge, as the presence of photon conversions and changes in the trajectory due to radiation can lead to charge misidentification when only the GSF track is considered. Therefore, also the associated tracks from the Kalman filter tracking and the supercluster position are used to improve the charge identification [58].

Electrons are selected requiring p_T larger than 10 GeV and $|\eta| < 2.5$. The transition region between ECAL barrel and endcaps of $1.442 < |\eta| < 1.566$ is excluded. To suppress background from muons that radiate photons, electrons with a distance to the nearest *global* or *tracker muon* of less than $\Delta R = 0.1$ are rejected. Backgrounds from for example photon

conversions or misidentified charged hadrons are suppressed by a set of selection criteria. The matching of track and supercluster is quantified by the differences between the supercluster position and the parameters of the track extrapolated from the vertex to the ECAL surface in $\Delta\phi$ and $\Delta\eta$. As the energy of the electron is contained in the ECAL, the ratio H/E of hadronic energy deposited in the HCAL behind the electron candidate compared to the energy in the ECAL must be small. The energy spread in the ECAL due to bremsstrahlung occurs in ϕ direction. Therefore, no significant spread of the energy in η , parametrised as

$$\sigma_{i\eta i\eta}^2 = \frac{\sum_i^{5\times 5} w_i \cdot (\eta_i - \bar{\eta}_{5\times 5})^2}{\sum_i^{5\times 5} w_i}, \quad (4.1)$$

$$w_i = \max \left(0, 4.7 + \ln \left(\frac{E_i}{E_{5\times 5}} \right) \right), \quad (4.2)$$

is expected, where for 5×5 crystals around the seed crystal, which initiated the clustering, the distance in η from the mean η of the cluster is summed, weighted by the energy deposit in each crystal. For a well measured electron, there is good agreement between the energy deposited in the ECAL and the track momentum measured in the tracker. Therefore, the value of $\left| \frac{1}{E} - \frac{1}{p} \right|$ must be small. Requirements on the impact parameter of the track with the respect to the vertex are made. To reject electrons originating from converted photons, only one pixel layer with a missing hit is allowed. This suppresses most conversions occurring after the first layer of the pixel detectors. To reject also conversion in this first layer and in the beam pipe, vertex fits for the electron track with neighbouring tracks are performed in order to reconstruct the point of conversion. For a prompt electron, the probability of these fits is low and required to be smaller than 10^{-6} . Some of these requirements are already applied on HLT level. In order to select electrons for which the trigger is fully efficient, selections at least as strict are applied at analysis level. The specific requirements are listed in Table 4.2, separately for barrel and endcap, where appropriate.

4.1.4 Observables reconstructed with particle flow

The particle flow (PF) algorithm [47] is designed to combine information from all subdetectors to reconstruct a consistent description of the event, resulting in a list of reconstructed particles. The basic building blocks are PF elements, which are reconstructed in each sub-detector separately: Tracks of charged particles in the tracker or muon system and energy clusters in the calorimeters. A linking algorithm then combines elements into blocks based on their geometrical distance, for example by extrapolating a track into the ECAL and HCAL and searching for compatible clusters. Similarly, calorimeter clusters are linked between the preshower, ECAL, and HCAL and tracks from the tracker are associated with those from the muon system. *Particle candidates* are reconstructed from the objects inside each block. Muons are reconstructed first, followed by electrons, for which, similar to the standard algorithm described above, a refit of the track with the GSF algorithm is performed and bremsstrahlung photons are collected in the ECAL. Lastly, calorimeter clusters compatible with a track are identified as charged hadrons, while clusters without a matching track are either categorised as neutral hadrons, or, depending on the energy deposits in the HCAL, as photons.

Criterion	Selection at HLT		Selection at Analysis Level	
	EB	EE	EB	EE
Acceptance				
p_T	trigger dependent		$> 10 \text{ GeV}$	
$ \eta $	< 2.5		$< 2.5, \text{ excluding } 1.442 < \eta < 1.566$	
ID variables				
$ \Delta\eta $	0.01	0.01	0.007	0.009
$ \Delta\phi $	0.15	0.10	0.15	0.10
$\sigma_{inj\eta}$	0.011	0.031	0.01	0.03
H/E	0.10	0.075	0.12	0.10
$\left \frac{1}{E} - \frac{1}{p} \right $	-		0.05	0.05
Conversion rejection				
missing pixel hits	-		≤ 1	≤ 1
vertex fit probability	-		$< 10^{-6}$	$< 10^{-6}$
Impact parameter				
$d_0 = \sqrt{dx^2 + dy^2}$	-		$< 0.02 \text{ cm}$	$< 0.02 \text{ cm}$
dz	-		$< 0.1 \text{ cm}$	$< 0.1 \text{ cm}$

Table 4.2: Summary of requirements of the electron selection.

Jets

The particles produced in the hadronisation of quarks and gluons are grouped into jets by clustering algorithms. An anti- k_T algorithm [59], performed using a fast implementation [60, 61], is used in this analysis. Input to the clustering are the *particle candidates* reconstructed by the particle flow algorithm.

The anti- k_T algorithm is a sequential clustering algorithm. Two distance measures are introduced, the first between two particles or pseudo-jets i and j and the second between particle or pseudo-jet i and the beam axis:

$$d_{ij} = \min(k_{Ti}^{-2}, k_{Tj}^{-2}) \frac{\Delta_{ij}^2}{R^2}, \quad (4.3)$$

$$d_{iB} = k_{Ti}^{-2}, \quad (4.4)$$

with $\Delta_{ij}^2 = (y_i - y_j)^2 + (\phi_i - \phi_j)^2$ and k_{Ti} , y_i , and ϕ_i being the transverse momentum, rapidity, and azimuth of a particle. For an entity (particle, pseudo-jet) i all distances are calculated. If the smallest is a d_{ij} , i and j are combined in a new pseudo-jet. If the smallest distance is the distance to the beam d_{iB} , the pseudo-jet is considered a final jet and removed from the list of particles available for clustering. The parameter R governs the size of the resulting jet and is set to 0.5 in this analysis.

The measured jet momentum p_μ^{raw} has to be corrected for energy offsets and the non-uniform and non-linear response of the detector. Each component of the jet's four-momentum vector is corrected by a multiplicative factor [62]

$$p_\mu^{\text{cor}} = C \cdot p_\mu^{\text{raw}}. \quad (4.5)$$

The correction is applied as a sequence of different factors:

$$C = C_{\text{offset}}^{L1}(p_{\text{T}}^{\text{raw}}) \cdot C_{\text{MC}}^{L2L3}(p_{\text{T}}, \eta) \cdot C_{\text{rel}}^{\text{L2Residual}}(\eta) \cdot C_{\text{abs}}^{\text{L3Residual}}(p_{\text{T}}''). \quad (4.6)$$

The $L1$ correction, applied to the raw jet, corrects for offsets due to the underlying event and pileup using a jet area approach. The jet area A_j is determined for each jet and the particles in the event are clustered with a k_T jet clustering algorithm [63] with a distance parameter $R = 0.6$, which clusters a large number of soft jets in each event. The median p_{T} density ρ is then defined as the median of the distribution of $p_{\text{T},j}/A_j$ for all of these jets. Because of the large number of jets originating from secondary interactions, ρ is not influenced by the presence of hard jets from the primary interaction in the event and is a measure for the pileup activity, the underlying event, and electronic noise. Jets are then corrected by the factor $C_{\text{offset}}^{L1}(p_{\text{T}}^{\text{raw}}) = 1 - \frac{(\rho - \langle \rho_{\text{UE}} \rangle) \cdot A_j}{p_{\text{T}}^{\text{raw}}}$, where $\langle \rho_{\text{UE}} \rangle$ is the mean p_{T} density due to the underlying event, measured in events with no pileup interactions. C_{MC}^{L2L3} , derived from simulation, corrects for the non-linearities and non-uniformities of the detector response to jets of different p_{T} and η and are applied to the offset-corrected jets. To correct for residuals differences between simulation and data, $C_{\text{rel}}^{\text{L2Residual}}(\eta)$ and $C_{\text{rel}}^{\text{L3Residual}}(p_{\text{T}}'')$, derived from dijet and $Z/\gamma + \text{jets}$ data, are applied to jets in data events.

In this analysis, the p_{T} of a jet is required to exceed 40 GeV and jets are required to lie inside the fiducial volume of the ECAL of $|\eta| < 3.0$. A set of loose quality selections is applied to suppress jets reconstructed because of detector noise, ensuring that the jet is reconstructed in more than one subdetector and has more than one constituent. To prevent an overlap between selected objects, jets within $\Delta R = 0.4$ to leptons identified with the criteria described above are rejected.

Because of their long lifetime, b-hadrons decay at a measurable distance from their production vertex, allowing for the reconstruction of a secondary vertex. In this analysis the *combined secondary vertex* (CSV) algorithm is used. Likelihood ratios based on a variety of variables characterizing the secondary vertex and the tracks inside the jet are used to construct a single discriminator. If the value of this discriminator exceeds a given threshold, the jet is tagged as originating from a b-quark [64]. The performance of the b-tagging algorithms have been measured on the dataset recorded at $\sqrt{s} = 8$ TeV [65]. The average identification efficiency as a function of the discriminator value is shown in Figure 4.1 (top). In this analysis, a jet is tagged as a b-jet if the discriminator is larger than 0.679. For this working point the efficiency is about 70% while the probability to misidentify a jet originating from a light quark as a b-jet is between 1% and 3%, depending on the p_{T} of the jet, as shown in Figure 4.1 (bottom). In this analysis b-jets with a p_{T} larger than 30 GeV and $|\eta| < 2.4$ are considered.

Missing transverse energy

As discussed in Section 1.1, $E_{\text{T}}^{\text{miss}}$ measures the imbalances of the energy depositions in the detector in the plane transverse to the beam direction. As this imbalance is the only experimental signature of this class of particles, a good $E_{\text{T}}^{\text{miss}}$ resolution is a key factor for the discovery of processes that include the production of new weakly interacting particles.

Several algorithms have been developed in CMS to reconstruct $E_{\text{T}}^{\text{miss}}$ [66]. Calorimetric (Calo) $\vec{E}_{\text{T}}^{\text{miss}}$ is calculated as the negative vector sum of the energy deposits in each calorimeter tower. Muons deposit only very small amounts of energy in the calorimeters, which are

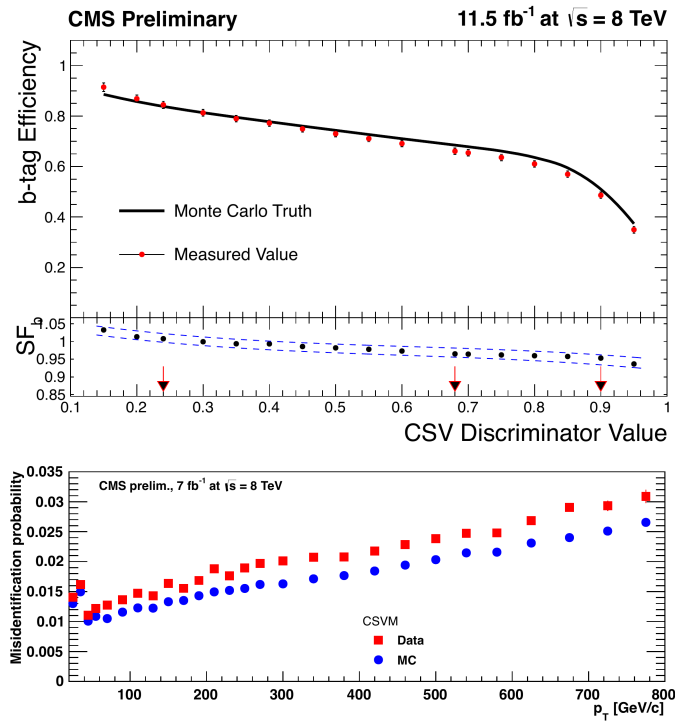


Figure 4.1: Performance of the CSV b-tagging algorithm. Shown is the identification efficiency as a function of the discriminator value (top) and the probability of misidentifying a jet originating from a light quark as a b-jet (bottom) as a function of p_T [65]. In the top figure, the scale factor between data and simulation is shown below the plot. The black arrows indicate three working points used in CMS.

replaced by the measured muon p_T for this calculation. Track-corrected (TC) \vec{E}_T^{miss} differs from Calo \vec{E}_T^{miss} in the treatment of charged hadrons. For well reconstructed tracks, the track measurement is more precise than the measurement of a hadron's energy in the HCAL. Therefore, for tracks not associated with an electron or muon, the track measurement is used in the calculation of \vec{E}_T^{miss} . The energy deposit in the calorimeter is excluded, based on a model of the calorimeter response, treating all hadrons as pions. In contrast to these subdetector-based approaches, the event description of the particle flow algorithm can be used to calculate \vec{E}_T^{miss} . It is defined as the negative vector sum over the p_T vectors of all *particle candidates*

$$\vec{E}_T^{\text{miss}} = - \sum_{\text{particle candidates}} \vec{p}_T. \quad (4.7)$$

Several corrections can be applied to the calculation of E_T^{miss} . The *type-I* corrections propagate the corrections to the jet energy to the E_T^{miss} calculation for all jets with p_T larger than 10 GeV and with less than 90% of their energy deposited in the ECAL. The effects of pileup on the E_T^{miss} reconstruction can be mitigated by applying *type-0* corrections, which are calculated on minimum bias events to parametrise the effects of such interactions on E_T^{miss} . Additionally, *type-I* corrected E_T^{miss} can be further adjusted using *type-II* corrections that take into account effects caused by the underlying event. Further corrections can be applied to correct for modulations of the E_T^{miss} in ϕ [67]. As this analysis searches for events with a large genuine E_T^{miss} and is therefore not very sensitive to E_T^{miss} introduced by resolution effects, none of these corrections are applied.

Comparing the resolution for the E_T^{miss} components in x and y direction, as shown in Figure 4.2 for the data collected in 2011, PF E_T^{miss} performs better than TC and Calo E_T^{miss} and is therefore used in this analysis. However, the other two, as well as *type-I* corrected PF E_T^{miss} , are considered as cross-checks.

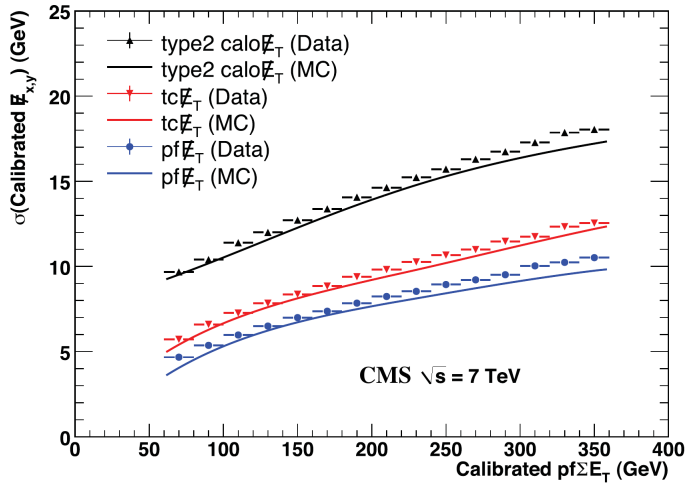


Figure 4.2: Calibrated E_T^{miss} resolution as a function of the sum of the E_T of all particle flow candidates in an event. Shown are *type-II* corrected Calo E_T^{miss} as black upward pointing triangles, TC E_T^{miss} as red downward pointing triangles, and PF E_T^{miss} as blue points [66].

Lepton isolation

While the lepton selection criteria described above are sufficient to reject backgrounds from particles misidentified as leptons, they do not suppress real leptons not originating from the primary interaction. As these are often produced in decays of heavy flavour quarks inside a jet, a more suitable criterion is to consider the amount of activity in the detector close to the lepton candidate, called lepton isolation. In this analysis, particle based isolation is used. For this the energy deposited by charged hadron, neutral hadron, and photon *particle candidates* in a cone of $\Delta R = 0.3$ around the lepton is summed:

$$\text{Iso}^{\text{uncorrected}} = \sum_{\text{charged hadrons}} p_T + \sum_{\text{neutral hadrons}} p_T + \sum_{\text{photons}} p_T. \quad (4.8)$$

The calculation of the isolation is distorted by pileup if PF candidates originating from pileup interactions lie within the cone and are counted in the isolation sum. This is easily remedied for charged hadrons, as those originating from a pileup vertex can be excluded from the calculation. For neutral hadrons and photons there is no track that can be associated to a vertex and a direct identification as pileup particles is not possible. Different approaches are pursued to correct for this contribution for electrons and muons. In both cases, an estimate for the contribution of neutral pileup is subtracted from the isolation sum, which changes the isolation variable to:

$$\text{Iso} = \sum_{\text{charged hadrons from PV}} p_T + \max \left(0, \sum_{\text{neutral hadrons}} p_T + \sum_{\text{photons}} p_T - \sum_{\text{neutral PU}} p_T \right), \quad (4.9)$$

where $\sum_{\text{neutral PU}} p_T$ is the estimated pileup contribution from neutral hadrons. For electrons the correction is similar to the L1 offset correction for jets described above. As a measure of the pileup contribution in the isolation cone the median p_T density in the event ρ is multiplied by the effective area of the electron in the detector, which is calculated in bins of η . The pileup correction is therefore defined as $\sum_{\text{neutral PU}} E_T = \rho \cdot A_{\text{electron}}^{\text{eff}}$. For muons $\Delta\beta$ corrections are applied. On average, the contribution of neutral particles from pileup is half that of charged particles, leading to a correction defined as $\sum_{\text{neutral PU}} E_T = \Delta\beta \cdot \sum_{\text{charged PU}} E_T$ with $\Delta\beta = 0.5$.

Because of the stochastic nature of these approaches, overcorrection is possible. Therefore, no negative contribution from neutral particles is allowed in Equation 4.9. For both electrons and muons the isolation sum divided by the lepton candidate p_T (relative isolation $\frac{\text{Iso}}{p_T}$) must not exceed 15%. The choice of this requirement is discussed in more detail in Section 4.3.2.

4.2 Event processing and datasets

Events accepted by the HLT are reconstructed using the algorithms described above, implemented in the CMS software (CMSSW) framework [68, 69]. While a first reconstruction is performed immediately after the data is recorded, making it available to analysis within a few days, the full dataset recorded by CMS in 2012 has been reprocessed in a second reconstruction with updated calibrations and detector alignment in the first months of 2013. The software version used for this purpose was “CMSSW 5.3.7 patch6”. The events are stored in the analysis object data (AOD) format, which contains mostly high level objects, such as electrons and

muons, and does not provide access to detailed detector information such as energy deposits, which are not of interest for many analyses. This allows to reduce the event size to $\approx 0.1\text{ MB}$, compared to about 2 MB for the raw detector output.

The data processing in this analysis is split into two parts. As a first step, the events in AOD format are processed utilising the resources of the worldwide LHC computing grid [70, 71], a system of cross-linked computing centres providing storage and computing capacities to the LHC experiments. Datasets stored on grid sites can be accessed through the CMS remote analysis builder [72]. At this stage, dilepton events are selected based on the identification criteria described above and the properties of the lepton pairs, together with other event characteristics, are stored. This is done with version “V00-05-24” of the SuSyAachen framework, which utilises tools provided within the CMSSW framework, notably the physics analysis toolkit [73]. All datasets used in this analysis have been processed using “CMSSW 5.3.8 patch3”. Detector calibrations and alignment constants used in the processing of events in CMSSW are specified in so called Global Tags. The tags used in this analysis are “FT53_V21A_AN6” for data and “START53_V27” for simulation.

The second part consists of all further analysis performed on the events selected in the previous processing. As the event size is much reduced, it can be performed using conventional desktop PCs. Throughout the event processing chain, the ROOT framework [74] for data analysis in particle physics is frequently used. In the final analysis steps, ROOT version 5.34.21 is used.

4.2.1 Primary datasets

Events are sorted into different primary datasets based on the HLT decisions, grouping together events accepted by related triggers. As this allows for events to appear in several of these datasets, precautions against double counting have to be taken when combining different data streams in one analysis. The primary datasets most relevant to this analysis are DoubleElectron, DoubleMu, and MuEG, containing, amongst others, events triggered by the different dilepton triggers. As auxiliary datasets, events from primary datasets triggered by H_T (HT , JetHT), single leptons (SingleElectron, SingleMu), and α_T (HT , HTMHT) are used (see Section 3.3). Each primary dataset is split into four subsets, labelled Run2012A to Run2012D, each run defined by the run period of the LHC between two technical stops. The primary datasets are summarised in Table 4.3, where also the dataset paths by which the samples can be accessed in the CMS bookkeeping system (DBS) [75] is given.

4.2.2 Simulated datasets

Simulated datasets of SM processes and SUSY models are used throughout the analysis in the design and validation of methods and the interpretation of the results in terms of potential signals. However, as the estimation of the SM backgrounds is performed almost exclusively on data, only a short overview over the simulation techniques is given. Dedicated methods are used for the different steps needed to achieve a complete model of the proton-proton interactions and the detector response.

Primary dataset	purpose	dataset
DoubleElectron	Signal	/DoubleElectron/Run2012A-22Jan2013-v1/AOD /DoubleElectron/Run2012B-22Jan2013-v1/AOD /DoubleElectron/Run2012C-22Jan2013-v1/AOD /DoubleElectron/Run2012D-22Jan2013-v1/AOD
DoubleMu	Signal	/DoubleMu/Run2012A-22Jan2013-v1/AOD /DoubleMuPark/Run2012B-22Jan2013-v1/AOD /DoubleMuPark/Run2012C-22Jan2013-v1/AOD /DoubleMuPark/Run2012D-22Jan2013-v1/AOD
MuEG	Background prediction	/MuEG/Run2012A-22Jan2013-v1/AOD /MuEG/Run2012B-22Jan2013-v1/AOD /MuEG/Run2012C-22Jan2013-v1/AOD /MuEG/Run2012D-22Jan2013-v1/AOD
HT, JetHT	trigger efficiencies	/HT/Run2012A-22Jan2013-v1/AOD /JetHT/Run2012B-22Jan2013-v1/AOD /JetHT/Run2012C-22Jan2013-v1/AOD /JetHT/Run2012D-22Jan2013-v1/AOD
HTMHT	additional trigger studies	/HTMHTPark/Run2012B-22Jan2013-v1/AOD /HTMHTPark/Run2012C-22Jan2013-v1/AOD /HTMHTPark/Run2012D-22Jan2013-v1/AOD
SingleElectron	additional trigger studies	/SingleElectron/Run2012A-22Jan2013-v1/AOD /SingleElectron/Run2012B-22Jan2013-v1/AOD /SingleElectron/Run2012C-22Jan2013-v1/AOD /SingleElectron/Run2012D-22Jan2013-v1/AOD
SingleMu	additional trigger studies	/SingleMu/Run2012A-22Jan2013-v1/AOD /SingleMu/Run2012B-22Jan2013-v1/AOD /SingleMu/Run2012C-22Jan2013-v1/AOD /SingleMu/Run2012D-22Jan2013-v1/AOD

Table 4.3: List of primary datasets used in the analysis. Additionally, the main purpose of the dataset and datasetpaths in DBS are given.

Simulation of the physical processes

Monte Carlo (MC) methods are used to generate events according to the properties of physical processes [9]. At the beginning of the description of a process stands the calculation of the cross section for the given hard scattering of fundamental particles, using perturbation theory (see for example [11]). For many SM processes and also some BSM models, calculations in next-to-leading order (NLO) or next-to-next-to-leading order (NNLO) order in QCD have been performed. The automated calculations performed in the event generators used for the simulation in this analysis are however mostly restricted to leading-order (LO) accuracy. Scaling the events to calculated cross sections retains the higher order accuracy in the total cross section. Differential cross sections are, however, restricted to the order at which the events are generated at.

At a hadron collider, the total cross section for a process is given by the cross section for the hard parton scattering $\hat{\sigma}$, convolved with the parton density functions (PDFs) $f_i^p(x, Q^2)$, which give the probability that a parton i with a fraction x of the proton's momentum will take part in the interaction at the momentum scale Q^2 . Considering all possible combinations of partons (three valence quarks, sea quarks and gluons), the total cross section is given by

$$\sigma(pp \rightarrow C) = \sum_{i,j} \int dx_1 dx_2 f_i^p(x_1, Q^2) f_j^p(x_2, Q^2) \hat{\sigma}(ij \rightarrow C). \quad (4.10)$$

The PDFs have to be inferred from data and have been studied in numerous fixed-target experiments and, most importantly, in deep-inelastic electron-proton scattering at the HERA collider [76]. Different approaches are used by several groups to parametrise the PDFs based on the available data. In the generation of simulated datasets for CMS analyses, the CTEQ6L1 [77] PDF set has been used. To study systematic effects introduced by the choice of PDF set, the NNPDF2.3 [78], MSTW2008 [79], and CT10 [80] PDF sets are used. The dependence of the PDFs on the momentum scale is described by the DGLAP (Dokshitzer, Gribov, Lipatov, Altarelli, Parisi) evolution equations [81, 82, 83], which are used to extrapolate to the regime of the LHC.

For most processes, Madgraph 5.1.3.30 [84] is used to calculate the hard scattering process, together with additional emissions of partons as part of initial and final state radiation (ISR and FSR). The inclusion of these emissions at matrix element level allows for the modelling of the radiation of hard partons that are well separated from other final state particles. However, this treatment breaks down for soft or collinear emissions, which can in turn be described by dedicated parton shower models. For this, Pythia 6.4.22 [85] has been used for all samples relevant to this analysis. To achieve a consistent description of the parton shower, events are rejected in which the parton shower in Pythia produces jets in the phase space already covered by the emissions in Madgraph, using the MLM matching scheme [86].

The production of single top quarks is simulated using Powheg [87, 88, 89] at NLO in perturbative QCD for the leading jet. For these samples, a similar matching of the parton showers in Powheg and Pythia is applied.

The hadronisation of colour-charged particles produced in the hard scattering or the parton shower is a non-perturbative process which can only be described by phenomenological models. The *string fragmentation* model, as used in Pythia, is based on the idea of colour strings connecting the colour-charged particles. The energy stored in the strings increases linearly with

the distance between the particles, until the string breaks and a $q\bar{q}$ pair is created, allowing for the formation of colour-singlets. These singlets may in turn break, until there is no longer enough energy available to continue with this process [85]. The hadronisation model, as well as the description of the underlying event and multi-parton interactions, has to be tuned to best describe existing data. For all samples used in this analysis, the tune $Z2^*$ [90] is used.

The decays of τ leptons are simulated with the dedicated software Tauola [91], which includes polarisation, spin correlations effects and intermediate hadron resonances.

To simulate the effects of pileup, several simulated proton-proton interactions from a sample containing mostly soft QCD processes are added to the simulated events, including pileup interactions with a time distance with respect to the event of ± 50 ns to emulate the effects of out-of-time pileup. The distribution of the number of additional interactions used in the simulation had to be estimated before the data taking and therefore differs from that observed in the recorded dataset. This effect is corrected for, see section 4.3.2.

Simulation of the detector response

A model of the CMS detector has been created using the GEANT4 toolkit [92]. It allows for a detailed description of the detector geometry and material budget and simulates the interactions of particles with the detector material. It also models the propagation of the particles inside different materials, taking into account for example the magnetic field inside the CMS solenoid. The energy deposits created by the interactions of the particles with the detector are converted into detector hits on which the full event reconstruction is performed. The simulation also includes modelling of detector noise and dead readout channels.

As this detailed simulation is time consuming, a fast simulation of the CMS detector has been developed [93]. Trading accuracy for gains in processing time, the fast simulation is used in cases where large numbers of events have to be generated, for example in scans of the parameter space of a new physics model. Simplifications include for example an approximation of the tracker geometry, where the modelling of millions of individual modules has been replaced by thin cylinders of active and non-active material placed around the interaction point. A charged particle traversing these layers deposits some energy at the point at which it crosses an active layer with a predefined probability. Also, the reconstruction algorithms for tracks have been simplified. Similar approaches have been applied to all subdetectors. The simulation of detector noise is reduced. A decrease of processing time per event by two orders of magnitude is achieved.

Simulated events are stored in the AODSIM data format, which is identical to the AOD format but also includes Monte Carlo truth information about the simulated particles and their production and decay history. This allows for a processing of simulated datasets with the same software as used in the analysis of data events.

Background datasets

Possible background contributions in the analysis arise from all SM processes producing lepton pairs or one lepton with the possibility for other particles in the final state to be misidentified

as a second lepton. The properties of these processes can be studied in simulation. Therefore, an extensive list of simulated processes is considered in the analysis. In many cases, processes are divided into different samples based on the different possible final states. This allows to produce larger sample sizes for decays with small branching fraction without having to generate enormous amounts of more abundant final states. The full list of considered processes is shown in Table 4.4. The samples have to be scaled according to the appropriate integrated luminosity, taking into account the number of generated events $N_{\text{events}}^{\text{gen}}$ and the cross section σ of the process. The weight is then given by $w = \frac{L \cdot \sigma}{N_{\text{events}}^{\text{gen}}}$. The top pair production is normalised to the cross section measured by CMS in the dileptonic decay channel [94]. Cross sections for the production and dileptonic decays of W and Z bosons have been calculated using FEWZ 3.1 [95], including corrections in NLO (NNLO) in electronweak theory (QCD). MCFM 6.6 [96] is used for the calculation of cross sections for diboson production. Cross sections for single top production have been calculated at approximately NNLO [97]. Cross sections at NLO in QCD for triboson production have been calculated using aMC@NLO [98], while for $t\bar{t}$ production in association with one additional vector boson, MCFM 6.6 has been used [99]. For $t\bar{t}\text{WW}$ the cross section calculated by Madgraph is used. The cross section for top-pair production in association with a photon has been measured by CMS [100].

For all occurrences of results based on simulation, the events are scaled by the trigger efficiency measured on data (see Section 5.1.2). If systematic uncertainties on the simulation are shown, they include uncertainties on the jet energy scale, trigger efficiencies, cross sections, and the pileup reweighting. In the case of $t\bar{t}$, the events are reweighted to correct for differences in the distribution of the p_T of the top quarks between data and simulation [101]. For this process the systematic uncertainties additionally include uncertainties introduced by this reweighting as well as uncertainties on the choice of the matching and factorisation scale in the generation of the events. Notably, no uncertainties on the parton distribution functions are considered. Also, many smaller uncertainties on the modelling of physics objects are not considered. Therefore, the shown uncertainty presents a lower bound on the actual systematic uncertainty on the simulation. As the background contributions are estimated from data in this analysis, neither the imperfect knowledge of these uncertainties nor their size affect the results.

To correctly reproduce the effects of pileup in the simulated samples, the simulated events have to be reweighted based on the number of simultaneous interactions in the events. For simulation the distribution of these interactions is precisely known, for data it has to be inferred from the observed events, taking into account the total inelastic proton-proton interaction cross section. The effects of the reweighting procedure are illustrated in Figure 4.3, where the distribution of the number of reconstructed vertices is shown for an inclusive selection of $e^\pm e^\mp$ and $\mu^\pm \mu^\mp$ events (see Section 4.3.2). The left side shows the distribution before reweighting. The difference between data and simulation is clearly visible, but is almost completely compensated by the reweighting, except for very low numbers of reconstructed vertices. However, this affects only a tiny fraction of the data sample.

Signal datasets

For simulated signals used in the analysis, initial squark pair production is simulated with Madgraph, including the emission of up to two additional partons at matrix element level. Sparticle decays and parton showers are generated with Pythia. The fast simulation of the

category	process	generator	cross section [pb]	processed events	weight
$t\bar{t}$	$t\bar{t} \rightarrow b\bar{b}\ell\nu\ell\nu$	Madgraph	23.84	11952631	0.04
	$t\bar{t} \rightarrow b\bar{b}q\bar{q}\ell\nu$	Madgraph	99.43	24913744	0.07
	$t\bar{t} \rightarrow b\bar{b}q\bar{q}q\bar{q}$	Madgraph	103.74	31172356	0.06
Z + jets	$Z/\gamma^* \rightarrow \ell\ell$ $10 \text{ GeV} < m_{\ell\ell} < 50 \text{ GeV}$	Madgraph	876.80	7132223	2.43
	$Z/\gamma^* \rightarrow \ell\ell$ $m_{\ell\ell} > 50 \text{ GeV}$	Madgraph	3532.80	30000624	2.33
W	$W \rightarrow \ell\nu$	Madgraph	37509	55996720	13.26
WW,WZ,ZZ	$ZZ \rightarrow \ell\ell q\bar{q}$	Madgraph	2.45	1936727	0.03
	$ZZ \rightarrow \ell\ell\nu\nu$	Madgraph	0.36	954911	0.01
	$ZZ \rightarrow \ell\ell\ell\ell$	Madgraph	0.18	4789250	<0.01
	$WZ \rightarrow \ell\nu\ell\ell$	Madgraph	1.06	2017979	0.01
	$WZ \rightarrow qq'\ell\ell$	Madgraph	2.32	3205557	0.01
	$WW \rightarrow \ell\nu\ell\nu$	Madgraph	5.81	1933235	0.06
single top	t s-Channel	Powheg	3.79	259961	0.29
	t t-Channel	Powheg	56.40	3746457	0.30
	t tW-Channel	Powheg	11.10	497658	0.44
	\bar{t} s-Channel	Powheg	1.76	139974	0.25
	\bar{t} t-Channel	Powheg	30.70	1935072	0.31
	\bar{t} tW-Channel	Powheg	11.10	493460	0.45
Other SM	WWW	Madgraph	0.08	220549	0.01
	$WW\gamma$	Madgraph	0.53	215121	0.05
	WWZ	Madgraph	0.06	222234	0.01
	WZZ	Madgraph	0.02	219835	<0.01
	$t\bar{t}\gamma$	Madgraph	2.17	71598	0.60
	$t\bar{t}W$	Madgraph	0.23	196046	0.02
	$t\bar{t}Z$	Madgraph	0.21	210160	0.02
	$t\bar{t}WW$	Madgraph	<0.01	217820	<0.01
$t\bar{t}$ Systematics	$t\bar{t}$	Madgraph	227	6923750	0.65
	$t\bar{t}, m_{top} = 166.5 \text{ GeV}$	Madgraph	227	4469095	1.01
	$t\bar{t}, m_{top} = 169.5 \text{ GeV}$	Madgraph	227	5202817	0.86
	$t\bar{t}, m_{top} = 175.5 \text{ GeV}$	Madgraph	227	5186494	0.87
	$t\bar{t}, m_{top} = 178.5 \text{ GeV}$	Madgraph	227	4723379	0.95
	$t\bar{t}$, Matching scale up	Madgraph	227	5393645	0.83
	$t\bar{t}$, Matching scale down	Madgraph	227	5467170	0.82
	$t\bar{t}$, Factorisation scale up	Madgraph	227	5009488	0.90
	$t\bar{t}$, Factorisation scale down	Madgraph	227	5377388	0.84

Table 4.4: Simulated datasets used in the analysis. The samples are grouped by physics processes and information about the generator, the cross section of the processes, the number of processed events, and the resulting weight used to scale the simulation to the recorded luminosity are given.

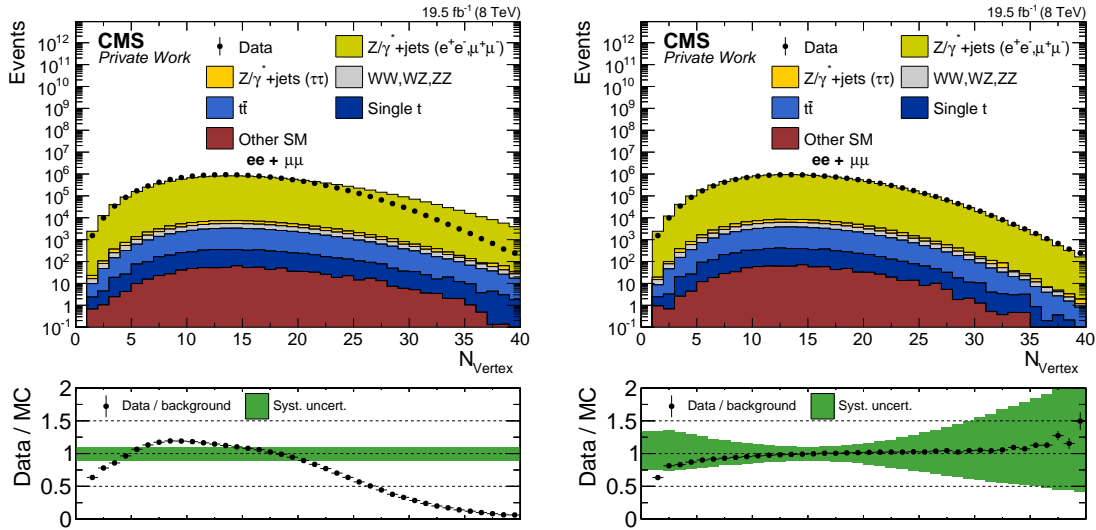


Figure 4.3: Distribution of the number of reconstructed vertices in an inclusive dilepton selection before (left) and after (right) pileup reweighting. The data are shown as black points. The different physical processes contributing to the sample are shown as stacked coloured histograms. Below the plots the ratio of data to simulation is shown. The error bars on the black points include the statistical uncertainties of both data and simulation, while the green band shows the systematic uncertainty on the simulation.

CMS detector is used to model the detector response. Details of the physical models have been discussed in Section 2.2.2.

4.3 Event selection

A series of selection criteria are applied to the events to select signal-like topologies and reduce the contributions from SM backgrounds to the final sample. Also, requirements are defined to select control regions enriched in certain SM processes for the purpose of background prediction and the validation of methods. Additionally, events are rejected that exhibit signs of detector noise or are otherwise not suited for analysis.

4.3.1 Event cleaning

As a first step in the selection of reconstructed events, a series of quality requirements is applied. The quality of the data recorded by the CMS detector is assessed in several automated or manual steps, summarised as *data quality monitoring (DQM)* [102]. For each lumi section this results in a binary decision, flagging it as either *good* or *bad*, accepting only those lumi sections for which all subdetectors were fully operational during data taking and no problems occurred in the reconstruction of the events.

To reject non-collision events, vertex information is used. The presence of at least one primary vertex is required whose distance to the interaction point is less than 24 cm in z direction and

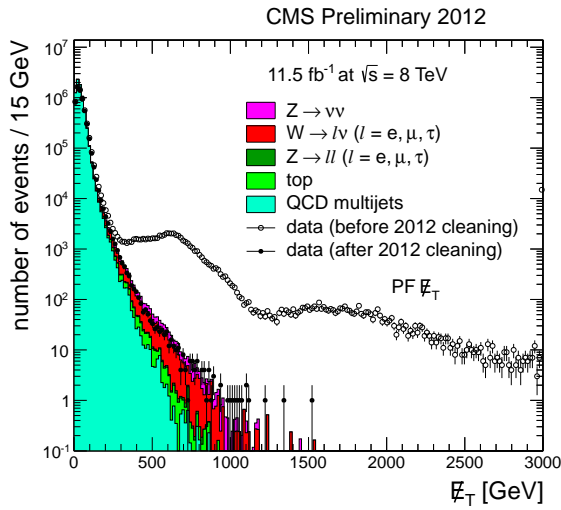


Figure 4.4: Distribution of E_T^{miss} in dijet events in 2012 data. The open data points show all events, while the black points show the data after application of E_T^{miss} filters. Simulated SM processes are shown as filled histograms. [67].

2 cm in the x - y plane. Also, the number of degrees of freedom, defined [49] as:

$$n_{\text{dof}} = -3 + 2 \sum_{i=1}^{N_{\text{tracks}}} w_i, \quad (4.11)$$

is required to be greater than four.

As it relies on the balance of all reconstructed objects, E_T^{miss} is especially sensitive to detector noise or particles not originating from the proton-proton collisions, which affect the event reconstruction. Several sources of these effects have been identified during the data taking and filters have been developed in CMS to reject events matching their signatures [67]. This includes filters for signal produced by interactions of the beam with gas molecules in the beam pipe or of protons in the beam halo with the LHC infrastructure, anomalous noise in the HCAL or ECAL, dead ECAL cells, calibration lasers mistakenly firing during collision events, or failures of the tracking algorithms. The effect of these filters on the tails of the E_T^{miss} distribution in dijet events is shown in Figure 4.4. Events with E_T^{miss} larger than 300 GeV are dominantly rejected by the filters, greatly improving the agreement between the data and simulation.

4.3.2 Inclusive dilepton selection

In the inclusive dilepton selection, events are selected containing two isolated electrons or muons with opposite electric charge, p_T larger than 20 GeV, and $|\eta|$ smaller than 2.4. Leptons with $1.4 < |\eta| < 1.6$ are rejected and the event sample is divided into events where both leptons have $|\eta| < 1.4$ (central) and events where at least one lepton has $|\eta| > 1.6$ (forward). The dilepton invariant mass is required to be larger than 20 GeV and the two leptons are required to be separated by more than $\Delta R(\ell\ell) = 0.3$. In the signal selection, only events

with two same flavour (SF) leptons are considered. Events with opposite flavour (OF) leptons are used to estimate SM backgrounds. These selection requirements are motivated in the following. A summary of this selection and other selection requirements defined in this section is given in Table 4.5.

The choice of the isolation requirement of $\frac{I_{\text{so}}}{p_T} < 0.15$ is illustrated in Figure 4.5 (left), where the distribution of the relative isolation is shown for the trailing lepton in $t\bar{t}$ simulation in the inclusive dilepton selection. Using the truth information of the simulation the sample is split into prompt leptons originating from W boson decays, leptons originating from heavy flavour hadron decays inside b-quark jets, and jets misreconstructed as leptons. The prompt leptons are concentrated at very low values, but a long tail extends to much higher values. The leptons from heavy flavour decays are less well isolated, with a broad maximum of the distribution between 0.5 and 1. Misreconstructed leptons are spread more evenly between high and low values of isolation. The cut value of 0.15 allows for a strong suppression of non-prompt leptons while a high efficiency is retained for prompt leptons. The isolation efficiency as a function of the number of reconstructed vertices is shown on the right side of Figure 4.5 separately for prompt electrons and muons in $t\bar{t}$ and Z + jets events. The efficiency in Z + jets events is about 5 percentage points higher compared to the more hadronic environment of $t\bar{t}$ events. While the efficiency for electrons shows only a slight dependency on the number of vertices and therefore on the amount of pileup, for muons a more strong decrease of efficiency is observed for high numbers of vertices. However, for $t\bar{t}$ events this is much less pronounced, as the efficiency is already diminished by the higher number of jets in this environment. The good separation of prompt and non-prompt leptons and the high efficiency for prompt leptons are therefore retained even in the challenging conditions of high pileup.

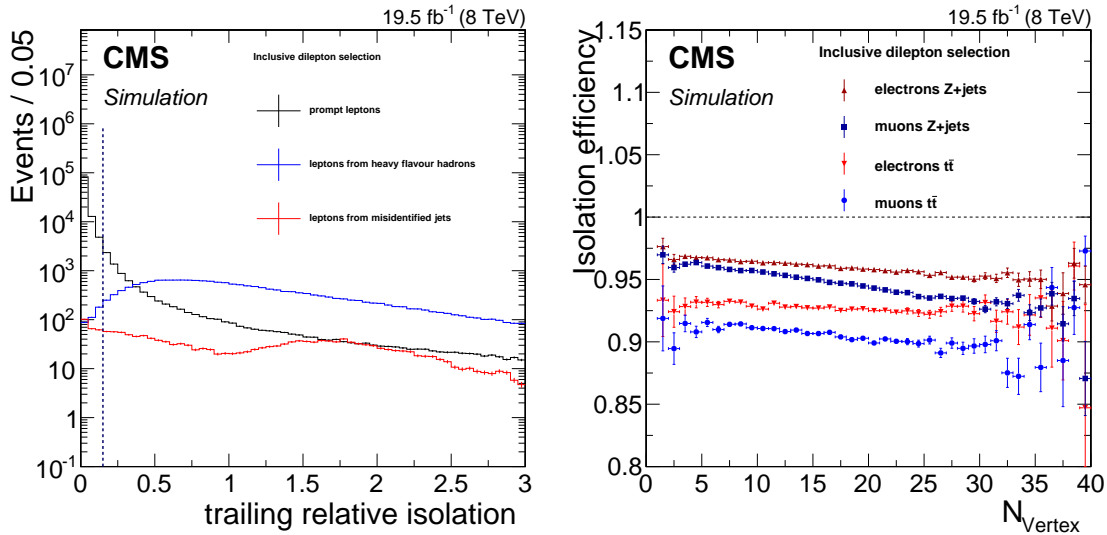


Figure 4.5: On the left, the distribution of the pileup corrected relative isolation of the trailing lepton for prompt leptons, leptons from heavy flavour decays, and misidentified jets in $t\bar{t}$ simulation is shown. On the right side, the efficiency for a prompt lepton to pass the isolation requirement is shown as a function of the reconstructed number of vertices for both $t\bar{t}$ and Z + jets simulation. In both cases, the inclusive dilepton selection is applied.

The p_T requirement is driven by the thresholds of the dilepton triggers, as discussed in Section 5.1.2, while the $|\eta|$ restriction is imposed by the coverage of the muon system. The acceptance for electrons could in principle be extended to $|\eta| = 2.5$, but is chosen to be the

same for both lepton flavours. Lepton pairs are required to be selected by the corresponding trigger, e.g. an event containing a pair of electrons has to have fired the dielectron trigger. If there is more than one pair of leptons fulfilling this basic requirements in one event, the pair with the largest scalar sum of lepton p_T is chosen. There is no explicit requirement of the two selected leptons to be matched to the objects that fired the trigger.

As the symmetry between lepton flavours is a key ingredient of the methods to estimate the backgrounds from SM processes, parts of the detector acceptance for which these symmetries are potentially violated are excluded:

As the efficiency to reconstruct electrons is reduced in the overlap region between the barrel and endcap detectors of the ECAL, the relative event yield for events with electrons with $|\eta|$ between 1.4 and 1.6 is reduced compared to those with muons in this range. This distribution of the $|\eta|$ of the leading lepton in $e^\pm e^\mp$ and $\mu^\pm \mu^\mp$ events is shown in Figure 4.6 (left), illustrating the greatly increased difference between the event yields for electrons and muons in the overlap region. Events containing a lepton with a pseudorapidity of $1.4 < |\eta| < 1.6$ are therefore rejected. Also, an increasing difference between electrons and muons can be seen for events where the leading leptons is in the endcap region of the detector. This motivates the split of the event samples into the two categories central, where both leptons are reconstructed with $|\eta| < 1.4$ and forward, where at least one lepton has to be reconstructed with $|\eta| > 1.6$. Also, the decay products of heavy SUSY particles are expected to be located dominantly in the central detector region, as the initially produced sparticles are not significantly boosted in forward direction. The efficiency drop for muons around $|\eta| = 0.25$ is caused by the transition between different DT chambers in the muon system [34]. While there are several of these transitions, the effect is most pronounced at low $|\eta|$ because the angle between the trajectory of the muon and the gap between the chambers is smaller.

Leptons with small spatial separation can interfere with each others reconstruction and isolation. These effects are different for electrons and muons, which can be seen in Figure 4.6 (right). The ratio of electrons to muons first rises for lower values of $\Delta R(\ell\ell)$ before dropping for values below 0.1. The leptons are therefore required to be separated in $\Delta R(\ell\ell)$ by more than 0.3. Some differences between electrons and muons can also be observed for very high values of $\Delta R(\ell\ell)$, but they are less pronounced and this region is less populated.

To avoid possible reconstruction problems, events with low lepton momenta and to avoid contamination from dilepton production in the decay of the bottomonium resonances, the dilepton invariant mass $m_{\ell\ell}$ is required to be greater than 20 GeV.

4.3.3 Selections in E_T^{miss} and jet multiplicity

Three subsets of the event sample obtained with the inclusive dilepton selection are defined, resulting in samples enriched by different processes. The variables used in the definitions of these regions are E_T^{miss} and the number of selected jets N_{jets} . The selections are illustrated in the plots of Figure 4.7, which also show the distribution of $t\bar{t}$ (left) and Z + jets (right) events in the $E_T^{\text{miss}}-N_{\text{jets}}$ plane for SF leptons.

The signal region, in which the search is performed, is defined by requiring either $N_{\text{jets}} \geq 3$ and $E_T^{\text{miss}} > 100$ GeV; or $N_{\text{jets}} \geq 2$ and $E_T^{\text{miss}} > 150$ GeV. This definition allows to select

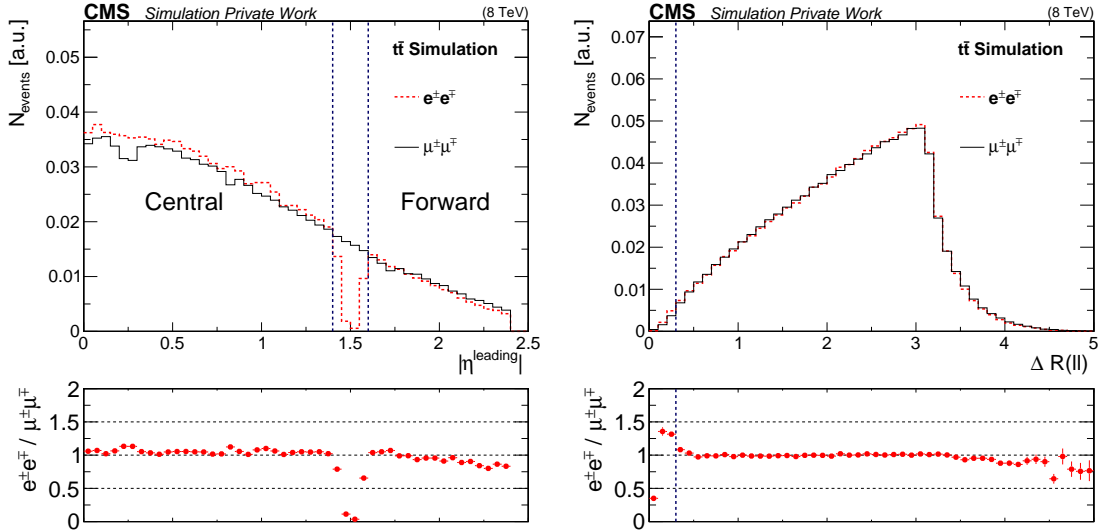


Figure 4.6: Distributions of $|\eta|$ (left) and $\Delta R(\ell\ell)$ (right) for the leading lepton for $\mu^\pm\mu^\mp$ (black line) and $e^\pm e^\mp$ (red dashed line) events in a simulation of $t\bar{t}$ events. Both histograms have been normalised to an area of 1.

signal events for points in the parameter space where more energy is distributed to the jets and less to the invisible component of the signature and vice versa. At the same time the rejection of background events with both lower N_{jets} and E_T^{miss} is maintained. A control region dominated by flavour-symmetric processes is defined by selecting events with $N_{\text{jets}} = 2$ and $100 \text{ GeV} < E_T^{\text{miss}} < 150 \text{ GeV}$.

To study lepton pairs produced via the Drell-Yan process and to obtain a high statistics sample of leptons for efficiency measurements, events with $N_{\text{jets}} \geq 2$ and $E_T^{\text{miss}} < 50 \text{ GeV}$ are selected. The N_{jets} requirement greatly reduces the statistics and the purity of this event sample. However, because of the large cross section of the Drell-Yan process, the event yield is still sufficient for the purposes of this analysis and Drell-Yan events dominate over those from $t\bar{t}$ production by two orders of magnitude. This allows to select events with kinematics close to those of the signal selection in terms of jet multiplicity.

For comparison the same distributions are shown for two signal points from the models discussed in Section 2.2.2 in Figure 4.8. On the left a point from the fixed-edge model with $m_{\tilde{b}} = 550 \text{ GeV}$ and $m_{\tilde{\chi}_2^0} = 275 \text{ GeV}$ (left) and on the right a point from the slepton-edge model with $m_{\tilde{b}} = 500 \text{ GeV}$ and $m_{\tilde{\chi}_2^0} = 175 \text{ GeV}$ are shown. For both signal points almost no events are observed with $N_{\text{jets}} < 2$, which is expected because at least two b-jets are produced in each event. Compared to the backgrounds, a clear tendency towards higher E_T^{miss} and N_{jets} is observed. However, also contributions to two control regions are present, which are small compared to the background contributions. Overall, the chosen selection offers a good separation of signal and backgrounds.

4.3.4 Selections in $m_{\ell\ell}$

Since the analysis is performed using two different approaches, several regions are defined in $m_{\ell\ell}$. In the “counting experiment”, an excess in the number of observed events over

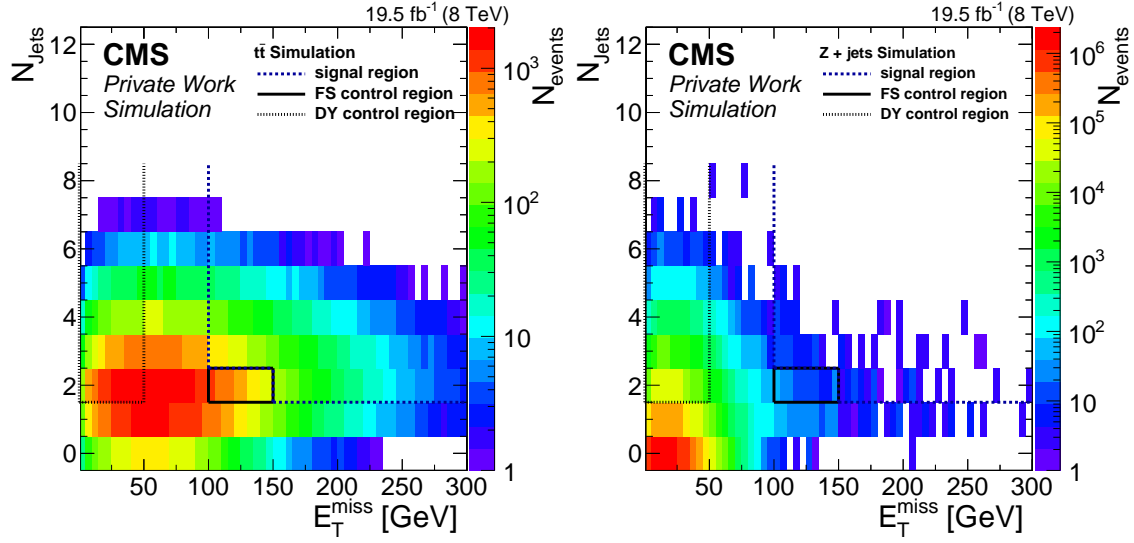


Figure 4.7: Distribution of background events with SF leptons in the $E_T^{\text{miss}}\text{-}N_{\text{jets}}$ plane for $t\bar{t}$ (left) and Drell-Yan (right) events from Simulation. The events are weighted according to the cross section of the process and the size of the generated event sample, assuming an integrated luminosity of 19.5 fb^{-1} . The three regions defined in the plane are indicated by lines. The central and forward dilepton selection are combined.

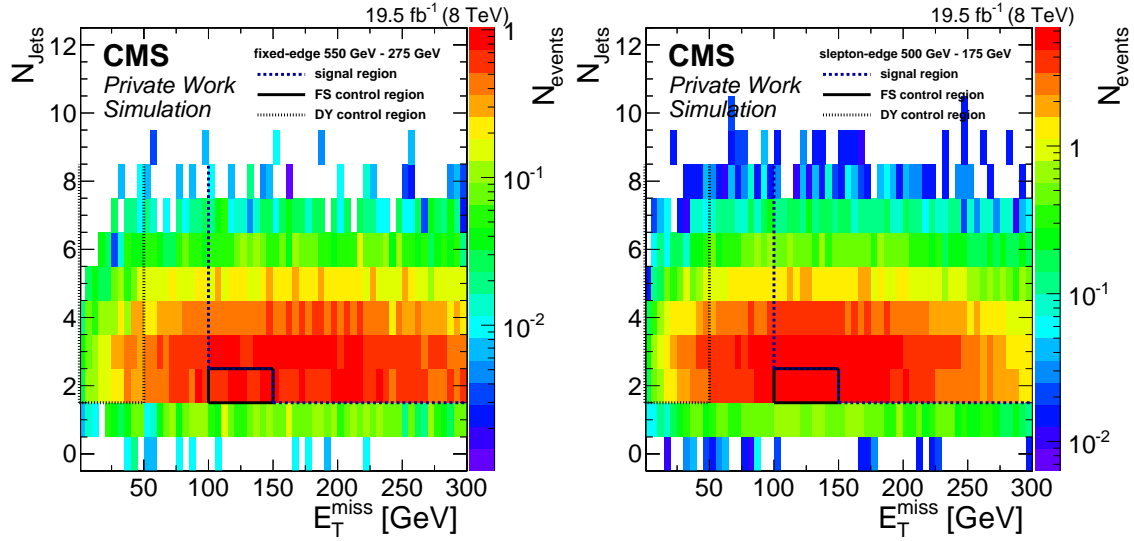


Figure 4.8: Distribution of signal events with SF leptons in the $E_T^{\text{miss}}\text{-}N_{\text{jets}}$ plane. Shown is one point from the fixed-edge model with $m_{\tilde{b}} = 550 \text{ GeV}$ and $m_{\tilde{\chi}_2^0} = 275 \text{ GeV}$ (left) and one from the slepton-edge model with $m_{\tilde{b}} = 500 \text{ GeV}$ and $m_{\tilde{\chi}_2^0} = 175 \text{ GeV}$ (right). The events are weighted according to their cross section and the size of the generated event sample, assuming an integrated luminosity of 19.5 fb^{-1} . The three regions defined in the plane are indicated by lines. The central and forward dilepton selection are combined.

the background expectation is sought in three regions of dilepton invariant mass $m_{\ell\ell}$: low-mass ($20 < m_{\ell\ell} < 70$ GeV), on-Z ($80 < m_{\ell\ell} < 101$ GeV) and high-mass ($120 \text{ GeV} > m_{\ell\ell}$). Figure 4.9 shows the $m_{\ell\ell}$ distribution in the central region for simulated SM backgrounds, which are shown separately for different physics processes. It can be seen that $t\bar{t}$ is the dominant background in all three mass bins. For the on-Z region also Drell–Yan backgrounds contribute significantly. The precise determination of these backgrounds from data are described in Section 5 and the results of the counting experiment are discussed in Section 6.

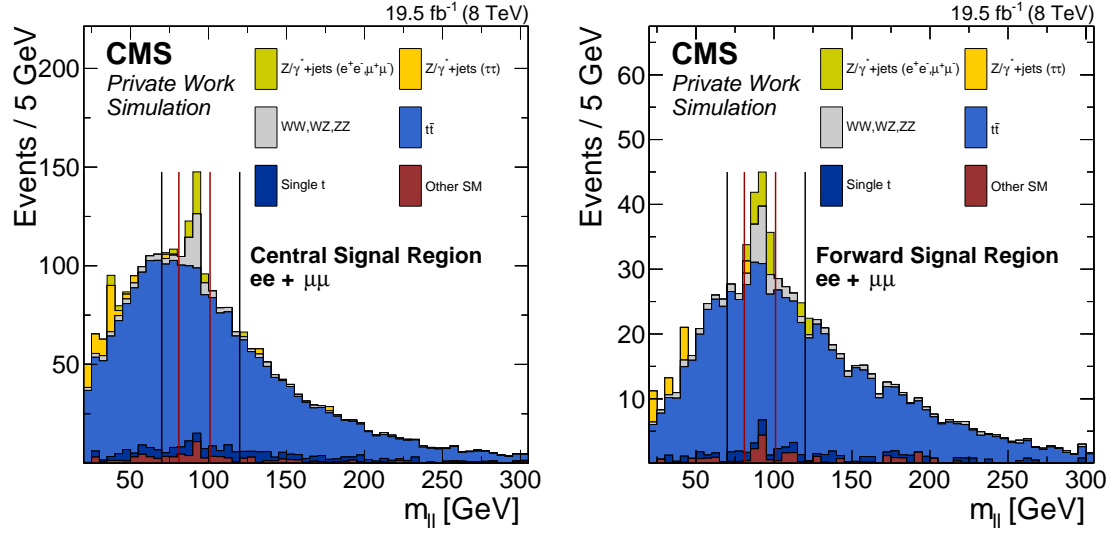


Figure 4.9: Distribution of $m_{\ell\ell}$ in SM simulation in the signal region. The different background contributions are shown as stacked histogram. The distribution is normalised to 19.5 fb^{-1} . The red lines indicate the on-Z region while the black lines show the boundaries of the low-mass and high-mass regions.

For the shape analysis searching for edges in the $m_{\ell\ell}$ spectrum, the mass range $20 < m_{\ell\ell} < 300$ GeV is studied. It is described in Section 7.

Table 4.5: Summary of event selections applied in the analysis. Each of the selections in N_{jets} and $E_{\text{T}}^{\text{miss}}$ (Drell–Yan control region, flavour-symmetric control region, and signal region) are applied on top of the inclusive dilepton selection. Selections in $m_{\ell\ell}$ and lepton $|\eta|$ are applied to select subsets of these regions.

	selection
inclusive dilepton selection	event cleaning two isolated opposite-sign leptons lepton $p_{\text{T}} > 20 \text{ GeV}$ $\Delta R(\ell\ell) > 0.3$ $m_{\ell\ell} > 20 \text{ GeV}$ lepton $ \eta < 2.4$ excl. $1.4 < \eta < 1.6$
Drell–Yan control region	inclusive dilepton selection $N_{\text{jets}} \geq 2$ $E_{\text{T}}^{\text{miss}} < 50 \text{ GeV}$
Flav.-sym. control region	inclusive dilepton selection $N_{\text{jets}} \geq 2$ $100 \text{ GeV} < E_{\text{T}}^{\text{miss}} < 50 \text{ GeV}$
Signal region	inclusive dilepton selection $N_{\text{jets}} \geq 2$ and $E_{\text{T}}^{\text{miss}} > 150 \text{ GeV}$ or $N_{\text{jets}} \geq 3$ and $E_{\text{T}}^{\text{miss}} > 100 \text{ GeV}$
sub selections based on lepton kinematics	
$m_{\ell\ell}$	low-mass: $20 < m_{\ell\ell} < 70 \text{ GeV}$ on-Z: $80 < m_{\ell\ell} < 101 \text{ GeV}$ high-mass: $120 \text{ GeV} > m_{\ell\ell}$ fit: $20 < m_{\ell\ell} < 300 \text{ GeV}$
$ \eta $	central: both $ \eta < 1.4$ forward: at least one $ \eta > 1.4$

5 Estimation of Standard Model backgrounds

As indicated in Figure 4.7, different SM processes contribute to the event sample in the signal region. To distinguish a potential signal from these backgrounds, a precise estimation of the background contributions is essential. While the simulation of these processes and the response of the CMS detector gives a good description of the data for the majority of the phase space, a large number of uncertainty sources are introduced in the modelling of the physical processes and the detector. Therefore, a higher precision can be achieved by deriving the background estimates directly from the recorded data. Dedicated methods are applied for the flavour-symmetric and Drell–Yan backgrounds (see Section 2.3). The results of these methods are used directly in the counting experiment (see Section 6). The fit in search for a kinematic edge performs shape based estimates of the SM backgrounds. However, the results of the studies of flavour-symmetry described below are used to constrain these backgrounds in the fit procedure.

5.1 Flavour-symmetric backgrounds

Processes that are symmetric in the production of SF and OF lepton pairs allow for the estimation of their contribution to the SF event sample from the OF yield. The relevant backgrounds contributing to this class have been discussed in Section 2.3. Additional contributions are coming from misidentified leptons, as will be demonstrated later.

No significant deviation from flavour-symmetry has been observed in the decays of the W boson, with a measured ratio of the branching fractions into $e + \nu$ and $\mu + \nu$ of $\frac{BF(W \rightarrow e\nu)}{BF(W \rightarrow \mu\nu)} = 1.007 \pm 0.021$ [9]. In the decays of the τ lepton the different masses of electron and muon have a small, but noticeable effect, resulting in a slightly favoured decay into electrons with ratio of branching fractions of $\frac{BF(\tau \rightarrow e\nu)}{BF(\tau \rightarrow \mu\nu)} = 1.0241 \pm 0.0032$ [9]. As backgrounds with τ leptons are a sub-dominant contribution to the flavour-symmetric background, these can be considered to be fully flavour-symmetric on particle level.

However, deviations from flavour-symmetry are introduced by the different efficiencies for triggering, reconstructing, and identifying electrons and muons in CMS. The background estimation from OF events, therefore, has to include a correction for this deviation, which is applied as a multiplicative factor:

$$N_{SF}^{pred} = R_{SF/OF} \cdot N_{OF}.$$

Similarly, the factors $R_{ee/OF}$ and $R_{\mu\mu/OF}$ are used to derive separate background estimates for the $e^\pm e^\mp$ and $\mu^\pm \mu^\mp$ channels. Two independent methods are utilised to measure $R_{SF/OF}$ on data. In the first approach the ratio is directly measured as the ratio of SF to OF events in the control region for flavour-symmetric backgrounds (see Table 4.5). The second approach studies

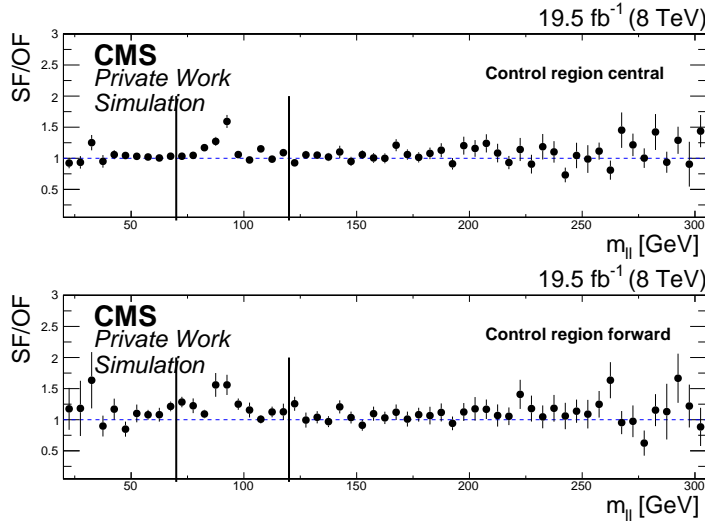


Figure 5.1: Ratio of SF to OF events as a function of $m_{\ell\ell}$ in the $t\bar{t}$ control region in simulation. All contributing background processes have been considered. Shown are the results for the central (top) and forward (bottom) lepton selection. The black vertical lines indicate the upper boundary of the low-mass region and the lower boundary of the high-mass region.

the lepton efficiencies and derives $R_{SF/OF}$ factorised into the effects of trigger efficiencies and reconstruction and identification efficiencies.

5.1.1 Direct measurement of $R_{SF/OF}$

The ratio $R_{SF/OF}$ is calculated in the control region for flavour-symmetric backgrounds. As an initial step, possible dependencies of $R_{SF/OF}$ are studied in simulation, as the statistical uncertainties are lower compared to the data. The ratio of SF to OF events in the flavour-symmetric control region as a function of $m_{\ell\ell}$ in simulation is shown in Figure 5.1, separately for the central and forward lepton selection. The ratio is very close to one and independent of $m_{\ell\ell}$, except at the Z boson peak, where a significant Drell–Yan contribution spoils the SF-OF symmetry. It can be concluded that an universal factor can be applied for flavour-symmetric backgrounds over the full mass range. To exclude the Z boson peak from the calculation only events in the mass regions $20 \text{ GeV} < m_{\ell\ell} < 70 \text{ GeV}$ and $m_{\ell\ell} > 120 \text{ GeV}$ are considered.

The observed ratio in data as a functions of $m_{\ell\ell}$ is shown in Figure 5.2. As expected from the simulation, no significant dependence on $m_{\ell\ell}$ is observed both in the central and forward signal lepton selection. The numerical results are summarised in Table 5.1 for $R_{SF/OF}$ as well as $R_{ee/OF}$ and $R_{\mu\mu/OF}$. Agreement between the values measured in data and simulation is observed within the statistical uncertainties. The observed values in data are $R_{SF/OF} = 1.007 \pm 0.037$ for the central and 1.015 ± 0.062 for the forward dilepton selection.

The extrapolation of the measured value of $R_{SF/OF}$ into the signal region is tested in simulation by calculating the ratio of $R_{SF/OF}$ observed in the signal region to that in the control region. No deviation of the values measured in the signal region from those obtained in the control region is observed within the statistical uncertainties of the simulation. This uncertainty of

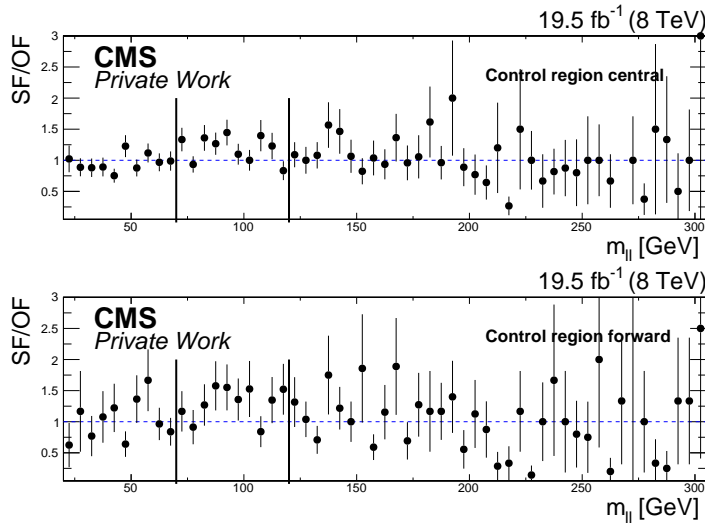


Figure 5.2: Ratio of SF to OF events as a function of $m_{\ell\ell}$ in the $t\bar{t}$ control region in data. Shown are the results for the central (top) and forward (bottom) lepton selection. The black vertical lines indicate the upper boundary of the low-mass region and the lower boundary of the high-mass region.

0.020 for the central and 0.034 for the forward dilepton selection is therefore assigned as a systematic uncertainty of the method.

5.1.2 Determination of $R_{SF/OF}$ with the factorisation method

Asymmetries between the lepton flavours introduced by differing reconstruction and selection efficiencies can be corrected for if the ratio of efficiencies for muons and electrons $r_{\mu e}^* = \frac{\epsilon_\mu}{\epsilon_e}$ is known. Here and in the following, the “ $*$ ” indicates quantities that do not consider the effect of trigger efficiencies. They have, therefore, to be expressed in terms of the measurable event yields which include these effects. Under the assumption that the efficiencies for the two leptons in the event have negligible correlation and the dilepton efficiency factorises, i.e. $\epsilon_{\ell\ell} = \epsilon_\ell \cdot \epsilon_\ell$, the number of dielectron and dimuon events can be expressed in terms of the opposite-flavour yield using the relations

$$N_{ee}^* = \frac{1}{2} \cdot \frac{N_{OF}^*}{r_{\mu e}^*}$$

and

$$N_{\mu\mu}^* = \frac{1}{2} \cdot r_{\mu e}^* \cdot N_{OF}^*.$$

The combined same-flavour yield is therefore given by

$$N_{SF}^* = \frac{1}{2} \cdot \left(r_{\mu e}^* + \frac{1}{r_{\mu e}^*} \right) N_{OF}^*.$$

In practice, all measured quantities are affected by the efficiencies of the different dilepton triggers. The observable SF yield, taking the trigger efficiencies into account, is given by

$$N_{SF} = \epsilon_{ee}^T \cdot N_{ee}^* + \epsilon_{\mu\mu}^T \cdot N_{\mu\mu}^*,$$

Table 5.1: Observed event yields in the control region and the resulting values of $R_{SF/OF}$, $R_{ee/OF}$, and $R_{\mu\mu/OF}$. The results are shown separately for the central and forward lepton selection and the same quantities derived on simulation are shown for comparison.

Control region				
	N_{SF}	N_{OF}	$R_{SF/OF} \pm \sigma_{stat}$	signal/control region $\pm \sigma_{stat}$
Central				
Data	1458	1448	1.007 ± 0.037	–
MC	1484.2	1436.1	1.034 ± 0.015	1.016 ± 0.020
Forward				
Data	545	537	1.015 ± 0.062	–
MC	565.1	517.5	1.092 ± 0.026	0.997 ± 0.034
	N_{ee}	N_{OF}	$R_{ee/OF} \pm \sigma_{stat}$	signal/control region $\pm \sigma_{stat}$
Central				
Data	663	1448	0.458 ± 0.021	–
MC	670.0	1436.1	0.467 ± 0.008	1.017 ± 0.025
Forward				
Data	239	537	0.445 ± 0.035	–
MC	237.9	517.5	0.460 ± 0.014	1.023 ± 0.043
	$N_{\mu\mu}$	N_{OF}	$R_{\mu\mu/OF} \pm \sigma_{stat}$	signal/control region $\pm \sigma_{stat}$
Central				
Data	795	1448	0.549 ± 0.024	–
MC	814.2	1436.1	0.567 ± 0.010	1.015 ± 0.025
Forward				
Data	306	537	0.570 ± 0.041	–
MC	327.3	517.5	0.632 ± 0.018	0.978 ± 0.039

where $\epsilon_{\ell\ell}^T$ denotes the trigger efficiency for the given dilepton combination.

The trigger efficiencies also affect the calculation of N_{ee}^* and $N_{\mu\mu}^*$. To take this into account, $r_{\mu e}^*$ is expressed in terms of the measured value $r_{\mu e}$, which is derived from the $e^\pm e^\mp$ and $\mu^\pm \mu^\mp$ event yields in the Drell-Yan control region (see Section 5.1.2) as

$$r_{\mu e} = \sqrt{\frac{N_{\mu\mu}}{N_{ee}}} \approx \sqrt{\frac{\epsilon_\mu^2 \epsilon_{\mu\mu}^T}{\epsilon_e^2 \epsilon_{ee}^T}} = r_{\mu e}^* \cdot \sqrt{\frac{\epsilon_{\mu\mu}^T}{\epsilon_{ee}^T}}.$$

Finally, the measured yield in the OF channel also includes the trigger efficiencies. Therefore, using $N_{OF} = \epsilon_{e\mu}^T \cdot N_{OF}^*$, the final expressions for the yields in the same-flavour channels become

$$N_{ee} = \frac{1}{2r_{\mu e}} \cdot \frac{\sqrt{\epsilon_{ee}^T \epsilon_{\mu\mu}^T}}{\epsilon_{e\mu}^T} N_{OF} = R_{ee/\text{OF}} N_{OF} \quad (5.1)$$

and

$$N_{\mu\mu} = \frac{1}{2} r_{\mu e} \cdot \frac{\sqrt{\epsilon_{ee}^T \epsilon_{\mu\mu}^T}}{\epsilon_{e\mu}^T} N_{OF} = R_{\mu\mu/\text{OF}} N_{OF}. \quad (5.2)$$

The combined prediction of the SF yield is, therefore:

$$N_{SF} = \frac{1}{2} \left(r_{\mu e} + \frac{1}{r_{\mu e}} \right) \cdot \frac{\sqrt{\epsilon_{ee}^T \epsilon_{\mu\mu}^T}}{\epsilon_{e\mu}^T} N_{OF} = R_{SF/\text{OF}} N_{OF}. \quad (5.3)$$

The factor containing the trigger efficiencies is abbreviated as

$$R_T = \frac{\sqrt{\epsilon_{ee}^T \epsilon_{\mu\mu}^T}}{\epsilon_{e\mu}^T}. \quad (5.4)$$

Measurement of $r_{\mu e}$

The measurement of $r_{\mu e}$ is performed in the Drell-Yan control region (see Table 4.5) as the ratio of $\mu^\pm \mu^\mp$ to $e^\pm e^\mp$ events on the Z boson peak, requiring $60 \text{ GeV} < m_{\ell\ell} < 120 \text{ GeV}$. A comparison of the recorded data to the different contributions from SM processes, estimated from simulation, is shown in Figure 5.3. The Drell-Yan process is the dominating source of events in this selection. Good agreement between data and simulation is observed, indicating a good understanding of this kinematic region by the CMS simulation. Towards higher masses the data is underestimated by the simulation because higher order effects are not included in the simulation and result in a lack of events in the simulated samples. The results of the calculation of $r_{\mu e}$ are shown in Table 5.2. Given are the observed yields for $\mu^\pm \mu^\mp$ and $e^\pm e^\mp$ events and the resulting value of $r_{\mu e}$ with statistical and systematic uncertainties. In the central lepton selection, the $\mu^\pm \mu^\mp$ yield is about 18% higher than the $e^\pm e^\mp$ yield. Similar results are observed on Drell-Yan simulation. For events with leptons in the forward region, a larger asymmetry between muons and electrons is observed, as expected since the harsher pileup environment in the detector endcaps has a stronger effect on the electron efficiencies. Here the $\mu^\pm \mu^\mp$ yield is about 40% higher than the $e^\pm e^\mp$ yield.

The systematic uncertainties assigned to the measured values of $r_{\mu e}$ are 10% for the central and 20% for the forward lepton selection. These values are obtained by studying the dependency

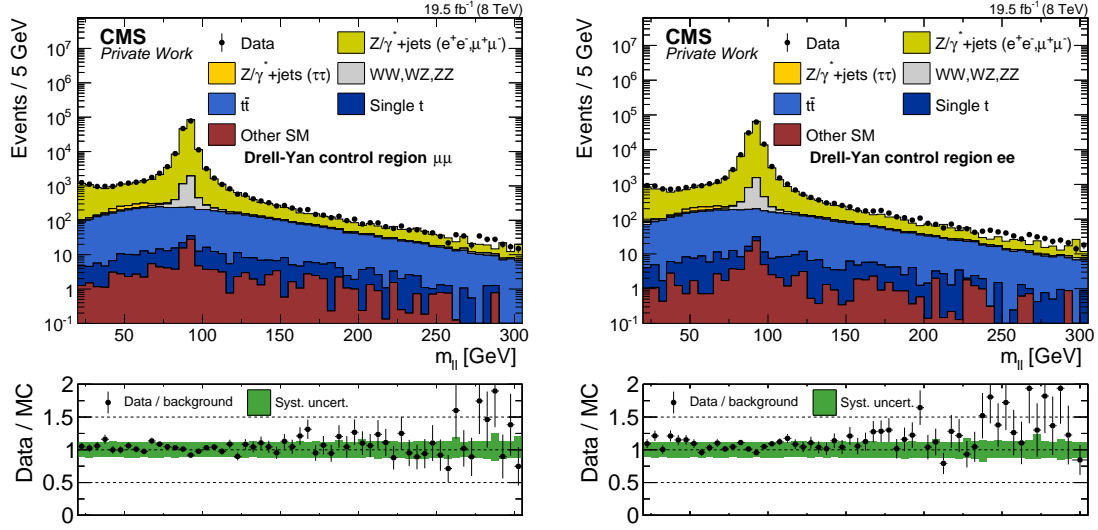


Figure 5.3: Distribution of m_{ll} in the Drell-Yan control region for $\mu^\pm\mu^\mp$ events (left) and $e^\pm e^\mp$ events (right). The data is shown as the black dots, while the contributions from SM processes, estimated from simulation, are shown as the stacked histograms.

Table 5.2: Result of the calculation of $r_{\mu e}$. Shown are the observed event yields in the Drell-Yan control region for the central and forward lepton selection in the $e^\pm e^\mp$ and $\mu^\pm\mu^\mp$ channels and the resulting values of $r_{\mu e}$. The same quantities derived from simulation are shown for comparison.

	$N_{\mu\mu}$	N_{ee}	$r_{\mu e} \pm \sigma_{\text{stat.}} \pm \sigma_{\text{syst.}}$
Central			
Data	98284	83035	$1.09 \pm 0.01 \pm 0.11$
MC	99719	82035	$1.10 \pm 0.00 \pm 0.11$
Forward			
Data	62212	44437	$1.18 \pm 0.01 \pm 0.24$
MC	66327	45541	$1.21 \pm 0.00 \pm 0.24$

of $r_{\mu e}$ on relevant observables. These are on the one hand properties of the lepton pairs, while on the other hand event properties as the jet multiplicity and E_T^{miss} are studied to ensure the applicability of $r_{\mu e}$ in the signal region. The dependencies of $r_{\mu e}$ on $m_{\ell\ell}$, E_T^{miss} , and N_{jets} are shown in Figure 5.4. Some dependency is observed in the case of $m_{\ell\ell}$, where the values are higher for low $m_{\ell\ell}$ below the Z boson mass. This can be traced back to a dependency on the p_T of the leptons, where the efficiencies for muons have sharper turn-ons compared to electrons. In data, there is a strong effect visible around the Z boson mass for forward leptons. This is caused by a systematic shift of the position of the Z boson peak between electrons and muons and is not a general property of $r_{\mu e}$, as is evident from the comparison with $t\bar{t}$ simulation shown in the upper right of Figure 5.4. No strong dependencies can be observed for E_T^{miss} and N_{jets} within the statistical uncertainties. All observed deviations from the central values are covered by the systematic uncertainties assigned to the measurement. Further information on the dependency studies can be found in Appendix C.

Measurement of R_T

The trigger efficiencies are measured utilizing an event sample collected with the H_T triggers discussed in Section 3.3. Lepton pairs corresponding to the flavour combination of the trigger in question are selected. To ensure that only correctly reconstructed events are considered in the calculation of the trigger efficiencies, the events are required to have $H_T > 200 \text{ GeV}$. This excludes events which are completely different in their properties on trigger and analysis level and at the same time is lower than the threshold applied in the trigger because the H_T definition on trigger level differs from the one used offline. To ensure that the factorisation method is performed on event samples completely orthogonal to the signal region and the flavour-symmetric control region, events with $N_{\text{jets}} \geq 2$ and $E_T^{\text{miss}} > 100 \text{ GeV}$ are rejected. As the offline lepton selection has more strict requirements compared to the one applied at HLT level, the dilepton triggers should have accepted all these events. The trigger efficiency is therefore defined as the ratio of accepted events by the total number of events:

$$\epsilon_{\ell\ell}^T = \frac{N_{\text{events}}(H_T \text{ trigger} \cap \ell\ell \text{ selection} \cap \ell\ell \text{ trigger})}{N_{\text{events}}(H_T \text{ trigger} \cap \ell\ell \text{ selection})}.$$

In case of $\mu^\pm\mu^\mp$ and OF events, two triggers are used in the event selection. Therefore, their combined efficiency is measured, requiring the logical OR of both. The resulting efficiencies are summarised in Table 5.3, separately for the central and forward lepton selections. The efficiencies on simulation are measured with much higher statistical precision because the trigger prescales are not applied there. The trigger efficiencies for $e^\pm e^\mp$ and $\mu^\pm\mu^\mp$ are about 97% in both the central and forward selection. The efficiency for OF events is lower, about 95% in the central and 90% in the forward selection. This shows how the flavour symmetry is broken at trigger level by the inclusion of the additional dimuon trigger, which recovers efficiency for the trailing muon leg of the trigger and is not present in the OF triggers.

To assess the systematic uncertainties of the trigger efficiency measurement, potential biases due to the choice of the orthogonal trigger are studied on simulation, using dileptonic $t\bar{t}$ events. On simulation the efficiency can be measured without the requirement of the H_T triggers, as no trigger is needed to select the events. The ratio of this true trigger efficiencies to those measured with the H_T triggers as a function of $m_{\ell\ell}$ is shown in Figure 5.5, separately for SF and OF events. In both cases all deviations from unity are in the order of 0.1% and well

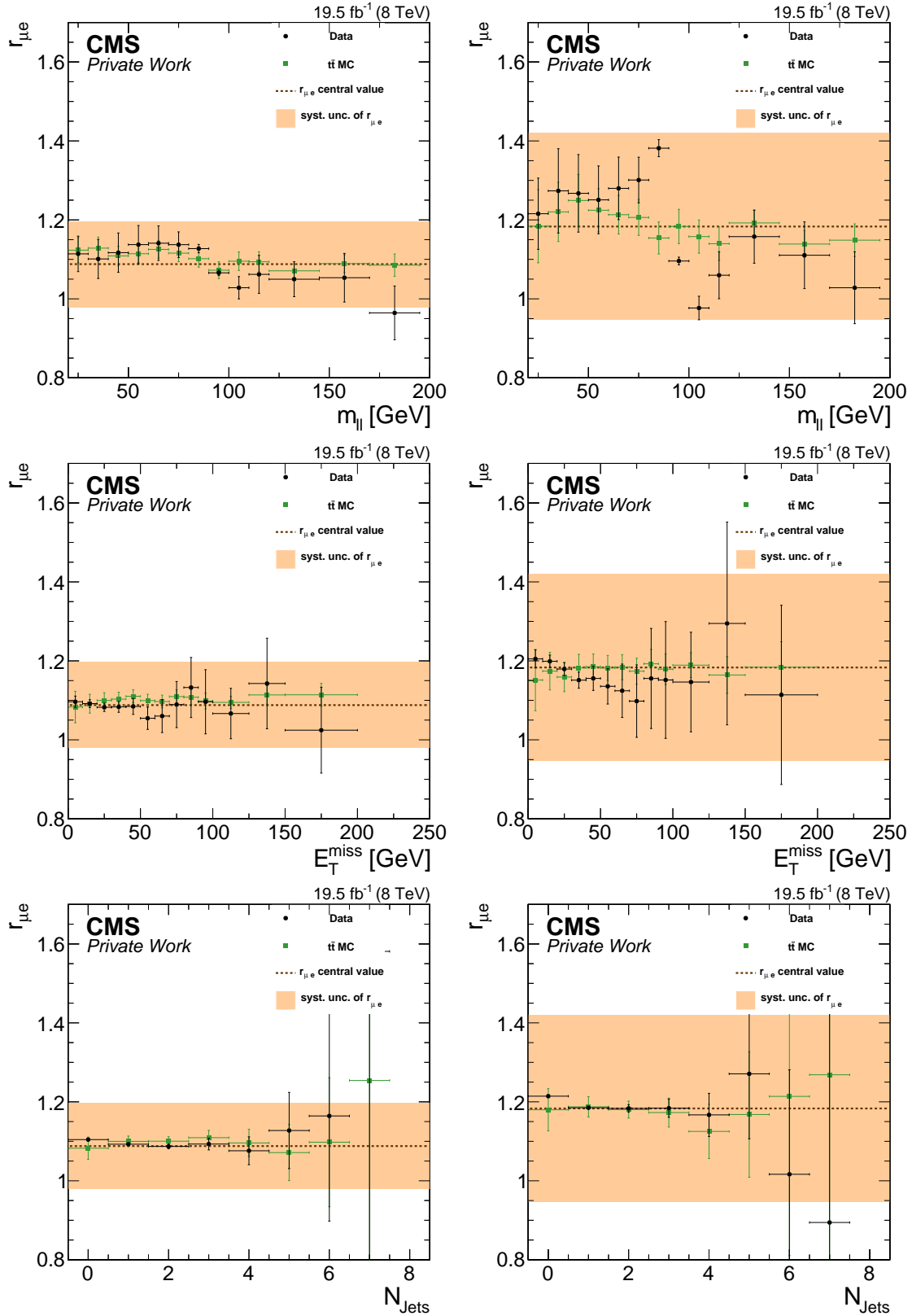


Figure 5.4: Dependencies of $r_{\mu e}$ on m_{ll} (top), E_T^{miss} (middle), and N_{Jets} (bottom) for the central (left) and forward (right) lepton selection. The results on data are shown in black while $t\bar{t}$ simulation is shown in green. The central value is shown as a brown dashed line while the systematic uncertainty is shown as an orange band.

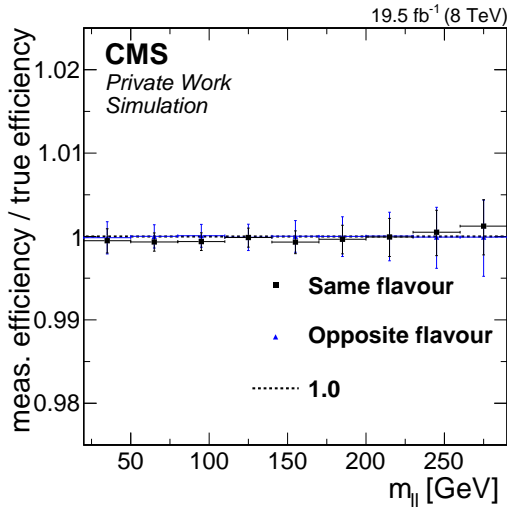


Figure 5.5: Ratio of true trigger efficiencies to those calculated using the H_T triggers separately for SF and OF events.

compatible with it inside the statistical uncertainties. No bias of the efficiency measurement due to the H_T triggers is observed and therefore no systematic uncertainty due to this choice is assigned to the measurement.

The turn-on of the triggers at low lepton p_T is of particular interest because asymmetries between the lepton flavours are more likely to occur in this difficult environment. The dependence of the trigger efficiency on the p_T of the trailing lepton can be studied using datasets triggered by single lepton triggers. Triggers with p_T thresholds of 24(27) GeV for muons (electrons) are available. These thresholds are relatively low for single lepton triggers, resulting in very strict selection criteria applied on HLT level. Dilepton events are selected, in which the leading lepton can be matched geometrically to the trigger object that fired the single lepton trigger. The trailing lepton is matched to trigger objects that have fired the trailing leg of the dilepton trigger. The efficiency is defined as the ratio of the number of events in which the dilepton trigger has fired, over the total number of dilepton events. The resulting efficiency curves are shown in Figure 5.6 for four different trailing lepton trigger legs and combining the central and forward selection. The efficiency for trailing electrons is virtually the same for the dielectron and OF triggers (black and light blue markers). The same is not true for trailing muons in the dimuon and OF triggers (red and dark blue markers), caused by the increased efficiency for trailing muons in the $\mu\mu$ channel, which is significantly higher than those in the trigger paths not using the tracker information, as expected. Trailing muons have a much sharper turn-on than trailing electrons and are fully efficient already at a p_T of 10 GeV. For electrons the plateau is reached only at about ≈ 30 GeV. The turn-on is steeper for trailing electrons in the dielectron trigger compared to those in the OF trigger, resulting in an increased deviation from flavour symmetry below 20 GeV. As the precision and stability of the background prediction was given priority over lepton acceptance in the design of the analysis, events with trailing leptons in this p_T range are rejected.

To assess the systematic uncertainties of the trigger efficiency measurement, the dependency of R_T , as used in the calculation of $R_{SF/OF}$, on different observables is tested. Here a dataset triggered by α_T triggers is used, as the H_T triggers do not provide enough events for these

Table 5.3: Trigger efficiencies measured using H_T baseline trigger. The results are shown for the central and forward regions separately.

	nominator	denominator	$\epsilon_{\text{trigger}} \pm \sigma_{\text{stat}}$	nominator	denominator	$\epsilon_{\text{trigger}} \pm \sigma_{\text{stat}}$
Data						
	Central			Forward		
ee	3592	3692	0.973 ± 0.003	954	980	0.973 ± 0.006
$\mu\mu$	1375	1420	0.968 ± 0.005	547	566	0.966 ± 0.009
$e\mu$	493	521	0.946 ± 0.012	102	114	0.895 ± 0.037
MC						
	Central			Forward		
ee	2912.8	2994.6	0.973 ± 0.001	943.0	969.9	0.972 ± 0.001
$\mu\mu$	3241.6	3287.9	0.986 ± 0.001	1141.6	1183.4	0.965 ± 0.001
$e\mu$	6279.1	6523.1	0.963 ± 0.001	2138.8	2249.0	0.951 ± 0.001

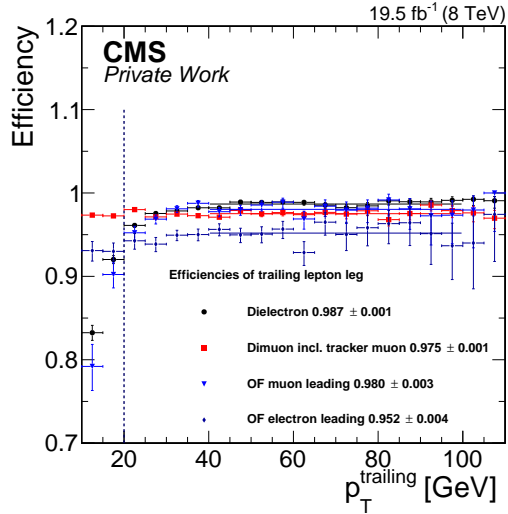


Figure 5.6: Efficiency of the trailing lepton legs of the dilepton trigger measured on a sample of data events selected with single lepton triggers as a function of the p_T of the trailing lepton. The asymptotic efficiency with its statistical uncertainties are determined by fitting a constant in the range $p_T > 40$ GeV

studies. A 5% systematic uncertainty is assigned to each trigger efficiency, resulting in an uncertainty of 6.4% on R_T , covering all observed deviations from the measured value of R_T within the statistical uncertainties, as shown in Figure 5.7. Studies of further variables can be found in Appendix D. The mean R_T values displayed in the figures are obtained using the α_T trigger as baseline and therefore differ from the nominal result obtained using the H_T triggers.

Results of the factorisation method

The results of the factorisation methods are summarised in Table 5.4. The factor R_T is calculated from the trigger efficiencies in Table 5.3 via Equation 5.4. The resulting correction factors $R_{SF/OF}$, $R_{ee/OF}$, and $R_{\mu\mu/OF}$ are calculated as described in Equations 5.1-5.3.

Table 5.4: Result of the determination of $R_{SF/OF}$, $R_{ee/OF}$, and $R_{\mu\mu/OF}$ using the factorisation method.

	Central		Forward	
	Data	MC	Data	MC
$r_{\mu e}$	1.088 ± 0.109	1.103 ± 0.110	1.183 ± 0.237	1.207 ± 0.241
R_T	1.026 ± 0.066	1.017 ± 0.065	1.084 ± 0.079	1.018 ± 0.069
$R_{SF/OF}$	1.029 ± 0.067	1.031 ± 0.067	1.099 ± 0.088	1.103 ± 0.091
$R_{ee/OF}$	0.471 ± 0.116	0.465 ± 0.117	0.458 ± 0.259	0.449 ± 0.264
$R_{\mu\mu/OF}$	0.558 ± 0.117	0.565 ± 0.119	0.641 ± 0.261	0.654 ± 0.266

As for the direct measurements in the control region, the observed deviations of $R_{SF/OF}$ from one are small and inside the uncertainties of the method. Because the uncertainty on $r_{\mu e}$ cancels out to a large degree in the calculation $R_{SF/OF}$, the total uncertainty is dominated by the uncertainty on R_T , while for $R_{ee/OF}$ and $R_{\mu\mu/OF}$ the uncertainty of $r_{\mu e}$ is the dominant one. This results in much larger uncertainties on the latter two factors. The dependency of $R_{SF/OF}$ on $r_{\mu e}$ and R_T as given by Equation 5.3 is illustrated in Figure 5.8. The measured values of $r_{\mu e}$ and $R_{SF/OF}$ are shown as straight lines, surrounded by bands indicating their uncertainties. The red line shows the value of $R_{SF/OF}$ corresponding to a given $r_{\mu e}$, under the assumption that the trigger efficiencies stay constant. The dashed black lines show the impact, that the uncertainties on the trigger efficiencies have on the resulting $R_{SF/OF}$. It can be seen that variations of $r_{\mu e}$ inside the systematic uncertainties have only little effect on $R_{SF/OF}$, while changes in the trigger efficiencies have a much larger impact.

5.1.3 Combined correction factors and resulting background estimates

An overview of the resulting corrections factors of the measurement in the control region and the factorisation method are shown in Table 5.5. In all cases the results of the two methods agree very well within their uncertainties.

Given the fact that they are performed on exclusive datasets and under the assumption that their uncertainties follow a Gaussian distribution, which is justified by the fact that they are

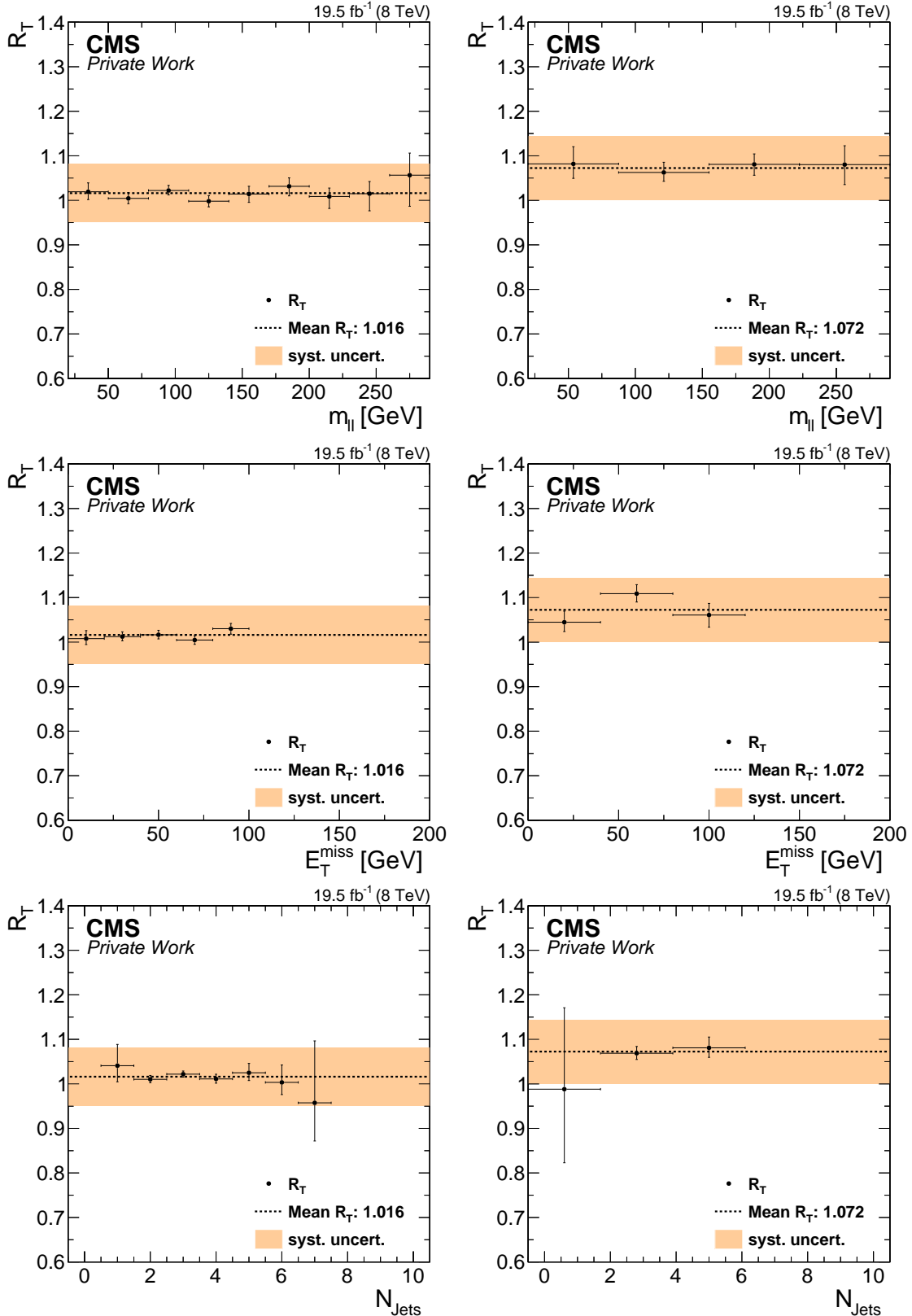


Figure 5.7: Dependencies of R_T on $m_{\ell\ell}$ (top), E_T^{miss} (middle), and N_{jets} (bottom) for the central (left) and forward (right) lepton selection. The results on data are shown in black. The central value is shown as a black dashed line while the systematic uncertainty is shown as an orange band.

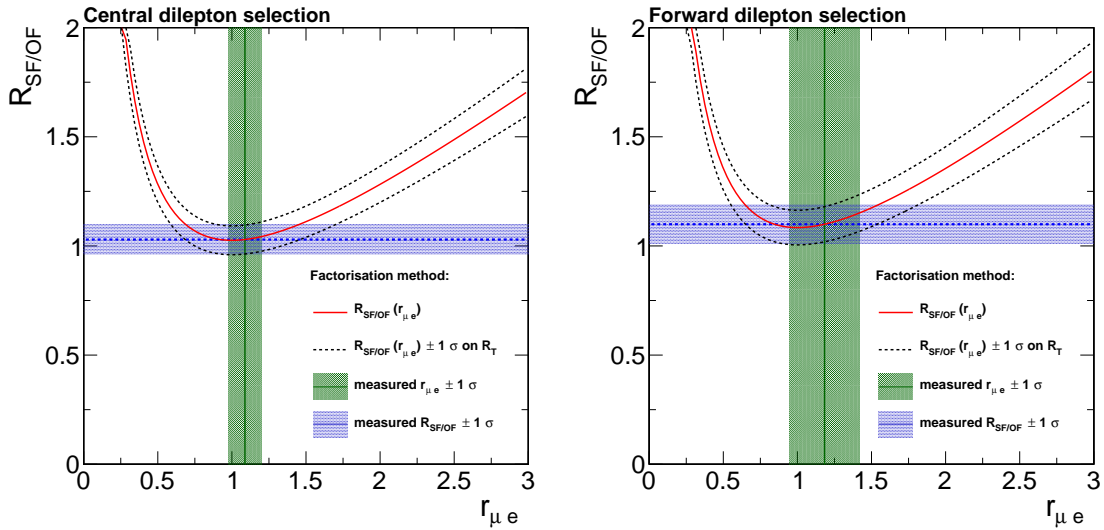


Figure 5.8: Dependency of R_{SF}/OF on $r_{\mu e}$ in the factorisation method. The measured central values of R_{SF}/OF and $r_{\mu e}$ and their uncertainty are shown as the blue and green lines and bands. The red line illustrates the value of R_{SF}/OF for a given $r_{\mu e}$ if R_T is kept constant. The impact of a variation of R_T within its uncertainties on R_{SF}/OF is shown by the dashed black lines.

either statistical in nature (and the samples sizes are sufficiently large), or assigned to cover statistical fluctuations in the dependency studies of $r_{\mu e}$ and R_T , they can be combined using a weighted average.

A precision of about 4% and 6% on the translation from opposite flavour to same flavour is reached in the central and forward dilepton selection, respectively. Separating the lepton flavours, the uncertainty in R_{ee}/OF and $R_{\mu\mu}/OF$ is about 6% for central and 9-10% for forward leptons. This increase is caused by the missing cancellation of the uncertainty on $r_{\mu e}$ and the increased statistical uncertainty in the direct measurement in the control region. However, only R_{SF}/OF is used in the background estimates for both counting experiment and the shape analysis and the separate $e^\pm e^\mp$ and $\mu^\pm \mu^\mp$ channels are only studied as cross-checks. Therefore, the increased uncertainty in the separate channels has no impact on the sensitivity of the result.

Given that the weighted average is calculated separately for each flavour combination, R_{ee}/OF and $R_{\mu\mu}/OF$ do not add up exactly to R_{SF}/OF , which in turn means that the sum of the background estimates for flavour-symmetric backgrounds in the $e^\pm e^\mp$ and $\mu^\pm \mu^\mp$ channels does not equal that in the SF channel. The OF yields in the $m_{\ell\ell}$ bins of the counting experiment together with the resulting background estimates in the different dilepton channels are shown in Table 5.6.

5.1.4 Validation of background estimates

To judge the performance of the estimation methods for flavour-symmetric backgrounds, they are applied to simulation. In Table 5.7 the resulting SF and OF yields after application of the signal selection are shown separately for the central and forward dilepton selection. The OF yields are corrected by the R_{SF}/OF values derived for simulation shown in Table 5.5. For completely flavour-symmetric processes, such as $t\bar{t}$, $Z/\gamma^* \rightarrow \tau\tau$, or single top-quark

Table 5.5: Correction factors $R_{SF/OF}$, $R_{ee/OF}$, and $R_{\mu\mu/OF}$ determined from direct measurement and the factorisation method together with the weighted averages.

	$R_{SF/OF}$			
	Central		Forward	
	Data	MC	Data	MC
from factorisation method	1.029±0.067	1.031±0.067	1.099±0.088	1.103±0.091
from direct measurement	1.007±0.043	1.034±0.015	1.015±0.106	1.092±0.026
weighted avarage	1.013±0.036	1.033±0.014	1.048±0.055	1.093±0.025
	$R_{ee/OF}$			
	Central		Forward	
	Data	MC	Data	MC
from factorisation method	0.471±0.116	0.465±0.117	0.458±0.259	0.449±0.264
from direct measurement	0.458±0.033	0.467±0.008	0.445±0.092	0.460±0.014
weighted avarage	0.459±0.027	0.467±0.008	0.445±0.044	0.460±0.014
	$R_{\mu\mu/OF}$			
	Central		Forward	
	Data	MC	Data	MC
from factorisation method	0.558±0.117	0.565±0.119	0.641±0.261	0.654±0.266
from direct measurement	0.549±0.035	0.567±0.010	0.570±0.095	0.632±0.018
weighted avarage	0.550±0.029	0.567±0.010	0.572±0.049	0.632±0.018

Table 5.6: Resulting estimates for flavour-symmetric backgrounds. Given is the observed event yield in $e^\pm\mu^\mp$ events and the resulting estimate after applying the correction, separately for the SF, $e^\pm e^\mp$, and $\mu^\pm\mu^\mp$ channels. Statistical and systematic uncertainties are given separately. Low-mass refers to $20 < m_{\ell\ell} < 70, on-Z to $81 < m_{\ell\ell} < 101 and high-mass to $m_{\ell\ell} > 120.$$$

	low-mass		on-Z		high-mass	
	Central	Forward	Central	Forward	Central	Forward
Observed OF	737	138	364	131	779	393
Estimate (SF)	746±27±26	144±12±7	368±19±13	137±11±7	789±28±27	411±20±21
Estimate ($e^\pm e^\mp$)	337±12±19	61±5±6	166±8±9	58±5±5	357±12±20	175±8±17
Estimate ($\mu^\pm\mu^\mp$)	405±14±21	78±6±6	200±10±10	74±6±6	428±15±22	224±11±19

production, the difference between the SF and OF yields is compatible with zero within the statistical uncertainties of the simulation and the systematic uncertainties of the method. Other systematic uncertainties affecting the simulation are the same for SF and OF lepton pairs and are therefore not considered here.

Table 5.7: Event yields in the signal region in simulation for both SF and OF lepton pairs. The OF yield is multiplied with $R_{SF/OF}$ and the uncertainty on the OF yields includes the systematic uncertainty on $R_{SF/OF}$. The event yields are compared separated into flavour-symmetric and Drell–Yan backgrounds. Processes contributing to both categories have been sorted into the Drell–Yan category.

	Central			Forward		
	SF	OF	SF-OF	SF	OF	SF-OF
$t\bar{t}$	2214 ± 9	2200 ± 32	14 ± 33	689 ± 5	684 ± 16	5 ± 17
$Z/\gamma^* \rightarrow \ell\ell (e^\pm e^\mp, \mu^\pm \mu^\mp)$	49 ± 11	0 ± 0	49 ± 11	24 ± 8	4 ± 4	20 ± 9
$Z/\gamma^* \rightarrow \ell\ell (\tau\tau)$	72 ± 13	59 ± 12	13 ± 18	14 ± 6	17 ± 6	-3 ± 9
Single t	144 ± 8	137 ± 8	6 ± 12	38 ± 4	43 ± 4	-6 ± 6
WW, ZZ, WZ	121 ± 2	77 ± 2	45 ± 3	51 ± 1	34 ± 2	17 ± 2
Other SM	89 ± 6	81 ± 6	9 ± 8	30 ± 4	22 ± 3	8 ± 5
Flav. sym. backgrounds	2559 ± 19	2531 ± 41	28 ± 45	795 ± 10	793 ± 22	1 ± 24
Drell–Yan backgrounds	130 ± 11	21 ± 1	109 ± 11	51 ± 8	11 ± 4	40 ± 9
Total simulation	2689 ± 22	2553 ± 40	136 ± 46	846 ± 13	804 ± 21	42 ± 25

As expected, deviations from flavour-symmetry are observed only for processes containing a Z boson, most notable $Z/\gamma^* \rightarrow \ell\ell$, but also WZ or ZZ production and more rare processes like $t\bar{t}Z$ production. It can therefore be concluded that the background prediction for flavour-symmetric processes performs well within the uncertainties of the methods presented above. The validity of this cross check is restricted to processes well modelled in simulation. As the modelling of leptons not produced in the hard physics process is in general less reliable, more detailed studies are performed on data to ensure that flavour-symmetry also holds for the small contribution of non-prompt leptons, to the final event selection.

Study of non-prompt leptons

As a preface to studies performed on data, the flavour-symmetry of non-prompt leptons is examined using the truth information of the simulation. A data driven estimate is derived from leptons with relaxed isolation criteria.

Non-prompt leptons in simulation The origin of the leptons in the events contribution to the signal selection is studied in simulation by matching the reconstructed lepton to the generated particles with the smallest spatial separation ΔR . The difference in generated and reconstructed p_T must not exceed twice the generated p_T . The parentage of the matched generated particle is used to determine if the lepton originates from a the decay of a Z or W

boson or a τ lepton, a decay of a heavy flavour quark inside a jet, or a jet that was misidentified as a lepton. The contribution of non-prompt leptons to the signal selection is studied in $t\bar{t}$ events, where the two b-jets are a source for leptons from heavy flavour decays.

All events where at least one of the leptons is not matched to a generated electron or muon and/or does not originate directly or via an intermediate τ lepton from a W boson are considered non-prompt. The resulting $m_{\ell\ell}$ distributions are shown in Figure 5.9 for the inclusive dilepton selection (see Section 4.3.2) on the left and the combined central and forward signal regions on the right. Good agreement between SF and OF pairs can be seen, with a slight tendency towards more OF. The event yields are summarised in Table 5.8. The contribution

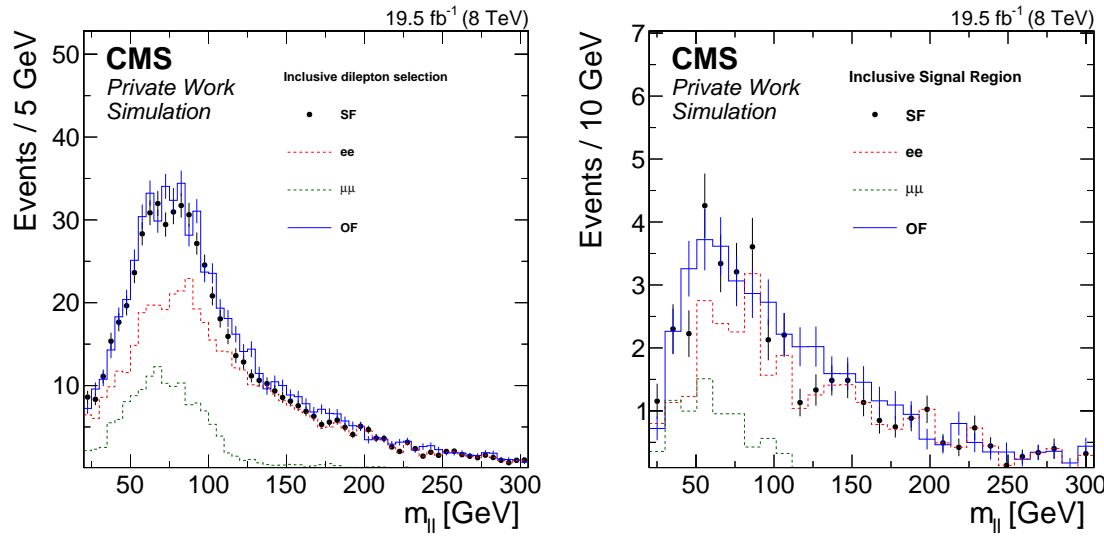


Figure 5.9: Distribution of $m_{\ell\ell}$ for lepton pairs with at least one non-prompt lepton in simulation for an inclusive dilepton selection (left) and the signal selection (right). The contributions of $e^\pm e^\mp$, $\mu^\pm \mu^\mp$, and $e^\pm \mu^\mp$ pairs are shown as red, green, and blue lines, respectively. The combined SF pairs are shown as the black points.

of non-prompt electrons exceeds that of non-prompt muons. Nevertheless, the event yields for SF and OF lepton pairs are very similar, with a slight preference to OF leptons. This indicates that this type of backgrounds is covered by the estimates for flavour-symmetric backgrounds, at least in simulation.

Table 5.8: Number of events with non-prompt leptons in an inclusive dilepton selection and the central and forward signal regions for $t\bar{t}$ simulation.

	$e^\pm e^\mp$	$\mu^\pm \mu^\mp$	SF	$e^\pm \mu^\mp$	$R_{SF/OF}$
Inclusive	456.0 ± 5.2	140.3 ± 3.3	596.2 ± 8.4	637.5 ± 6.3	0.94 ± 0.02
Signal central	20.2 ± 1.0	4.9 ± 0.6	25.0 ± 1.6	26.2 ± 1.2	0.95 ± 0.07
Signal forward	9.8 ± 0.7	2.8 ± 0.5	12.6 ± 1.2	14.2 ± 0.9	0.89 ± 0.10

Testing the flavour-symmetry of non-prompt leptons on data The contribution of non-prompt leptons to the signal selection can be estimated on data from control samples enriched

in non-prompt leptons [103, 104]. These samples are obtained by relaxing the isolation requirements on the leptons from $\frac{|\text{iso}|}{p_T} < 0.15$ (“tight”) to $\frac{|\text{iso}|}{p_T} < 1.0$ (“loose”). The probabilities of a prompt or non-prompt lepton that passes the loose selection to pass also the default tight selection are often referred to as “fake rate” f for non-prompt leptons and “prompt rate” p for prompt leptons. They are calculated as tight-to-loose ratios in two control regions that are enriched in either prompt or non-prompt leptons:

$$f = \frac{N_{\text{tight}}}{N_{\text{loose}}} (\text{non-prompt sample}), \quad p = \frac{N_{\text{tight}}}{N_{\text{loose}}} (\text{prompt sample}). \quad (5.5)$$

The fake rate f is calculated on an event sample collected with prescaled low- p_T single lepton triggers (see Section 3.3). At least one jet with $p_T > 50 \text{ GeV}$ is required. To reject prompt leptons from $W + \text{jets}$ events, E_T^{miss} and the transverse mass of the lepton- E_T^{miss} system are both required to be less than 20 GeV . The resulting fake rates as a function of lepton p_T and η are shown in Figure 5.10. For low p_T , the value for electrons is about 0.25 while for muons it is about 0.07. Dependencies on both p_T and η are observed. The fake rate is therefore measured and applied as a function of both variables. The increase for higher p_T is however understood as arising from an increasing contamination from prompt leptons. Therefore, for all leptons with $p_T > 40 \text{ GeV}$, the values measured for $35 \text{ GeV} < p_T < 40 \text{ GeV}$ are used.

Similarly, to calculate the prompt rate, a sample enriched in prompt lepton is selected by requiring exactly two reconstructed leptons, of which the leading one is required to be a tight lepton while the trailing one is a loose lepton. To further enrich the sample in prompt leptons from Z boson decays, $m_{\ell\ell}$ is required to be within 15 GeV of the Z boson mass and E_T^{miss} is required to be $< 20 \text{ GeV}$. The resulting prompt ratios p are shown in Figure 5.11. They are again applied as functions of p_T and η . For low p_T they are about 0.85 for muons and 0.9 for electrons and approach values close to one for $p_T > 60 \text{ GeV}$ for both flavours. The systematic uncertainty assigned to the tight-to-loose ratios in the sources cited above is 50%. As the definition of loose electrons differs from that used in the analyses referred above and modifications have been made to the definition of the control samples in which the ratios are measured, this number is not directly applicable here. However, the overall normalisation of the non-prompt background is not the focus of this study. Therefore no attempt is made to evaluate this uncertainty for this analysis and no systematic uncertainty is quoted.

Using the measured fake and prompt rates $f_{1,2}$ and $p_{1,2}$ for the two leptons, the contributions of the four possible combination of prompt and non-prompt leptons (prompt-prompt, prompt-non-prompt, non-prompt-prompt, and non-prompt-non-prompt) are calculated from the observed numbers of events with two tights (N_{tt}), one tight and one loose lepton (N_{tl} and N_{lt}) and two loose leptons (N_{ll}), where the first index indicates the trailing and the second the leading lepton, and using the following formulas

$$\begin{aligned} N_{pp} &= N_{tt} \cdot (f_1 - 1)(f_2 - 1)p_1 p_2 + N_{tl} \cdot (f_1 - 1)f_2 p_1 p_2 + N_{lt} \cdot (f_2 - 1)f_1 p_1 p_2 + N_{ll} \cdot f_1 f_2 p_1 p_2, \\ N_{pn} &= N_{tt} \cdot (f_1 - 1)(1 - p_2)p_1 f_2 - N_{tl} \cdot (f_1 - 1)f_2 p_1 p_2 + N_{lt} \cdot (1 - p_2)f_1 p_1 f_2 - N_{ll} \cdot f_1 f_2 p_1 p_2, \\ N_{np} &= N_{tt} \cdot (1 - p_1)(f_2 - 1)f_1 p_2 + N_{tl} \cdot (1 - p_1)f_2 f_1 p_2 - N_{lt} \cdot (f_2 - 1)f_1 p_1 p_2 - N_{ll} \cdot f_1 f_2 p_1 p_2, \\ N_{nn} &= N_{tt} \cdot (1 - p_1)(1 - p_2)f_1 f_2 - N_{tl} \cdot (1 - p_1)f_2 f_1 p_2 - N_{lt} \cdot (1 - p_2)f_1 p_1 f_2 + N_{ll} \cdot f_1 f_2 p_1 p_2, \end{aligned}$$

where each of the contributions has to be weighted by $(f_1 - p_1)(f_2 - p_2)$. As the fake and prompt rates depend on p_T and η of the leptons, in practice each event is assigned a weight

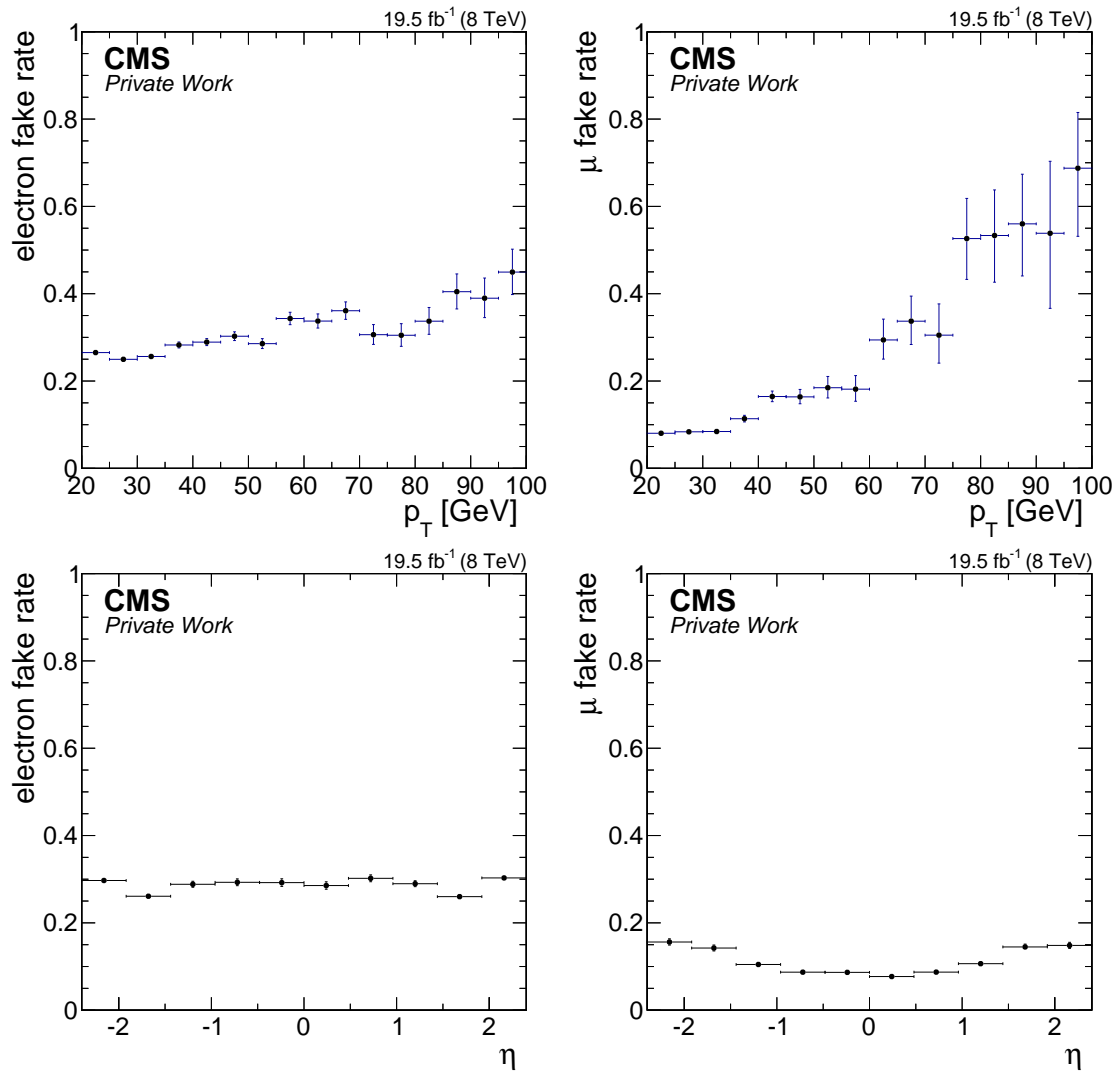


Figure 5.10: Measured fake rate for electrons (left) and muons (right) as a function of the p_T (top) and η (bottom) of the trailing lepton.

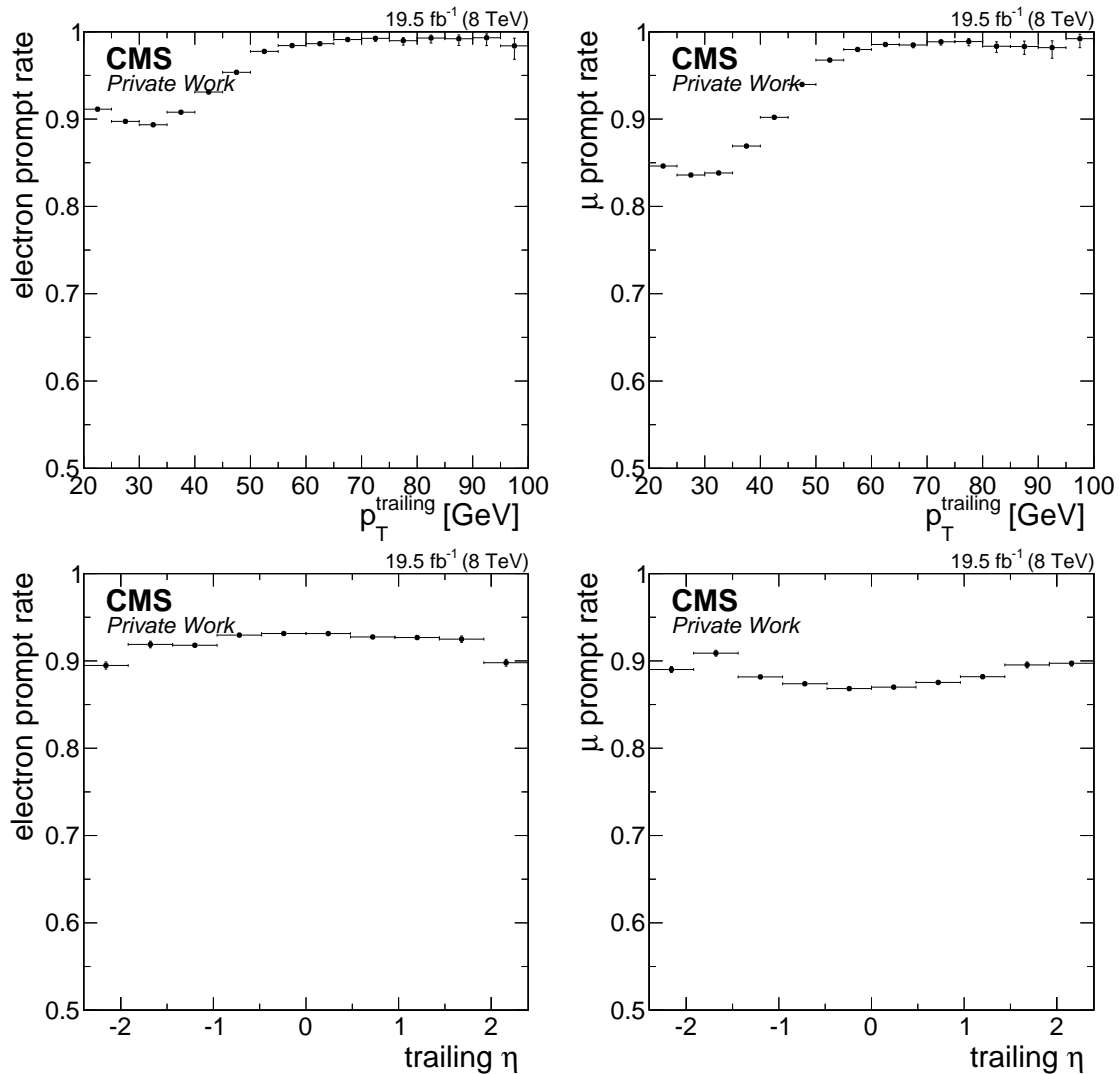


Figure 5.11: Measured prompt rate for electrons (left) and muons (right) as a function of the p_T (top) and η (bottom) of the trailing lepton.

based on whether the leptons are tight or loose and their kinematic properties according to the formulas above. The estimates for the number of events with two prompt (N_{pp}), one prompt and one non-prompt (N_{pn} and N_{np}), and two non-prompt (N_{nn}) are obtained as the sums of these weights. As before, the first index indicates the trailing and the second the leading lepton. The total contribution of non-prompt backgrounds is given by the sum of N_{pn} , N_{np} , and N_{nn} . The resulting estimates in the central and forward signal regions are shown in Table 5.9.

Table 5.9: Results of the estimation of backgrounds with non-prompt leptons in the signal region using the tight-to-loose ratios for prompt and non-prompt leptons. The total non-prompt estimate is given by the sum of the contributions for events with one or two non-prompt leptons N_{pp} , N_{np} , and N_{pn} .

	$e^\pm e^\mp$	$\mu^\pm \mu^\mp$	SF	$e^\pm \mu^\mp$
Signal central				
N_{tt}	1257	1450	2707	2326
$N_{lt} + N_{tl}$	247	740	987	812
N_{ll}	11	114	125	50
Non-prompt estimate	44.9 ± 14.8	34.6 ± 3.8	79.6 ± 18.6	86.7 ± 12.4
Signal forward				
N_{tt}	405	473	878	827
$N_{lt} + N_{tl}$	130	233	363	234
N_{ll}	6	38	44	32
Non-prompt estimate	27.3 ± 8.0	17.9 ± 3.5	45.1 ± 11.5	43.4 ± 8.4

The contribution of non-prompt leptons is small compared to the total number of tight lepton pairs and the estimates are well compatible between SF and OF events within the statistical uncertainties. This type of backgrounds is therefore accounted for by the background estimates for flavour-symmetric backgrounds.

5.2 Drell–Yan backgrounds

To estimate the contribution of Drell–Yan backgrounds (see Section 2.3) to the event sample in the signal region, both the Jet-Z balance (JZB) and E_T^{miss} templates methods [105] are used. The first studies the balance of Z boson candidates against the jets in the event. In the E_T^{miss} template method, the E_T^{miss} distribution of $\gamma + \text{jets}$ events are used to estimate that of Z + jets events. As the development and application of these methods have not been part of the work covered in this thesis, only a short description will be given.

5.2.1 JZB method

The JZB variable is defined as the balance of the p_T of the jets in the event with the p_T of the Z boson candidate. To avoid biases due to jet selection, \vec{E}_T^{miss} is used as a measure of the

hadronic recoil of the Z boson:

$$\text{JZB} = \left| \sum_{\text{jets}} \vec{p}_T \right| - \left| \vec{p}_T^Z \right| \approx \left| \vec{E}_T^{\text{miss}} - \vec{p}_T^Z \right| - \left| \vec{p}_T^Z \right|. \quad (5.6)$$

For SM processes such as Z + jets, where E_T^{miss} is caused by mismeasurements of the jets, the JZB distribution is symmetric around 0. For BSM processes, where the Z boson is produced correlated with invisible particles, the JZB distribution is expected to be asymmetric, favouring positive sign especially for large values of JZB and, by extension, high E_T^{miss} . Therefore, it is possible to predict the contribution of SM processes containing a Z boson at high E_T^{miss} from the events in that region with negative values of JZB, after subtraction of flavour-symmetric processes from OF events. The assumption that the JZB distribution is symmetric around 0 for SM processes with only instrumental E_T^{miss} is studied in MC and 20% systematic uncertainty are assigned [4].

5.2.2 E_T^{miss} templates method

The E_T^{miss} templates method utilises the similarity of Z+jets and γ +jets events, especially the fact that mismeasurement is only source of E_T^{miss} in both cases. Therefore, after corrections for residual kinematic differences, the contribution of Z+jets events at high E_T^{miss} can be estimated from γ +jets events passing the same selection. The dominant systematic uncertainties are assigned based on tests of the method on simulation and are in the order of 15–100% for E_T^{miss} values falling into the signal selection of this analysis. The large uncertainties for higher E_T^{miss} values are driven by the available number of simulated events to validate the method.

In contrast to the JZB method, the E_T^{miss} templates method does only account for Z + jets events. Other backgrounds containing Z bosons, such as WZ, ZZ or more rare SM processes like $t\bar{t}Z$ or triboson production are estimated from simulation and assigned 50% uncertainty [4].

5.2.3 Extrapolation to off-Z regions

Both methods described above result in background estimates for the on-Z region ($81 \text{ GeV} < m_{\ell\ell} < 101 \text{ GeV}$). Contributions to the low-mass and high-mass selections from off-shell Z bosons or the Drell–Yan continuum are estimated by applying an extrapolation factor $R_{\text{out/in}}$ to the on-Z prediction. This approach relies on the assumption that the $m_{\ell\ell}$ distribution of Drell–Yan events, and especially the ratio of the contribution on the Z boson peak to that at lower or higher masses, is the same independent of E_T^{miss} and N_{Jets} . $R_{\text{out/in}}$ is measured in the Drell–Yan control region, separately for the low-mass and high-mass region as well as $e^\pm e^\mp$, $\mu^\pm \mu^\mp$, and SF leptons. It is defined as the ratio of the event yield in the mass region in question (*out*) by that in the on-Z mass region (*in*), after subtraction of contribution from flavour-symmetric processes from the OF sample:

$$R_{\text{out/in}} = \frac{N_{\text{out}}^{\text{SF}} - N_{\text{out}}^{\text{OF}} R_{\text{SF/OF}}}{N_{\text{in}}^{\text{SF}} - N_{\text{in}}^{\text{OF}} R_{\text{SF/OF}}}, \quad (5.7)$$

where the SF can be substituted for $e^\pm e^\mp$ or $\mu^\pm \mu^\mp$ according to the desired lepton flavour. The $m_{\ell\ell}$ distribution in the Drell–Yan control region is shown in Figure 5.12. The resulting

values range from about 6–8% for the low-mass region to 2–3% for the high-mass region, as summarised in Table 5.10.

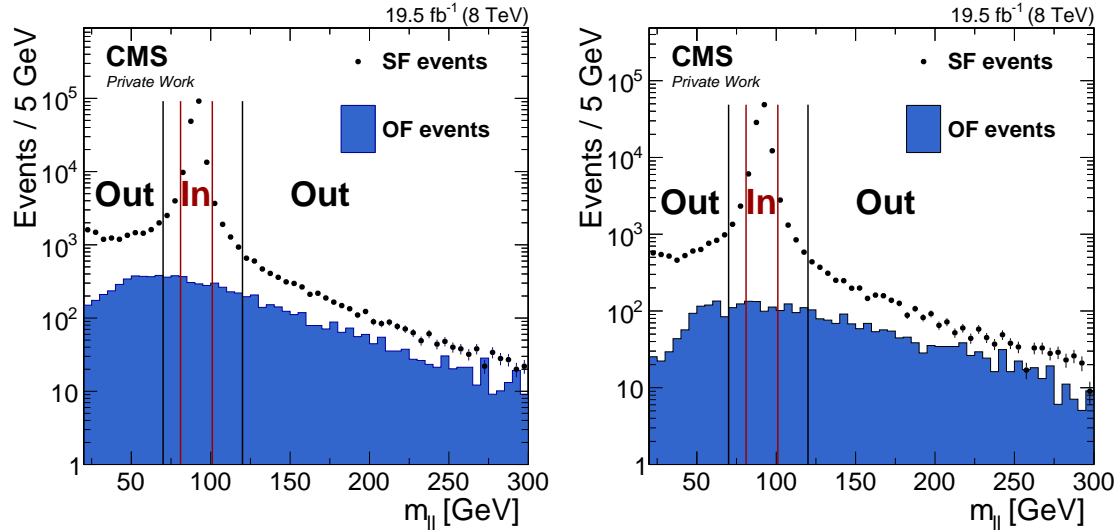


Figure 5.12: The $m_{\ell\ell}$ distribution in the Drell–Yan control region in the central (left) and forward (right) dilepton selection. SF data is shown as the black points while OF data is shown as the blue histogram. The black lines indicate the boundaries of the two *out* regions and the dark red lines those of the *in* region.

The validity of applying the $R_{\text{out/in}}$ as measured in the Drell–Yan control region in the signal region is checked by studying the behaviour of the quantity as a function of E_T^{miss} and N_{Jets} . The results for the low-mass selection and the case of SF leptons is shown in Figure 5.13 for both the central and forward lepton selections. In neither selection a dependency on E_T^{miss} is observed. However, above 70 GeV there is not enough statistics left after subtraction of the flavour-symmetric backgrounds, so it is not possible to judge the behaviour all the way up to the signal region. The value of $R_{\text{out/in}}$ clearly increases with the number of jets. As the requirement on N_{Jets} is the same between the Drell–Yan control region and the signal region, the events do not differ much in terms of jet multiplicity and this dependency does not restrict the applicability of the $R_{\text{out/in}}$ factors in the signal region. In total, a systematic uncertainty of 25% is assigned to cover the observed effects. Consistent results are observed also for the high-mass region and for the split into $e^\pm e^\mp$ and $\mu^\pm \mu^\mp$, as can be seen in Appendix E.

5.2.4 Resulting background prediction

The predictions for the on-Z region from the JZB and E_T^{miss} templates methods agree within their uncertainties. As for the $R_{\text{SF/OF}}$ factor, a weighted average is used to combine the two estimates. The results of both methods as well as the combination are shown in Table 5.11. Shown are also the $R_{\text{out/in}}$ values and the resulting estimates for the low- and high-mass regions. In this analysis a different reconstruction version of the data is used, compared to the one used in [4]. The on-Z predictions are scaled by 1.03 ± 0.03 to take into account a slight increase in jet multiplicity observed in the present dataset.

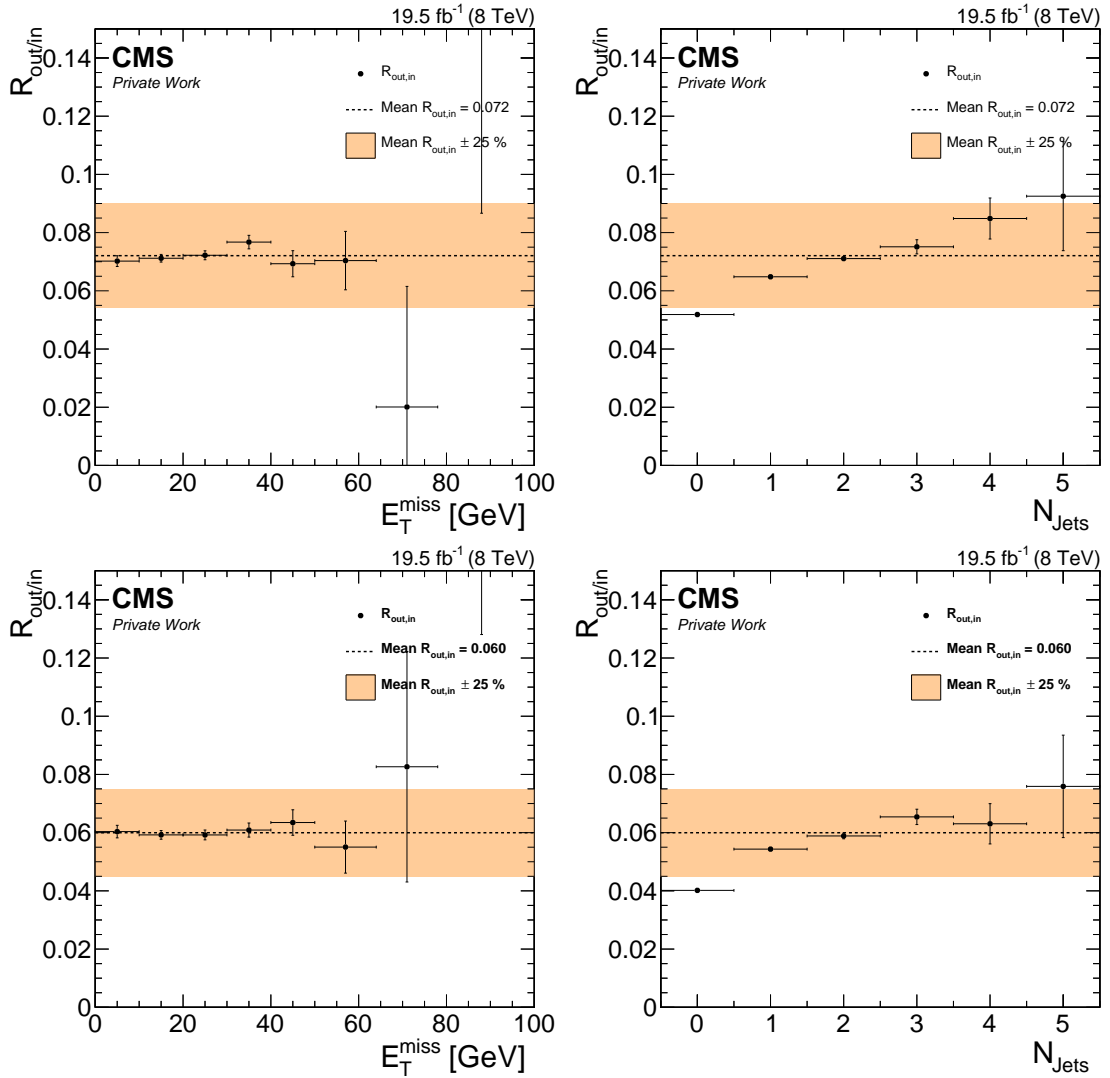


Figure 5.13: Dependencies of $R_{\text{out,in}}$ for the low-mass region on E_T^{miss} (left) and N_{jets} (right) for the central (top) and forward (bottom) lepton selection. The results on data are shown in black. The central value is shown as a black dashed line while the systematic uncertainty is shown as an orange band.

Table 5.10: Results of the calculation of $R_{\text{out/in}}$ separately for the low-mass and high-mass regions in the central and forward dilepton selection.

	N_{out}	N_{in}	$R_{\text{out/in}}(\text{SF}) \pm \sigma_{\text{stat}} \pm \sigma_{\text{syst}}$
Central			
low-mass			
Data	11608.6 ± 131.7	160645.8 ± 403.9	$0.072 \pm 0.001 \pm 0.018$
MC	10725.8 ± 128.7	167291.6 ± 412.0	$0.064 \pm 0.001 \pm 0.016$
high-mass			
Data	3571.3 ± 91.2	160645.8 ± 403.9	$0.022 \pm 0.001 \pm 0.006$
MC	3243.0 ± 88.9	167291.6 ± 412.0	$0.019 \pm 0.001 \pm 0.005$
Forward			
low-mass			
Data	5657.6 ± 84.2	94407.6 ± 308.7	$0.060 \pm 0.001 \pm 0.015$
MC	5695.8 ± 85.5	103407.4 ± 323.0	$0.055 \pm 0.001 \pm 0.014$
high-mass			
Data	2672.5 ± 75.8	94407.6 ± 308.7	$0.028 \pm 0.001 \pm 0.007$
MC	2459.1 ± 72.3	103407.4 ± 323.0	$0.024 \pm 0.001 \pm 0.006$

Table 5.11: Estimate of the Z background yields in the Z peak region and extrapolation to the signal mass region for the full dataset.

	central		
Drell–Yan estimate	$e^\pm e^\mp$	$\mu^\pm \mu^\mp$	SF
on-Z (JZB)	$57.9 \pm 13.8 \pm 10.1$	$46.1 \pm 13.8 \pm 8.0$	$104 \pm 21 \pm 18$
on-Z (E_T^{miss} templates)	$63.2 \pm 4.3 \pm 15.3$	$69.5 \pm 4.0 \pm 16.9$	$133 \pm 7 \pm 32$
on-Z (Combined)	60.7 ± 11.6	56.8 ± 11.7	116 ± 21
$R_{\text{out/in}}$ low-mass	$0.069 \pm 0.001 \pm 0.017$	$0.075 \pm 0.001 \pm 0.019$	$0.072 \pm 0.001 \pm 0.018$
low-mass	4.3 ± 1.3	4.4 ± 1.4	8.6 ± 2.7
$R_{\text{out/in}}$ high-mass	$0.025 \pm 0.001 \pm 0.006$	$0.020 \pm 0.001 \pm 0.005$	$0.022 \pm 0.001 \pm 0.006$
high-mass	1.5 ± 0.5	1.2 ± 0.4	2.7 ± 0.8
	forward		
Drell–Yan estimate	$e^\pm e^\mp$	$\mu^\pm \mu^\mp$	SF
on-Z (JZB)	$15.6 \pm 8.3 \pm 2.9$	$13.8 \pm 8.3 \pm 2.8$	$29 \pm 11 \pm 6$
on-Z (MET templates)	$24.4 \pm 1.8 \pm 6.0$	$32.3 \pm 2.2 \pm 7.9$	$56.9 \pm 3.6 \pm 14.0$
on-Z (Combined)	21 ± 5	25 ± 6	42 ± 9
$R_{\text{out/in}}$ low-mass	$0.055 \pm 0.001 \pm 0.014$	$0.064 \pm 0.001 \pm 0.016$	$0.060 \pm 0.001 \pm 0.015$
low-mass	1.2 ± 0.4	1.6 ± 0.6	2.6 ± 0.8
$R_{\text{out/in}}$ high-mass	$0.031 \pm 0.001 \pm 0.008$	$0.026 \pm 0.001 \pm 0.007$	$0.028 \pm 0.001 \pm 0.007$
high-mass	0.7 ± 0.2	0.7 ± 0.2	1.2 ± 0.4

6 Counting experiment

In the counting experiment approach, the observed yield of SF events is compared to the combined background estimates from flavour-symmetric and Drell–Yan backgrounds in the six region defined in $m_{\ell\ell}$ and lepton $|\eta|$. Here, the results are presented and further investigations into their properties are discussed. Also the implications of these results on the simplified models discussed in section 2.2.2 is examined.

6.1 Results and further studies

The distribution of the dilepton invariant mass in the central and forward signal regions (see Table 4.5) are shown in Figure 6.1. The resulting event yields are compared to the expectation from SM backgrounds in Table 6.1. A maximum likelihood fit is performed in each region to find the best estimator for the difference of expected and observed yield. The significances of deviations of this difference from zero are evaluated using the profile likelihood ratio of the signal and signal plus background hypotheses [106]. In general, the observed data is in agreement with the background estimation within about one standard deviation, except for the low-mass region for central leptons. Here, the observed yield exceeds the expectation by 109 ± 48 events. The size of this excess corresponds to a local significance of 2.2σ .

Table 6.1: Results of the counting experiment in the six signal regions. The statistical and systematic uncertainties are added in quadrature, except for the flavor-symmetric backgrounds.

	low-mass		on-Z		high-mass	
	Central	Forward	Central	Forward	Central	Forward
Observed	865	154	494	176	849	381
Flavor-symmetric	$746 \pm 27 \pm 26$	$144 \pm 12 \pm 7$	$368 \pm 19 \pm 13$	$137 \pm 11 \pm 7$	$789 \pm 28 \pm 28$	$411 \pm 20 \pm 21$
Drell–Yan	8.6 ± 2.7	2.6 ± 0.8	119 ± 21	43 ± 9	2.7 ± 0.8	1.2 ± 0.4
Total estimated	755 ± 38	147 ± 14	488 ± 31	180 ± 16	792 ± 39	413 ± 30
Observed - estimated	109 ± 48	7 ± 19	6 ± 38	-5 ± 21	57 ± 50	-32 ± 37
Significance	2.2σ	0.4σ	0.1σ	$<0.1\sigma$	1.1σ	$<0.1\sigma$

In the Tables 6.2 and 6.3, the results are shown separately for $e^\pm e^\mp$ and $\mu^\pm \mu^\mp$ events. As expected from the fact that $r_{\mu e}$ is larger than one, the yields in the $\mu^\pm \mu^\mp$ channel are slightly larger than in the $e^\pm e^\mp$ channel. For the flavour-symmetric backgrounds, and therefore also for the total background estimates and the difference of observation and estimation, the yields in the $e^\pm e^\mp$ and $\mu^\pm \mu^\mp$ channels do not exactly add up to those in the combined SF channel presented in Table 6.1. This is caused by the weighted average of the two methods to determine the correction factors used to translate from OF into the different SF channels, which is calculated separately for $R_{SF/OF}$, $R_{ee/OF}$, and $R_{\mu\mu/OF}$, as discussed in Section 5.1.3. Comparing the two channels, consistent results are observed between them, except for the slight excess in the high-mass central region, which is driven dominantly from $e^\pm e^\mp$ events. Especially for the larger excess in the low-mass central region, the observation agrees with

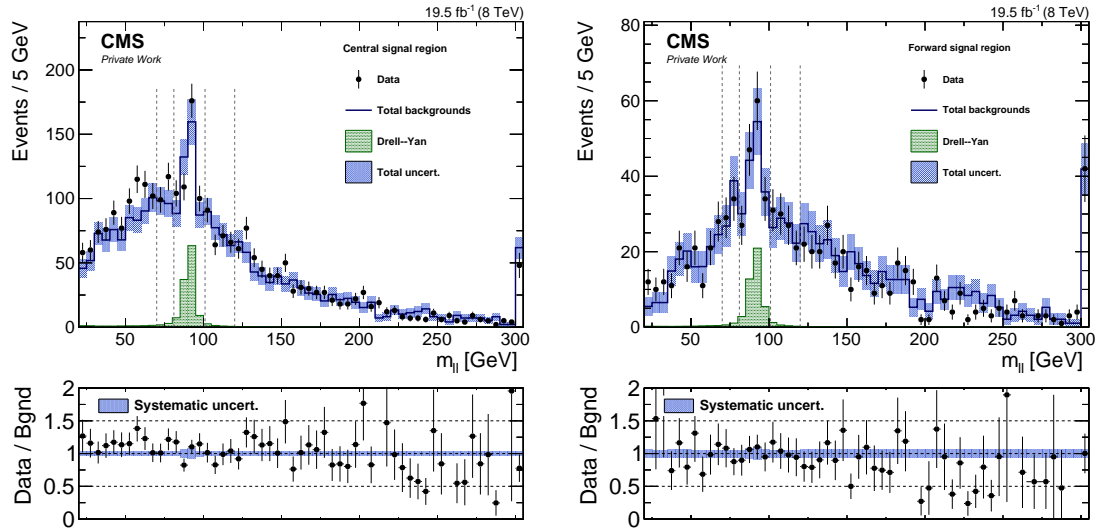


Figure 6.1: Distribution of m_{ll} in the signal region for the central (left) and forward (right) dilepton selection. The data is shown as black dots, while the total background prediction from data is shown as a blue histogram. The blue error bars indicate the combined statistical and systematic background uncertainty in each bin. The contribution from Drell–Yan backgrounds is shown as a green histogram. The dashed lines indicates the boundaries of the three mass bins. Beneath the plot the ratio of data to the background prediction is shown. The error bars include the statistical uncertainties of data and background, while the blue band indicates the systematic uncertainties on the background.

the expected behaviour of the different flavours. The signal yields of 47 ± 25 and 67 ± 29 in the $e^\pm e^\mp$ and $\mu^\pm \mu^\mp$ channels correspond to a value of $r_{\mu e}$ for this hypothetical signal of 1.19 ± 0.41 , in good agreement with the value of 1.09 ± 0.11 measured in the Drell–Yan control region (see Section 5.1.2).

Table 6.2: Results of the counting experiment for $e^\pm e^\mp$ events only. The statistical and systematic uncertainties are added in quadrature, except for the flavor-symmetric backgrounds.

	low-mass		on-Z		high-mass	
	Central	Forward	Central	Forward	Central	Forward
Observed	389	53	232	86	401	195
Flavor-symmetric	$337 \pm 12 \pm 19$	$61 \pm 5 \pm 6$	$166 \pm 8 \pm 9$	$58 \pm 5 \pm 5$	$357 \pm 12 \pm 21$	$175 \pm 8 \pm 17$
Drell–Yan	4.3 ± 1.3	1.2 ± 0.4	62 ± 11	21 ± 5	1.5 ± 0.5	0.7 ± 0.2
Total estimated	342 ± 23	62 ± 8	229 ± 17	79 ± 9	358 ± 24	175 ± 19
Observed - estimated	47 ± 25	-10 ± 9	3 ± 21	6 ± 12	42 ± 26	19 ± 18
Significance	1.9σ	$<0.1 \sigma$	0.1σ	0.5σ	1.7σ	1.1σ

Investigating the low-mass central region

While a significance of 2.2σ is no clear indication for the presence of new physics, more detailed studies into the properties of this excess are conducted.

The development of the excess during the data taking period in 2012 is shown on the left side of Figure 6.2, while the right side shows the low-mass forward region for comparison.

Table 6.3: Results of the counting experiment for $\mu^\pm\mu^\mp$ events only. The statistical and systematic uncertainties are added in quadrature, except for the flavor-symmetric backgrounds.

	low-mass		on-Z		high-mass	
	Central	Forward	Central	Forward	Central	Forward
Observed	476	101	262	90	448	186
Flavor-symmetric	$405 \pm 14 \pm 21$	$79 \pm 6 \pm 6$	$200 \pm 10 \pm 10$	$74 \pm 6 \pm 6$	$428 \pm 15 \pm 23$	$224 \pm 11 \pm 19$
Drell-Yan	4.4 ± 1.4	1.6 ± 0.6	58 ± 10	25 ± 6	1.2 ± 0.4	0.7 ± 0.2
Total estimated	409 ± 26	80 ± 9	258 ± 18	100 ± 11	429 ± 27	225 ± 22
Observed - estimated	67 ± 29	20 ± 13	3 ± 23	-11 ± 13	19 ± 29	-40 ± 21
Significance	2.3σ	1.6σ	0.2σ	$<0.1\sigma$	0.6σ	$<0.1\sigma$

The data sample is split into 10 bins, each corresponding to 2 fb^{-1} within 1%, except for the last which corresponds to only about 1.5 fb^{-1} . For each of these bins the observed SF yield and the prediction for flavour-symmetric backgrounds from OF is shown, together with the difference of the two. The very small contribution from Drell-Yan backgrounds of typically less than 1 event per bin is neglected in this representation of the result. For the first four bins, corresponding to the first 8 fb^{-1} of data collected in 2012, the SF yield is significantly higher than the prediction from OF. This effect diminishes in the fifth bin, where the SF yield decreases and the prediction from OF increases. In the following five bins, representing the second half of the data sample, good agreement is observed between the observed SF yield and the prediction from OF. This change in behaviour between the two halves is caused in roughly equal manner by a decrease in the observed SF yield and an increase in the observed OF yield per bin. In contrast to this observations, the SF yield and the background prediction are compatible within uncertainties for all bins in the low-mass forward region. The difference between the two therefore fluctuates around zero.

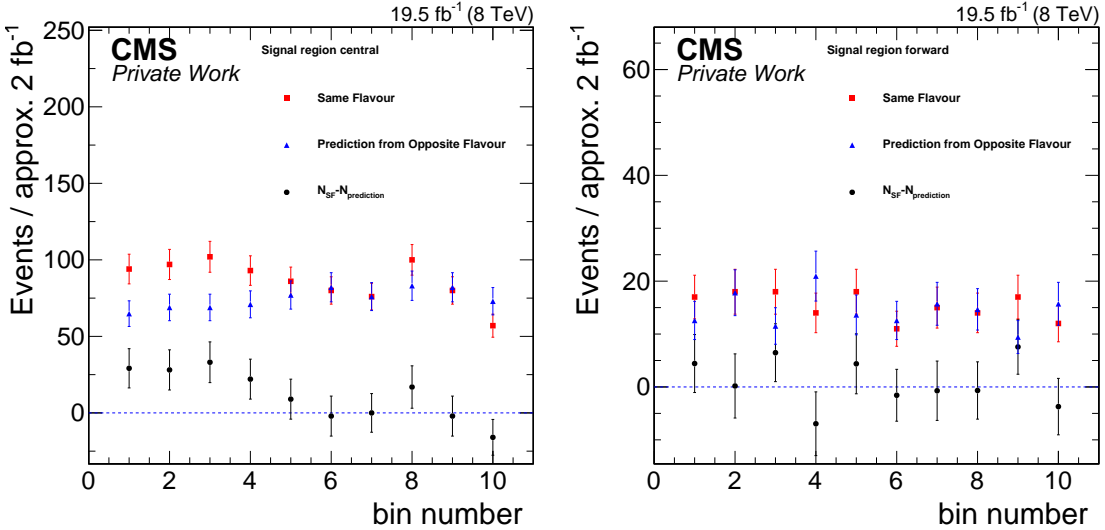


Figure 6.2: Observed SF yields and background prediction from OF as well as the difference of these two in the low-mass central (left) and forward (right) signal region in 10 bins of roughly equal integrated luminosity. Non-flavour-symmetric backgrounds are not included in this representation of the result.

To get a clearer picture of the properties of the excess and also to check for some of the more obvious possible systematic effects that might cause it, the counting experiment in the

low-mass central region is repeated several times, varying the selection requirements. The results are shown in Table 6.4. As no Drell-Yan prediction for the on-Z region is available for the different configurations, the observed yield is extrapolated into the low-mass region after subtraction of flavour-symmetric background using the prediction from OF. For all these cross-checks presented here one has to keep in mind that for the background prediction from OF the $R_{SF/OF}$ factor derived for the default selection is used.

As the signal region is dominated by events containing b-tagged jets, it seems natural to test the excess for its b-tag content. Splitting the data sample into events with at least one and those without a b-tag, it is evident that, while constituting about 23% of the total yield, less than 10% of the excess is located in events without a b-tagged jet.

In addition to the default selection of $p_T > 20 \text{ GeV}$, four other configurations for the lepton p_T requirement are tested. Three of them feature asymmetric cuts on the p_T of the leading and trailing lepton. The selection of $p_T > 20(10)$ and $p_T > 30(10) \text{ GeV}$ extend the acceptance of the analysis to lower trailing lepton p_T . For both of these selections, an increased signal yield is observed. On the other hand, raising the trailing p_T threshold to 30 GeV disproportionately reduces the observed excess, retaining only about 13% of the excess yield compared to 23% of the overall event yield.

Although it has already been established in Section 5.1.4 that non-prompt leptons only account for a small part of the selected data sample and are also fully flavour-symmetric, the counting experiment is repeated with significantly tighter isolation requirements. The relative isolation is required to be smaller than 5%, reducing the size of the selected sample by about one third. The number of observed signal events is reduced by almost exactly the same amount. This further increases the confidence that the observed effect is due to prompt lepton production.

To test for a possible pileup dependence of the observed effect, the sample is split into three subsets of similar size depending on the number of reconstructed vertices (N_{Vertex}). The events are categorised as either low-pileup ($N_{\text{Vertex}} < 13$), mid-pileup ($13 \leq N_{\text{Vertex}} < 17$) or high-pileup ($N_{\text{Vertex}} \geq 17$). The excess is observed consistently in all three subsets, excluding a possible pileup dependence of excess.

Three additional E_T^{miss} reconstructions are tested. TC E_T^{miss} and type-I corrected PF E_T^{miss} have been described in Section 4.1.4. In addition to these general algorithms, an analysis-specific definition of missing H_T is used, which is calculated using only selected jets and leptons. It is defined as the absolute value of the negative vector sum of the transverse momenta of these objects:

$$H_T^{\text{miss}} = \left| - \left(\sum_{\text{jets}} \vec{p}_T + \sum_{\text{leptons}} \vec{p}_T \right) \right|.$$

The signal region requirements of 100 GeV and 150 GeV, depending on N_{jets} , are applied for each of these E_T^{miss} values. Both the use of type-I corrected PF E_T^{miss} and missing H_T lead to higher event yields in the signal region. Judging by the size of the Drell-Yan background, TC E_T^{miss} and H_T^{miss} have significantly worse E_T^{miss} resolution compared to both types of PF E_T^{miss} . The excess is present in all three cases and is therefore not likely to be caused by a faulty E_T^{miss} reconstruction.

Separating the data sample into events with low H_T ($100 \text{ GeV} < H_T < 300 \text{ GeV}$) and high

H_T ($H_T > 300 \text{ GeV}$) creates two subsets of roughly the same size. The excess is present in both subsets with similar strength.

The distributions of several observables in the low-mass signal region is shown in Figure 6.3. Each time the observed data is compared to the prediction from OF events. The contribution from Drell–Yan backgrounds is neglected. The excess is located predominantly in events with one or two b-tagged jets, but no excess is observed for higher b-tag multiplicities. Furthermore, it is located almost inclusively in events with three jets. It is present in events with a p_T of the leading lepton of up to 60 GeV. For events with a trailing lepton p_T above 25 GeV, only a small deviation from the expectation is observed. The excess seems to favour low values of E_T^{miss} and is roughly uniformly distributed in H_T .

In all performed studies, no evidence for systematic effects causing the observed excess is found. The two major distinguishing features of the events causing the deviation are the presence of at least one b-tagged jet and trailing leptons with very low p_T . In general, no features distinguishing the events in the excess from the dominant $t\bar{t}$ background are observed in any of the performed studies.

6.2 Interpretation in simplified models

The absence of a clear indication for the existence of SUSY in the results of the counting experiment presented in Section 6.1 constrains the validity of supersymmetric models. To quantify the impact these results have on the allowed parameter space, they are interpreted in specific signal scenarios. Here, the two simplified models discussed in Section 2.2.2 are used.

Selection efficiencies

The impact of branching fractions, detector acceptance, and selection efficiencies on the different signal points is shown in Figure 6.4 for the example of the central signal region for the fixed-edge (left) and slepton-edge (right) models. Because of the much larger branching fraction into lepton pairs in the case of the slepton-edge model, caused by the presence of the slepton in decay chain, the overall acceptance \times efficiency is an order of magnitude larger in this case. As the event kinematics vary depending on the sparticle masses, the efficiency strongly depends on the position of the signal point in the $m_{\tilde{b}} \text{--} m_{\tilde{\chi}_2^0}$ plane. In general, the efficiency is low along the diagonal, where little energy is available for the decay products. Another notable feature is a decrease in efficiency around $\tilde{\chi}_2^0$ masses of about 225 GeV in the case of the slepton-edge model. This is caused by the gaps in the signal acceptance between the three invariant mass regions of the counting experiment. No such effect is visible for the fixed-edge case because the signal is concentrated in the low-mass region in this model.

Systematic uncertainties

A variety of systematic uncertainties in the signal modelling have to taken into account. The integrated luminosity is measured with a precision of 2.6% [107]. Variations of the parton distribution functions (PDF) according to the PDF4LHC recommendations [108, 109, 78,

Table 6.4: Results of the counting experiment in the low-mass central signal region for different variations of the event selection. The observed event yield in SF events is compared with the combined estimate from flavour-symmetric and Drell–Yan backgrounds. The estimate for the Drell–Yan backgrounds is obtained by extrapolating the event yield in the on-Z signal region after subtraction of flavour-symmetric backgrounds to the low-mass region using the $R_{\text{out/in}}$ factor.

	SF	Flav-symm.	Drell–Yan	Obs. - Est.	(Obs. - Est.) / σ
default selection					
default	865	746±38	8.6±2.7	109±48	2.2
b tagging					
no b -tagged jets	202	188±15	7.1±2.5	6±21	0.3
≥ 1 b -tagged jets	663	558±30	1.9±0.7	102±40	2.6
lepton p_T requirement					
$p_T > 20(10)$ GeV	1474	1290±58	11.4±4.1	172±69	2.5
$p_T > 30(10)$ GeV	1262	1114±51	11.3±4.1	135±63	2.2
$p_T > 30(20)$ GeV	761	673±35	9.0±3.3	78±45	1.7
$p_T > 30$ GeV	296	275±19	6.5±2.3	13±26	0.5
tight lepton isolation					
$\frac{l_{\text{iso}}}{p_T} < 0.05$	572	491±28	7.1±2.6	73±37	2.0
pileup					
$N_{\text{Vertex}} < 13$	332	289±19	3.3±1.2	38±27	1.4
$13 \leq N_{\text{Vertex}} < 17$	242	212±16	0.9±0.3	28±22	1.2
$N_{\text{Vertex}} \geq 17$	291	244±17	4.8±1.7	41±24	1.7
$E_{\text{T}}^{\text{miss}}$ reconstructions					
type-I corrected PF $E_{\text{T}}^{\text{miss}}$	1034	923±44	9.4±3.4	101±55	1.8
TC $E_{\text{T}}^{\text{miss}}$	850	702±36	26.3±9.4	121±47	2.5
$H_{\text{T}}^{\text{miss}}$	1171	942±45	50.8±18.1	177±59	3.0
H_{T}					
$100 \text{ GeV} < H_{\text{T}} < 300 \text{ GeV}$	455	401±24	1.4±0.5	52±32	1.6
$H_{\text{T}} > 300 \text{ GeV}$	410	344±22	7.5±2.7	57±30	1.9

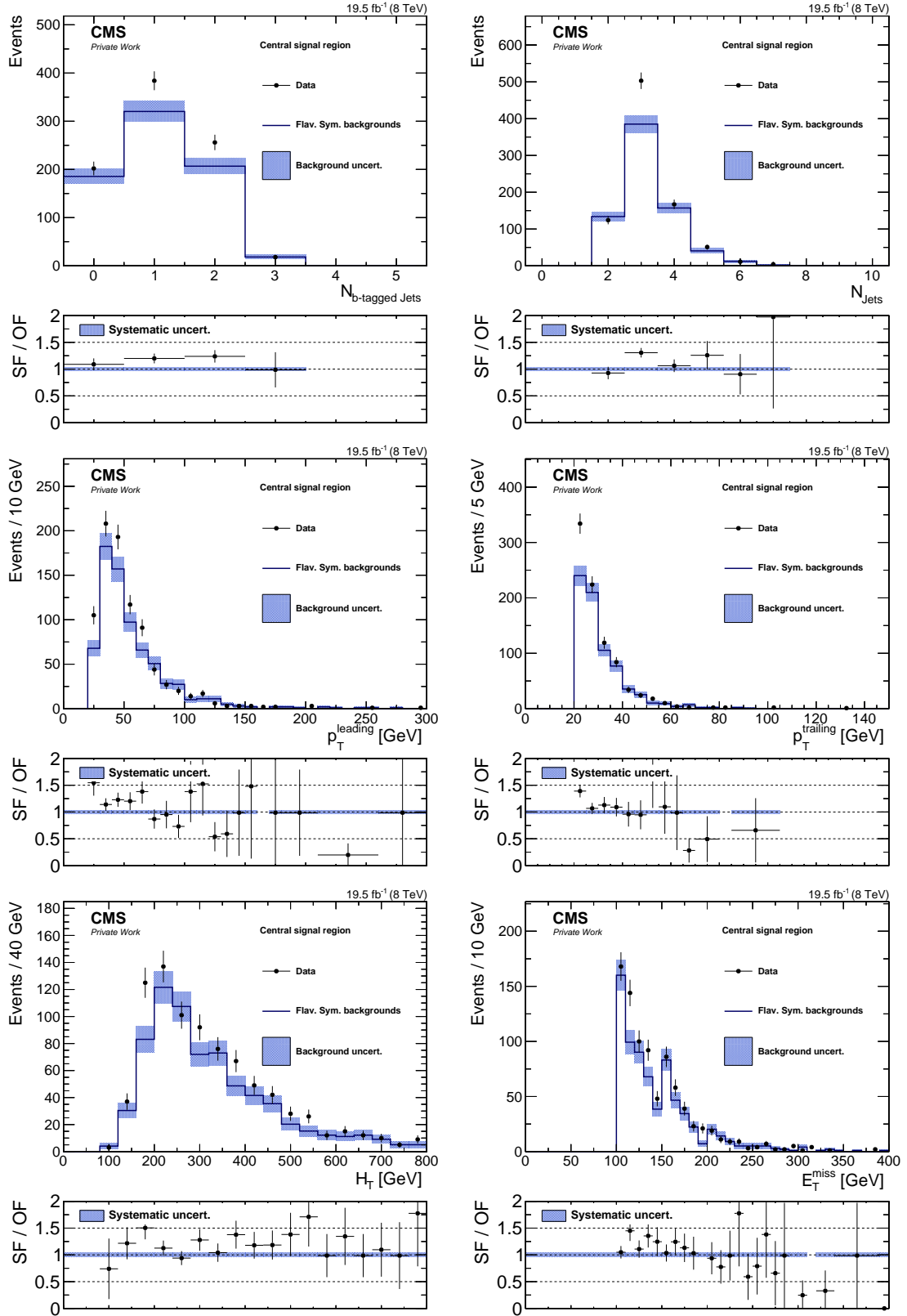


Figure 6.3: Distribution of the number of b-tagged jets (top left), jets (top right), p_{T} of the leading (middle left) and trailing (middle right) lepton, H_{T} (bottom left), and $E_{\text{T}}^{\text{miss}}$ (bottom right) in the low-mass central signal region. The data is shown as black dots, while the total background prediction from data is shown as a blue histogram. The blue error bars indicate the combined statistical and systematic background uncertainty in each bin. The contribution from Drell-Yan backgrounds is neglected.

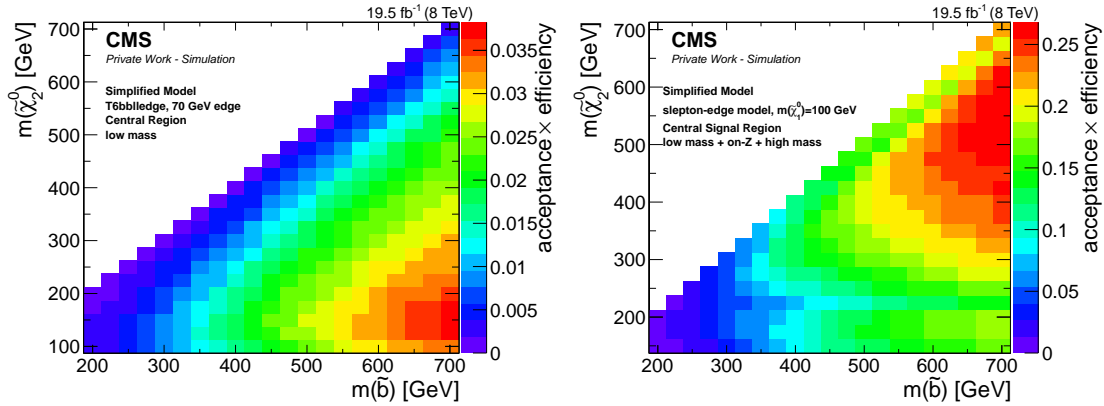


Figure 6.4: Signal acceptance \times efficiency in the $m_{\tilde{b}}\text{-}m_{\tilde{\chi}_2^0}$ plane for the fixed-edge (left) and slepton-edge (right) model for the central signal region.

Table 6.5: Summary of systematic uncertainties on the signal efficiency.

Uncertainty source	Impact on signal yield [%]
Luminosity	2.6
PDFs on acceptance	0–6
Lepton identification/isolation	2
Fast simulation lepton identification/isolation	2
Dilepton trigger	5
Lepton energy scale	0–5
E_T^{miss}	0–8
Jet energy scale/resolution	0–8
ISR modeling	0–14
Additional interactions	1

[79, 80] result in an uncertainty of 0–6% in the signal acceptance. Uncertainties related to lepton efficiencies are of the size of 1% per lepton. Furthermore, the corrections of the lepton efficiency differences between fast and full detector simulation amount to another 1% per lepton. The dilepton trigger efficiencies are measured with a precision of 5%, as described in Section 5.1.2. Uncertainties on the muon momentum scale have negligible impact on the signal acceptance, whereas the uncertainty in the electron energy scale is 0.6% for central and 1.5% for forward leptons. Jet energy scale uncertainties [62] result in an uncertainty in the signal yield of 0–8%. The uncertainties in the modeling of the objects in the events are propagated to the E_T^{miss} measurements, resulting in an uncertainty in the signal acceptance of 0–8%. Here the contributions from the jet energy scale uncertainties are dominant. The events are corrected for difference between observed data and the modelling of initial-state-radiation (ISR) in Madgraph [110]. Uncertainties in these corrections are propagated to the event selection and result in an uncertainty of 0–14% in the signal yield. The uncertainty associated with pileup reweighting is evaluated by shifting the inelastic cross section by $\pm 5\%$, resulting in an uncertainty on the signal acceptance of about 1%. The uncertainties are summarised in Table 6.5.

The combined systematic uncertainties are shown in Figure 6.5. For the most part of the $m_{\tilde{b}}\text{-}m_{\tilde{\chi}_2^0}$ plane it ranges from 5–7%. However, close to the diagonal this increases, caused

by a larger impact of JES and ISR uncertainties. This is due to the overall lower jet p_T in this region, increasing the probability for threshold effects around the jet p_T requirement of 40 GeV. The largest uncertainties are observed for both low masses of the \tilde{b} and $\tilde{\chi}_2^0$, exceeding 20% for the fixed-edge model and reaching 15% for the slepton-edge model.

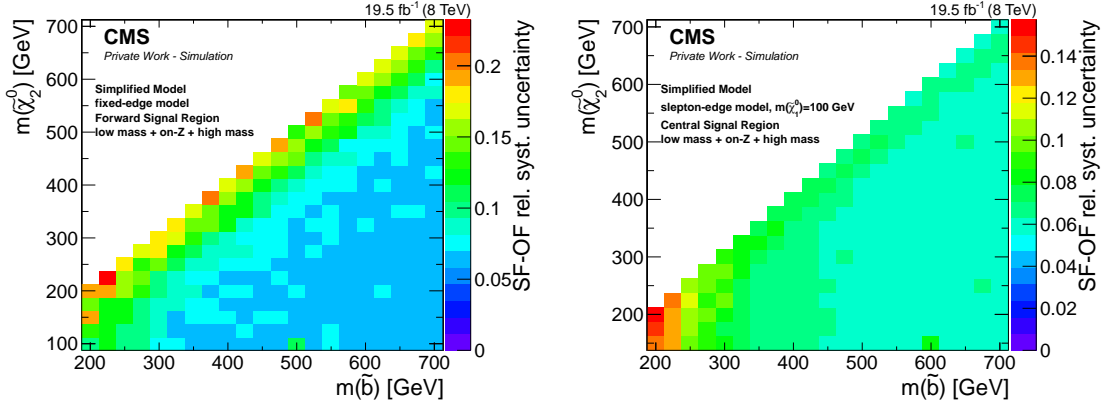


Figure 6.5: Systematic uncertainty on the signal yield in the central signal region in the $m_{\tilde{b}}-m_{\tilde{\chi}_2^0}$ plane for the fixed-edge (left) and slepton-edge (right) model.

6.2.1 Statistical interpretation

The results of the counting experiment are translated into exclusion limits by testing the compatibility of the signal plus background ($s+b$) and background only (b) hypothesis, treating each signal point in the parameter scans as a separate signal hypothesis. For this purpose, a likelihood function is defined [106]

$$\mathcal{L}(\text{data}|\mu, \theta) = \text{Poisson}(\text{data}|\mu \cdot s(\theta) + b(\theta)) \cdot p(\tilde{\theta}|\theta), \quad (6.1)$$

where μ is a signal strength parameter, $\mu = 0$ corresponding to the background only hypothesis and $\mu > 0$ to the $s+b$ hypothesis, and $p(\tilde{\theta}|\theta)$ parametrises the nuisance parameters θ , with $\tilde{\theta}$ being the nominal value of these parameters. Based on these likelihoods, a test statistic is defined utilizing a profile likelihood ratio:

$$\tilde{q}_\mu = -2\ln \frac{\mathcal{L}(\text{data}|\mu, \hat{\theta}_\mu)}{\mathcal{L}(\text{data}|\hat{\mu}, \hat{\theta})},$$

where the $\hat{\theta}_\mu$ represent the maximum likelihood estimators for the nuisance parameters for a given μ , whereas $\hat{\mu}$ and $\hat{\theta}$ indicate the global maximum of the likelihood. For the parametrisation of the nuisance parameters $p(\tilde{\theta}|\theta)$ in Equation 6.1, log-normal distributions are chosen. The distribution of the test statistics is then sampled dicing pseudo-experiments for some $\mu > 0$ and $\mu = 0$, representing the $s+b$ and b hypotheses that are tested. The p-values p_{s+b} and p_b are defined as the probability to obtain a value of the test statistics as large or larger than the one observed in data for the given hypothesis. To obtain an upper limit on the signal cross section the value of μ is chosen where $\text{CL}_s = \frac{p_{s+b}}{p_b}$ equals 0.05, corresponding to a 95% confidence level (CL). In the calculation, all six bins of the counting experiment are combined

by multiplying the likelihoods of the different channels. In this procedure, all uncertainties on both background and signal are assumed to be uncorrelated among each other but fully correlated among the different bins.

The resulting exclusion limits are shown in Figure 6.6. The left plot shows the exclusion limit in the $m_{\tilde{b}}\text{-}m_{\tilde{\chi}_2^0}$ plane for the fixed-edge model. As this model is specifically tuned to provide signals consistent with the excess observed in the low-mass central signal region, the observed limit deviates from the expected one by about 75 GeV. Given the assumption of this model, \tilde{b} masses up to about 375 GeV are excluded, depending on the mass of the $\tilde{\chi}_2^0$. The right plot shows the limit for the slepton-edge model. Because of the much larger branching fraction into leptons in this model, higher masses can be excluded. The expected limit reaches \tilde{b} masses of about 600 GeV roughly independent of $m_{\tilde{\chi}_2^0}$, except for the region around $m_{\tilde{\chi}_2^0} = 225$ GeV, where it drops below 550 GeV because of the gaps in acceptance discussed above. For lower $m_{\tilde{\chi}_2^0}$ the observed limit is significantly weaker than the expected one as here the limit is dominated by the low-mass signal region in which the excess was observed. For higher $m_{\tilde{\chi}_2^0}$, the observed limit agrees with the expected one within one standard deviation. The observed lower limit on $m_{\tilde{b}}$ ranges from 470 GeV to 590 GeV, depending on $m_{\tilde{\chi}_2^0}$.

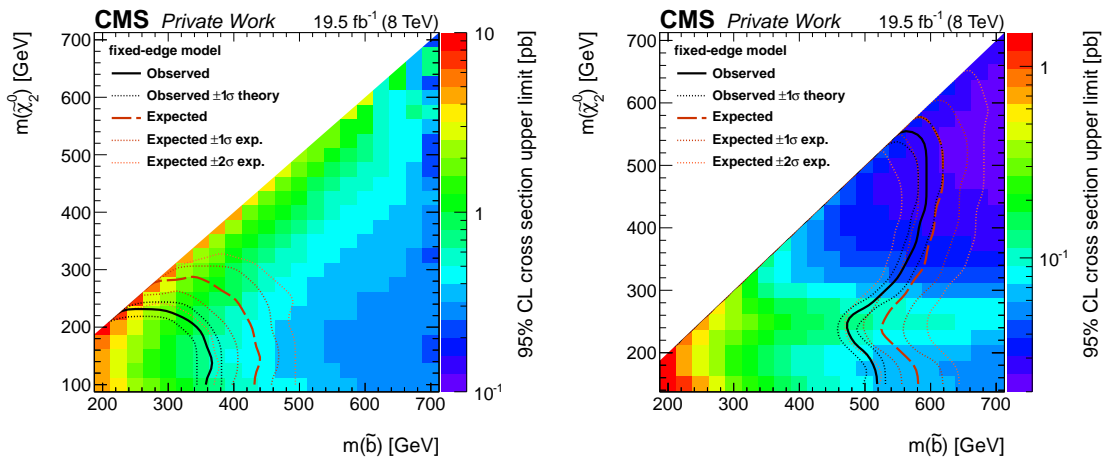


Figure 6.6: Exclusion limits in the $m_{\tilde{b}}\text{-}m_{\tilde{\chi}_2^0}$ plane for the fixed-edge (left) and slepton-edge (right) model. For each signal point the upper cross section limit is shown colour coded. The intersection of the theoretical with the excluded cross section is shown as a solid black line, with every signal point to the left and below the curve being excluded. The $1 - \sigma$ uncertainty interval on the observed limit is shown as dotted black lines. The expected limit together with the $1 - \sigma$ and $2 - \sigma$ interval are shown as brownish solid and dashed lines.

7 Search for a kinematic edge

A fit to the $m_{\ell\ell}$ distribution is performed in search of the characteristic edge signature described in Section 2.2.2. Different functions are used to model the contributions of the potential signal, flavour-symmetric backgrounds, and Drell–Yan backgrounds. To fully exploit the available information, an unbinned maximum-likelihood fit is performed simultaneously to the $e^\pm e^\mp$, $\mu^\pm \mu^\mp$, and $e^\pm \mu^\mp$ event samples for both the central and forward dilepton selection in the signal region using the RooFit toolkit [111].

7.1 Background and signal models

The different parametrisations of the two types of background and the signal are discussed in the following. In some cases, different functional forms or even non-analytical descriptions are used to validate the chosen models.

7.1.1 Model for Drell–Yan backgrounds

The background model for Drell–Yan events contains of two components: one model for the Z boson peak and one for the contribution of the Drell–Yan continuum. The latter one can be described by a simple falling exponential function \mathcal{P}_{exp} . The peak model consists of a Breit-Wigner function \mathcal{P}_{BW} with mean and widths fixed to the PDG values for the Z boson, convolved with a double-sided crystal ball function (DSCB) [112]. The first component models the physical peak while the latter accounts for the detector resolution and radiative corrections to the Z boson lineshape. The double-sided crystal ball itself consists of a Gaussian core and exponential falloffs to both sides of the peak, parametrised as

$$\mathcal{P}_{DSCB}(m_{\ell\ell}) = \begin{cases} A_1(B_1 - \frac{m_{\ell\ell} - \mu_{CB}}{\sigma_{CB}})^{-n_1} & \text{if } \frac{m_{\ell\ell} - \mu_{CB}}{\sigma_{CB}} < -\alpha_1 \\ \exp\left(-\frac{(m_{\ell\ell} - \mu_{CB})^2}{2\sigma_{CB}^2}\right) & \text{if } -\alpha_1 < \frac{m_{\ell\ell} - \mu_{CB}}{\sigma_{CB}} < \alpha_2 \\ A_2(B_2 + \frac{m_{\ell\ell} - \mu_{CB}}{\sigma_{CB}})^{-n_2} & \text{if } \frac{m_{\ell\ell} - \mu_{CB}}{\sigma_{CB}} > \alpha_2 \end{cases}$$

where σ_{CB} and μ_{CB} are the parameters of the central Gaussian and the n_i and α_i govern the exponential falloffs. The A_i and B_i are substitutions for

$$A_i = \left(\frac{n_i}{|\alpha_i|}\right)^{n_i} \cdot \exp\left(-\frac{|\alpha_i|^2}{2}\right) \quad \text{and} \quad B_i = \frac{n_i}{|\alpha_i|} - |\alpha_i|.$$

Convolving \mathcal{P}_{DSCB} and \mathcal{P}_{DSCB} , and taking into account also the exponential function describing the Drell–Yan continuum, the full description is therefore

$$\mathcal{P}_{DY}(m_{\ell\ell}) = (1 - f_{\text{peak}})\mathcal{P}_{exp}(m_{\ell\ell}) + f_{\text{peak}} \int \mathcal{P}_{DSCB}(m_{\ell\ell})\mathcal{P}_{BW}(m_{\ell\ell} - m')dm',$$

Table 7.1: List of all parameters of the model for Drell–Yan backgrounds for the fit in the Drell–Yan control region. Given are intial values, allowed ranges and the status of the parameters. A set of these parameters exists for both the central and forward dilepton selection.

	parameter	status	initial value	minimum	maximum
\mathbf{p}_Z^{ee}	$m_Z[\text{GeV}]$	fixed	91.1876	-	-
	$\sigma_Z[\text{GeV}]$	fixed	2.4952	-	-
	$\mu_{CB}^{ee}[\text{GeV}]$	floating	3.0	-10	10
	$\sigma_{CB}^{ee}[\text{GeV}]$	floating	1.6	0	20
	α_1^{ee}	floating	1.16	0	10
	α_2^{ee}	floating	2.5	0	10
	n_1^{ee}	floating	2.9	0	20
	n_2^{ee}	floating	1.04	0	20
	f_{peak}^{ee}	floating	0.9	0	1
	$\mu_{exp}^{ee}[\text{GeV}^{-1}]$	floating	-0.02	-0.1	0
$\mathbf{p}_Z^{\mu\mu}$	$m_Z[\text{GeV}]$	fixed	91.1876	-	-
	$\sigma_Z[\text{GeV}]$	fixed	2.4952	-	-
	$\mu_{CB}^{\mu\mu}[\text{GeV}]$	floating	3.0	-10	10
	$\sigma_{CB}^{\mu\mu}[\text{GeV}]$	floating	1.6	0	20
	$\alpha_1^{\mu\mu}$	floating	1.16	0	10
	$\alpha_2^{\mu\mu}$	floating	2.5	0	10
	$n_1^{\mu\mu}$	floating	2.9	0	20
	$n_2^{\mu\mu}$	floating	1.04	0	20
	$f_{\text{peak}}^{\mu\mu}$	floating	0.9	0	1
	$\mu_{exp}^{\mu\mu}[\text{GeV}^{-1}]$	floating	-0.02	-0.1	0

Table 7.2: Fitted $m_{\ell\ell}$ resolution in the central and forward dilepton selections for $e^{\pm}e^{\mp}$ and $\mu^{\pm}\mu^{\mp}$ pairs.

	$e^{\pm}e^{\mp}$	$\mu^{\pm}\mu^{\mp}$
Central	1.71 ± 0.03 GeV	1.44 ± 0.01 GeV
Forward	2.70 ± 0.04 GeV	2.01 ± 0.03 GeV

where f_{peak} is the fraction that the peak component contributes to the full PDF. A full list of the parameters of the model is given in Table 7.1.

This model is fitted to the data in the Drell–Yan control region separately for $e^{\pm}e^{\mp}$ and $\mu^{\pm}\mu^{\mp}$ events after flavour-symmetric backgrounds are subtracted using OF events. Afterwards, all parameters of the model are fixed and only the normalisation is left floating in the fit in the signal region. The resulting fits are shown in Figure 7.1 and are a good description of the distribution in all cases.

From the Gaussian core component of the double-sided crystal ball the $m_{\ell\ell}$ resolution σ_{CB} in the different channels is obtained, which is used as an input in the modelling of a potential signal. The resulting resolution values are shown in Table 7.2. The fitted values range from about 1.4 GeV to 2.7 GeV depending on lepton flavour and rapidity. In general it is smaller for $\mu^{\pm}\mu^{\mp}$ pairs and for lepton pairs in the central part of the detector.

7.1.2 Model for flavour-symmetric backgrounds

The flavour-symmetric model accounts for most of the events in the signal region. To ensure the validity of the chosen parametrisation, a variety of alternative models are studied. Here the nominal parametrisation used in the final result is discussed followed by a description of alternatives that are used as cross-checks.

Nominal parametrisation

Flavour-symmetric models are described with a model consisting of three parts. The rising flank of the distribution is modelled by a power law, the peak region with a third order polynomial and the falling flank with an exponential fall-off.

$$\mathcal{P}_{FS}(m_{\ell\ell}) = \begin{cases} \mathcal{P}_{FSE,1}(m_{\ell\ell}) = c_1 \cdot m_{\ell\ell}^{\alpha} & \text{if } 20 \text{ GeV} < m_{\ell\ell} < m_{\ell\ell}^{(1)} \\ \mathcal{P}_{FS,2}(m_{\ell\ell}) = \sum_{i=0}^3 c_{2,i} \cdot m_{\ell\ell}^i & \text{if } m_{\ell\ell}^{(1)} < m_{\ell\ell} < m_{\ell\ell}^{(2)} \\ \mathcal{P}_{FS,3}(m_{\ell\ell}) = c_3 \cdot e^{-\beta m_{\ell\ell}} & \text{if } m_{\ell\ell}^{(2)} < m_{\ell\ell} < 300 \text{ GeV} \end{cases}$$

where $m_{\ell\ell}^{(1)}$ and $m_{\ell\ell}^{(2)}$ are the transition points between the different parts of the model. The model is required to be normalised and also to be continuously differentiable in $m_{\ell\ell}^{(1)}$ and $m_{\ell\ell}^{(2)}$, reducing the number of free parameters to five. A full list of the parameters and their properties is given in Table 7.3.

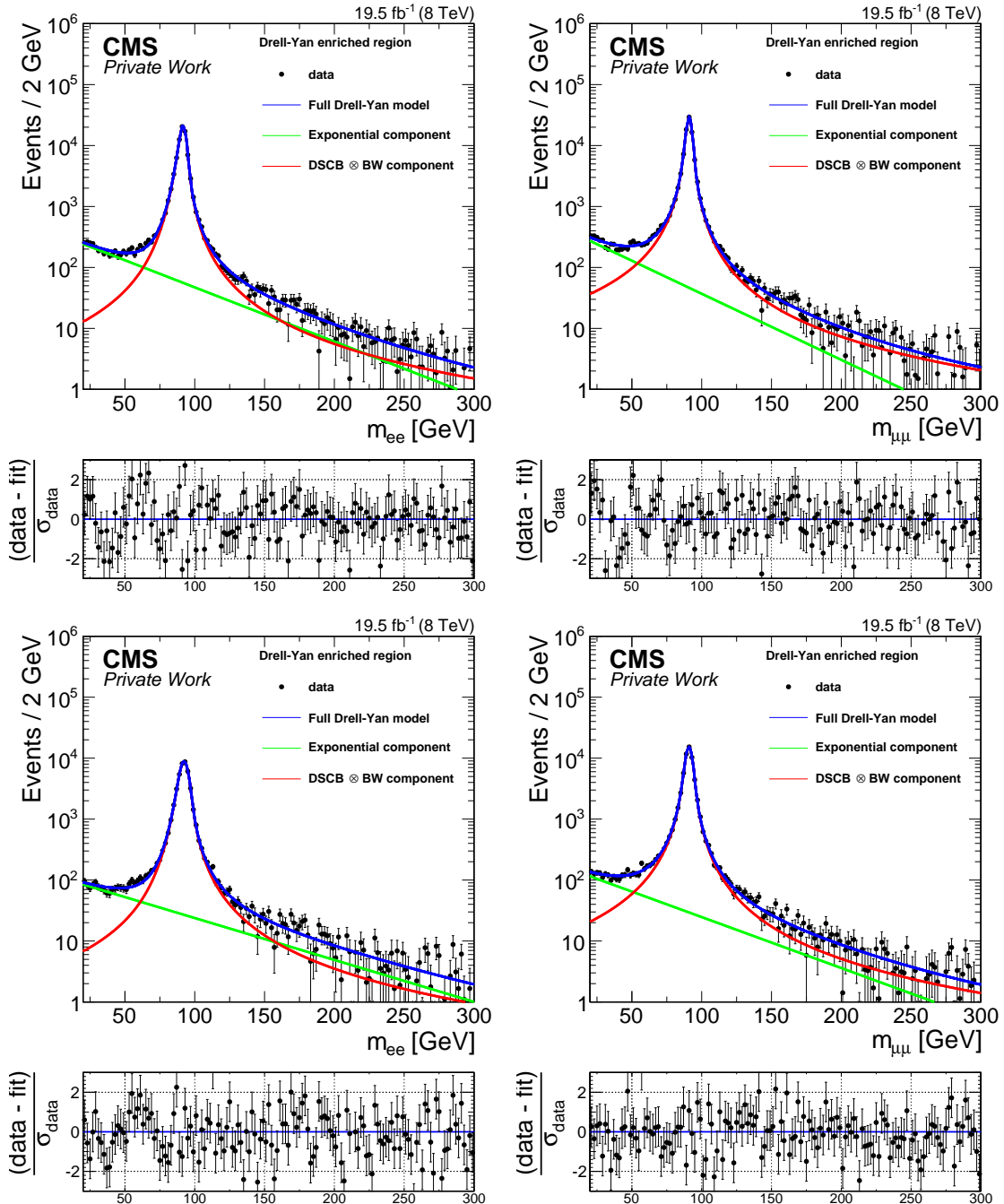


Figure 7.1: Fit to the $m_{\ell\ell}$ distribution in the Drell–Yan control region separately for $e^\pm e^\mp$ (left) and $\mu^\pm \mu^\mp$ (right) events in the central (top) and forward (bottom) dilepton selection. The data is shown as black points while the resulting fit is shown in blue. The red and green lines show the contributions of the continuum model and the convolution of the Breit-Wigner with the double-sided crystal ball to the combined fit.

Table 7.3: List of all parameters of the nominal model for flavour-symmetric backgrounds. Given are initial values, allowed ranges and the status of the parameters. A set of these parameters exists for both the central and forward dilepton selection.

	parameter	status	initial value	minimum	maximum
PFS	$m_{\ell\ell}^{(1)}$ [GeV]	floating	50	20	80
	$m_{\ell\ell}^{(2)}$ [GeV]	floating	120	100	160
	$c_{2,0}$	floating	-1800	-5000	5000
	$c_{2,1}$	floating	120	-400	400
	$c_{2,2}$	fixed	1	-	-
	$c_{2,3}$	floating	$2.5 \cdot 10^{-3}$	$1 \cdot 10^{-4}$	$1 \cdot 10^{-2}$

Parametrisation from 2011 analysis

This parametrisation was used in a previous version of the analysis [113]:

$$\mathcal{P}_{FSE}(m_{\ell\ell}) = c_1 m_{\ell\ell}^{\alpha} e^{-\beta m_{\ell\ell}}$$

It was found to not describe the distribution of flavour-symmetric backgrounds after lepton p_T cuts had been raised with respect to the analysis of the 2011 dataset, but is still a useful tool for fit performance studies, as the low number of parameters reduces the runtime of the fit, allowing for tests using a large number of simulated datasets.

Sum of three Gaussians

In this case the sum of three Gaussians is chosen as an analytical parametrisation of the flavour-symmetric backgrounds. The free parameters of the shape are the means μ_i and widths σ_i of the Gaussians.

$$\mathcal{P}_{FS}(m_{\ell\ell}) = \text{Gauss}(\mu_1, \sigma_1) + \text{Gauss}(\mu_2, \sigma_2) + \text{Gauss}(\mu_3, \sigma_3)$$

The shape is found to well describe the flavour-symmetric background and to be in good agreement with the nominal parametrisation.

Binned Subtraction

As an alternative to analytical functions, the binned dilepton-mass distribution in the OF channel is directly used as template of the distribution of flavour-symmetric backgrounds in the same-flavour channels. This results in a bin-by-bin subtraction of the flavour-symmetric background estimation from same-flavour yields taking into account the $R_{SF/OF}$ correction factor, similar to the counting experiment.

This approach has the advantage of not needing any prior knowledge on the shape of the flavour-symmetric background. It is, however, more susceptible to statistical fluctuations, as they are not smoothed out (for a smoothed approach see below). In order to minimise the impact of these fluctuations, a bin width of 5 GeV is chosen. This method is not suited to provide quantitative results because the statistical uncertainties on shape are not considered in the fit after it has been fixed on the OF data.

Smoothed Subtraction

Similarly to the binned subtraction, the opposite flavour data distribution is directly used to predict the background in the same flavour distribution using a kernel density estimator (KDE). The shape is constructed as a sum of Gaussian distributions, one for each event in the considered dataset with the mean set to the $m_{\ell\ell}$ value of that event. For this the implementation of one-dimensional kernel PDFs in RooFit is used (*RooKeysPdf* class). In this approach, the probability density function for a sample of a random variable of size n is estimated by a kernel density

$$\hat{f}_h(m_{\ell\ell}) = \frac{1}{nh} \sum_{i=1}^n K\left(\frac{m_{\ell\ell} - m_{\ell\ell,i}}{h}\right).$$

Here K is the so called kernel, for which a Gaussian distribution is chosen in this analysis, and h is a smoothing parameter [114]. The width of the Gaussians is adapted depending on the density of events at a given point. For both borders, the low- $m_{\ell\ell}$ and the high- $m_{\ell\ell}$ border, parts of the Gaussians extending beyond the considered range of $m_{\ell\ell}$ are mirrored back into the considered range to achieve the correct integral. Again, this method is not suited to provide quantitative results because no uncertainties on the background shape can be included because it has to be fixed on the OF data before the combined fit can be performed.

7.1.3 Signal model

The signal is modelled by a simple triangular shape, which will be shown to be a good approximation of its actual shape, which is model dependent. The signal parametrisation is therefore given by a triangle, convolved with a Gaussian distribution. The width of the Gaussian $\sigma_{\ell\ell}$ depends on the detector resolution in the corresponding channel and is obtained from the fit to the Z boson peak in the Drell–Yan control region described in Section 7.1.1. The model can be parametrised as

$$\mathcal{P}_S(m_{\ell\ell}) = \frac{1}{\sqrt{2\pi\sigma_{\ell\ell}^2}} \int_0^{m_{\ell\ell}^{\text{edge}}} y \cdot \exp\left(-\frac{(m_{\ell\ell} - y)^2}{2\sigma_{\ell\ell}^2}\right) dy,$$

with the endpoint of the triangle $m_{\ell\ell}^{\text{edge}}$ as the only free parameter. as the starting point is always 0 GeV.

To cross check the dependence of the results on the parametrisation of the signal, two additional signal shapes with strongly differing shapes are defined. Here the linear dependence on $m_{\ell\ell}$ is replaced by quartic dependencies with different signs, resulting in concave and convex shapes instead of the simple triangle:

$$\mathcal{P}_S^{\text{convex}}(m_{\ell\ell}) = \frac{1}{\sqrt{2\pi\sigma_{\ell\ell}^2}} \int_0^{m_{\ell\ell}^{\text{edge}}} y^4 \cdot \exp\left(-\frac{(m_{\ell\ell} - y)^2}{2\sigma_{\ell\ell}^2}\right) dy, \quad (7.1)$$

$$\mathcal{P}_S^{\text{concave}}(m_{\ell\ell}) = \frac{1}{\sqrt{2\pi\sigma_{\ell\ell}^2}} \int_0^{m_{\ell\ell}^{\text{edge}}} (m_{\ell\ell}^{\text{edge},4} - (y - m_{\ell\ell}^{\text{edge}})^4) \cdot \exp\left(-\frac{(m_{\ell\ell} - y)^2}{2\sigma_{\ell\ell}^2}\right) dy. \quad (7.2)$$

The parameters of the signal model are listed in Table 7.4.

Table 7.4: List of all parameters of the signal model. Given are initial values, allowed ranges and the status of the parameters. A set of these parameters exists for both the central and forward dilepton selection.

	parameter	status	initial value	minimum	maximum
\mathbf{p}_S^{ee}	$m_{\ell\ell}^{\text{edge}}[\text{GeV}]$	floating	varying	30	300
	$\sigma_{CB}^{ee}[\text{GeV}]$	fixed	see Table 7.2	-	-
$\mathbf{p}_S^{\mu\mu}$	$m_{\ell\ell}^{\text{edge}}[\text{GeV}]$	floating	varying	30	300
	$\sigma_{CB}^{\mu\mu}[\text{GeV}]$	fixed	see Table 7.2	-	-

The signal model is fitted to simulation using four parameter points of the fixed-edge and slepton-edge models described in Section 2.2.2. The points are chosen to study edges produced in decays both via an off-shell Z boson and sleptons and also to test the fit performance for edge positions below, on, and above the Z boson peak. The signal parameters are summarised in Table 7.5 and will be referenced by their labels S1-S4 in the following.

Table 7.5: Overview of the benchmark signal points used in fit performance studies.

name	S1	S2	S3	S4
model	fixed-edge	slepton-edge	slepton-edge	slepton-edge
$m_{\tilde{b}} [\text{GeV}]$	400	500	500	450
$m_{\tilde{\chi}_2^0} [\text{GeV}]$	150	175	200	275
$m_{\tilde{\chi}_1^0} [\text{GeV}]$	80	100	100	100
gen. $m_{\ell\ell}^{\text{edge}} [\text{GeV}]$	70	74.3	98.6	170.2

If more than two leptons are reconstructed in an event, the wrong combination might be chosen, leading to a flavour-symmetric, background-like contribution of the signal. This happens more often in the slepton-edge model because of the much higher branching fraction into leptons. Therefore, a model for flavour-symmetric backgrounds is also fitted to the signal. For these tests, the KDE shape is used because of its fast convergence.

Fits to the fixed-edge model points S1 are shown in Figure 7.2. After subtraction of the very small flavour-symmetric contribution, this model predicts about 122 events in the central and 15 events in the forward region with a mass difference of 70 GeV, in agreement with the expectation that the decay products of heavy SUSY particles are located dominantly in the central region of the detector. In the upper plots fits are shown using the nominal triangular shape, which is clearly not a good approximation of the actual shape of the signal, which is peaked towards the Z boson mass as the decay of the $\tilde{\chi}_2^0$ occurs exclusively via an off-shell Z boson. However, the signal parameters $m_{\ell\ell}^{\text{edge}}$ and N_S are still reproduced very well. In the lower two plots, the convex signal shape was used, but the exponent, which is 4 in Equation 7.1, is left as a free parameter. The resulting shape is a much better description of the signal, with a fitted exponent of about 2.62. However, no significant change in the other signal parameters

is observed.

In Figure 7.3 a fit to the slepton-edge model point S2 is shown. As the decays occur dominantly via an intermediate slepton, the triangular shape is a much better approximation of the signal shape. Because of the much higher branching fraction into leptons of this model, a significant flavour-symmetric contribution due to combinatorics is present, which is accounted for by the background description and reduces the observable signal yield. Again, the signal parameters are well reproduced by the fit. Similar performance is also observed for the points S3 and S4.

7.2 Combined model

The full models fitted to the different event categories are constructed by adding yield parameters for each component. For opposite flavour events, the model is simply given by

$$\mathcal{P}_{OF}(m_{\ell\ell}) = N_{FS} \cdot \mathcal{P}_{FS}(m_{\ell\ell}).$$

For $e^\pm e^\mp$ and $\mu^\pm \mu^\mp$ events, also yield parameters for the Drell–Yan background and the signal models have to be introduced.

$$\begin{aligned}\mathcal{P}_{ee}(m_{\ell\ell}) &= N_{FS}^{ee} \cdot \mathcal{P}_{FS}(m_{\ell\ell}) + N_Z^{ee} \cdot \mathcal{P}_{Z,ee}(m_{\ell\ell}) + N_S^{ee} \cdot \mathcal{P}_S(m_{\ell\ell}, \sigma_{ee}) \\ \mathcal{P}_{\mu\mu}(m_{\ell\ell}) &= N_{FS}^{\mu\mu} \cdot \mathcal{P}_{FS}(m_{\ell\ell}) + N_Z^{\mu\mu} \cdot \mathcal{P}_{Z,\mu\mu}(m_{\ell\ell}) + N_S^{\mu\mu} \cdot \mathcal{P}_S(m_{\ell\ell}, \sigma_{\mu\mu})\end{aligned}$$

To reduce the number of free parameters, a universal fraction of $e^\pm e^\mp$ events in both background and signal is assumed and expressed as $0 < f_{ee} < 1$. Also, the flavour-symmetric yields in the two SF channels are connected to that in the OF channel via $R_{SF/OF}$, which allows to construct the following relations:

$$\begin{aligned}N_S^{ee} &= f_{ee} \cdot N_S, & N_S^{\mu\mu} &= (1 - f_{ee}) \cdot N_S, \\ N_Z^{ee} &= f_{ee} \cdot N_Z, & N_Z^{\mu\mu} &= (1 - f_{ee}) \cdot N_Z, \\ N_{FS}^{ee} &= f_{ee} \cdot R_{SF/OF} \cdot N_{FS}, & N_{FS}^{\mu\mu} &= (1 - f_{ee}) \cdot R_{SF/OF} \cdot N_{FS}.\end{aligned}$$

The systematic uncertainty on $R_{SF/OF}$ is included in the fit as a constraint in form of a Gaussian function with mean and width set to the values measured in Section 5.1.3:

$$\text{Gauss}\left(R_{SF/OF}; R_{SF/OF}^{\text{measured}}, \sigma_{R_{SF/OF}}^{\text{measured}}\right).$$

The full likelihood of the model as a function of $m_{\ell\ell}$ for a given set of parameters \mathbf{p} that is fit to the data in the six channels ($e^\pm e^\mp, \mu^\pm \mu^\mp$, and OF for central and forward lepton selection) is constructed by multiplying the PDFs of the different channels and is given by

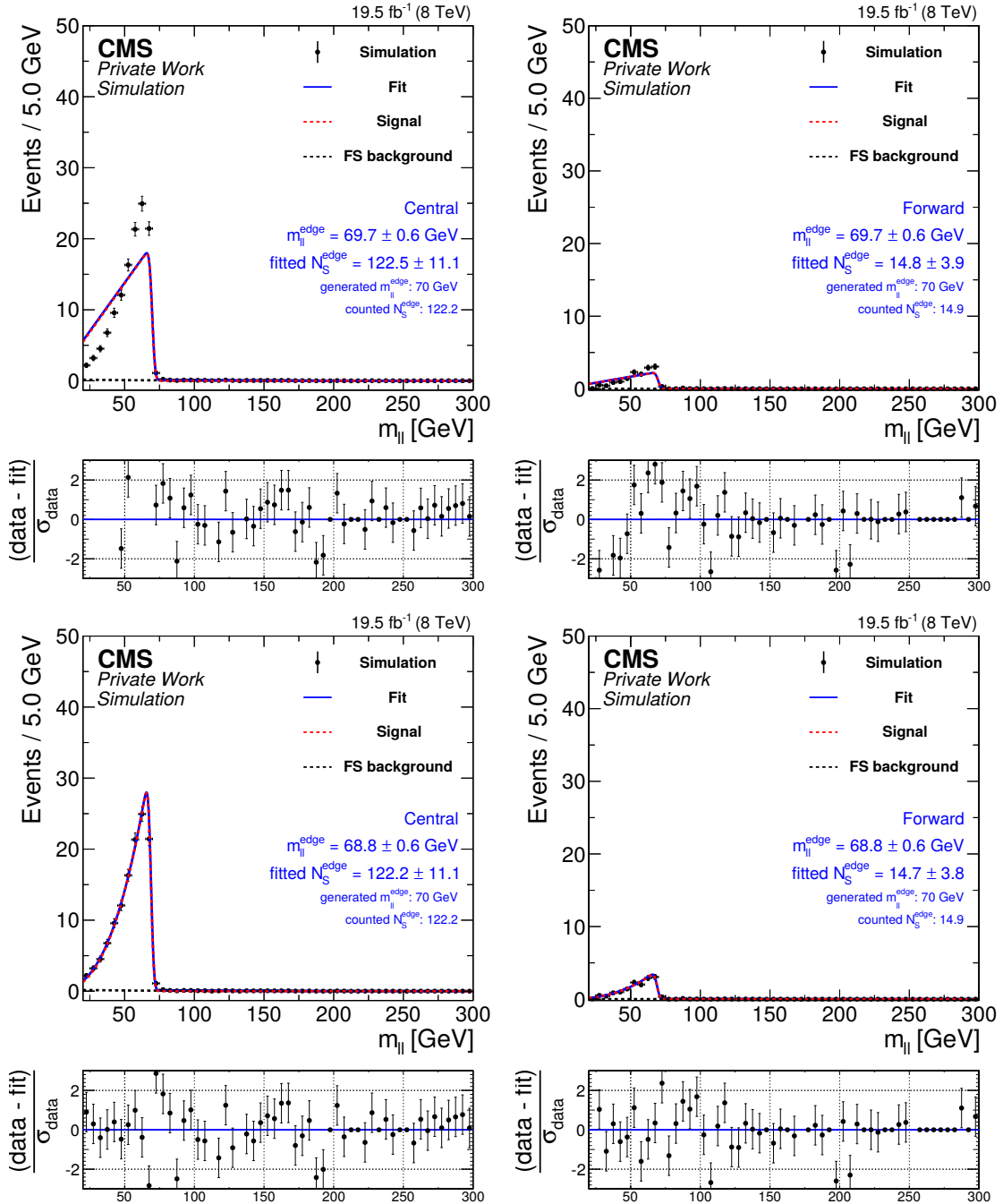


Figure 7.2: Fit of the signal model to the fixed-edge model S1 (see Table 7.5). Shown are fits with the nominal triangular shape (top) and the convex shape with floating exponent (bottom) in both the central (left) and forward (right) signal regions.

$$\begin{aligned}
\mathcal{L}(m_{\ell\ell}; \mathbf{p}) = & \prod_{i \in \text{central, forward}} \mathcal{N}_i \\
& \times \prod_{e^\pm e^\mp, i} \left[N_{FS}^{ee,i} \cdot \mathcal{P}_{FS}^i(m_{\ell\ell}; \mathbf{p}_{FS}^i) + N_Z^{ee,i} \cdot \mathcal{P}_Z^i(m_{\ell\ell}; \mathbf{p}_Z^{ee,i}) + N_S^{ee,i} \cdot \mathcal{P}_S^i(m_{\ell\ell}; \mathbf{p}_S^{ee,i}) \right] \\
& \times \prod_{\mu^\pm \mu^\mp, i} \left[N_{FS}^{\mu\mu,i} \cdot \mathcal{P}_{FS}^i(m_{\ell\ell}; \mathbf{p}_{FS}^i) + N_Z^{\mu\mu,i} \cdot \mathcal{P}_Z^i(m_{\ell\ell}; \mathbf{p}_Z^{\mu\mu,i}) + N_S^{\mu\mu,i} \cdot \mathcal{P}_S^i(m_{\ell\ell}; \mathbf{p}_S^{\mu\mu,i}) \right] \\
& \times \prod_{e^\pm \mu^\mp, i} \left[N_{FS}^{OF,i} \cdot \mathcal{P}_{FS}^i(m_{\ell\ell}; \mathbf{p}_{FS}^i) \right] \\
& \times \text{Gauss}^i(R_{SF/OF}^i),
\end{aligned}$$

where the different \mathbf{p}_x^i denote the sets of free parameters of the models and the \mathcal{N}_i are Poisson factors describing the normalisation of the different samples. These factors take the form of

$$\mathcal{N}_i = \frac{(N_{FS}^{\ell\ell,i} + N_Z^{\ell\ell,i} + N_S^{\ell\ell,i})^{N_i^{\ell\ell}} e^{-(N_{FS}^{\ell\ell,i} + N_Z^{\ell\ell,i} + N_S^{\ell\ell,i})}}{N_i^{\ell\ell}!}$$

for $\ell\ell = e^\pm e^\mp, \mu^\pm \mu^\mp$ and

$$\mathcal{N}_i = \frac{(N_{FS}^{\ell\ell,i})^{N_i^{\ell\ell}} e^{-(N_{FS}^{\ell\ell,i})}}{N_i^{\ell\ell}!}$$

for $\ell\ell = e^\pm \mu^\mp$, with $i = \text{Central, Forward}$. $N_i^{\ell\ell}$ is the number of observed events in the respective channel.

A full overview over all parameters of the model is shown in Table 7.6. In total, the model has 59 parameters, of which 21 are free parameters in the signal region, 34 describe the Drell–Yan model and four are the mean values and widths of $R_{SF/OF}$ used in the constraints.

7.3 Fit validation

Before the fit is applied to data, several studies are performed to assess its performance in different scenarios. The fit is performed on simulated SM backgrounds and several benchmark signal points. As the results are subject to the fluctuations of the specific MC samples available for this study, the fit performance is studied in detail using a large number of toy datasets generated from the fit model itself.

7.3.1 Fit performance on simulation

The ability of the fit to correctly describe different datasets is tested using the simulation of SM and signal processes described in Section 4.2.2, normalized to 19.5 fb^{-1} . The full list of background processes is considered and fits are performed with and without the addition of signal points from the fixed-edge and slepton-edge models described in Section 2.2.2. To retain an acceptable runtime of the unbinned fit a smaller inclusive $t\bar{t}$ sample is used instead of the large samples separated into the different final states.

Table 7.6: List of parameters of the full fit model. For more details on the parameter sets \mathbf{p}_{FS} , \mathbf{p}_Z , and \mathbf{p}_S see Tables 7.1, 7.3, and 7.4. For yield parameters the initial value and allowed ranges are calculated from the observed yields N_{SF} and N_{OF} in the signal region for both the central (C) and forward (F) dilepton selection.

parameter	status	initial value	minimum	maximum
Normalisation parameters				
N_{FS}^C	floating	$0.7 \cdot N_{OF}^C$	0	$2 \cdot N_{OF}^C$
N_{FS}^F	floating	$0.7 \cdot N_{OF}^F$	0	$2 \cdot N_{OF}^F$
N_S^C	floating	0	$-0.4 \cdot N_{SF}^C$	$0.4 \cdot N_{SF}^C$
N_S^F	floating	0	$-0.8 \cdot N_{SF}^F$	$0.8 \cdot N_{SF}^F$
N_Z^C	floating	pred. from data	0	$N_{SF}^C(81 \text{ GeV} < m_{\ell\ell} < 101 \text{ GeV})$
N_Z^F	floating	pred. from data	0	$N_{SF}^F(81 \text{ GeV} < m_{\ell\ell} < 101 \text{ GeV})$
Shape parameters				
\mathbf{p}_Z^C	mixed			
\mathbf{p}_Z^F	mixed	see Table 7.1		
\mathbf{p}_{FS}^C	mixed			
\mathbf{p}_{FS}^F	mixed	see Table 7.3		
\mathbf{p}_S^C	mixed			
\mathbf{p}_S^F	mixed	see Table 7.4		
Constraint parameters				
$R_{SF/OF}^C$	constrained	$R_{SF/OF}^{C,\text{meas.}}$	$R_{SF/OF}^{C,\text{meas.}} - 4 \cdot \sigma_{R_{SF/OF}}^{C,\text{meas.}}$	$R_{SF/OF}^{C,\text{meas.}} + 4 \cdot \sigma_{R_{SF/OF}}^{C,\text{meas.}}$
$R_{SF/OF}^F$	constrained	$R_{SF/OF}^{F,\text{meas.}}$	$R_{SF/OF}^{F,\text{meas.}} - 4 \cdot \sigma_{R_{SF/OF}}^{F,\text{meas.}}$	$R_{SF/OF}^{F,\text{meas.}} + 4 \cdot \sigma_{R_{SF/OF}}^{F,\text{meas.}}$

The result of a fit to background-only simulation is shown in Figure 7.4. The combined model is a good description of the simulation. A negative signal yield is fitted in both the central and forward signal region. While in the central region this is a small effect compared to the fitted uncertainty, in the forward region there is a large underfluctuation of the background at lower invariant masses, leading to a fitted signal yield of -38 ± 15 events. To verify that this is indeed the global minimum, a scan of the log-likelihood versus $m_{\ell\ell}^{\text{edge}}$ is performed. The result is shown in Figure 7.5. Above the Z boson peak the result is only little dependent on $m_{\ell\ell}^{\text{edge}}$. Below the peak, however, there is relatively broad minimum with a large rise directly above the global minimum, which reflects the fluctuation in the simulation in the forward region around 70 GeV. Several relevant fit parameters in the central signal region are shown in Table 7.7.

Table 7.7: Fit result in the central signal region on simulation. Shown are fits to background-only simulation as well as to the signal points described in Section 7.1.3.

	bgkd only	S1	S2	S3	S4
gen. $m_{\ell\ell}^{\text{edge}}$ [GeV]	-	70	74.3	98.6	170.2
fitted $m_{\ell\ell}^{\text{edge}}$ [GeV]	63.2 ± 3.1	68.8 ± 2.5	73.7 ± 1.7	98.6 ± 2.3	169.6 ± 1.6
gen. N_S^{central}	0	122.1	259.1	266.6	547.5
fitted N_S^{central}	-21.5 ± 34.9	116.9 ± 40.4	237.8 ± 42.3	245.6 ± 68.1	441.8 ± 70.4
fitted N_{DY}^{central}	90.5 ± 22.5	87.1 ± 22.5	89.9 ± 22.6	93.6 ± 27.0	96.3 ± 23.8
fitted N_{FS}^{central}	2802 ± 49	2803 ± 49	2840 ± 29	2841 ± 49	2876 ± 50
fitted $R_{SF/OF}^{\text{central}}$	1.004 ± 0.024	1.000 ± 0.024	1.004 ± 0.024	1.003 ± 0.025	1.022 ± 0.026

The signal points S1-S4 discussed in Section 7.1.3 are used to test the fits ability to reproduce the parameters of a signal. Figure 7.6 shows the results for the SF dataset in the central signal region for all four hypothesis.

In all four cases, the correct edge position is found with good precision. In case of the fixed-edge signal point S1, the signal shape differs significantly from the triangular shape assumed in the fit. However, in the absence of background, the parameters of the signal model are reproduced with high accuracy as demonstrated in Section 7.1.3. Comparing the fitted values for the number of signal events (119.3 ± 40.8 and 122.2 ± 11.1) and $m_{\ell\ell}^{\text{edge}}$ (68.8 \pm 3.6 GeV and 68.8 \pm 0.6 GeV) with and without backgrounds, the presence of the backgrounds does not significantly affect the result, except for much increased uncertainties. It can be concluded that the triangular shape is suitable to extract the signal parameters of more convex shapes. A more detailed study of the biases introduced by different signal shapes is described in Section 7.3.2.

For the three slepton-edge signals S2-S4, the edge position is well reproduced by the fit. The fitted signal yield, however, can be lower than the injected one. This effect increases with $m_{\ell\ell}^{\text{edge}}$ because the fit is able to accommodate higher values of $R_{SF/OF}$, increasing the background contribution. This is accompanied by a slight increase of the fitted Drell-Yan yield. Another notable feature is the contribution of the signal to the flavour-symmetric backgrounds, which is of the order of 40-80 events for the studied signal points.

7.3.2 Fit performance studies using toy datasets

The performance of the fit is studied using toy datasets. These are generated by fitting the background shape for flavour-symmetric backgrounds to OF events in simulation. From

this shape new opposite-flavour datasets are generated, fluctuating the normalisation using a Poisson distribution. Electron-electron and muon-muon datasets are generated from the sum of the shape for flavour-symmetric backgrounds and the Drell-Yan model. The normalisation of this shape is given by the normalisation for flavour-symmetric backgrounds multiplied by $R_{\text{SF}/\text{OF}}$ plus the combined JZB and E_T^{miss} -template predictions. This yield is split into the $e^\pm e^\mp$ and $\mu^\pm \mu^\mp$ datasets according to the measured $R_{ee/\text{OF}}$ and $R_{\mu\mu/\text{OF}}$ values. Each of the two yields is fluctuated independently according to a Poisson distribution when dicing the toy datasets. If desired, a signal is injected in the same-flavour datasets using the nominal signal shape in a similar fashion. To reflect that the signal yield is expected to be higher in the central dilepton selection, the signal contribution in the forward selection is chosen to be smaller by a factor of three. The combined fit is performed on each of the datasets generated in this fashion. As the nominal background shape is quite resource intensive, the parametrisation from the 2011 analysis is used in these studies in order to generate sufficient statistics, after verifying that this has no significant impact of the results. In general around 1000 toys are generated for each configuration.

Studies without signal injection

The edge fit is performed on toys generated from the background models. In one case, the toys are fitted with a floating edge position. In the other, it is fixed at 70 GeV. Figure 7.7 shows resulting distributions. On the left side, the number of fitted signal events in the central region divided by its uncertainty is shown. In case of the fixed edge the fit results are distributed following a unit Gaussian centred around zero, as expected in absence of a signal. For the case of a floating edge position, however, the distribution exhibits two peaks, symmetrically below and above zero. This is a manifestation of the “look-elsewhere-effect” introduced by the degree of freedom of the edge position. On the right side of Figure 7.7, the distributions of the fitted values of $R_{\text{SF}/\text{OF}}$ are shown, again for the central selection. In both cases, the value used in the generation of the toys of 1.013 is well reproduced. Also, the width of the distribution is identical in both cases, illustrating that the floating edge position does not introduce biases apart from favouring results with a higher number of signal events.

The distribution of the fitted edge position versus the initial value is shown in Figure 7.8. The initial values have been randomised between 0 and 300 GeV. To ensure that the initial value is inside the allowed range for $m_{\ell\ell}^{\text{edge}}$ and not too close to the lower boundary, diced values below 35 GeV are set to this value. In absence of a signal a strong correlation between the initial and observed value of $m_{\ell\ell}^{\text{edge}}$ is observed. This suggests that the fit tends to converge to the next local minimum of the negative log-likelihood. It is therefore necessary to choose a suitable initial value close to the global minimum before the fit is performed.

As an additional check, toys are generated with $R_{\text{SF}/\text{OF}}$ shifted by $\pm 1\sigma$. These toys are fitted with a Gaussian constraint to the central value and the results are shown in Figure 7.9. The same distributions are shown as above. In the case of the signal yield divided by its uncertainty, the double peak structure observed in the nominal configuration changes to a single peak that is shifted to negative signal yields for the toys generated with lower and to positive signal yields for those generated with higher values of $R_{\text{SF}/\text{OF}}$. For the fitted values of $R_{\text{SF}/\text{OF}}$, the width of the distribution is unchanged, but the systematic shifts in the generation of the toys is reflected in their means. The fit is therefore able to correct for systematic biases in $R_{\text{SF}/\text{OF}}$. However, the observed shifts of the mean (0.025 and -0.023) are smaller than those introduced

in the generation of the toys (± 0.037 , the uncertainty of $R_{\text{SF}/\text{OF}}$), suggesting that part of the systematic shift is absorbed by the fit by introducing a signal contribution. Still, this is a significant improvement over the counting experiment approach, where no such correction is possible.

Toy studies with signal injection

The fit performance in the presence of a signal is tested by injection of a signal of 125 events with an edge position of 70 GeV in the central region and a third of that number in the forward region. Figure 7.10 shows the resulting distribution of fit results for a selection of observables in the central signal region. The distribution of the number of signal events is well described by a Gaussian with a mean of about 124 events, very close to the injected number, and a width of 41 events. Divided by the fitted uncertainty, this gives a unit Gaussian with a mean of about 2.9. The edge position is also Gaussian distributed, with a mean of about 70 GeV, also reproducing the injected value very well, with a width of about 1.8 GeV. Comparing the distribution of $R_{SF/OF}$ with that in Figure 7.7, it can be seen that the presence of a signal does not bias the result towards higher values.

To study the dependence of the fit result on the edge position, toys are generated with a signal of 125 events in the central signal region, injected at different values of $m_{\ell\ell}^{\text{edge}}$ between 40 and 200 GeV in steps of 10 GeV. For each configuration, about 1000 fits are performed. The initial value of $m_{\ell\ell}^{\text{edge}}$ is chosen to coincide with the generated one. The distributions of the fitted $m_{\ell\ell}^{\text{edge}}$ and number of signal events for each generated $m_{\ell\ell}^{\text{edge}}$ are shown in Figure 7.11. In the case of the fitted $m_{\ell\ell}^{\text{edge}}$ on the left side, the generated value is in general very well reproduced by the fit. The best results are obtained for low values of $m_{\ell\ell}^{\text{edge}}$, as the signal shape is much steeper and easier to separate from the background than for higher values. Towards higher values the spread of the results and especially the probability for very large deviation from the generated value increases, before they decrease towards very high values of the generated $m_{\ell\ell}^{\text{edge}}$. A notable feature is observed for generated values of 100 GeV, where for a small number of fits the fitted value is very close to the Z boson mass. However, the fact that the initial value is set to the correct position a priori introduces a bias towards this good performance. This is demonstrated for the example of an injected signal at $m_{\ell\ell}^{\text{edge}} = 70$ GeV in Figure 7.12, where the fitted value is plotted versus the initial value of $m_{\ell\ell}^{\text{edge}}$. For initial values below m_Z , the correct edge position is found with a high probability. If the initial value is located on the other side of the Z boson peak, it is much less likely to find the signal at its injected position.

Similar behaviour is also observed for the number of fitted signal events. Here, the relative size of the deviation from the generated value is much larger, as the event yields are fluctuated in the generation of the toys.

The width of the distribution of the fitted $m_{\ell\ell}^{\text{edge}}$ is shown on the left side of Figure 7.13. It is quantified both with the root mean square (RMS) of the distribution and the width of a Gaussian fitted in a range of ± 3 GeV around the generated value. The first is sensitive to the non-Gaussian tails of the distribution while the latter is a measure of the core resolution. For generated values of $m_{\ell\ell}^{\text{edge}}$ of 40 GeV, the two values are the same, but quickly deviate for higher edge positions. The Gaussian width rises from about 1 GeV to about 2 – 2.5 GeV for edge position above 80 GeV and is roughly constant for higher edge positions. The RMS reaches values of 4 GeV for edges below the Z mass. For $m_{\ell\ell}^{\text{edge}} = 100$ GeV it is much larger, caused by the bias towards the Z boson mass observed in Figure 7.11. Above the Z boson peak, the RMS of the distribution is roughly stable at 8 GeV before it drops off again for edge positions above 180 GeV, when the separation between $m_{\ell\ell}^{\text{edge}}$, where most of the signal is located, and the Z boson peak becomes large.

The right side of Figure 7.13 shows the means and widths of fits of Gaussian functions to the distributions of N_S^{central} , again as a function of the generated $m_{\ell\ell}^{\text{edge}}$. The distributions do not exhibit significant non-Gaussian tails, so the RMS value is not shown in this case. The injected value of 125 events is reproduced within about 8 events for all values of $m_{\ell\ell}^{\text{edge}}$. The width increases with $m_{\ell\ell}^{\text{edge}}$ from roughly 25 to 65 events at $m_{\ell\ell}^{\text{edge}}$ of 100 GeV and decreases slightly for higher values.

To test deviations from the assumed signal shape, toys are generated with a signal injected at $m_{\ell\ell}^{\text{edge}} = 70$ GeV and a size of 125 events, but following the convex and concave signal shapes described in Section 7.1.3. They are then fitted using the nominal triangular signal shape. Resulting distributions are shown in Figure 7.14. When fitting a convex signal with the triangular shape a bias towards higher signal yields of 20 events is introduced, together with a preference of slightly higher values for $m_{\ell\ell}^{\text{edge}}$. This higher signal yield is achieved by systematically reducing the value of $R_{\text{SF}/\text{OF}}$. Less strong effects are observed in the case of a convex signal. Here, a bias towards a reduced signal yield of about 10 events is present, together with a much wider distribution of the fitted $m_{\ell\ell}^{\text{edge}}$. In this case, no change in the distribution of the fitted $R_{\text{SF}/\text{OF}}$ compared to the nominal signal shape is observed.

In summary, the fit shows good performance reproducing signal properties. The triangular shape has been shown to be a sufficient approximation to measure the signal yield and $m_{\ell\ell}^{\text{edge}}$. In case of a fixed edge position, the fit does not exhibit biases towards a signal. A floating edge, however, makes the fit susceptible to the look-elsewhere-effect, which has to be taken into account when assessing the significance of a result. If found correctly, the edge position can be measured with high precision. The variability of $R_{\text{SF}/\text{OF}}$ in the fit allows it to at least partially correct for biases in the SF to OF mapping.

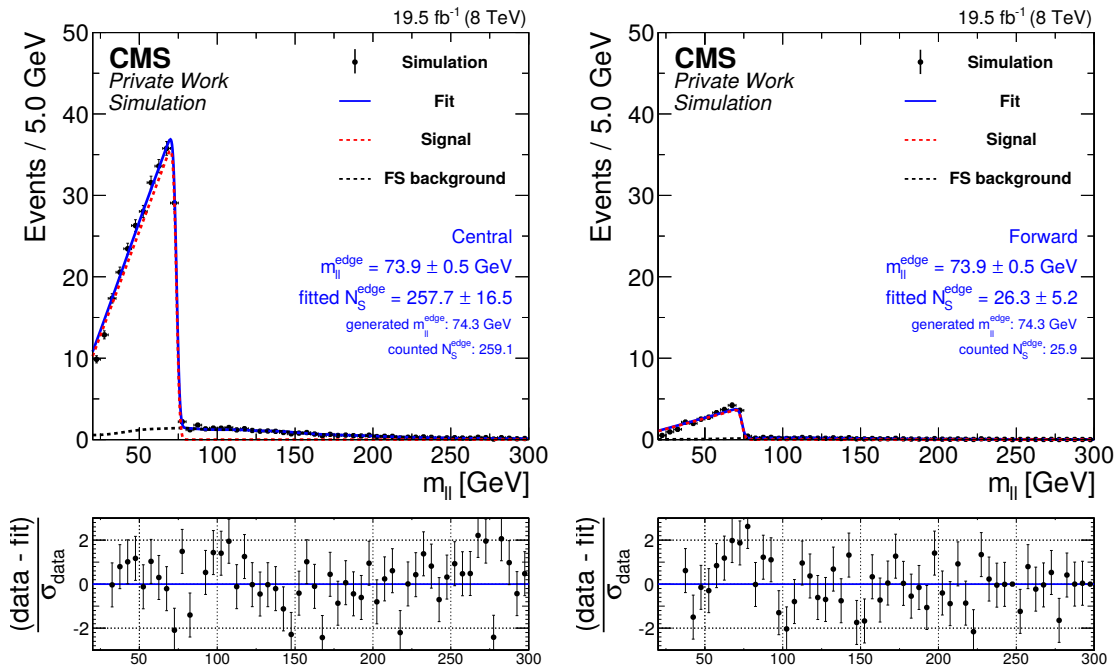


Figure 7.3: Fit of the signal model to the slepton-edge model S2 (see Table 7.5). Shown are fits in both the central (left) and forward (right) signal regions.

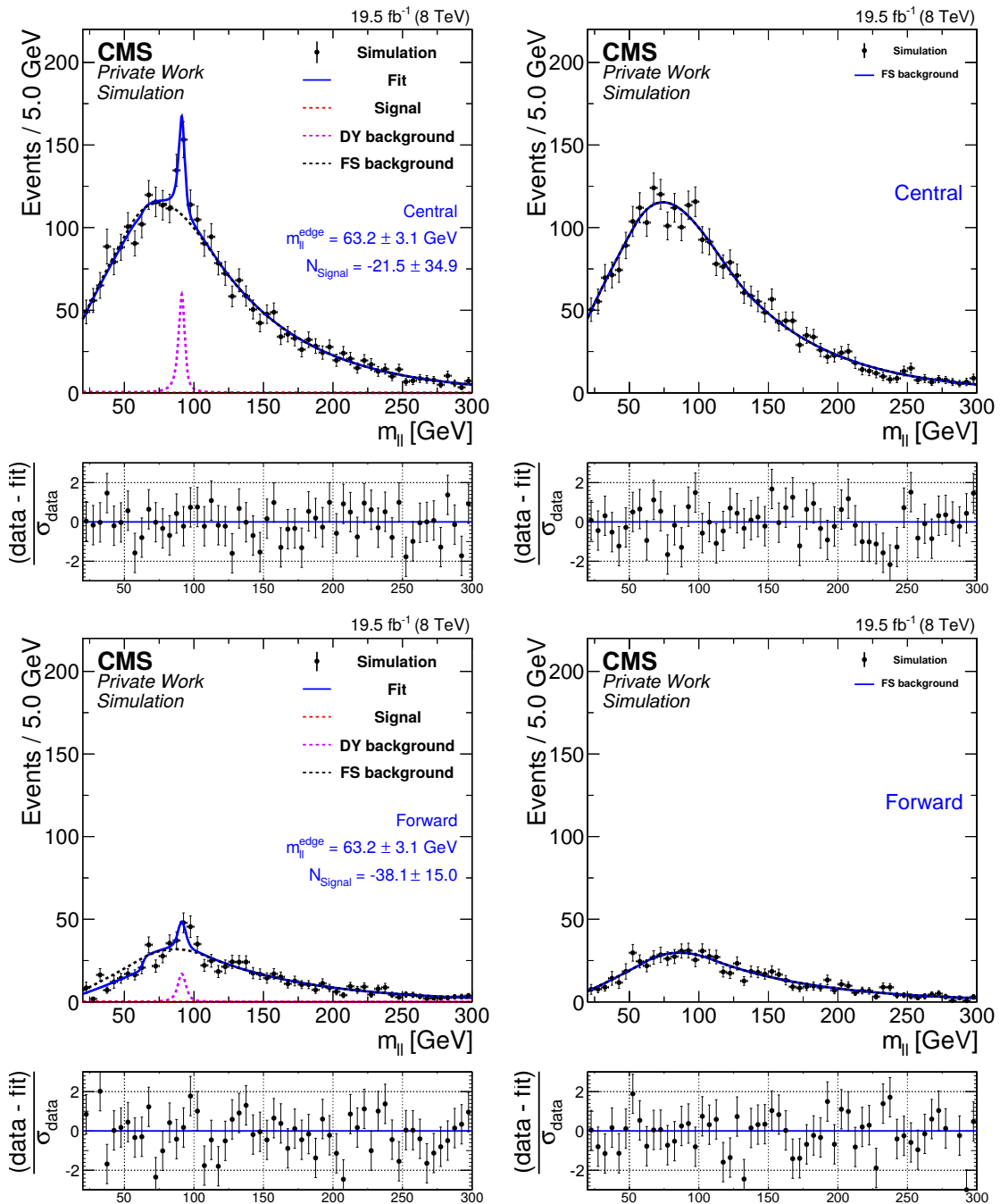


Figure 7.4: Fit results for a fit to background-only simulation. Shown are the results for the SF (left) and OF (right) samples in the central (top) and forward (bottom) signal regions. The simulation is shown as black data points. The combined fit is shown as a solid blue line, while the flavour-symmetric and Z backgrounds are shown as black and violet dashed lines. The signal model is shown as a red dashed line.

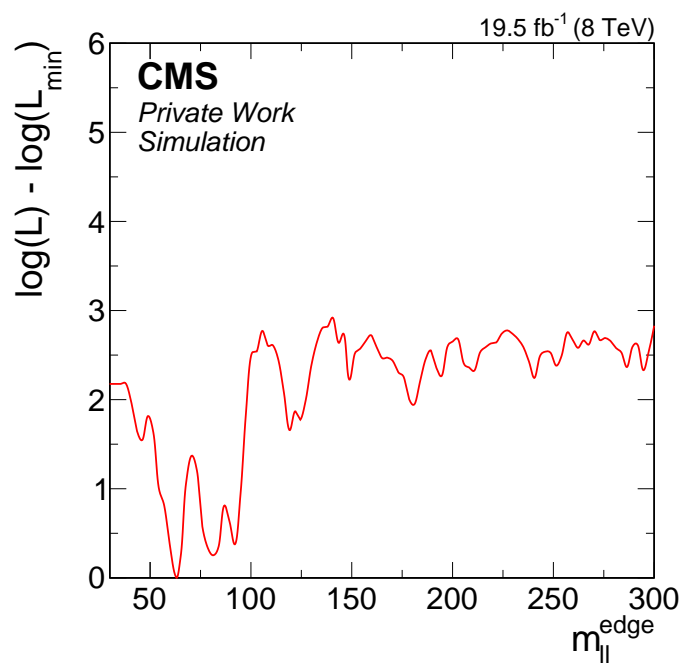


Figure 7.5: Scan of the observed log-likelihood in the signal region subtracted by the minimal value as a function of $m_{\ell\ell}^{\text{edge}}$.

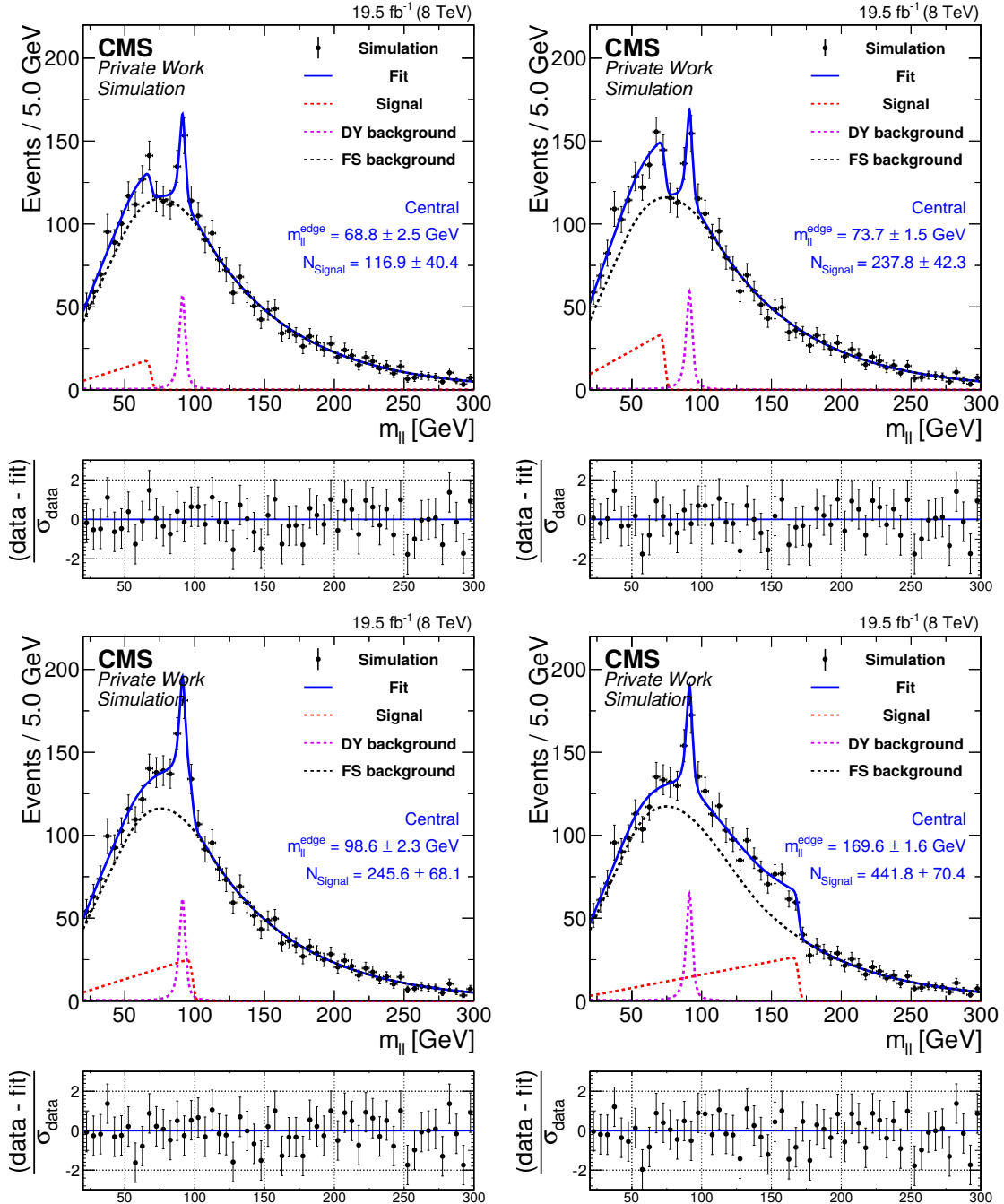


Figure 7.6: Fit results in the central signal region for the signal point from the fixed-edge model S1 (top left) and the three points from the slepton-edge model S2 (top right), S3 (bottom left), and S4 (bottom right). The combined fit is shown as a solid blue line, while the flavour-symmetric and Z backgrounds are shown as black and violet dashed lines. The signal model is shown as a red dashed line.

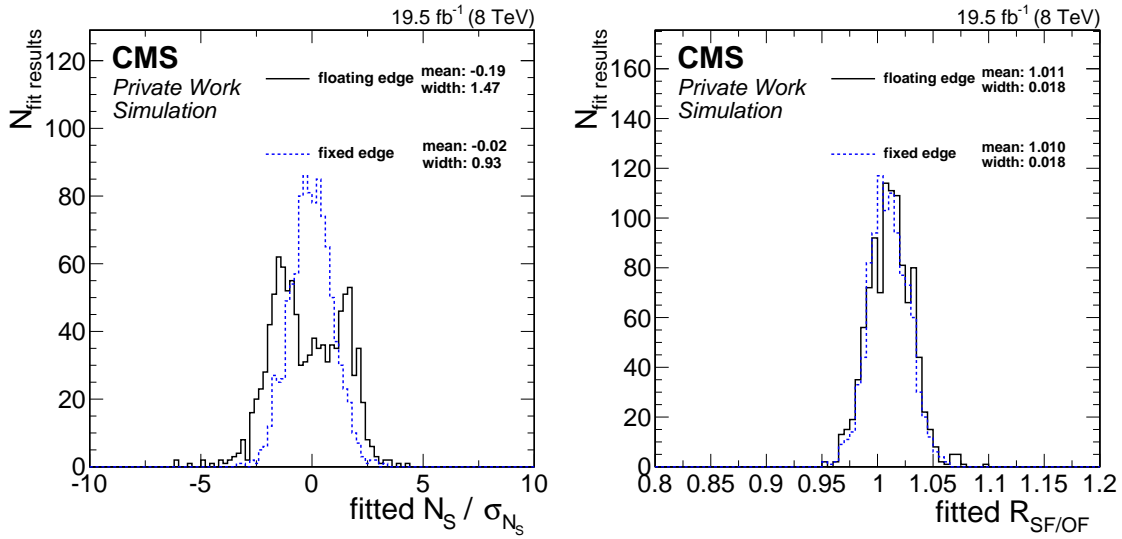


Figure 7.7: Distribution of fit observables in toy studies for a background only scenario. Shown are the fitted number of signal events divided by their uncertainty in the central region (left) and the corresponding fitted values of $R_{SF/OF}$ (right). The results for a floating edge are shown in black and those for a fixed edge position in blue.

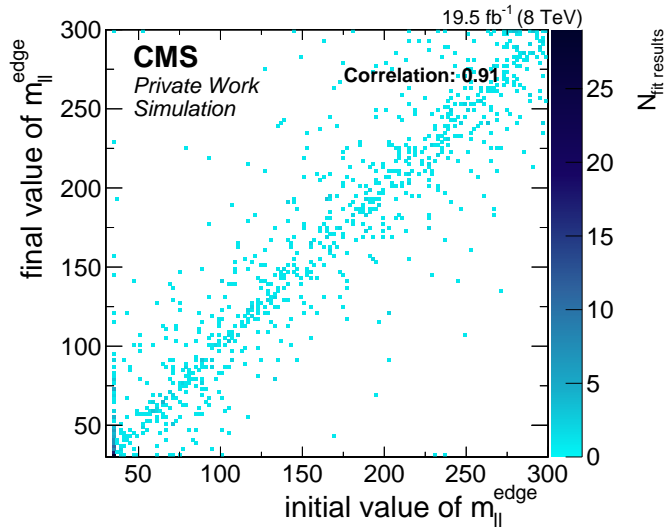


Figure 7.8: Distribution of fitted versus initial values of $m_{\ell\ell}^{\text{edge}}$ in the case of the randomised initial values for toys without an injected signal.

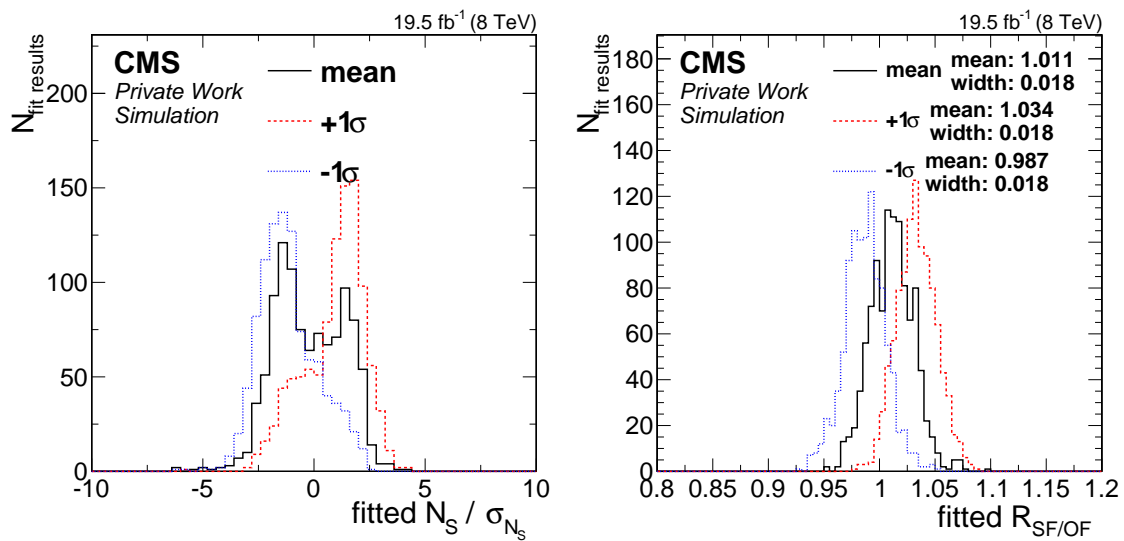


Figure 7.9: Distribution of fit observables in toy studies for background only toys with and without systematically shifted $R_{SF/OF}$ in the generation of the toys. Shown are the fitted number of signal events divided by its uncertainty in the central region (left) and the fitted value of $R_{SF/OF}$ (right) in the signal region.

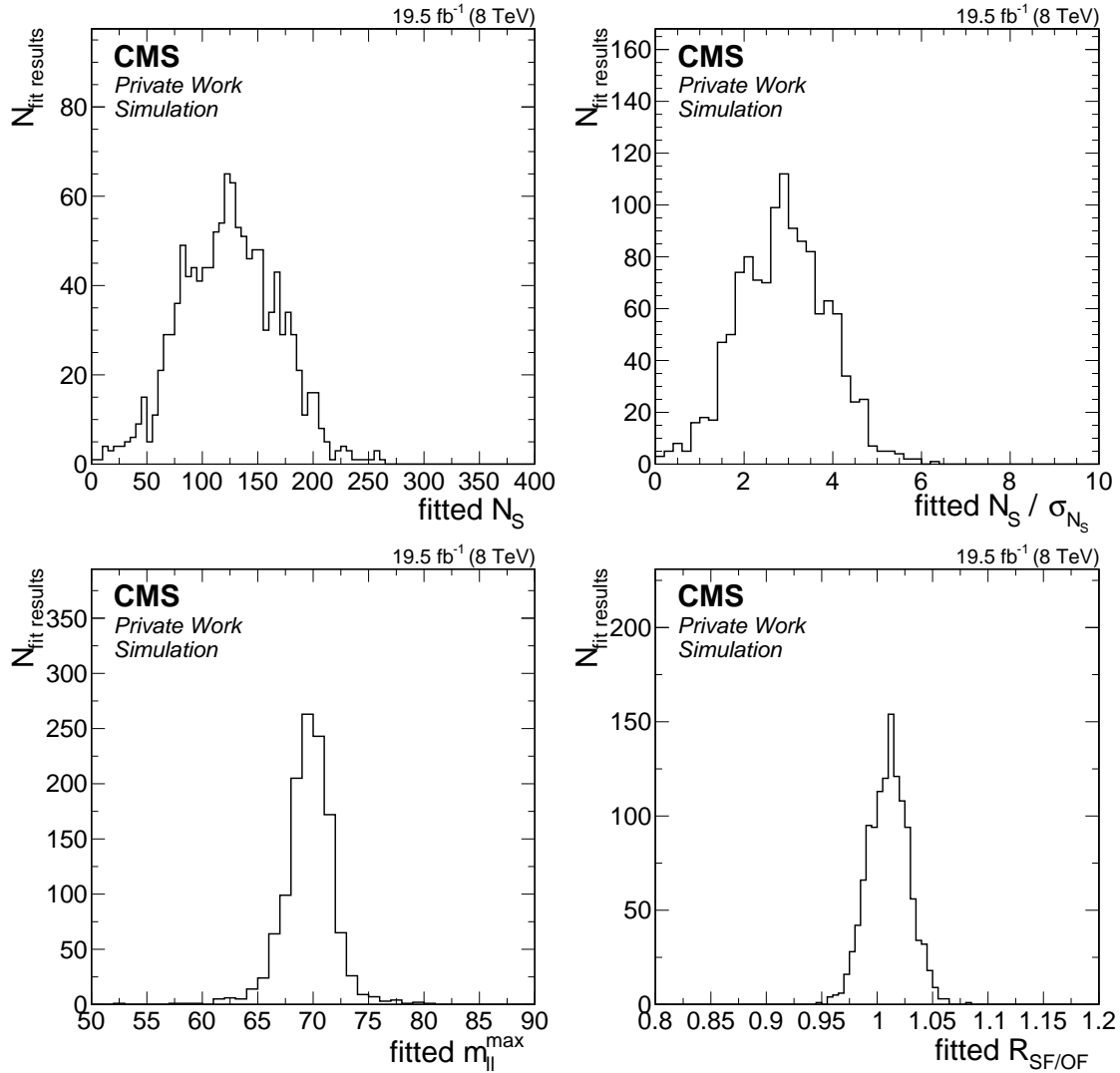


Figure 7.10: Distribution of fit observables in toy studies with a signal injected. Shown are the fitted number of signal events in the central region (upper left), the fitted number of signal events divided by the fitted uncertainty in the central region (upper right), the fitted edge position (lower left) and the fitted $R_{\text{SF/OF}}$ in the central region (lower right).

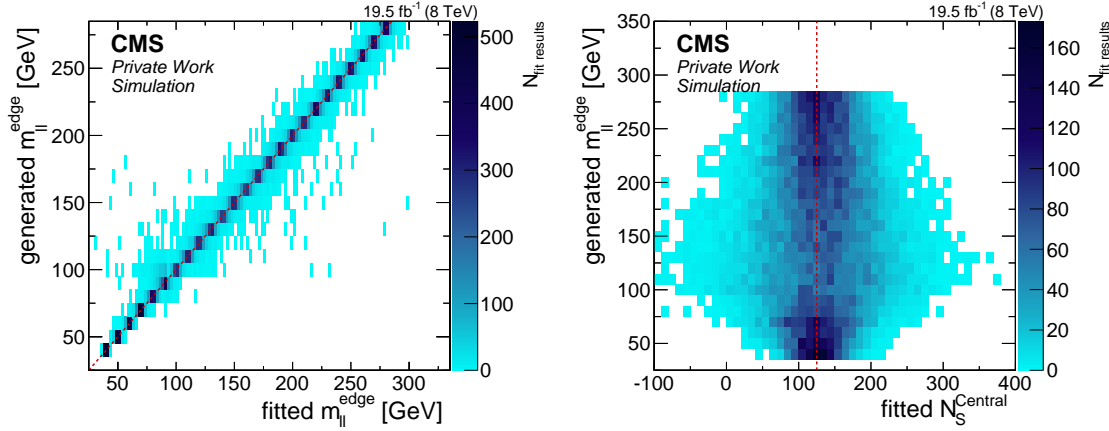


Figure 7.11: Distributions of the fitted $m_{\ell\ell}^{\text{edge}}$ (left) and the number of signal events (right) for each generated $m_{\ell\ell}^{\text{edge}}$. The frequency of the results is colour-coded, darker colours indicating higher values. The dashed red lines indicate the points at which the fitted result matches the generated value.

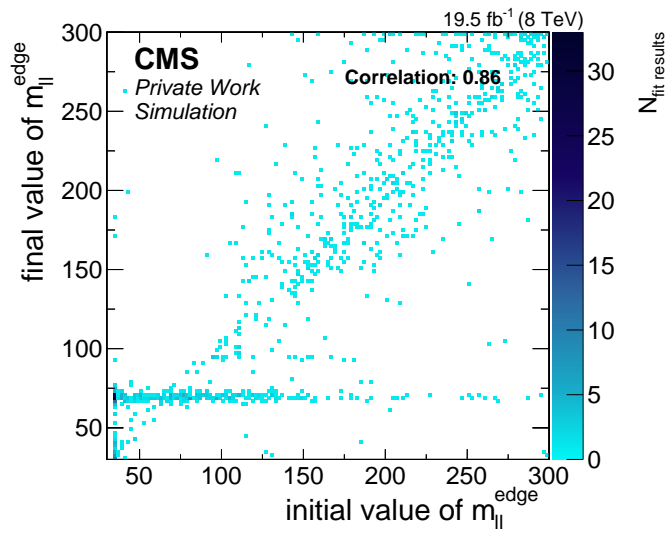


Figure 7.12: Distribution of fitted versus initial values of $m_{\ell\ell}^{\text{edge}}$ in the case of the randomised initial values for toys with an injected signal at $m_{\ell\ell}^{\text{edge}} = 70 \text{ GeV}$.

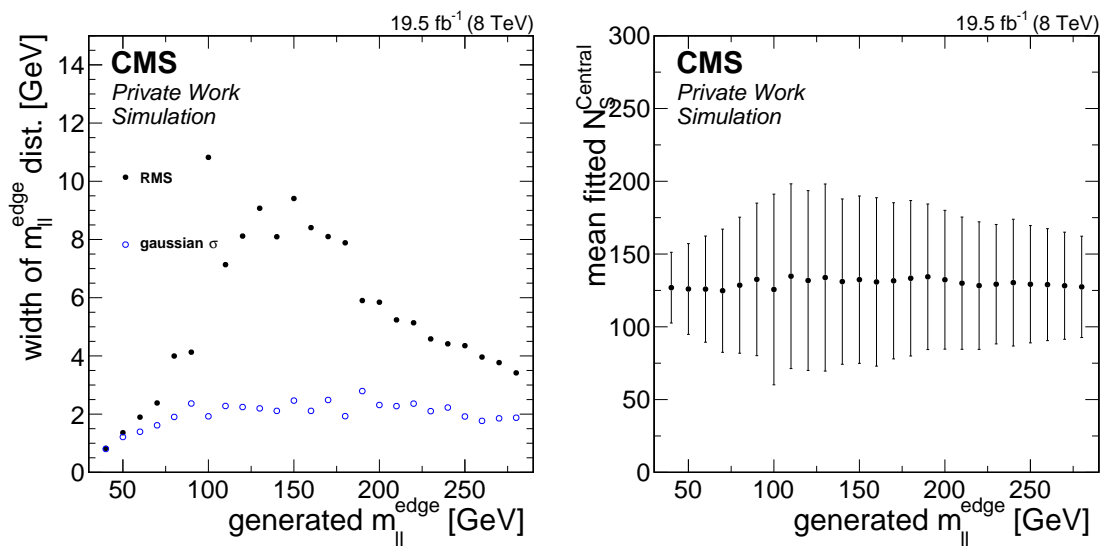


Figure 7.13: Fitted idths of the $m_{\ell\ell}^{edge}$ (left) and means and widths $N_S^{central}$ distributions (right) as a function of the generated $m_{\ell\ell}^{edge}$.

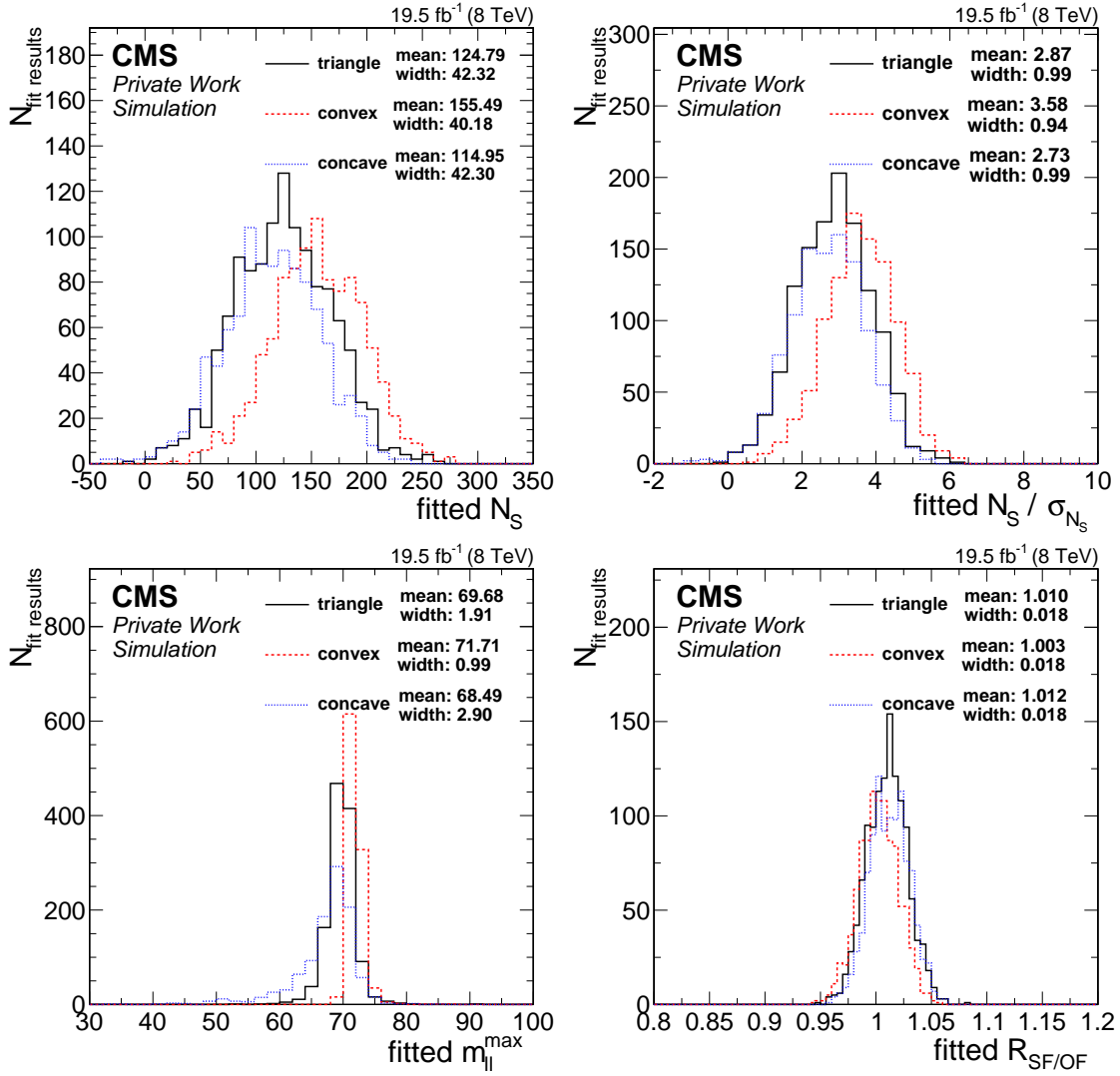


Figure 7.14: Distribution of fit observables in toy studies with signals following different distributions. Toys are generated using the nominal (black) as well as the concave (red) and convex (blue) signal shape. Shown are the fitted number of signal events in the central region (upper left), the fitted number of signal events divided by the fitted uncertainty in the central region (upper right), the fitted edge position (lower left), and the fitted $R_{SF/OF}$ in the central region (lower right).

7.4 Fit results on data

The result of the fit performed in the signal region on data is shown in Figure 7.15. Shown are the $m_{\ell\ell}$ distributions in the SF and OF channels for the central and forward dilepton selection. The quantitative results are shown in Table 7.8. Similar to the counting experiment, an excess of events is observed below the Z boson peak in the central signal region. The best fit value for the position of an edge is found to be 82.4 GeV, with a signal yield of 140 ± 43 events. No significant contribution of a signal is found in the forward region, where the fitted signal yield is 1 ± 22 events. In the central region the fitted value of $R_{SF/OF}$ is slightly larger than the initial value, indicating that the fit absorbs some fraction of the excess into the background prediction. However, the difference is small compared to the fitted uncertainty and the uncertainty on the predicted value. In the forward region, the fitted value is smaller than the initial value, but also this deviation is well within the uncertainties.

Table 7.8: Results of the fit in search for a kinematic edge in the signal region.

	Central	Forward
Drell–Yan background	170 ± 23	55 ± 15
Flav. Sym. background in OF	2293 ± 45	792 ± 25
$R_{SF/OF}$	1.024 ± 0.027	1.012 ± 0.042
signal events	140 ± 44	2 ± 22
$m_{\ell\ell}^{edge}$ [GeV]		$82.4^{+2.1}_{-3.3}$
local significance [σ]		2.5

A scan of the log-likelihood as a function of the edge position $m_{\ell\ell}^{edge}$ is shown in Figure 7.16. The values have been shifted to set the minimum to zero. The curve exhibits a sharp drop at the best fit value for $m_{\ell\ell}^{edge}$, which is indeed the global minimum over the considered mass range.

The local fit significance is calculated applying Wilk's Theorem [115], which states that the distribution of $-2(\log(L_1) - \log(L_0))$ ($-2\Delta(\log(L))$ in short) is distributed as a χ^2 distribution with n degrees of freedom, where n is the number of free parameters of the signal model and L_0 and L_1 are the likelihood values of the background only and the signal plus background hypothesis. The p-Value of a result can be obtained by simply integrating this χ^2 distribution for values larger than the one observed in data. However, Wilk's Theorem does not hold in cases where one parameter of the signal model is not defined in the background only model. This is the case for signal models including the position of a bump, or in this case an edge, as a free parameter.

The applicability of Wilk's theorem is demonstrated using the toy fits described in Section 7.3.2. They can also be used to calculate the significance directly and are also able to provide global results. Considered are toy dataset without signal injection. The fits are performed both with a floating edge position and fixed $m_{\ell\ell}^{edge}$. Figure 7.17 shows the resulting distributions of $-2\Delta(\log(L))$ for both scenarios. The χ^2 distributions for two and three degrees of freedom are shown for illustration. In the case of the fixed edge the results of the fits follow the distribution for two degrees of freedom, as expected from the presence of the free parameters

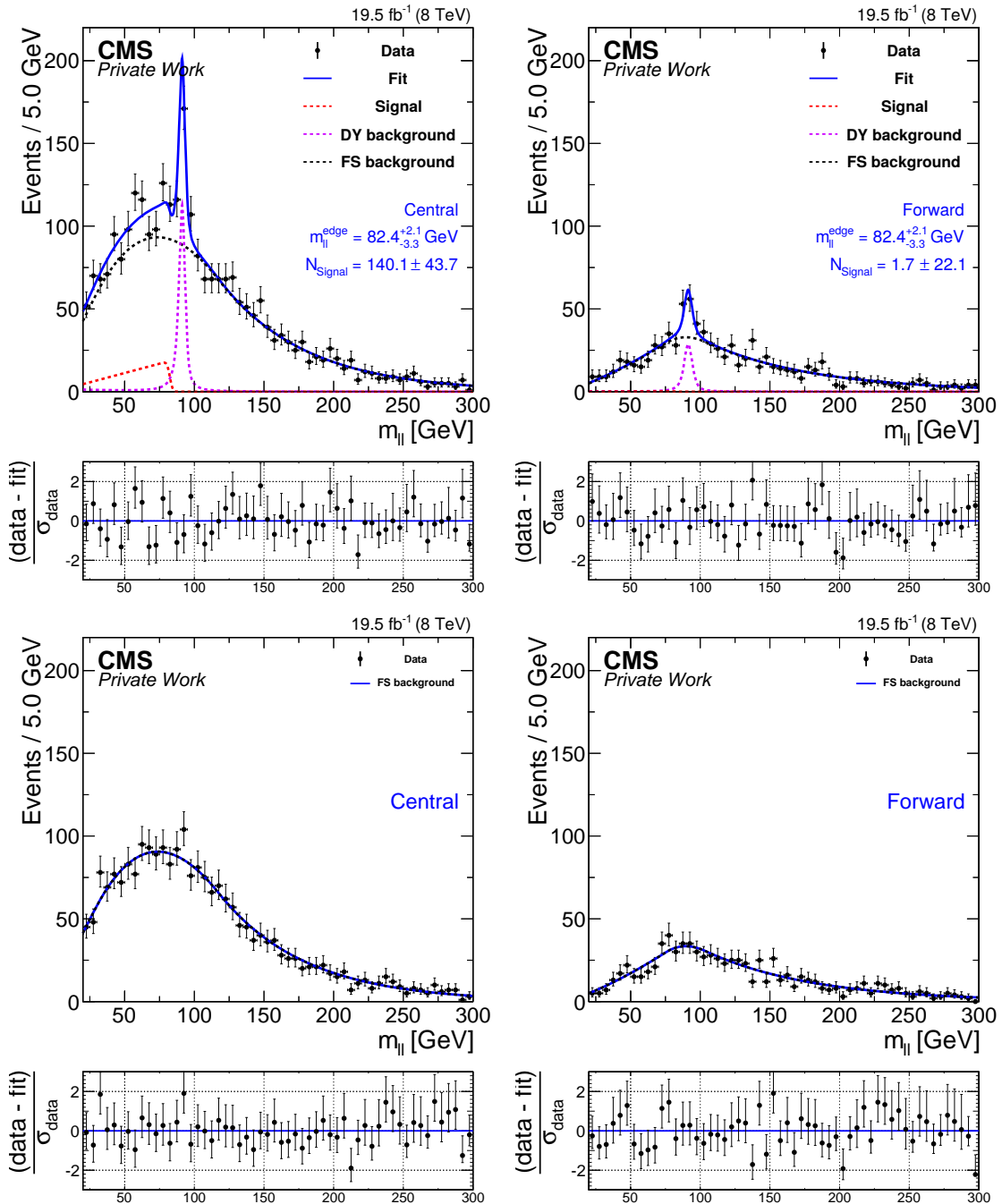


Figure 7.15: Fit results in the signal region. Shown are the m_{ll} distributions in SF (top) and OF (bottom) events for the central (right) and forward (left) dilepton selection. The fit is shown as a solid blue line while the different components are shown as dashed line, the signal model in red, the Drell–Yan model in violet, and the flavour-symmetric model in black.

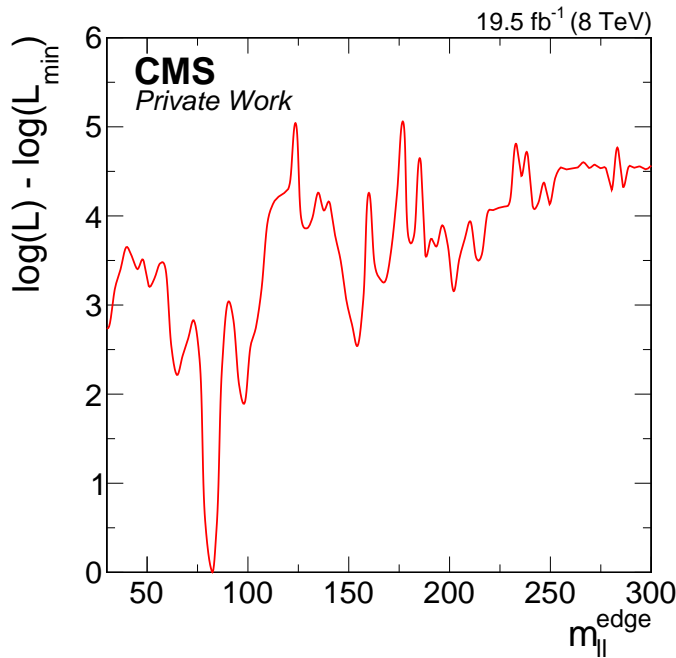


Figure 7.16: Scan of the observed log-likelihood in the signal region subtracted by the minimal value as a function of $m_{\ell\ell}^{\text{edge}}$.

N_S^{central} and N_S^{forward} . This proves the applicability of Wilk's theorem in this case. The floating edge position, however, clearly does not simply act as an additional degree of freedom as the distribution of the toy results is shifted to higher values of $-2\Delta(\log(L))$, indicating that Wilk's theorem does indeed not hold for this type of models. The p-Value of the fit result is in both cases given by the fraction of results for which $-2\Delta(\log(L))$ exceeds the one observed on data. The result for a fixed edge can then be interpreted as a local p-Value while the one for a floating edge gives a global p-Value taking into account the so called “Look-elsewhere-effect” [116]. However, as the signal yield is allowed to be negative, the resulting p-Values have to be reduced by a factor of two to take into account that we only consider positive signals to have physical meaning [116]. This corrected p-Value is translated into a significance interpreting it as the one-sided tail probability of a unit Gaussian. The resulting uncorrected p-Values are $0.012^{+0.004}_{-0.003}$, corresponding to 2.5σ , in the local and $0.091^{+0.009}_{-0.009}$, corresponding to 1.7σ , in the global case.

As the applicability of Wilk's theorem has been established for the case of fixed edge positions, local p-Values and significances can be calculated analytically from the χ^2 function for two degrees of freedom. The p-Value is defined as the integral of the function above the value of $-2\Delta(\log(L))$ observed on data for a fit performed with fixed edge position. Performing such a fit on data with $m_{\ell\ell}^{\text{edge}}$ set to the observed value, this results in a p-Value of 0.014, corresponding to a significance of 2.5σ . This is well compatible with the result observed using toy datasets. The local significances reported in Table 7.8 and those discussed in the following are calculated using the analytical calculation as it is much faster and not affected by statistical uncertainties. Also, the toys have the small caveat that a different background shape than in the nominal fit is used.

As further validation of the result on data, the results obtained with different parametrisations

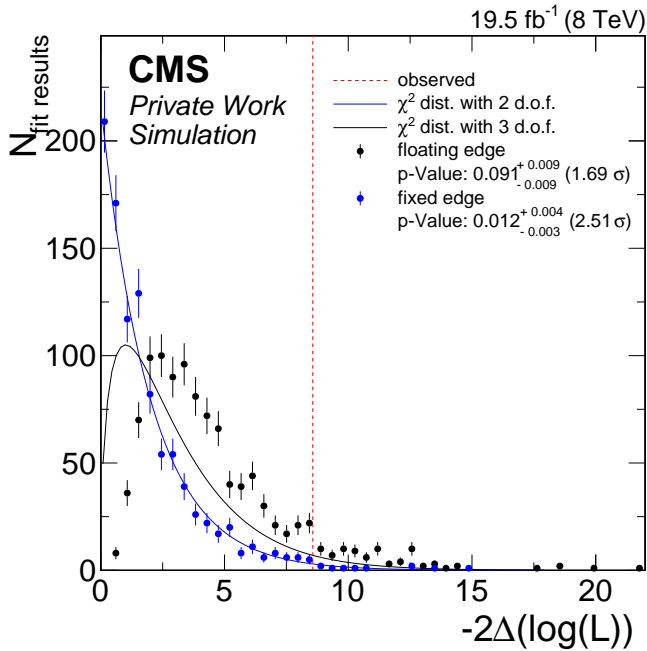


Figure 7.17: Calculation of the fit significance using background only toy datasets. Shown are the distribution of $-2\Delta(\log(L))$ for fits with floating (black) and fixed (blue) edge position. Also shown are χ^2 distributions for two (blue) and three (black) degrees of freedoms. The dashed red line indicates the value of $-2\Delta(\log(L))$ observed on data in case of a floating edge.

of the flavour-symmetric background are compared to the nominal result in Table 7.9. In each case first a fit has been performed with a floating edge position to find the best value for $m_{\ell\ell}^{\text{edge}}$ followed by a fit with a fixed edge at that position to calculate the local significance. For the sake of clarity, only yields in the central signal region are shown. However, similar agreement is observed in the forward signal region. In general, there is good agreement between all considered parametrisations. The best agreement is seen in the number of fitted flavour-symmetric events in the OF sample, which is expected as here the fit is most simple, consisting only of the shape for flavour-symmetric backgrounds. Good agreement is also observed for $m_{\ell\ell}^{\text{edge}}$ and the number of signal events, which are stable against the choice of background model. The largest differences are observed for $R_{\text{SF}/\text{OF}}$ and the yield of the Drell-Yan model, which the fit can trade off against each other, depending on the parametrisation of the flavour-symmetric background. Here, the largest deviations are observed for the shape used in the analysis of the 7 TeV dataset. As this shape is known to not satisfactorily describe the flavour-symmetric background, it is encouraging to see that the fit result is stable against such biases. The observed local significance is very similar among all analytical parametrisations. In the case of the KDE and the binned parametrisation, the shape of the distribution is not free in the fit, as discussed above, excluding the statistical uncertainty of the OF sample from the fit and resulting in a systematically larger local significance.

To compare the fit result with that of the counting experiment, the fitted event yields in the low-mass region for central dilepton events have been derived. They are shown in Table 7.10, together with the background predictions and the observed yield of the counting experiment in that region. Also, the fitted yield for Drell-Yan backgrounds in the on-Z region is compared to

Table 7.9: Comparison of edge fit results in the signal region for different parametrisations of the flavour-symmetric background. Results are given for the central signal region only. Similar agreement between the parametrisations is also observed in the forward signal region.

	N_{DY}	N_{FS}	$R_{SF/OF}$	N_S	$m_{\ell\ell}^{edge}$ [GeV]	local σ
nominal	170 ± 23	2293 ± 45	1.024 ± 0.027	140 ± 43	$82.4^{+2.1}_{-3.3}$	2.5
sum of Gaussians	168 ± 24	2292 ± 44	1.023 ± 0.027	146 ± 50	$82.1^{+2.2}_{-3.7}$	2.7
kernel density estimation	154 ± 22	2296 ± 43	1.028 ± 0.026	141 ± 41	$81.7^{+2.3}_{-3.4}$	3.1
histogram	140 ± 23	2296 ± 43	1.029 ± 0.026	153 ± 41	$83.0^{+1.7}_{-2.4}$	3.5
2011 shape	181 ± 23	2290 ± 43	1.020 ± 0.026	146 ± 46	$82.8^{+1.9}_{-2.5}$	2.7

the prediction. The fitted yield exceeds that of the prediction by 26 events, a difference that is well covered by the uncertainties of the fit and the prediction. In the low-mass region good agreement between counting experiment and fit is observed, also. The Drell–Yan background is again fitted higher than expected from the prediction, as the ratio between the off-shell component and the peak is fixed and the normalisation of this model is determined dominantly on the Z boson peak. In the fit the contribution of flavour-symmetric backgrounds is increased, caused by the increased value of $R_{SF/OF}$. This is reflected in a signal yield that is lower by 11 events. For all considered components the use of shape information has allowed for reduced uncertainties on the event yields, most notably on the yield for flavour-symmetric backgrounds.

Table 7.10: Comparison of the fit result and the result of the counting experiment in the low mass region for central leptons. The probability density functions contributing to the fit model are integrated in the region $20 < m_{\ell\ell} < 70$ GeV to obtain the fitted yields in this interval. Also, the yield in the on-Z region is calculated and compared to the prediction.

	Fit	Counting experiment
on-Z region		
Drell–Yan background	145 ± 19	119 ± 21
low-mass region		
Drell–Yan background	10 ± 1	8 ± 2
Flav. Sym. background	760 ± 14	746 ± 37
signal events	98 ± 30	109 ± 48

8 Conclusion

In this thesis a search for supersymmetry in final states with two same-flavour opposite-sign leptons, using full dataset of proton-proton collisions recorded by the CMS in 2012, corresponding to 19.5 fb^{-1} , has been presented. The analysis has focused on the correlated production of leptons in the decay of a neutralino, resulting in a distinct edge structure in the distribution of the invariant mass of the lepton pairs.

The characteristic signature of the strong production of supersymmetric particles in R-parity conserving models, namely the presence of hadronic jets and missing transverse energy, has been exploited to separate a potential signal from the Standard Model backgrounds. The contributions of Standard Model processes to the thereby defined event selection have been estimated exclusively from the data itself. The most dominant backgrounds are symmetric in the production of same-flavour and opposite flavour lepton pairs. Therefore, the estimates for these backgrounds have been derived from the opposite-flavour event sample. Corrections for efficiency effects were derived using two independent methods and taken into account in these estimates, for which a precision of 5-10% have been achieved. The validity of this approach has been established using both data and simulated events.

In search of edges in the dilepton mass distribution, shape information have been used by performing an unbinned maximum likelihood fit to both the same-flavour and opposite-flavour event samples. The fit consists of parametrisations for flavour-symmetric and Drell-Yan background and a triangular signal model. The best fit is found including a signal contribution with an endpoint of the signal shape of $82.4^{+2.1}_{-3.3} \text{ GeV}$ and signal yields of 140 ± 44 events for events where both leptons are reconstructed in the central part of the CMS detector and 2 ± 22 events for events where at least one of the leptons is located in the one of the endcaps. The observed effect corresponds to a local significance of 2.5σ , which reduces to 1.7σ if the probability to observe an equal or large effect anywhere in the considered mass range is taken into account.

In a second approach event yields are compared to the background estimates in six regions of dilepton mass and lepton pseudorapidity. They are found to be consistent with each other except in the mass range $20 \text{ GeV} < m_{\ell\ell} < 70 \text{ GeV}$, where an excess of 109 ± 48 events is observed, corresponding to a local significance of 2.2σ . The results of this approach are found to be consistent with the fit.

The properties of the events in the excess differ not significantly from those of the backgrounds. No systematic effects responsible for the observation have been found. The development of the effect over time shows that it is only present in roughly the first half of the recorded data.

As no clear hint for the presence of supersymmetry has been observed, exclusion limits are set in two simplified models which simulate the pair production of bottom squarks. These models contain the decay $\tilde{\chi}_2^0 \rightarrow \tilde{\chi}_1^0 \ell\ell$ either via an off-shell Z boson (fixed-edge model) or via both sleptons or on- and off-shell Z bosons (slepton-edge model). In the first model, \tilde{b} masses up to 375 GeV have been excluded, depending on the mass of the $\tilde{\chi}_2^0$. In the second model, in which the branching ratio into lepton pairs is much higher, the limit ranges from 470 GeV to

590 GeV, again depending on $m_{\tilde{\chi}_2^0}$.

At the time of writing this thesis, the Large Hadron Collider has begun the commissioning of the machine for the next run at an increased centre-of-mass energy of 13 TeV. After two years of shut-down, new data is eagerly awaited and preparations are ongoing for the analysis of the new dataset. The expected integrated luminosity for 2015 of about 10 fb^{-1} will probably not be sufficient to reach the same sensitivity of the analysis presented here. Nevertheless it is expected to provide an indication if the observed excess in the 2012 dataset might have been a first hint of a signal for new physics after all.

A Trigger paths

An overview of the dilepton trigger paths used in the analysis is given in Table A.1. Shown are the names of the HLT paths and the underlying L1 trigger requirements. Numbers indicate thresholds in GeV, while Open indicates a threshold of 0 GeV. Auxiliary trigger used in the analysis are shown in Table A.2.

Table A.1: Dilepton HLT paths used in this analysis.

$\ell\ell$	L1 seed	HLT path
ee	L1_DoubleEG_13_7	HLT_Ele17_CaloIdT_CaloIsoVL_TrkIdVL_TrkIsoVL_Ele8_CaloIdT_CaloIsoVL_TrkIdVL_TrkIsoVL
$\mu\mu$	L1_DoubleMu_10_Open L1_DoubleMu_10_3p5	HLT_Mu17_Mu8 or HLT_Mu17_TkMu8
$e\mu$	L1_Mu3p5_EG12 L1_MuOpen_EG12 L1_Mu12_EG7	HLT_Mu8_Ele17_CaloIdT_CaloIsoVL_TrkIdVL_TrkIsoVL HLT_Mu17_Ele8_CaloIdT_CaloIsoVL_TrkIdVL_TrkIsoVL

Table A.2: Auxiliary HLT paths used in this analysis. In the case of the α_T triggers, for each H_T threshold a set of triggers with different requirements on the α_T variable exists.

	object	HLT path
Single lepton	ee	HLT_Ele27_WP80
	$\mu\mu$	HLT_IsoMu24
Trigger efficiencies	H_T	HLT_PFNopUHT650 HLT_PFNopUHT700 HLT_PFNopUHT750 HLT_PFHT650 HLT_PFHT700 HLT_PFHT750 HLT_HT200_AlphaT* HLT_HT250_AlphaT* HLT_HT300_AlphaT* HLT_HT350_AlphaT* HLT_HT400_AlphaT* HLT_HT450_AlphaT*
Non-prompt studies	μ	HLT_Mu17 HLT_Mu8
	e	HLT_Ele17_CaloIdT_CaloIsoVL_TrkIdVL_TrkIsoVL_Jet30 HLT_Ele17_CaloIdT_CaloIsoVL_TrkIdVL_TrkIsoVL HLT_Ele8_CaloIdT_CaloIsoVL_TrkIdVL_TrkIsoVL_Jet30 HLT_Ele8_CaloIdT_CaloIsoVL_TrkIdVL_TrkIsoVL

B Simulated Samples

The list of a simulated samples of SM background processes is shown in Table B.1. Given is the physics process together with relevant information about the simulated decays or generator selections. Also the name of the dataset in DBS is given. Example DBS entries for the fixed-edge and slepton-edge simplified models are given in Table B.2 for the points with the lowest masses in both models. The names of all other points can be constructed by replacing the masses in examples given in the Table.

Table B.1: List of background processes and the corresponding samples in DBS.

process	sample
$t\bar{t} \rightarrow b\bar{b}\ell\nu\ell\nu$	/TTJets_FullLeptMGDecays_8TeV-madgraph-tauola/*_V7C-v2/AODSIM
$t\bar{t} \rightarrow b\bar{b}q\bar{q}\ell\nu$	/TTJets_SemiLeptMGDecays_8TeV-madgraph-tauola/*_V7C-v1/AODSIM
$t\bar{t} \rightarrow b\bar{b}q\bar{q}q\bar{q}$	/TTJets_HadronicMGDecays_8TeV-madgraph/*_V7A_ext-v1/AODSIM
$Z/\gamma^* \rightarrow \ell\ell$ $10 \text{ GeV} < m_{\ell\ell} < 50 \text{ GeV}$	/DYJetsToLL_M-10To50filter_8TeV-madgraph/*_V7A-v1/AODSIM
$Z/\gamma^* \rightarrow \ell\ell$ $m_{\ell\ell} > 50 \text{ GeV}$	/DYJetsToLL_M-50_TuneZ2Star_8TeV-madgraph-tarball/*_V7A-v1/AODSIM
$W \rightarrow \ell\nu$	/WJetsToLNu_TuneZ2Star_8TeV-madgraph-tarball/*_V7A-v2/AODSIM
$ZZ \rightarrow \ell\ell q\bar{q}$	/ZZJetsTo2L2Q_TuneZ2star_8TeV-madgraph-tauola/*_V7A-v1/AODSIM
$ZZ \rightarrow \ell\ell\nu\nu$	/ZZJetsTo2L2Nu_TuneZ2star_8TeV-madgraph-tauola/*_V7A-v3/AODSIM
$ZZ \rightarrow \ell\ell\ell\ell$	/ZZJetsTo4L_TuneZ2star_8TeV-madgraph-tauola/*_V7A-v1/AODSIM
$WZ \rightarrow \ell\nu\ell\ell$	/WZJetsTo3LNu_TuneZ2_8TeV-madgraph-tauola/*_V7A-v1/AODSIM
$WZ \rightarrow q\bar{q}\ell\ell$	/WZJetsTo2L2Q_TuneZ2star_8TeV-madgraph-tauola/*_V7A-v1/AODSIM
$WW \rightarrow \ell\nu\ell\nu$	/WWJetsTo2L2Nu_TuneZ2star_8TeV-madgraph-tauola/*_V7A-v1/AODSIM
t s-Channel	/T_s-channel_TuneZ2star_8TeV-powheg-tauola/*_V7A-v1/AODSIM
t t-Channel	/T_t-channel_TuneZ2star_8TeV-powheg-tauola/*_V7A-v1/AODSIM
t tW-Channel	/T_tW-channel-DR_TuneZ2star_8TeV-powheg-tauola/*_V7A-v1/AODSIM
\bar{t} s-Channel	/Tbar_s-channel_TuneZ2star_8TeV-powheg-tauola/*_V7A-v1/AODSIM
\bar{t} t-Channel	/Tbar_t-channel_TuneZ2star_8TeV-powheg-tauola/*_V7A-v1/AODSIM
\bar{t} tW-Channel	/Tbar_tW-channel-DR_TuneZ2star_8TeV-powheg-tauola/*_V7A-v1/AODSIM
WWW	/WWWJets_8TeV-madgraph/*_V7A-v1/AODSIM
$WW\gamma$	/WWGJets_8TeV-madgraph/*_V7A-v1/AODSIM
WWZ	/WWZNuGstarJets_8TeV-madgraph/*_V7A-v1/AODSIM
WZZ	/WWZNuGstarJets_8TeV-madgraph/*_V7A-v1/AODSIM
$t\bar{t}\gamma$	/TTGJets_8TeV-madgraph/*_V7A-v1/AODSIM
$t\bar{t}W$	/TTWJets_8TeV-madgraph/*_V7A-v1/AODSIM
$t\bar{t}Z$	/TTZJets_8TeV-madgraph_v2/*_V7A-v1/AODSIM
$t\bar{t}WW$	/TTWWJets_8TeV-madgraph/*_V7A-v1/AODSIM
$t\bar{t}$	/TTJets_MassiveBinDECAY_TuneZ2star_8TeV-madgraph-tauola/*_V7A-v1/AODSIM
$t\bar{t}, m_{top} = 166.5 \text{ GeV}$	/TTJets_mass166_5_TuneZ2star_8TeV-madgraph-tauola/*_V7A-v1/AODSIM
$t\bar{t}, m_{top} = 169.5 \text{ GeV}$	/TTJets_mass169_5_TuneZ2star_8TeV-madgraph-tauola/*_V7A-v1/AODSIM
$t\bar{t}, m_{top} = 175.5 \text{ GeV}$	/TTJets_mass175_5_TuneZ2star_8TeV-madgraph-tauola/*_V7A-v1/AODSIM
$t\bar{t}, m_{top} = 178.5 \text{ GeV}$	/TTJets_mass178_5_TuneZ2star_8TeV-madgraph-tauola/*_V7A-v1/AODSIM
$t\bar{t}$, Matching scale up	/TTJets_matchingup_TuneZ2star_8TeV-madgraph-tauola/*_V7A-v1/AODSIM
$t\bar{t}$, Matching scale down	/TTJets_matchingdown_TuneZ2star_8TeV-madgraph-tauola/*_V7A-v1/AODSIM
$t\bar{t}$, Factorization scale up	/TTJets_scaleup_TuneZ2star_8TeV-madgraph-tauola/*_V7A-v1/AODSIM
$t\bar{t}$, Factorization scale down	/TTJets_scaledown_TuneZ2star_8TeV-madgraph-tauola/*_V7A-v1/AODSIM
*	Summer12_DR53X-PU_S10_START53

Table B.2: Examples of DBS dataset names for the fixed-edge and slepton-edge simplified models. The three-digit numbers represent the number of \tilde{b} and $\tilde{\chi}_2^0$ in GeV. The names for other mass points are obtained by replacing the values for $m_{\tilde{b}}$ and $m_{\tilde{\chi}_2^0}$ by the desired ones. Exceptions are the sample for $m_{\tilde{b}}$ between 400 GeV and 475 GeV, where the hash `b7ae8e1adb016da4a96f7b394c3a565a` has been replaced by `56193729e3030b18064f6ae9be549394`.

process	sample
fixed-edge example	<code>/SUSY_Simplified_Model_Madgraph_FastSim_T6bbledge_200_100_8TeV/</code> <code>cschomak-SUSY_Simplified_Model_Madgraph_FastSim_T6bbledge_200_100_8TeV</code> <code>-b7ae8e1adb016da4a96f7b394c3a565a/USER</code>
slepton-edge example	<code>/SUSY_Simplified_Model_Madgraph_FastSim_T6bbslepton_200_150_8TeV/</code> <code>cschomak-SUSY_Simplified_Model_Madgraph_FastSim_T6bbslepton_200_150_8TeV-</code> <code>-b7ae8e1adb016da4a96f7b394c3a565a/USER</code>

C Dependencies of $r_{\mu e}$

Several dependency studies for $r_{\mu e}$ in addition to what is presented in Section 5.1.2 are presented here. It can be seen that $r_{\mu e}$ decreases with both increasing leading and trailing lepton p_T (Figure C.1). For the leading lepton, it stabilizes at the central value for $p_T > 45$ GeV, while for the trailing lepton it decreases further, because the effect maximises if both leptons have sizeable p_T . For lepton $|\eta|$, no strong dependence is seen, while for $\Delta R(\ell\ell)$, $r_{\mu e}$ seems to decrease towards smaller values (both Figure C.2). No significant dependencies are observed for H_T and N_{vertex} in Figure C.3.

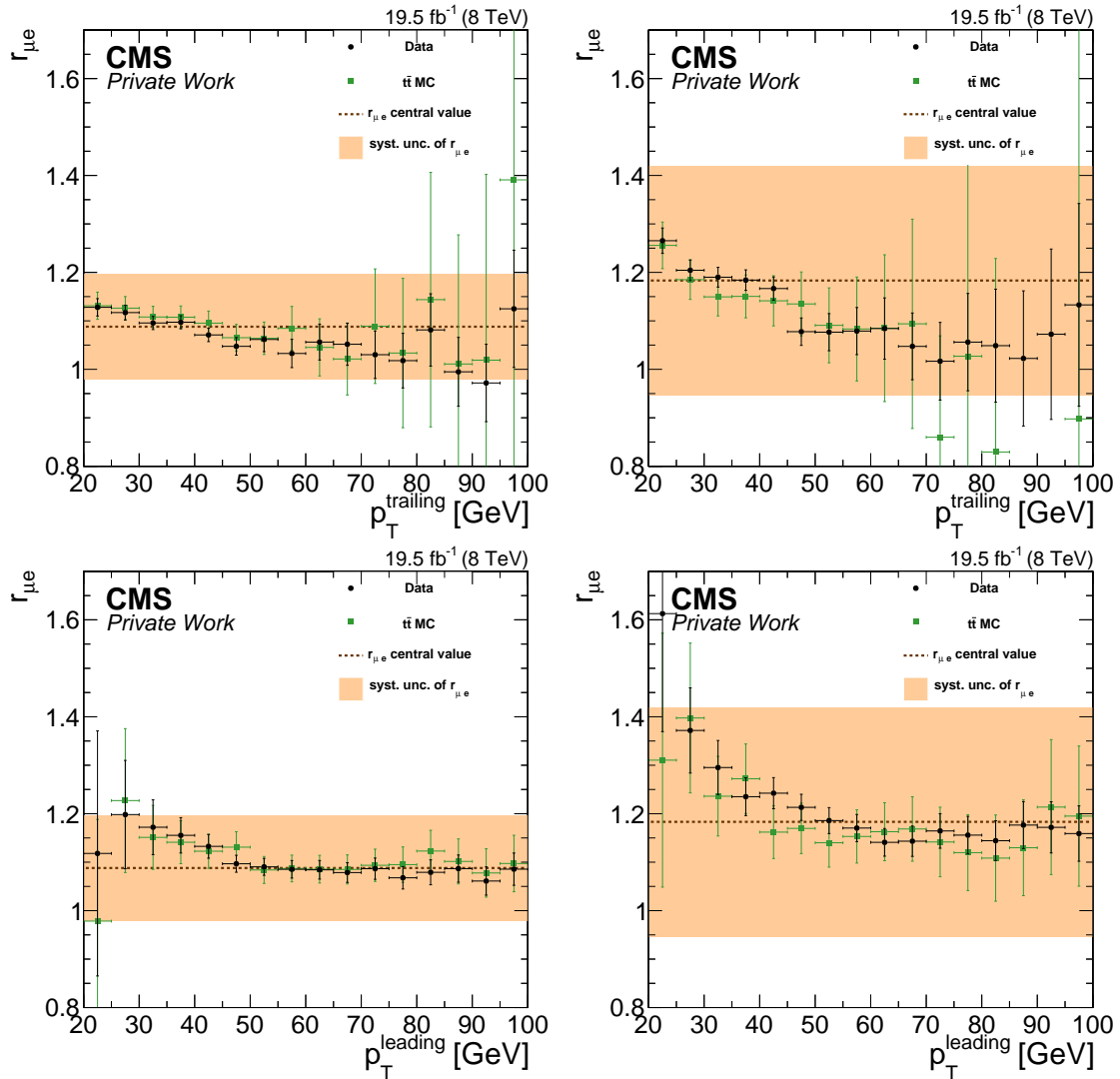


Figure C.1: Dependencies of $r_{\mu e}$ on the p_T of the trailing (top) and the leading (bottom) lepton for the central (left) and forward (right) lepton selection. The results on data are shown in black while $t\bar{t}$ simulation is shown in green. The central value is shown as a brown dashed line while the systematic uncertainty is shown as an orange band.

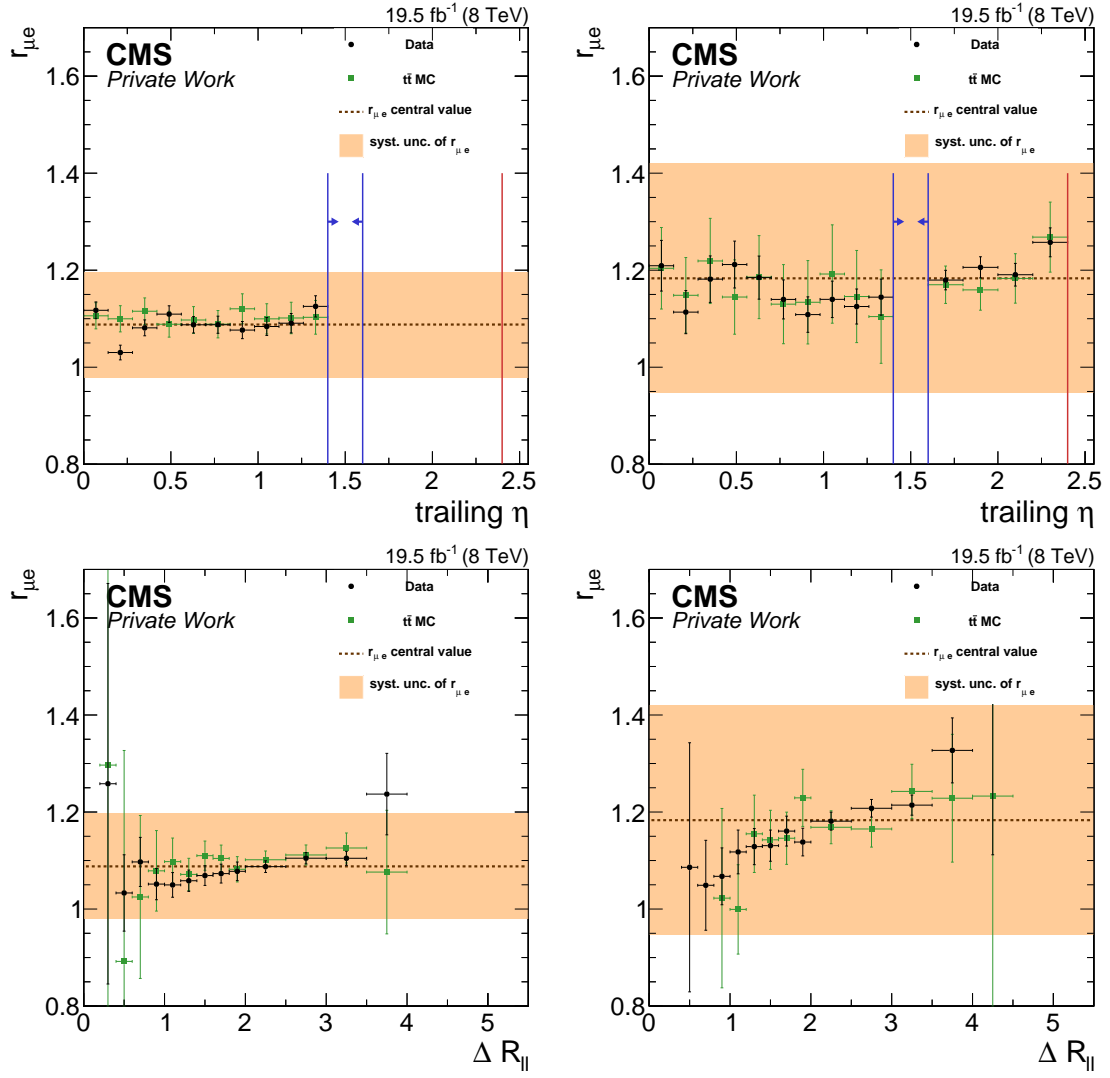


Figure C.2: Dependencies of $r_{\mu e}$ on the $|\eta|$ of the trailing lepton (top) and $\Delta R(\ell\ell)$ (bottom) for the central (left) and forward (right) lepton selection. The results on data are shown in black while $t\bar{t}$ simulation is shown in green. The central value is shown as a brown dashed line while the systematic uncertainty is shown as an orange band.

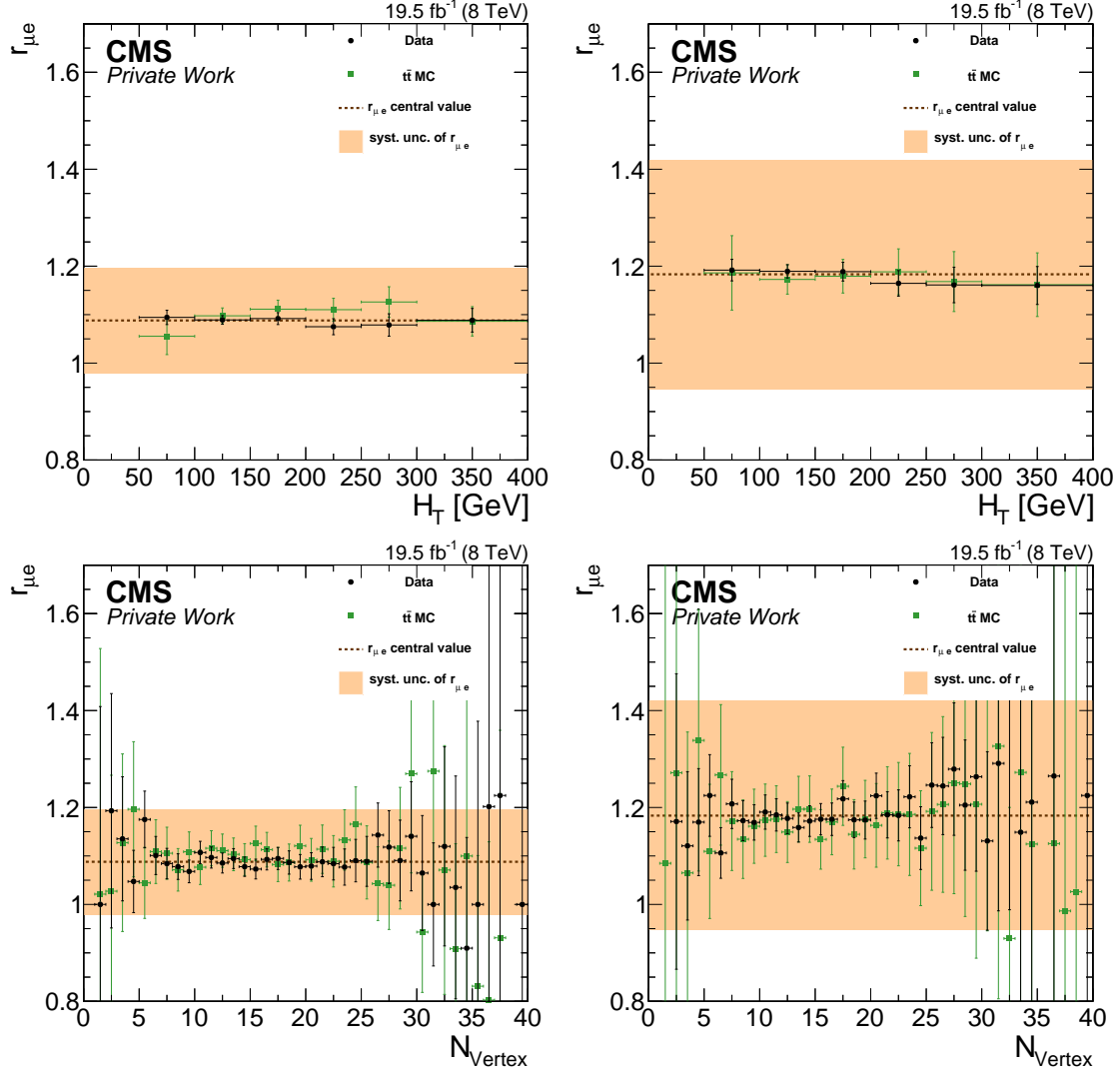


Figure C.3: Dependencies of $r_{\mu e}$ on H_T (top) and N_{vertex} (bottom) for the central (left) and forward (right) lepton selection. The results on data are shown in black while $t\bar{t}$ simulation is shown in green. The central value is shown as a brown dashed line while the systematic uncertainty is shown as an orange band.

D Dependencies of R_T

In Section 5.1.2, the dependency of R_T on $m_{\ell\ell}$, N_{jets} , and E_T^{miss} has been shown. Here, additional dependency plots are given here for the p_T of the leading and trailing lepton (Figure D.1), the $|\eta|$ of the trailing lepton and H_T (Figure D.2), and N_{vertex} in Figure D.3. No significant dependency is observed for either of those variables.

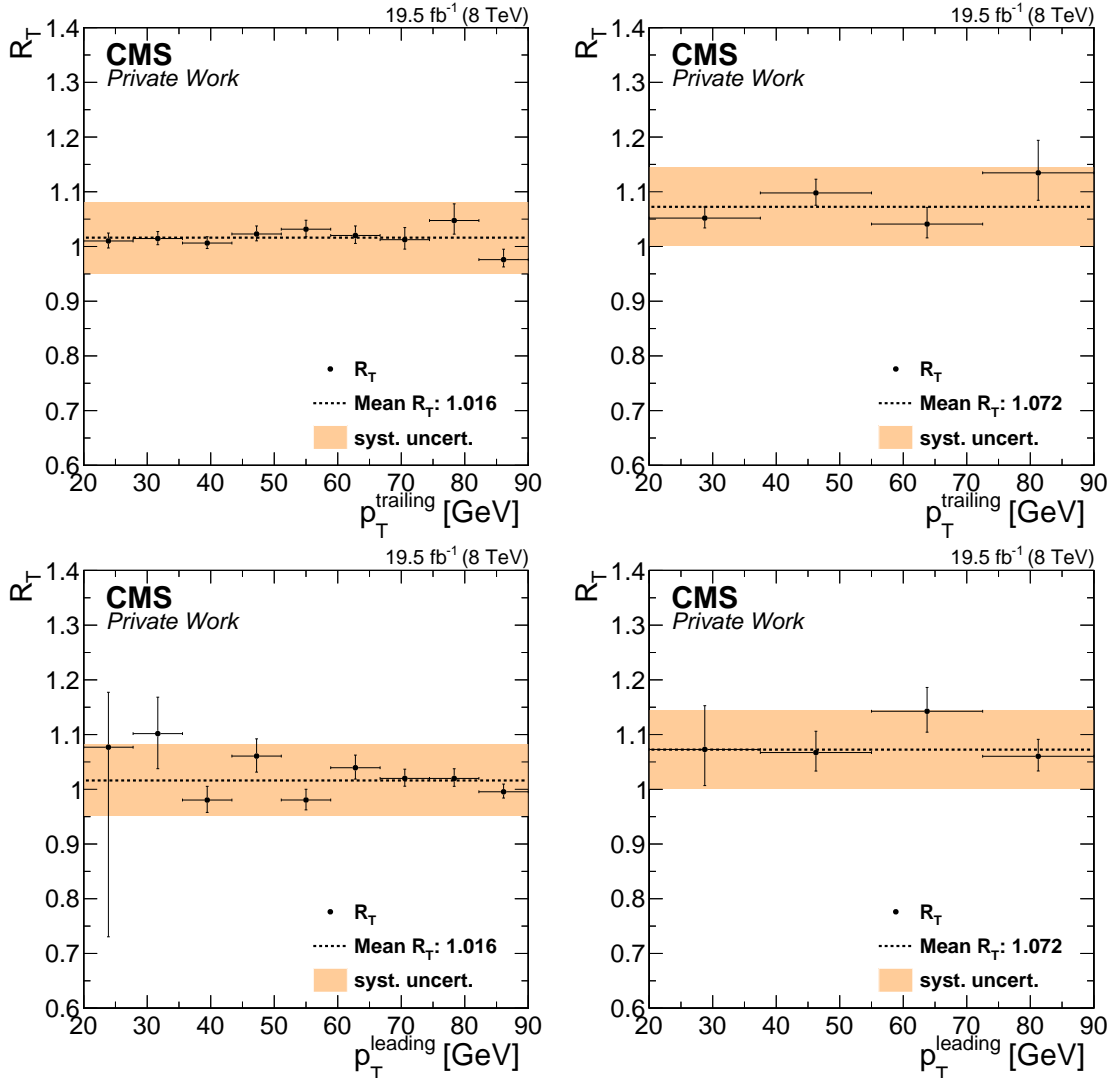


Figure D.1: Dependencies of R_T on leading lepton p_T (top), trailing lepton p_T (bottom) for the central (left) and forward (right) lepton selection. The results on data are shown in black. The central value is shown as a black dashed line while the systematic uncertainty is shown as an orange band.

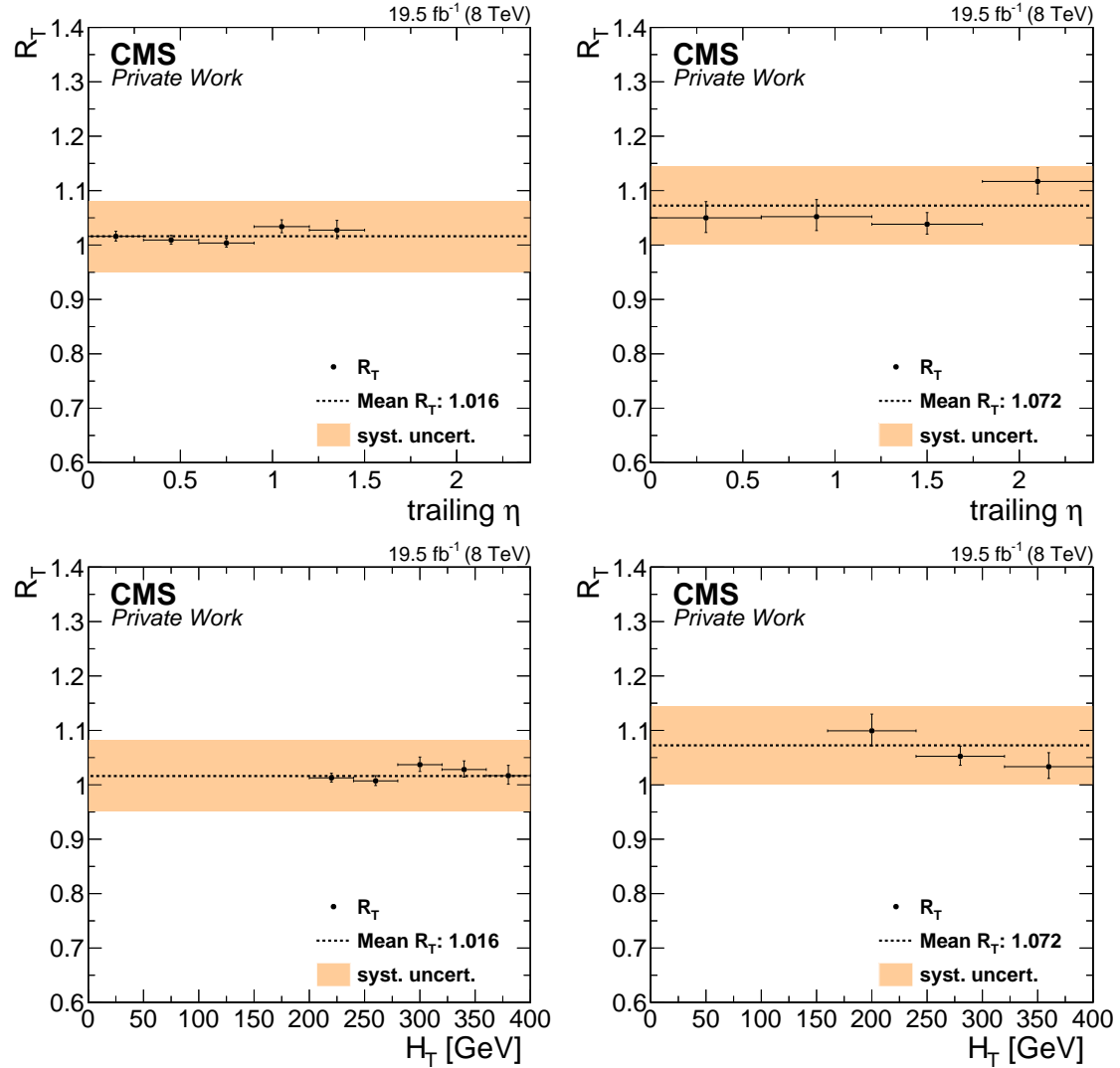


Figure D.2: Dependencies of R_T on the $|\eta|$ of the trailing lepton (top) and H_T (bottom) for the central (left) and forward (right) lepton selection. The results on data are shown in black. The central value is shown as a black dashed line while the systematic uncertainty is shown as an orange band.

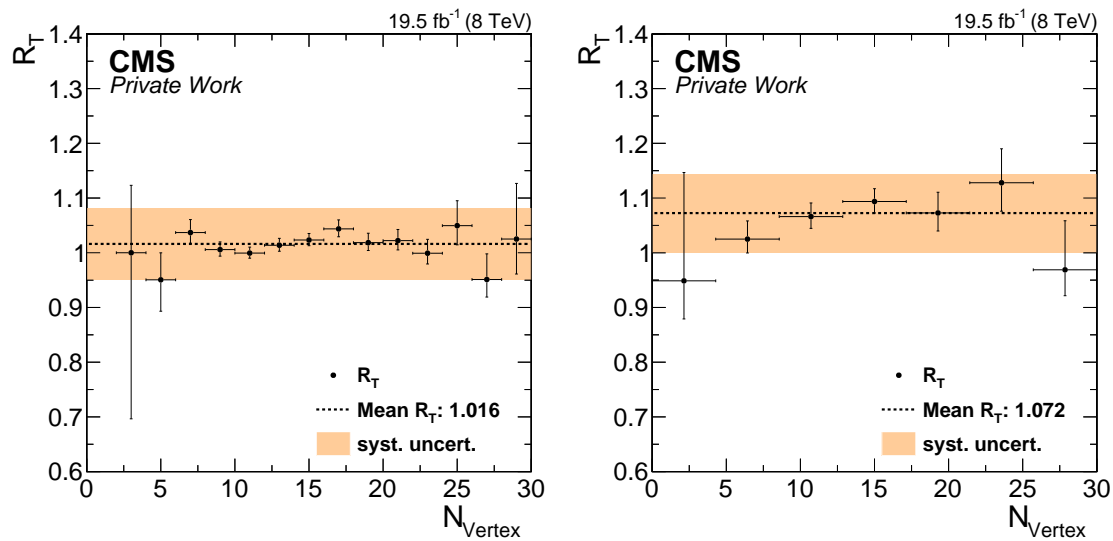


Figure D.3: Dependencies of R_T on N_{vertex} for the central (left) and forward (right) lepton selection. The results on data are shown in black. The central value is shown as a black dashed line while the systematic uncertainty is shown as an orange band.

E Dependencies of $R_{\text{out/in}}$

In addition to the results for the low-mass region already shown in Section 5.2.3, the dependency of $R_{\text{out/in}}$ on $E_{\text{T}}^{\text{miss}}$ and N_{jets} is also studied for the high-mass region. The corresponding results are shown in Figure E.1. As for the low-mass region, no significant dependencies are observed.

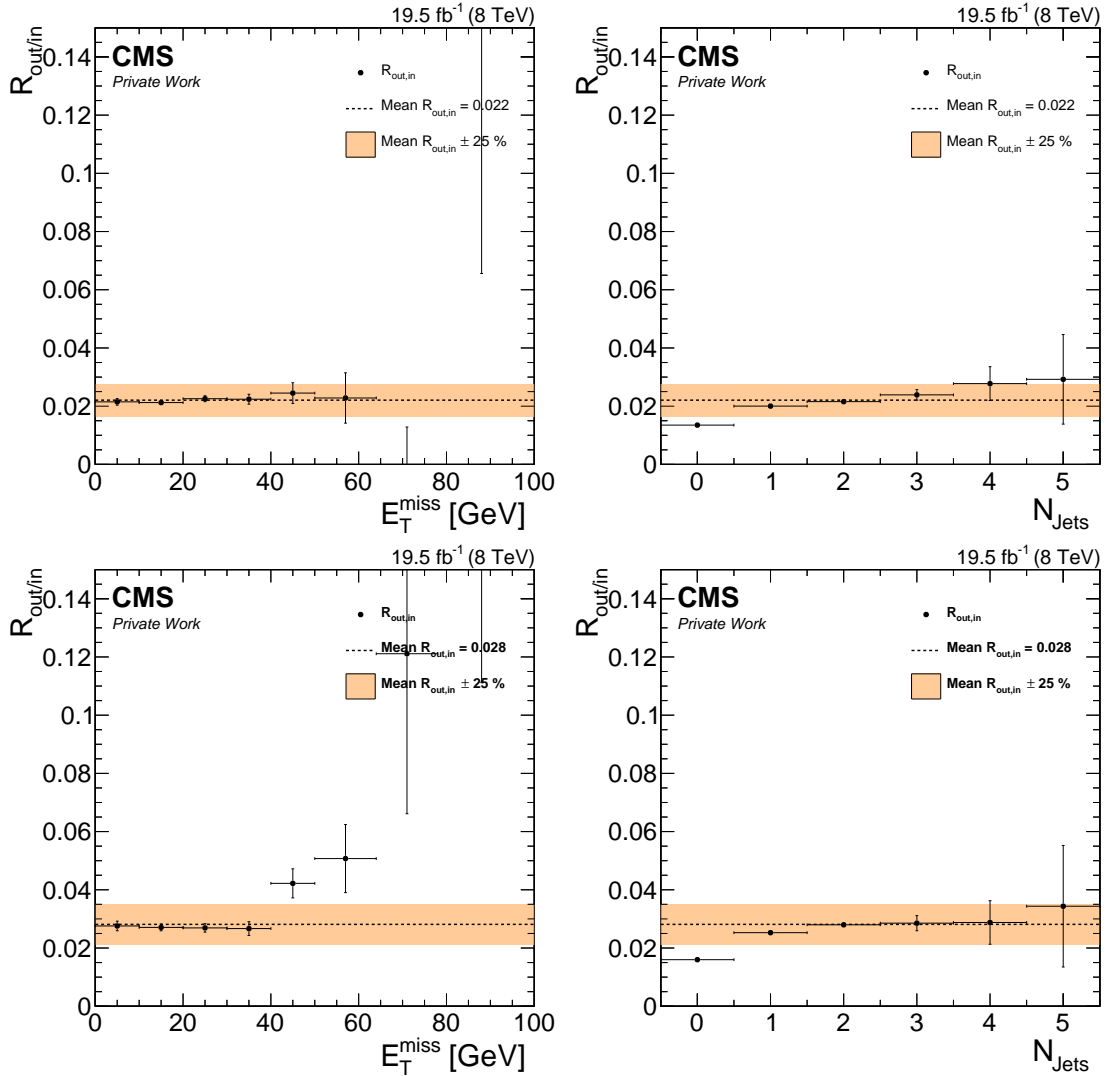


Figure E.1: Dependencies of $R_{\text{out/in}}$ for the high-mass region on $E_{\text{T}}^{\text{miss}}$ (left) and N_{jets} (right) for the central (top) and forward (bottom) lepton selection. The results on data are shown in black. The central value is shown as a black dashed line while the systematic uncertainty is shown as an orange band.

Bibliography

- [1] N. Mohr, "Search for Supersymmetry in Opposite-sign Dilepton Final States with the CMS Experiment". PhD thesis, Aachen, RWTH Aachen University, 2011.
<https://cds.cern.ch/record/1423334>.
- [2] D. Sprenger, "Search for Supersymmetry in Opposite-sign Dilepton Final States with the CMS Experiment". PhD thesis, Aachen, RWTH Aachen University, 2012.
<https://cds.cern.ch/record/1501963>.
- [3] M.-A. Buchmann, "Search for Physics Beyond the Standard Model in the Opposite-Sign Same-Flavor Dilepton Final State with the CMS Detector". PhD thesis, Zurich, ETH, 2014. <https://cds.cern.ch/record/1704399>.
- [4] CMS Collaboration, "Search for physics beyond the standard model in events with two leptons, jets, and missing transverse momentum in pp collisions at $\sqrt{s} = 8$ TeV", [arXiv:1502.06031](https://arxiv.org/abs/1502.06031). Accepted by JHEP **FIXME: look for publication**.
- [5] S. L. Glashow, "Partial-symmetries of weak interactions", *Nuclear Physics* **22** (1961) 579, [doi:
http://dx.doi.org/10.1016/0029-5582\(61\)90469-2](https://doi.org/10.1016/0029-5582(61)90469-2).
- [6] A. Salam and J. Ward, "Electromagnetic and weak interactions", *Physics Letters* **13** (1964) 168, [doi:
http://dx.doi.org/10.1016/0031-9163\(64\)90711-5](https://doi.org/10.1016/0031-9163(64)90711-5).
- [7] S. Weinberg, "A Model of Leptons", *Phys. Rev. Lett.* **19** (1967) 1264, [doi:
10.1103/PhysRevLett.19.1264](https://doi.org/10.1103/PhysRevLett.19.1264).
- [8] S. Weinberg, "Effects of a Neutral Intermediate Boson in Semileptonic Processes", *Phys. Rev. D* **5** (1972) 1412, [doi:
10.1103/PhysRevD.5.1412](https://doi.org/10.1103/PhysRevD.5.1412).
- [9] K.A. Olive et al. (Particle Data Group), "Review of particle physics", *Chin. Phys. C* **38** (2014).
- [10] A. Pich, "The Standard model of electroweak interactions", [arXiv:0705.4264](https://arxiv.org/abs/0705.4264).
- [11] F. Halzen and A. Martin, "Quarks and Leptons: An Introductory Course in Modern Particle Physics". John Wiley & Sons, 1984.
- [12] P. W. Higgs, "Broken Symmetries and the Masses of Gauge Bosons", *Phys. Rev. Lett.* **13** (1964) 508, [doi:
10.1103/PhysRevLett.13.508](https://doi.org/10.1103/PhysRevLett.13.508).
- [13] F. Englert and R. Brout, "Broken Symmetry and the Mass of Gauge Vector Mesons", *Phys. Rev. Lett.* **13** (1964) 321, [doi:
10.1103/PhysRevLett.13.321](https://doi.org/10.1103/PhysRevLett.13.321).
- [14] G. S. Guralnik, C. R. Hagen, and T. W. B. Kibble, "Global Conservation Laws and Massless Particles", *Phys. Rev. Lett.* **13** (1964) 585, [doi:
10.1103/PhysRevLett.13.585](https://doi.org/10.1103/PhysRevLett.13.585).

- [15] ATLAS, CMS Collaboration, “Combined Measurement of the Higgs Boson Mass in pp Collisions at $\sqrt{s} = 7$ and 8 TeV with the ATLAS and CMS Experiments”, [arXiv:1503.07589](https://arxiv.org/abs/1503.07589). Accepted by PRL **FIXME: Check for publication**.
- [16] CMS Collaboration, “Observation of a new boson at a mass of 125 GeV with the CMS experiment at the LHC”, *Phys. Lett. B* **716** (2012) 30, [doi:10.1016/j.physletb.2012.08.021](https://doi.org/10.1016/j.physletb.2012.08.021), [arXiv:1207.7235](https://arxiv.org/abs/1207.7235).
- [17] ATLAS Collaboration, “Observation of a new particle in the search for the Standard Model Higgs boson with the ATLAS detector at the LHC”, *Phys. Lett. B* **716** (2012) 1, [doi:10.1016/j.physletb.2012.08.020](https://doi.org/10.1016/j.physletb.2012.08.020), [arXiv:1207.7214](https://arxiv.org/abs/1207.7214).
- [18] CMS Collaboration, “Precise determination of the mass of the Higgs boson and tests of compatibility of its couplings with the standard model predictions using proton collisions at 7 and 8 TeV”, [arXiv:1412.8662](https://arxiv.org/abs/1412.8662). Submitted to Eur. Phys. J. C.
- [19] Planck Collaboration, “Planck 2015 results. I. Overview of products and scientific results”, (2015). [arXiv:1502.01582](https://arxiv.org/abs/1502.01582).
- [20] S. P. Martin, “A Supersymmetry primer”, *Adv. Ser. Direct. High Energy Phys.* **21** (2010) 1, [doi:10.1142/9789814307505_0001](https://doi.org/10.1142/9789814307505_0001), [arXiv:hep-ph/9709356](https://arxiv.org/abs/hep-ph/9709356).
- [21] J. Wess and B. Zumino, “Supergauge transformations in four dimensions”, *Nuclear Physics B* **70** (1974) 39, [doi:\[http://dx.doi.org/10.1016/0550-3213\\(74\\)90355-1\]\(http://dx.doi.org/10.1016/0550-3213\(74\)90355-1\)](http://dx.doi.org/10.1016/0550-3213(74)90355-1).
- [22] Prospino2, “SUSY cross sections at $\sqrt{s} = 8$ TeV”. http://www.thphys.uni-heidelberg.de/~plehn/includes/prospino/prospino_lhc8.eps. Accessed: 2015-04-19.
- [23] W. Beenakker et al., “The Production of charginos / neutralinos and sleptons at hadron colliders”, *Phys. Rev. Lett.* **83** (1999) 3780, [doi:10.1103/PhysRevLett.100.029901](https://doi.org/10.1103/PhysRevLett.100.029901), [10.1103/PhysRevLett.83.3780](https://doi.org/10.1103/PhysRevLett.83.3780), [arXiv:hep-ph/9906298](https://arxiv.org/abs/hep-ph/9906298).
- [24] W. Beenakker et al., “Stop production at hadron colliders”, *Nucl. Phys. B* **515** (1998) 3, [doi:10.1016/S0550-3213\(98\)00014-5](https://doi.org/10.1016/S0550-3213(98)00014-5), [arXiv:hep-ph/9710451](https://arxiv.org/abs/hep-ph/9710451).
- [25] W. Beenakker, R. Höpker, M. Spira, and P. M. Zerwas, “Squark and gluino production at hadron colliders”, *Nucl. Phys. B* **492** (1997) 51, [doi:10.1016/S0550-3213\(97\)00084-9](https://doi.org/10.1016/S0550-3213(97)00084-9), [arXiv:hep-ph/9610490](https://arxiv.org/abs/hep-ph/9610490).
- [26] C. Schomakers, “Studies of simplified models and projection to $\sqrt{s}=13$ TeV for the CMS SUSY dilepton edge search”, Master’s thesis, Aachen, RWTH Aachen University, 2014. http://web.physik.rwth-aachen.de/service/wiki/pub/FeldFeldAbschlussarbeiten/Masterarbeit_Christian_Schomakers.pdf.
- [27] A. Kulesza and L. Motyka, “Threshold resummation for squark-antisquark and gluino-pair production at the LHC”, *Phys. Rev. Lett.* **102** (2009) 111802, [doi:10.1103/PhysRevLett.102.111802](https://doi.org/10.1103/PhysRevLett.102.111802), [arXiv:0807.2405](https://arxiv.org/abs/0807.2405).
- [28] A. Kulesza and L. Motyka, “Soft gluon resummation for the production of

- gluino-gluino and squark-antisquark pairs at the LHC", *Phys. Rev. D* **80** (2009) 095004, [doi:10.1103/PhysRevD.80.095004](https://doi.org/10.1103/PhysRevD.80.095004), [arXiv:0905.4749](https://arxiv.org/abs/0905.4749).
- [29] W. Beenakker et al., "Soft-gluon resummation for squark and gluino hadroproduction", *JHEP* **12** (2009) 041, [doi:10.1088/1126-6708/2009/12/041](https://doi.org/10.1088/1126-6708/2009/12/041), [arXiv:0909.4418](https://arxiv.org/abs/0909.4418).
- [30] W. Beenakker et al., "Squark and gluino hadroproduction", *Int. J. Mod. Phys. A* **26** (2011) 2637, [doi:10.1142/S0217751X11053560](https://doi.org/10.1142/S0217751X11053560), [arXiv:1105.1110](https://arxiv.org/abs/1105.1110).
- [31] M. Krämer et al., "Supersymmetry production cross sections in pp collisions at $\sqrt{s} = 7$ TeV", (2012). [arXiv:1206.2892](https://arxiv.org/abs/1206.2892).
- [32] W.J. Stirling. Private communication.
- [33] L. Evans and P. Bryant, "LHC Machine", *JINST* **3** (2008) S08001, [doi:10.1088/1748-0221/3/08/S08001](https://doi.org/10.1088/1748-0221/3/08/S08001).
- [34] CMS Collaboration, "The CMS experiment at the CERN LHC", *JINST* **3** (2008) S08004, [doi:10.1088/1748-0221/3/08/S08004](https://doi.org/10.1088/1748-0221/3/08/S08004).
- [35] ATLAS Collaboration, "The ATLAS Experiment at the CERN Large Hadron Collider", *JINST* **3** (2008) S08003, [doi:10.1088/1748-0221/3/08/S08003](https://doi.org/10.1088/1748-0221/3/08/S08003).
- [36] ALICE Collaboration, "The ALICE experiment at the CERN LHC", *JINST* **3** (2008) S08002, [doi:10.1088/1748-0221/3/08/S08002](https://doi.org/10.1088/1748-0221/3/08/S08002).
- [37] LHCb Collaboration, "The LHCb Detector at the LHC", *JINST* **3** (2008) S08005, [doi:10.1088/1748-0221/3/08/S08005](https://doi.org/10.1088/1748-0221/3/08/S08005).
- [38] "Particle kickers". <https://cds.cern.ch/record/1706606/>. Accessed: 2014-08-06.
- [39] CMS Collaboration, "Public CMS Luminosity Information". <https://twiki.cern.ch/twiki/bin/view/CMSPublic/LumiPublicResults?rev=101>. Accessed: 2014-08-06.
- [40] "CMS detector design". <http://cms.web.cern.ch/news/cms-detector-design>. Accessed: 2014-08-08.
- [41] CMS Collaboration, "Electromagnetic calorimeter calibration with 7 TeV data", *Physics Analysis Summary CMS-PAS-EGM-10-003* (2010).
- [42] CMS Collaboration, "Performance of CMS muon reconstruction in pp collision events at $\sqrt{s} = 7$ TeV", *JINST* **7** (2012) P10002, [doi:10.1088/1748-0221/7/10/P10002](https://doi.org/10.1088/1748-0221/7/10/P10002), [arXiv:1206.4071](https://arxiv.org/abs/1206.4071).
- [43] CMS Collaboration, "The CMS high level trigger", *Eur. Phys. J. C* **46** (2006) 605, [doi:10.1140/epjc/s2006-02495-8](https://doi.org/10.1140/epjc/s2006-02495-8), [arXiv:hep-ex/0512077](https://arxiv.org/abs/hep-ex/0512077).
- [44] G. Bauer et al., "The CMS High Level Trigger System: Experience and Future Development", *Journal of Physics: Conference Series* **396** (2012) 012008, [doi:10.1088/1742-6596/396/1/012008](https://doi.org/10.1088/1742-6596/396/1/012008).
- [45] "CMS HLT config browser".

- <http://j2eeps.cern.ch/cms-project-confdb-hltdev/browser/>. Accessed: 2014-10-09.
- [46] CMS Collaboration, “Search for supersymmetry in pp collisions at 7 TeV in events with jets and missing transverse energy”, *Physics Letters B* **698** (2011) 196, [doi:10.1016/j.physletb.2011.03.021](https://doi.org/10.1016/j.physletb.2011.03.021), [arXiv:1101.1628](https://arxiv.org/abs/1101.1628).
- [47] CMS Collaboration, “Particle-Flow Event Reconstruction in CMS and Performance for Jets, Taus, and MET”, *Physics Analysis Summary CMS-PAS-PFT-09-001* (2009).
- [48] K. Rose, “Deterministic annealing for clustering, compression, classification, regression, and related optimization problems”, *Proceedings of the IEEE* **8** (1998) [doi:10.1109/5.726788](https://doi.org/10.1109/5.726788).
- [49] CMS Collaboration, “Description and performance of track and primary-vertex reconstruction with the CMS tracker”, *JINST* **9** (2014) P10009, [doi:10.1088/1748-0221/9/10/P10009](https://doi.org/10.1088/1748-0221/9/10/P10009), [arXiv:1405.6569](https://arxiv.org/abs/1405.6569).
- [50] R. Frühwirth, W. Waltenberger, and P. Vanlaer, “Adaptive vertex fitting”, *Journal of Physics G: Nuclear and Particle Physics* **34** (2007) N343, [doi:10.1088/0954-3899/34/12/N01](https://doi.org/10.1088/0954-3899/34/12/N01).
- [51] R. Frühwirth, “Application of Kalman filtering to track and vertex fitting”, *Nuclear Instruments and Methods in Physics Research Section A: Accelerators, Spectrometers, Detectors and Associated Equipment* **262** (1987) 444, [doi:\[http://dx.doi.org/10.1016/0168-9002\\(87\\)90887-4\]\(http://dx.doi.org/10.1016/0168-9002\(87\)90887-4\)](http://dx.doi.org/10.1016/0168-9002(87)90887-4).
- [52] “CMS Software Guide on Iterative Tracking”. <https://twiki.cern.ch/twiki/bin/view/CMSPublic/SWGuideIterativeTracking?rev=9>. Accessed: 2014-10-11.
- [53] C. Collaboration, “Performance of CMS muon reconstruction in cosmic-ray events”, *JINST* **5** (2010) T03022, [doi:10.1088/1748-0221/5/03/T03022](https://doi.org/10.1088/1748-0221/5/03/T03022), [arXiv:0911.4994](https://arxiv.org/abs/0911.4994).
- [54] CMS Collaboration, “Particle-flow commissioning with muons and electrons from J/Psi and W events at 7 TeV”, *Physics Analysis Summary CMS-PAS-PFT-10-003* (2010).
- [55] S. Baffioni et al., “Electron reconstruction in CMS”, *Eur. Phys. J. C* **49** (2007) 1099, [doi:10.1140/epjc/s10052-006-0175-5](https://doi.org/10.1140/epjc/s10052-006-0175-5).
- [56] CMS Collaboration, “Review of clustering algorithms and energy corrections in ECAL”, *CMS Internal Note IN-10-008* (2010).
- [57] W. Adam, R. Frühwirth, A. Strandlie, and T. Todorov, “Reconstruction of electrons with the Gaussian-sum filter in the CMS tracker at the LHC”, *Journal of Physics G: Nuclear and Particle Physics* **31** (2005) 9, [doi:10.1088/0954-3899/31/9/N01](https://doi.org/10.1088/0954-3899/31/9/N01), [arXiv:physics/0306087](https://arxiv.org/abs/physics/0306087).
- [58] CMS Collaboration, “Performance of electron reconstruction and selection with the CMS detector in proton-proton collisions at $\sqrt{s} = 8$ TeV”, [arXiv:1502.02701](https://arxiv.org/abs/1502.02701). Submitted to JINST.

- [59] M. Cacciari, G. P. Salam, and G. Soyez, “The Anti- k_t jet clustering algorithm”, *JHEP* **0804** (2008) 63, [doi:10.1088/1126-6708/2008/04/063](https://doi.org/10.1088/1126-6708/2008/04/063), [arXiv:0802.1189](https://arxiv.org/abs/0802.1189).
- [60] M. Cacciari, G. P. Salam, and G. Soyez, “FastJet User Manual”, *Eur. Phys. J. C* **72** (2012) 1896, [doi:10.1140/epjc/s10052-012-1896-2](https://doi.org/10.1140/epjc/s10052-012-1896-2), [arXiv:1111.6097](https://arxiv.org/abs/1111.6097).
- [61] M. Cacciari and G. P. Salam, “Dispelling the N^3 myth for the k_t jet-finder”, *Phys. Lett. B* **641** (2006) 57, [doi:10.1016/j.physletb.2006.08.037](https://doi.org/10.1016/j.physletb.2006.08.037), [arXiv:hep-ph/0512210](https://arxiv.org/abs/hep-ph/0512210).
- [62] CMS Collaboration, “Determination of jet energy calibration and transverse momentum resolution in CMS”, *JINST* **6** (2011), no. 11, P11002, [doi:10.1088/1748-0221/6/11/P11002](https://doi.org/10.1088/1748-0221/6/11/P11002), [arXiv:1107.4277](https://arxiv.org/abs/1107.4277).
- [63] S. Catani et al., “New clustering algorithm for multi - jet cross-sections in $e^+ e^-$ annihilation”, *Phys. Lett. B* **269** (1991) 432, [doi:10.1016/0370-2693\(91\)90196-W](https://doi.org/10.1016/0370-2693(91)90196-W).
- [64] CMS Collaboration, “Identification of b-quark jets with the CMS experiment”, *JINST* **8** (2013) P04013, [doi:10.1088/1748-0221/8/04/P04013](https://doi.org/10.1088/1748-0221/8/04/P04013), [arXiv:1211.4462](https://arxiv.org/abs/1211.4462).
- [65] CMS Collaboration, “Results on b-tagging identification in 8 TeV pp collisions”, *CMS Detector performance note CMS-DP-2013-005* (2013). <https://cds.cern.ch/record/1528183>.
- [66] CMS Collaboration, “Missing transverse energy performance of the CMS detector”, *JINST* **6** (2011) P09001, [doi:10.1088/1748-0221/6/09/P09001](https://doi.org/10.1088/1748-0221/6/09/P09001), [arXiv:1106.5048](https://arxiv.org/abs/1106.5048).
- [67] CMS Collaboration, “MET performance in 8 TeV data”, *Physics Analysis Summary CMS-PAS-JME-12-002* (2013).
- [68] CMS Collaboration, “CMS Physics: Technical Design Report Volume 1: Detector Performance and Software”. Technical Design Report CMS. CERN, Geneva, 2006.
- [69] “CMS Software Guide on the CMSSW Application Framework”. <https://twiki.cern.ch/twiki/bin/view/CMSPublic/WorkBookCMSSWFramework?rev=13>. Accessed: 2014-10-26.
- [70] I. Bird, “Computing for the Large Hadron Collider”, *Annual Review of Nuclear and Particle Science* **61** (2011) 99, [doi:10.1146/annurev-nucl-102010-130059](https://doi.org/10.1146/annurev-nucl-102010-130059).
- [71] “Worldwide LHC Computing Grid ”. <http://wlcg.web.cern.ch/>. Accessed: 2014-10-26.
- [72] D. Spiga et al., “The CMS Remote Analysis Builder (CRAB)”, *Lecture Notes in Computer Science* **4873** (2007) 580, [doi:10.1007/978-3-540-77220-0_52](https://doi.org/10.1007/978-3-540-77220-0_52).
- [73] W. Adam et al., “PAT: The CMS Physics Analysis Toolkit”, *Journal of Physics: Conference Series* **219** (2010) 032017, [doi:10.1088/1742-6596/219/3/032017](https://doi.org/10.1088/1742-6596/219/3/032017).
- [74] R. Brun and F. Rademakers, “ROOT - An Object Oriented Data Analysis Framework”,

- Nucl. Inst. & Meth. in Phys. Res. A* **389** (1996) 81. See also <http://root.cern.ch/>.
- [75] A. Afanasev et al., “The CMS dataset bookkeeping service”, *Journal of Physics: Conference Series* **119** (2008) 072001, [doi:10.1088/1742-6596/119/7/072001](https://doi.org/10.1088/1742-6596/119/7/072001).
- [76] H1 and ZEUS Collaboration, “Combined Measurement and QCD Analysis of the Inclusive $e^{+/-}$ p Scattering Cross Sections at HERA”, *JHEP* **1001** (2010) 109, [doi:10.1007/JHEP01\(2010\)109](https://doi.org/10.1007/JHEP01(2010)109), [arXiv:0911.0884](https://arxiv.org/abs/0911.0884).
- [77] J. Pumplin et al., “New generation of parton distributions with uncertainties from global QCD analysis”, *JHEP* **0207** (2002) 12, [doi:10.1088/1126-6708/2002/07/012](https://doi.org/10.1088/1126-6708/2002/07/012), [arXiv:hep-ph/0201195](https://arxiv.org/abs/hep-ph/0201195).
- [78] R. D. Ball et al., “Parton distributions with LHC data”, *Nucl. Phys. B* **867** (2013) 244, [doi:10.1016/j.nuclphysb.2012.10.003](https://doi.org/10.1016/j.nuclphysb.2012.10.003), [arXiv:1207.1303](https://arxiv.org/abs/1207.1303).
- [79] A. Martin, W. Stirling, R. Thorne, and G. Watt, “Parton distributions for the LHC”, *Eur. Phys. J. C* **63** (2009) 189, [doi:10.1140/epjc/s10052-009-1072-5](https://doi.org/10.1140/epjc/s10052-009-1072-5), [arXiv:0901.0002](https://arxiv.org/abs/0901.0002).
- [80] H.-L. Lai et al., “New parton distributions for collider physics”, *Phys. Rev. D* **82** (2010) 074024, [doi:10.1103/PhysRevD.82.074024](https://doi.org/10.1103/PhysRevD.82.074024), [arXiv:1007.2241](https://arxiv.org/abs/1007.2241).
- [81] V. N. Gribov and L. N. Lipatov, “Deep inelastic electron scattering in perturbation theory”, *Sov. J. Nucl. Phys.* **15** (1972) 438.
- [82] G. Altarelli and G. Parisi, “Asymptotic Freedom in Parton Language”, *Nucl. Phys. B* **126** (1977) 298, [doi:10.1016/0550-3213\(77\)90384-4](https://doi.org/10.1016/0550-3213(77)90384-4).
- [83] Y. L. Dokshitzer, “Calculation of the Structure Functions for Deep Inelastic Scattering and $e^{+}e^{-}$ Annihilation by Perturbation Theory in Quantum Chromodynamics”, *Sov. Phys. JETP* **46** (1977) 641.
- [84] J. Alwall et al., “MadGraph 5 : Going Beyond”, *JHEP* **1106** (2011) 128, [doi:10.1007/JHEP06\(2011\)128](https://doi.org/10.1007/JHEP06(2011)128), [arXiv:1106.0522](https://arxiv.org/abs/1106.0522).
- [85] T. Sjöstrand, S. Mrenna, and P. Z. Skands, “PYTHIA 6.4 Physics and Manual”, *JHEP* **05** (2006) 26, [doi:10.1088/1126-6708/2006/05/026](https://doi.org/10.1088/1126-6708/2006/05/026), [arXiv:hep-ph/0603175](https://arxiv.org/abs/hep-ph/0603175).
- [86] S. Hoeche et al., “Matching parton showers and matrix elements”, [arXiv:hep-ph/0602031](https://arxiv.org/abs/hep-ph/0602031).
- [87] P. Nason, “A New method for combining NLO QCD with shower Monte Carlo algorithms”, *JHEP* **0411** (2004) 40, [doi:10.1088/1126-6708/2004/11/040](https://doi.org/10.1088/1126-6708/2004/11/040), [arXiv:hep-ph/0409146](https://arxiv.org/abs/hep-ph/0409146).
- [88] S. Alioli, P. Nason, C. Oleari, and E. Re, “NLO single-top production matched with shower in POWHEG: s- and t-channel contributions”, *JHEP* **0909** (2009) 111, [doi:10.1007/JHEP02\(2010\)011](https://doi.org/10.1007/JHEP02(2010)011), [10.1088/1126-6708/2009/09/111](https://doi.org/10.1088/1126-6708/2009/09/111), [arXiv:0907.4076](https://arxiv.org/abs/0907.4076).
- [89] E. Re, “Single-top Wt-channel production matched with parton showers using the

- POWHEG method”, *Eur. Phys. J. C* **71** (2011) 1547,
`doi:10.1140/epjc/s10052-011-1547-z`, `arXiv:1009.2450`.
- [90] R. Field, “Min-Bias and the Underlying Event at the LHC”, *Acta Phys. Polon. B* **42** (2011) 2631, `doi:10.5506/APhysPolB.42.2631`, `arXiv:1110.5530`. Tune $Z2^*$ is a variation of Tune $Z2$ described in this reference.
- [91] S. Jadach, Z. Wąs, R. Decker, and J. Kühn, “The τ decay library TAUOLA, version 2.4”, *Computer Physics Communications* **76** (1993) 361,
`doi:http://dx.doi.org/10.1016/0010-4655(93)90061-G`.
- [92] GEANT4 Collaboration, “GEANT4: A Simulation toolkit”, *Nucl. Instrum. Meth. A* **506** (2003) 250, `doi:10.1016/S0168-9002(03)01368-8`.
- [93] CMS Collaboration, “The fast simulation of the CMS detector at LHC”, *J. Phys. Conf. Ser.* **331** (2011) 032049, `doi:10.1088/1742-6596/331/3/032049`.
- [94] CMS Collaboration, “Top pair cross section in dileptons”, *Physics Analysis Summary CMS-PAS-TOP-12-007* (2012).
- [95] Y. Li and F. Petriello, “Combining QCD and electroweak corrections to dilepton production in FEWZ”, *Phys. Rev. D* **86** (2012) 094034,
`doi:10.1103/PhysRevD.86.094034`, `arXiv:1208.5967`.
- [96] J. M. Campbell, R. K. Ellis, and C. Williams, “Vector boson pair production at the LHC”, *JHEP* **1107** (2011) 18, `doi:10.1007/JHEP07(2011)018`,
`arXiv:1105.0020`.
- [97] N. Kidonakis, “Differential and total cross sections for top pair and single top production”, `doi:10.3204/DESY-PROC-2012-02/251`, `arXiv:1205.3453`.
- [98] J. Alwall et al., “The automated computation of tree-level and next-to-leading order differential cross sections, and their matching to parton shower simulations”, *Journal of High Energy Physics* **79** (2014) `doi:10.1007/JHEP07(2014)079`.
- [99] M. Garzelli, A. Kardos, C. Papadopoulos, and Z. Trocsanyi, “ $t\bar{t} W^{+-}$ and $t\bar{t} Z$ Hadroproduction at NLO accuracy in QCD with Parton Shower and Hadronization effects”, *JHEP* **1211** (2012) 56, `doi:10.1007/JHEP11(2012)056`,
`arXiv:1208.2665`.
- [100] CMS Collaboration, “Measurement of the inclusive top-quark pair + photon production cross section in the muon + jets channel in pp collisions at 8 TeV”, *Physics Analysis Summary CMS-PAS-TOP-13-011* (2014).
- [101] CMS Collaboration, “CMS Twiki page on top p_T reweighting”.
`https://twiki.cern.ch/twiki/bin/view/CMS/TopPtReweighting?rev=18`. Accessed: 2015-04-16.
- [102] L. Tuura, A. Meyer, I. Segoni, and G. D. Ricca, “CMS data quality monitoring: Systems and experiences”, *Journal of Physics: Conference Series* **219** (2010) 072020,
`doi:10.1088/1742-6596/219/7/072020`.

- [103] P. Milenovic et al., “Computing the contamination from fakes in leptonic final states”, *CMS Analysis Note* **2010/261** (2010).
- [104] M. Dunser et al., “Search for New Physics in the Same-Sign Di-Lepton Channel at 8 TeV”, *CMS Analysis Note* **2012/199** (2012).
- [105] CMS Collaboration Collaboration, “Search for physics beyond the standard model in events with a Z boson, jets, and missing transverse energy in pp collisions at $\sqrt{s} = 7$ TeV”, *Phys. Lett. B* **716** (2012) 260, doi:10.1016/j.physletb.2012.08.026, arXiv:1204.3774.
- [106] CMS and ATLAS Collaborations, “Procedure for the LHC Higgs boson search combination in Summer 2011”, *CMS-NOTE-2011-005, ATL-PHYS-PUB-2011-011*.
- [107] CMS Collaboration, “CMS Luminosity Based on Pixel Cluster Counting - Summer 2013 Update”, *CMS Physics Analysis Summary CMS-PAS-LUM-13-001* (2013).
- [108] S. Alekhin et al., “The PDF4LHC Working Group Interim Report”, (2011). arXiv:1101.0536.
- [109] M. Botje et al., “The PDF4LHC Working Group Interim Recommendations”, (2011). arXiv:1101.0538.
- [110] CMS Collaboration, “Search for top-squark pair production in the single-lepton final state in pp collisions at $\sqrt{s} = 8$ TeV”, *Eur. Phys. J. C* **73** (2013) 2677, doi:10.1140/epjc/s10052-013-2677-2, arXiv:1308.1586.
- [111] W. Verkerke and D. P. Kirkby, “The RooFit toolkit for data modeling”, in *2003 Computing in High Energy and Nuclear Physics (CHEP03)*, p. 183. 2003. arXiv:physics/0306116. eConf C0303241 (2003) MOLT007.
- [112] M. Oreglia, “A study of the reactions $\psi' \rightarrow \gamma\gamma\psi$ ”, *Ph.D. thesis, Stanford University, SLAC Report SLAC-R-236* (1980). <http://www.slac.stanford.edu/pubs/slacreports/slac-r-236.html>.
- [113] CMS Collaboration, “Search for new physics in events with opposite-sign leptons, jets, and missing transverse energy in pp collisions at $\sqrt{s} = 7$ TeV”, *Phys. Lett. B* **718** (2013) 815, doi:10.1016/j.physletb.2012.11.036, arXiv:1206.3949.
- [114] K. S. Cranmer, “Kernel estimation in high-energy physics”, *Comput. Phys. Commun.* **136** (2001) 198, doi:10.1016/S0010-4655(00)00243-5, arXiv:hep-ex/0011057.
- [115] S. S. Wilks, “The Large-Sample Distribution of the Likelihood Ratio for Testing Composite Hypotheses”, *The Annals of Mathematical Statistics* **9** (1938) 60, doi:10.1214/aoms/1177732360.
- [116] E. Gross and O. Vitells, “Trial factors for the look elsewhere effect in high energy physics”, *The European Physical Journal C* **70** (2010) 525, doi:10.1140/epjc/s10052-010-1470-8, arXiv:1005.1891.